UNIVERSITY OF SOUTHAMPTON

FACULTY OF ENGINEERING AND THE ENVIRONMENT

Fluid Structure Interactions Group

Design practice for the stern hull of a future twin-skeg ship using a high fidelity numerical approach

by

Charles Erzan Badoe

Thesis for the degree of Doctor of Philosophy

April 2015

UNIVERSITY OF SOUTHAMPTON

ABSTRACT

FACULTY OF ENGINEERING AND THE ENVIRONMENT

Fluid Structure Interactions Group

Doctor of Philosophy

DESIGN PRACTICE FOR THE STERN HULL OF A FUTURE TWIN-SKEG SHIP USING A HIGH FIDELITY NUMERICAL APPROACH

By Charles Erzan Badoe

The ability to predict the powering performance of twin skeg LNG ship is a complex endeavour requiring appraisal of operating conditions and hydrodynamic analysis to arrive at a suitable stern design solution. Inherently coupled with the stern design process is the design optimization, namely the selection of most suitable geometrical parameters of the propulsor, control surface and their arrangements with respect to the hull. An approach to the stern design may commence with the prediction of general ship stern flow, hence its resistance and self-propulsion capabilities. Almost a century of experience exists regarding how to predict the resistance and powering capabilities of the twin skeg LNG ship. Despite this, improvement in numerical methods is still in high demand.

A RANS based numerical approach is presented in this thesis to predict the resistance and powering performance of future twin skeg ships. This is supported by a meshing approach which easily blends the hull-skeg boundary layer to the free surface. Predicting the non-uniform wake in the propeller plane due to the hull-skeg and control surface interaction was identified as one of the main challenges in the stern design and powering assessment. To predict this within acceptable cost a sectorial approach was developed as part of the numerical method which discretizes the propeller plane into a series of radial and circumferential subdivisions. The local axial and tangential inflow conditions at each location can then be considered. This was coupled to a blade element momentum theory propeller code. The two-way coupling was found to be a computationally efficient tool for studying the powering performance of ships.

To demonstrate the pertinence of the RANS based numerical approaches developed in this work a series of case studies has been analysed. These include: skeg-rudder-propeller interaction studies, propulsive characteristic of the KCS ship, and the resistance and self-propulsion characteristics of a future twin skeg LNG ship. These highlight the roles of the numerical approaches in the stern design process for future twin skeg ships. The techniques developed in this work enable the designer to predict the powering performance of future twin skeg LNG ships at a cost effective manner in the initial design stage.

Declaration of Authorship

I, Charles Erzan Badoe, declare that this thesis entitled 'Design practice for the stern hull of a future twin-skeg ship using a high fidelity numerical approach' and the work presented in this thesis are both my own, and have been generated by me as the result of my own original research. I confirm that:

- this work was done wholly or mainly while in candidature for a research degree at this University;
- where any part of this thesis has previously been submitted for a degree or any other qualification at this University or any institution, this has been clearly stated;
- where I have consulted the published work of others, this is always clearly attributed;
- where I have quoted from the work of others, the source is always given, With the exception of such quotations, this thesis is entirely my own work;
- I have acknowledge all main source of help;
- where the thesis is based on work done by myself jointly with others, I have made clear exactly what was done by others and what I have contributed myself;

The following aspects of this work have been presented at international conferences and published by or submitted to peer review journals.

Journal papers

Badoe, C., Turnock, S.R., and Phillips, A.B., 2014a. Influence of drift angle on propeller rudder interaction, Journal of ocean engineering (in review).

Badoe, C., Turnock, S.R., Windén, B., Lidtke, K.A., Hudson, D., and Phillips, A.B., 2014b. Analysis of ship resistance and propulsion using different approaches, Journal of marine science (pending submission).

Conferences and workshops

Badoe, C., Turnock, S.R., Windén, B., Lidtke, K.A., Hudson, D., and Phillips, A.B., 2014b. Comparison of various approaches to ship resistance and propulsion, *in* Proceedings of the SIMMAN workshop on verification and validation of ship manoeuvring simulation methods, Denmark, 8-10 December.

Badoe, C., Turnock, S.R., and Phillips, A.B., 2014a. Ship wake field analysis using a coupled BEMt-RANS approach, *in* 'Proceedings of the 17th Numerical Towing Tank Symposium, 28-30 September, Marstrand, Sweden.

Badoe, C., Turnock, S.R., Windén, B., Hudson, D., and Phillips, A.B., 2013. Self-propulsion in waves using a coupled RANS-BEMt model and active RPM control, *in* Proceedings of the 16th Numerical Towing Tank Symposium, 2-4 September, Duisburg, Germany.

Badoe, C., Lloyd, T.P., James, M, Turnock, S.R., Windén, B., Banks, J., and Phillips, A.B., 2012d. University of Southampton Fluid-Structure Interactions Group OpenFOAM research, *in* Proceedings of the 2nd Gothenburg OpenFOAM user-group meeting, 12-16 November Gothenburg, Sweden.

Badoe, C., Turnock, S.R., and Phillips, A.B., 2012c. Initial numerical propeller rudder interaction studies to assist fuel efficient shipping, *in* Proceedings of the 15th Numerical Towing Tank Symposium, 7-9 October, Cortona, Italy.

Badoe, C., Turnock, S.R., and Phillips, A.B., 2012b. Numerical propeller rudder interaction studies to assist fuel efficient shipping, *in* Proceedings of the Low Carbon Shipping Conference, 11-12 September Newcastle upon Tyne, England.

Badoe, C., Turnock, S.R., and Phillips, A.B., 2012a. Propeller -rudder interaction studies using RANS, *in* Proceedings of the 3rd Marine Technology Postgraduate Conference, 7-8 June Strathclyde, Glasgow.

I understand that my thesis may be made electronically available to the public.

Signed: .....

Date: .....

Table of Contents

List of Tables

List of Figures

Nomenclature

(1+k)	form factor
a	axial inflow factor
a'	circumferential inflow factor
A	area (m^2)
B	ship breadth (m)
c	blade chord (m)
C_B	block coefficient
C_{D_O}	drag at zero incidence
C_d	two dimensional drag coefficient
C_D	three dimensional drag coefficient
C_F	frictional resistance coefficient
C_l	two dimensional lift coefficient
C_L	three dimensional lift coefficient
C_R	residuary resistance coefficient
C_T	total resistance coefficient
C_{th}	thrust coefficient
C_v	viscous resistance coefficient
C_w	wave resistance coefficient
D_p	propeller diameter (m)
D_h	boss diameter (m)

D	ship depth (m)
E (%D)	error as a percentage of experimental value
fb_θ	tangential momentum source term $\left(\frac{N}{m^3}\right)$
fb_x	axial momentum source term $\left(\frac{N}{m^3}\right)$
Fn	Froude number
I	turbulence intensity
J	advance coefficient
k	turbulent kinetic energy $\left(\frac{m^2}{s^2}\right)$
K	Goldstein correction factor
K_Q	torque coefficient
K_T	thrust coefficient
L	length (m)
	lift force (N)
l	integral length scale (m)
n	revolutions per second (s^{-1})
N	number of blades
p	pressure (Pa)
P/D	pitch diameter ratio
P_B	brake power (W)
P_D	delivered power in behind conditions (W)
P_{Do}	delivered power in open-water conditions (W)
P_E	effective power (W)
P_T	thrust power (W)
Q	torque (Nm)
r^*	non-dimensionalized propeller radius
r_G	mesh refinement ratio
r_k	parameter refinement ratio

r_p	local propeller radius (m)
R	towed drag of ship (N)
R_G	ratio of solution changes
R_h	hub radius (m)
R_p	propeller radius (m)
Rn	Reynolds number
R_{SP}	self-propelled drag (N)
R_T	total resistance (N)
R_V	viscous resistance (N)
s	rudder span (m)
S	surface
S_{ij}	strain rate tensor
S_L	simulation lower bound
S_U	simulation upper bound
t	thrust deduction factor
T	draught (m)
	thrust (N)
T_{SP}	self-propelled thrust (N)
S_L	simulation lower bound
U_∞	freestream velocity $\left(\frac{m}{s}\right)$
U_G	grid uncertainty
U_{G1}	grid uncertainty 1
u^+	non-dimensional velocity in boundary layer based on wall stress
u_i	cartesian velocity component $\left(\frac{m}{s}\right)$
u_i'	fluctuating velocity component $\left(\frac{m}{s}\right)$
u_{inflow}	propeller inflow velocity $\left(\frac{m}{s}\right)$

v_a	axial flow velocity at a point on the propeller plane $\left(\frac{m}{s}\right)$
$v_a{}'$	local advance velocity $\left(\frac{m}{s}\right)$
V	velocity $\left(\frac{m}{s}\right)$
Va	efective or advance speed $\left(\frac{m}{s}\right)$
$\overline{Va'}$	averaged inflow velocity over propeller plane
Vs	ship speed $\left(\frac{m}{s}\right)$
w_t	nominal wake fraction
$w_t{}'$	local nominal wake fraction
w_T	effective wake fraction
X/D	rudder logitudinal separation
Y/D	rudder lateral separation
y^+	non-dimensionalised distance from wall in the boundary layer
Z/D	rudder vertical separation
α	incidence angle (deg)
a_0	no lift angle (deg)
a_E	effective rudder angle (deg)
β_{R}	geometric drift angle (deg)
β	ship drift angle (deg)
δ	rudder angle relative to ship axis (deg)
	boundary layer thickness (m)
∂K_T	local thrust coefficient
∂K_Q	local torque coefficient
$\delta_{RE,G1}$	first order error on fine mesh
δ_{ij}	Kronker delta

Δx	axial thickness of propeller domain (m)
Γ	diffusive coefficient $\left(\frac{m^2}{s}\right)$
ε	dissipation rate $\left(\frac{m^2}{s^3}\right)$
γ	flow straightening factor
η	efficiency
η_B	behind efficiency
η_D	quasi propulsive coefficient
η_H	hull efficiency
η_O	openwater efficiency
η_R	relative rotative efficiency
η_S	shaft transmission efficiency
η_i	ideal efficiency
μ	dynamic viscosity $\left(\frac{kg}{ms}\right)$
υ	kinematic viscosity $\left(\frac{m^2}{s}\right)$
ρ	fluid density $\left(\frac{kg}{m^3}\right)$
σ	standard deviation
Ω	rotational velocity (s^{-1})
Ω_{ij}	rotation rate tensor (s^{-1})
ω	vorticity (s^{-1})

Abbreviations

2D	Two Dimensional
3D	Three Dimensional
AoA	Angle of Attack
AMI	Arbitrary Mesh Interface
BAR	Blade Area Ratio
BEMt	Blade Element Momentum Theory
CFD	Computational Fluid Dynamics
CMT	Circular Motion Test
CPU	Central Processing Unit
DES	Detached Eddy Simulation
DNS	Direct Numerical Simulation
FS	Free Surface
HSVA	Hamburgische Schiffbau Versuchsanstalt GmbH Germany
ITTC	International Towing Tank Conference
KCS	KRISO Container Ship
KLNG	KRISO Liquefied Natural Gas carrier Ship
LES	Large Eddy Simulation
LNG	Liquefied Natural Gas
MOERI	Maritime and Ocean Engineering Research Institute, Korea
MULES	Multidimensional Universal Limiter with Explicit Solution
NACA	National Advisory Council for Aeronautics
NF	No Freesurface
NSE	Navier Stokes Equation

OpenFOAM	Open source Field Operation And Manipulation
PISO	Pressure Implicit Splitting of Operators
PMM	Planar Motion Mechnanism
RANS	Reynolds-averaged Navier-Stokes
RANS-BEMt	Reynolds Averaged Navier Stokes and Blade Element Momentum Theory coupling approach
RANS-HO	Reynolds Averaged Navier Stokes and Hough and Ordway coupling approach
RPM	Revolutions Per Minute
RPS	Revolutions Per Seconds
SIMMAN	SIMMAN Workshop on Verification and Validation of Ship Manoeuvring Simulation Methods
SIMPLE	Semi Implicit Pressure Linked Equations
SST	Shear Stress Transport
TBL	Turbulent Boundary Layer
TKE	Turbulent Kinetic Energy
TSLNG	Twin Skeg Liquefied Natural Gas carrier ship
URANS	Unsteady Reynolds-averaged Navier-Stokes

Acknowledgements

Thanks to...

Those who have helped me with using the OpenFOAM code especially the OpenFOAM community at the University of Southampton for providing advice when I needed it, Eric Svenning for providing the actuator disc code developed for OpenFOAM 1.5dev and the office colleagues for answering my many questions.

The University of Southampton for providing the use of the IRIDIS computing facility and associated support services, especially the technical support of David Baker and Ivan Wolton.

My sponsors Shell shipping and the University of Southampton for funding the project.

To my supervisors, Professors Stephen Turnock and Dr Alexander Phillips for the immense help and contribution provided to this stage and also for some interesting discussions, and feedbacks.

Everyone who has helped in the preparation of this thesis and made the group such a nice place to work, especially, Dr. Pareecha Rattanasiri, Dr Adam Sobey, Dr Joseph Banks, Dr. Christopher Phillips, Dr. Angus Webb, Dr. Nick Townsend, Dr. Bjorn Winden, Dr. Mirjam Furth, Mr. Arun Krishnan and Mrs. Aparna Subaiah-Verma and finally to Mrs. Linda Hesse Badoe, Ms. Leroy Bobby Hesse Badoe and Ms. Justyn-Martyn Augustus Badoe for being there through thick and thin and proof reading this thesis.

Chapter 1

1 Introduction

1.1 Motivation

Natural gas usage in the world has seen tremendous growth at about 3% in the past decade. The demand alone in 2013 increased by 1.2%, reaching around 3,500 billion cubic metres (IGU Report, 2013). Gas, as one of the cleanest fossil fuels is rapidly being recognized as the key fuel for meeting the ever increasing energy demand. The Liquefied Natural Gas (LNG) sector follows this increasing trend. As the LNG sector grows, its fleet is also experiencing tremendous growth. At the end of 2012, the global LNG fleet consisted of circa 362 vessels. This is more than one and half times the size of the fleet at the end of 2006 (IGU Report, 2013). However, the increasing prices of bunker[1] prices[2], coupled with implementation of new emission control regulations, has provided an economic imperative to improve the energy efficiency of LNG carrier ships.

Improving the energy efficiency of LNG carrier ships requires improving its engine, transmission, hydrodynamics, operations and maintenance. One way of improving the engine and transmission to reduce the fuel consumption of LNG carrier ships is to reduce the vessels speed, popularly known as slow steaming. This method was first seen by the industry as the most cost effective way to reduce ships fuel consumption. A cap on speed offer greater flexibility to increase the capacity again when market situation changes.

[1] Bunker is simply the name given to the fuel used to operate ships, examples of these are Marine gas oil (MGO); Marine diesel oil (MDO); Marine fuel oil (MFO) and Heavy fuel oil (HFO).
[2] Bunker prices quadrupled between 2001 and the end of 2007, when they reached a peak of about $500 per metric ton, (Notteboom and Vernimmen, 2008).

Also it is perceived that the main engines cylinder lubricating oil consumption is reduced at almost the same percentage as the fuel, hence reducing solid particle emission (Wiesmann, 2010). However, a cap on speed is now being opposed, as it may not be cost effective on all routes. The main engines have to be refit and requires more frequent maintenance to the owners own expense (Wiesmann, 2010). Because of this, greater interest has been placed on improving the hydrodynamics of the LNG carrier ships so that less energy is required to propel the ship through the water (Hafermann and Marzi, 2011).

The improvement in LNG ship hydrodynamics to improve its propulsive power is influenced by two primary factors:

1. Total towed resistance, R_T, of the ship;
2. Propulsive efficiency, η_D, (determined by the propulsor and interaction with the hull).

To improve LNG ship hydrodynamics, both aspects have to be addressed for future design, and optimum solutions found over a range of the ships operating conditions such as its entire speed range and design draught. This will then contribute to provide a step change in performance as sought by the fleet owners and expressed by the International Maritime Organization (IMO) Energy Efficiency Design Index (EEDI).

The total towed resistance of the LNG carrier ship may be decomposed into frictional and residual resistance. Frictional resistance is influenced by fouling and the coating of paints used for its prevention and the residual resistance arises from the form of the hull. Obtaining the right resistance is significant in the selection of the correct propulsor and in the subsequent choice of main engine. The efficiency of a typical marine propeller can be in the region of about 50% to 60%, therefore possibilities to improve propulsive performance lie in the recovery of some of the energy lost in the propeller race (Carlton, 2007). This requires good understanding of the hydrodynamic phenomena occurring at the stern of the ship, in particular the interaction between the propeller, rudder and hull. It is a challenging task, especially when the influence of the propeller requires the use of advanced numerical tool in resolving the complex flow field around the rudder and hull with adequate accuracy. There is still a need for improving these numerical tools to satisfy these requirements.

1.2 Aims and objectives

The purpose of this research is:

"To contribute to the improvement in LNG ship hydrodynamic design for improved powering performance by developing Computational Fluid Dynamics (CFD) methodologies which balances the trade-off between computational cost and fluid dynamic fidelity".

To accomplish this, the aim is to develop a numerical methodology capable of modelling the propulsion power requirements of a future LNG ship over its operational profile. Development of this methodology requires completion of the following objectives:-

1. to develop an open source numerical towing tank environment capable of addressing each aspect of the LNG ship design process.

2. to develop suitable model of the LNG ship's propeller without explicitly resolving the propeller flow.

3. to capture the influence of the ship's appendages on the propeller performance.

4. to gain an understanding of the LNG ship's flow and the three way interaction between the propeller-rudder and hull as well as effectively predicting the resistance and propulsion parameters of the ship.

1.3 Novel contributions

The novel contributions presented in this thesis are outlined below:-

- This thesis provides results, data and discussions on the impact of a ship's appendage (skeg) on the changes in propulsive forces associated with the downstream rudder and the acceleration of the propeller race. This is relevant to the field of twin skeg ship design since the knowledge on the changes in propulsive effect may aid in the design of future skegs.

- In defining the numerical methodology, a cost effective means of estimating the self-propulsion performance of LNG ship is presented. This includes capturing the radial and circumferential variation of the wake in the propeller plane within a RANS-BEMt coupling procedure by adopting a novel sectorial approach which divides the propeller plane into a series of nR, radial and nC, circumferential

subdivisions. The local wake may then be determined from these locations and used as input to a BEMt propeller code, which then calculates the local thrust and torque at these locations. A sensitivity study has been carried out to determine how many nR, radial and nC, circumferential variations give a better representation of the wake field.

- The RANS-BEMt coupling, using the sectorial approach, has been applied with other existing approaches to study in detail the resistance and self-propulsion characteristic of a ship. The study shows how the approach fares against the others on the prediction of the global forces and moments acting on the hull and rudder. A detailed discussion is made on all the various approaches in terms of cost, fidelity and suitability for design which is useful in the initial design stage and also opens doors for further studies and expansion of these approaches to other areas such as seakeeping and manoeuvring.

- This work has shown how varying simple parameters and dimensions on the propeller, rudder and hull have on self-propulsion coefficients, hence the overall propulsive power of a ship. This is relevant in the field of LNG ship design and general naval architecture as it provides in-depth knowledge to shipyards and designers on the use of previous concepts and existing regression analysis for ships self-propulsion coefficients.

1.4 Structure of report

In order to understand the current state of twin skeg LNG ships powering performances, Chapter 2 provides background on the ships operations, what factors are involved in the performance losses of the ships and the need for design. To provide answers to these, a detailed flow around the ships stern has to be understood. Chapter 2 also serves to discuss existing methods used to understand the stern flow. This may be classified into experimental and numerical methods. The last part of Chapter 2 gives the state of the art in numerical methods used to predict the stern flow. The solution of the Reynolds Average Navier-Stokes (RANS) equation was found to be the most widely used numerical method to predict the stern flow.

Drawing from the experience of the literature in Chapter 2, a numerical method was developed in Chapter 3 to help understand the stern flow in more detail so as to predict them. The method was implemented in the open source CFD code OpenFOAM (OpenFOAM, 2010). The method was then used as part of a step wise study to help understand different aspect of the LNG ship stern flow. The chapter also discusses

applicability of CFD to LNG ship stern design. Here a design cycle is identified and inputs to the stern modification process to achieve an overall power reduction is outlined.

Chapters 4, 5 and 6 present simulation results for increasing complexity of the various stern design predicting methods outlined as part of the numerical method. Chapter 4 looked at the impact of the skeg on the propeller-rudder interaction. Previous studies have examined the hull, skeg, rudder and propeller as a whole, but this work concentrated on the skeg, independent of the propeller and rudder. The limits of the numerical method in this study was identified and discussed.

Chapter 5 compares the numerical method to other existing approaches to investigate the three way interaction between the hull-propeller and rudder. Here the resistance and self-propulsion of the KCS container ship was chosen because of the wide range of available data. It is shown how well the method can predict the resistance and self-propulsion coefficients in calm water conditions. The computational cost of using the method compared to the other existing methods was discussed as well as fidelity and suitability for design purpose.

Chapter 6 makes use of the numerical method and experience gained from chapters 4 and 5 to design the stern of a future twin skeg ship after which its powering performance is assessed. Chapter 7 outlines a detailed stern design cycle for LNG ships after which conclusions and future work recommendations are then drawn in chapter 8.

Chapter 2

2 Hydrodynamic performance of ships

2.1 LNG operations and the need for design

The operation of the LNG carrier ship runs strictly between the production facility where LNG arrives from the terminal to the ship and a receiving terminal where after safe arrival and berthing of the ship, LNG is unloaded to storage tanks. Current demand for LNG has seen the rise in such operations with new proposals for both production and receiving facilities. This means increasing the size of LNG carrier ships to satisfy these demands. In addition to increasing the size, it is necessary to ensure the compatibility of the ships to existing receiving terminals as well as satisfy other economic factors such as fuel consumptions and emissions. This has resulted in the need for new hull design to satisfy these requirements. New hull design require new propulsor and appendage design to improve the overall propulsive performance. For example an increase in LNG hull dimensions will require an increase in machinery and greater power output to the propeller. The high loading of propellers leads to reduced propulsive efficiency and also increases the risk of excessive cavitation and vibrations. It is therefore paramount that a design is found which provides flexibility across the ships operational requirements.

Twin-skeg hull designs have become the technology of choice for new LNG carriers, as a consequence of these new operational requirements (SSPA, 2009). Twin-skeg offers redundancy advantages in lower thrust per propeller and thus higher efficiency due to its twin propeller. The Swedish testing facility SSPA statistics, based on over 400 different twin skeg configurations in over 200 projects have shown that twin skeg hull forms in general require 6% lower propulsion power compared with a single screw ship with the

same cargo capacity (Kim et al., 2013). Maersk's Triple-E's 'twin-skeg' container ship, the world's largest container ship consumes approximately 4% less energy than its single engine/single propulsion type (Maersk, 2011). The advantages of employing two skegs over an equivalent centre line skeg are outlined below:

- The skegs can generate pre swirl into the propeller.
- Each of the skegs can be made more slender to provide more control of the flow to the propellers hence better wake field, lesser cavitation and lower induced pressure pulses to the hull.
- Improved directional stability compared to the single screw.
- Twin skeg design can offer reduction in wavemaking resistance since there is more scope for favourable longitudinal centre of buoyancy positions.
- Twin skeg design can accommodate larger propeller area within vertical dimensions constraints, increasing propeller efficiency.

Whilst these advantages offer improvement in overall efficiency, the fitting of the twin skegs does have some draw backs, and outlined below:

- The twin skeg arrangements are expensive to build. Since the shape of the skegs are complex, care is needed in defining the shape and orientation at the design stage to realise the efficiency improvements (Giles et al., 2013).
- The twin skeg concepts have high wetted surface area compared to that of the centreline single skeg.
- It is not just the hydrodynamics where the complex skeg shape poses a problem, according to Giles et al. (2013) structural integration and therefore build can also be complex.
- The twin-skeg hull steel weight is increased by about 5% which places some restrictions on cargoes.
- Finally, the internal arrangement in terms of providing access to the skegs and accommodating gearboxes can prove challenging.

A detailed understanding of the propulsive performance of the LNG ships may offer further advantage to new designs by identifying other areas where gains may be made.

2.2 Propulsive performance assessment

The propulsive performance assessment of LNG carrier ship is a measure of their energy consumption over a range of design speeds and operational profiles. This can be categorised into three groups: resistive force, heat input and speed through water (Muntean, 2008). Each of these three components needs to be accurately measured to assess the overall energy consumption. Whilst the heat input and speed through water can be measured using available hardware, the resistive force presents a challenging task since it includes the sea state. It is unlikely for a ship to be in a similar situation each time, thus a measure of the resistive force is very difficult to achieve. Figure 2.1 by Muntean (2008) presents an extensive list of key blocks relating to the propulsive assessment of a ship. Here the ship overall efficiency is the product of the block efficiencies, as per the following:

$$\eta_{ship} = \eta_{engine} \times \eta_{transmission} \times \eta_{propeller} \times \eta_{hull} \tag{2.1}$$

These efficiency blocks can be further simplified into two main categories each of which is important if the overall efficiency of the ship is to be achieved. This is illustrated in equation 2.2 where the engine and transmission can be combined to form a single unit (engine+components) whilst the propeller and hull may also be combined to form the hydrodynamic aspect of the ship efficiency block. The main focus of this thesis is on the hydrodynamics aspect which concentrates on the hull, propeller and their interaction with the water (sea).

$$\eta_{ship} = \eta_{Engine+components} \times \eta_{hydrodynamics} \tag{2.2}$$

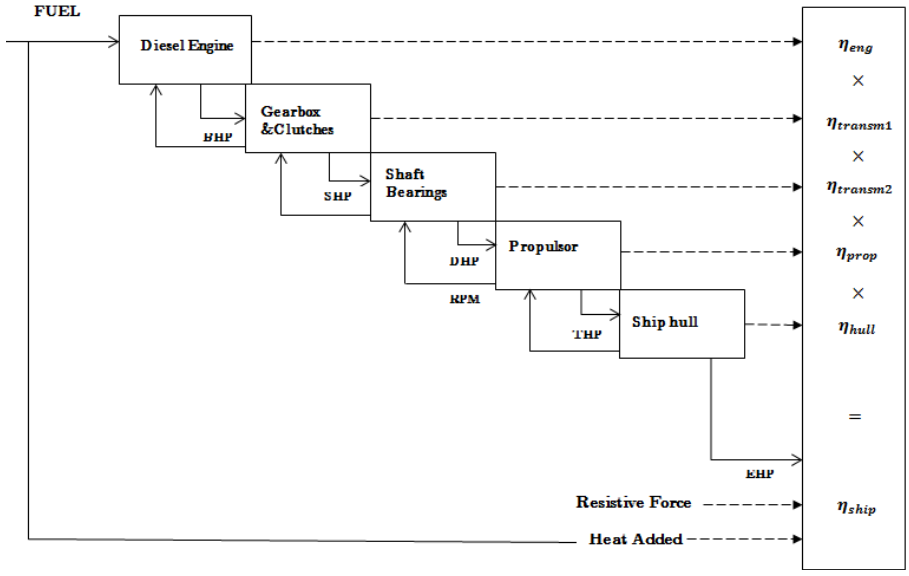

Figure 2.1: Schematic of the main components of propulsion drive train. The input and output of each of the components are indicated, as well as their corresponding efficiency, Muntean (2008).

Figure 2.2 is a detailed breakdown of the efficiencies in the ship powering process. Here the main focus is on the hydrodynamic related efficiency. In assessing this, attention is usually placed on the delivered power in behind hull conditions. The relationship between the power delivered to the propeller in behind hull conditions P_D, the effective speed of the ship P_E, and quasi propulsive efficiency η_D, can be expressed as:-

$$P_D = \frac{P_E}{\eta_D} = \frac{P_E}{\frac{P_E}{P_T}\times\frac{P_{Do}}{P_D}\times\frac{P_T}{P_{Do}}} = \frac{R\times V_S}{\eta_H\eta_R\eta_O} = \frac{R\times V_S}{\eta_H\eta_B} \tag{2.3}$$

where:-

- P_T is the thrust power
- P_{Do} is the delivered power in open water conditions
- η_H is the hull efficiency
- η_R is the relative rotative efficiency
- η_O is the open water efficiency
- η_B is the behind efficiency
- R is the towed drag
- V_s is the ship's speed

Equation 2.3 can then be further expressed as:-

$$P_D = \frac{C_w + (1+k)C_f + \Delta C_f}{\frac{1-t}{1-w_T} \times \eta_R \times \left[\frac{J}{2\pi} \times \frac{K_T}{K_Q}\right]} \times \frac{1}{2}\rho S V_s{}^3 \quad (2.4)$$

where:-

- ρ is the fluid density
- S is the wetted surface area of the ship
- C_w is the ships wave-making resistance coefficient
- k is the form factor of the ship
- C_f is the frictional resistance of the ship based on ITTC-57 friction line
- Δc_f is the allowance coefficient between model and ship
- t is the thrust deduction fraction, which is the interaction between the hull and propeller
- w_T is the effective wake fraction, which is the interaction between the hull and water
- J is the propeller advance coefficient
- K_T is the propeller thrust coefficient
- K_Q is the propeller torque coefficient

From equation 2.3 and 2.4 it can be seen that gains can be made or losses minimized to achieve a reduction in P_D. The parameters that can be maximized are 1-t and η_B and those to be minimized are 1-w_T, C_w and k.

Achieving these requires a better understanding of the hydrodynamic phenomena of the ship, especially at the stern. Hydrodynamics at the stern of a ship can be subdivided into three main components of hull, propulsor and appendage (rudder). The physics behind each component and the interaction effect has to be understood in order to predict these self-propulsion parameters.

The following sections are dedicated to summarising results in literature covering the general flow over a ship's stern, and the experimental and numerical methods used to predict them. Due to the interest in twin skeg across the LNG sector as discussed in section 2.1, particular focus on the general stern flow will be dedicated to twin skegs. It is not intended to give the theoretical background of all the available experimental and numerical techniques but rather provide an overview especially with the numerical techniques, its strength, weakness and associated cost.

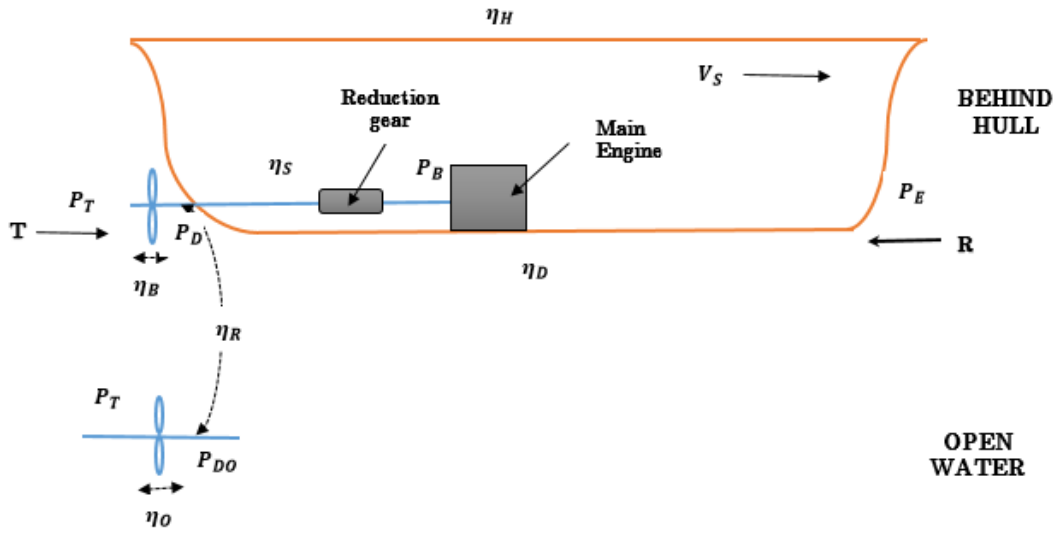

Figure 2.2: Summary of efficiencies in ship powering.

2.3 Ship stern and wake flows

Patel (1988) first reviewed the complex ship stern flow, which involves a thick boundary layer, viscous-inviscid interaction, complex turbulent flow-field and the action of a propulsor. As a ship advances through water at a constant speed, near the hull in the so called boundary layer, (see Figure 2.3) the flow acts as a force on the body against the motion. Since the fluid is in direct contact with the surface of the body, it is carried along with the surface. As the ship or body moves, its boundary layer gradually thickens from the bow to the stern. Boundary layer flow leaves the ship behind in the form of frictional wake and moves in the direction of the ship. This phenomenon represents a continual drain of energy and hence constitutes a resistance force on the hull.

The growth of boundary layer towards the stern is very rapid. As a result of pressure differences around the bilge, the boundary layer experiences cross flow which increases downstream, forming bilge vortices and creating a complex stern flow field, which results in the same order of magnitude for the three components of mean velocity, and the six Reynolds stress (ITTC, 1990). In order to understand the flow features at the stern in more detail so as to accurately predict them, then a detailed measurement of flow at the stern has to be carried out.

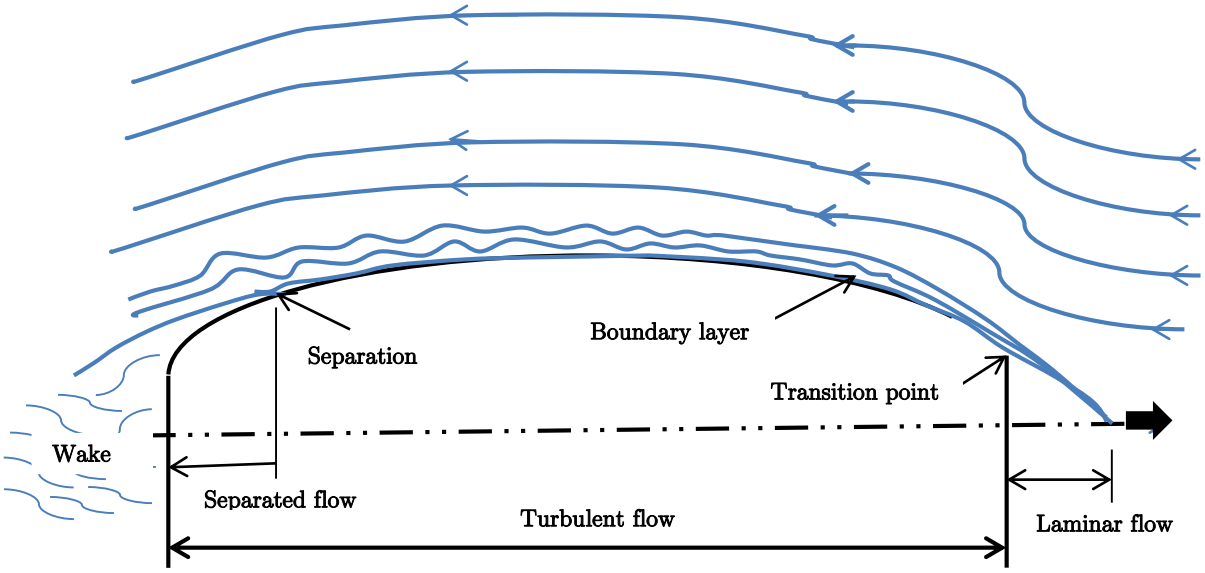

Figure 2.3: Typical flow around a ship's hull.

2.3.1 Experimental prediction of ship stern and wake flows

There are several experimental data sets for the flow around a ship model. These data are necessary in order to understand the interaction between the hull form and the water (sea). The International Towing Tank Conference (ITTC) summarised benchmark database for computational fluid dynamics (CFD) validation of resistances and propulsion (ITTC, 1999), but very few reports of detailed flow measurement have been made at the stern region. Wieghardt and Kux (1980) and Wieghardt (1982) have made measurements of all components of mean velocity at the stern of HSVA tanker hull form. Wieghardt and Kux (1980) have reported turbulence data in the stern and near wake regions of the same tanker. Study on the measurements revealed the viscous layer growth, mean flow field and the turbulence at the stern. These are very important for powering assessment of the ship especially at the propeller plane since these are used as initial conditions for the operating propeller.

Even though measurements made by Wieghardt and Kux (1980) provides insight in to ships stern flow, they are not enough to understand fully the complicated flow phenomena. The hull forms used by Wieghardt and Kux (1980) were old fashioned and quite different from modern hull forms. Improved measurements have since been made and on modern hull forms; for example Kim et al. (2006) performed measurements around a, KRISO[3] 138,000m^3 LNG carrier model (KLNG). Experimental data was presented for resistance and propulsive efficiency, wave elevation along hull surface, wave pattern and mean velocity components in the boundary layer and wake. In the resistance test the ship was towed at the speed of Froude's similarity law. The total drag coefficient

[3] Korea Research Institute of Ships and Ocean Engineering

including appendage was measured using a resistance dynamometer and subsequently divided into frictional resistance coefficient using ITTC 1957 formula (ITTC, 1999) and the 'rest' termed residuary resistance coefficient which comprises of the resistance due to wave-making and that due to the ship form. The propeller open-water and self-propulsion point was achieved using the thrust identity method (ITTC, 1999). The test revealed that the presence of the rudder reduces axial velocity components into the propulsor thus increasing the effective wake and reducing the propeller revolution (rps) at the self-propulsion point. The swirl in the propeller wake is also partially recovered by the rudder, hence increasing the relative rotative efficiency.

The global view of the wave pattern, Figure 2.4(a&b) showed a concentric bow wave rise followed by a large trough near the bow shoulder. The divergent wave pattern originating from the bow was more prominent compared with the KRISO container ship, KCS (Kim et al., 2001) because modern LNG carriers need to run fast in spite of large waterline entrance angles. The most important wave phenomena occurred behind the transom stern. At rest, the transom stern was above calm water surface. As the ship advanced the wave generated rose above the transom stern. Conclusions drawn from the wave pattern showed that wave generation could be ignored for very low Froude numbers (Fn $\leq$ 0.196), at high Froude numbers since the wave surface was parallel to the hull surface under the transom stern, the transom stern could appear out of water region in the so-called "dry transom". Mean velocity components, Figure 2.5(a-c) taken at various locations around the stern document the viscous boundary layer and wake with bilge vortices. Thick boundary layer is observed at St. 1.5 (X = 0.425). The thick boundary layer is formed with transverse velocity component towards the hull surface. At St. 1 (X = 0.45), as a result of formation of bilge vortex, rotational flow component is seen along the concave portion of the hull surface. The vortex is more clearly defined at the propeller plane, St. 0.42. The hook-like shape in the axial velocity vectors is as a result of the bilge vortices. The extent of the hook-like shape is proportional to the strength of the bilge vortices, with the fuller stern frame lines generating stronger bilge vortices. Figure 2.6(a&b) shows the nominal wake field with the strength of the bilge vortices and the thickness of the wake region being affected by the stern frame line shape.

Measurements were also made to determine the influence of the propeller on the flow. When a propeller is rotating inside a ship's wake, variation in local inflow angle into the propeller blade exist at each radial and circumferential location. The measured velocity field at St. 0.21, Figure 2.6(c) without the rudder revealed a clockwise rotating velocity component. Measurements made with the rudder in Figure 2.6(d) showed how the propeller wake was split by the presence of the rudder. Due to the swirl in the flow coming in contact with the rudder, a downwards flow covering most of the lower part of the rudder surface may be seen. The remaining upper part of the rudder shows upwards velocity component.

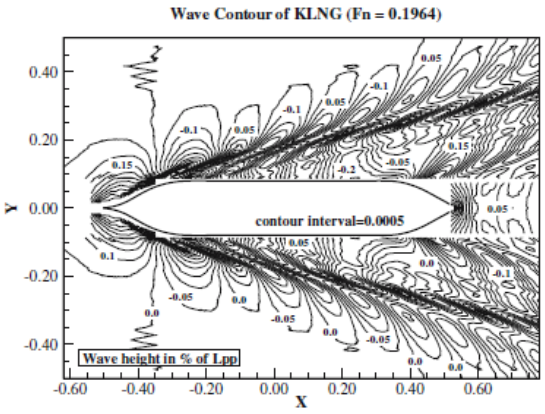

[a]

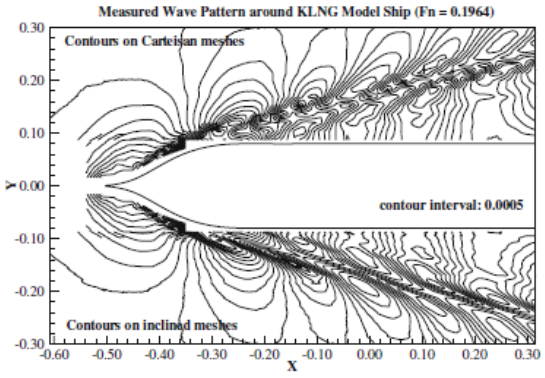

[b]

Figure 2.4: [a] Measured wave pattern around the model ship (Fn = 0.1964) and [b] Wave contours on the rectangular and inclined meshes with measured wave cut data, Kim et al. (2006).

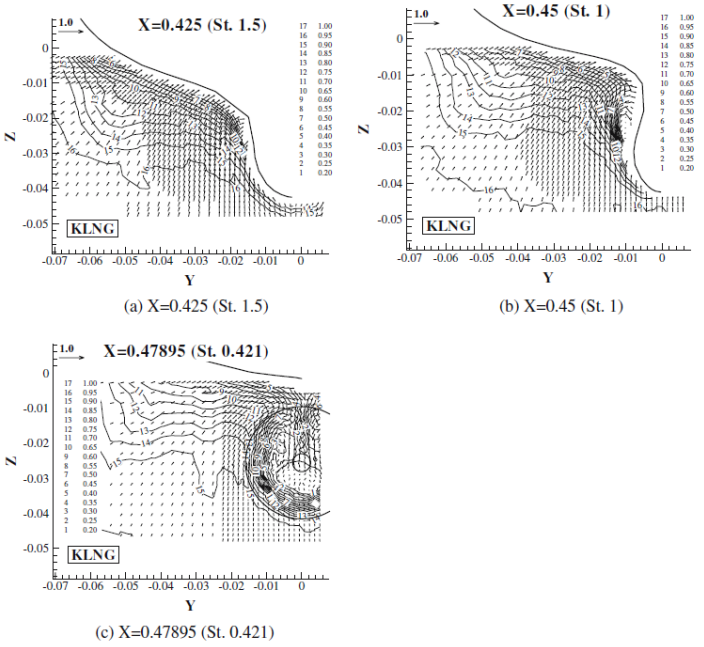

(a) X=0.425 (St. 1.5)

(b) X=0.45 (St. 1)

(c) X=0.47895 (St. 0.421)

Figure 2.5: Measured velocity fields at St. 1.5, 1.0 and 0.421 of the KLNG model ship without propeller [a] X=0.425 (St. 1.5), [b] X=0.450 (St. 1.0) and [c] X=0.47895 (St. 0.421), Kim et al., (2006).

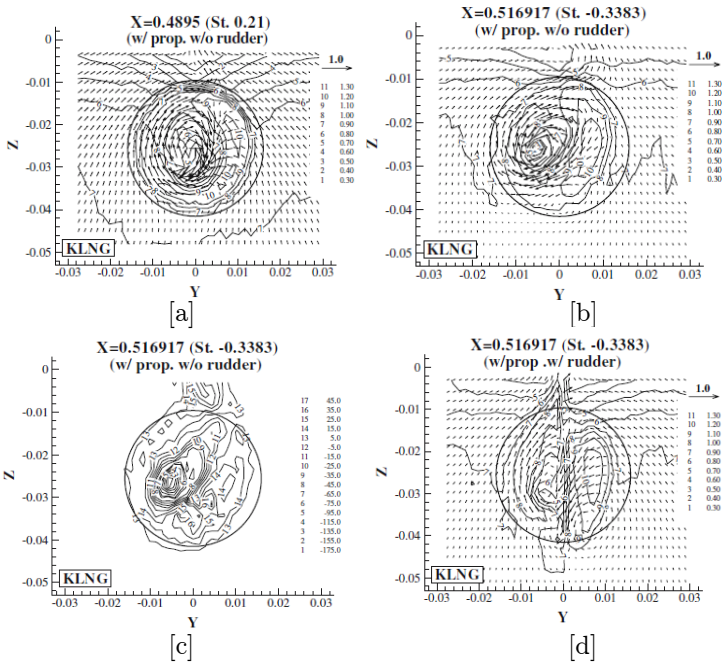

[a]

[b]

[c]

[d]

Figure 2.6: Measured velocity fields at [a] St.0.21, without propeller and rudder [b] St.-0.3383, without propeller and rudder [c] Axial vorticity contours at St.-0.3383, with propeller (7.76rps), no rudder [d] St.-0.3383, with propeller (7.76rps) and rudder, Kim et al., (2006).

There is limited experimental data for twin skeg ships reported in literature compared to single screw ships. The Swedish State Shipbuilding Experimental Tank (SSPA) as part of

its growing interest in green ship solutions conducted resistance and self-propulsion test on a 170,000m^3 LNG twin skeg hull form and compared it with a similar single screw ship at a design speed of 19.5knots (Kim et al., 2013). In the resistance computations, the viscous resistance yielded a form factor of about 0.180. The computation was able to reproduce the bent contour in the stern wake field, which was due to the presence of the skegs. Comparison of the twin skeg model's delivered power to that of a similar single screw ship at a design speed of 19.5knots showed a reduction in twin skeg ship's power of around 11%. Conclusions drawn from the experiment showed that at 19.5knots, the power requirement for the twin skeg was much lower than that of the single screw even though the block coefficient was slightly higher. The lower power was mainly attributed to the high relative rotative efficiency and propeller efficiency. According to Kim et al. (2013) further reduction in power could have been achieved if the constraint on the hull form was further released.

Sakamoto (2013) also conducted resistance and self-propulsion computations on a twin skeg container ship. Figure 2.7[a] shows the instantaneous wave pattern of the computations and the experiment at Froude number of 0.235. The diverging wave pattern compared well with the experiment. Pressure distribution and streamlines at the stern of the hull with and without propeller are also presented in Figure 2.7[b]. The streamline is coloured by the non-dimensional axial velocity. Without the propeller, the streamlines behind the housing rotates counter clockwise, viewed from the stern. When the propeller rotates, the clockwise rotation recovers the counter clockwise circulatory flow originated from the skegs. Rotation of the propeller also accelerates the flow in the axial direction, resulting in changes in the pressure distribution on the housing.

Even though experimental methods are reliable in the prediction of ships stern flow, they are very expensive and also scaling effects (from model to full scale) presents a problem. Numerical methods have become more available now with the advancement in computing power. One advantage of this method is its ability to provide local flow detail which is difficult to obtain from experiments.

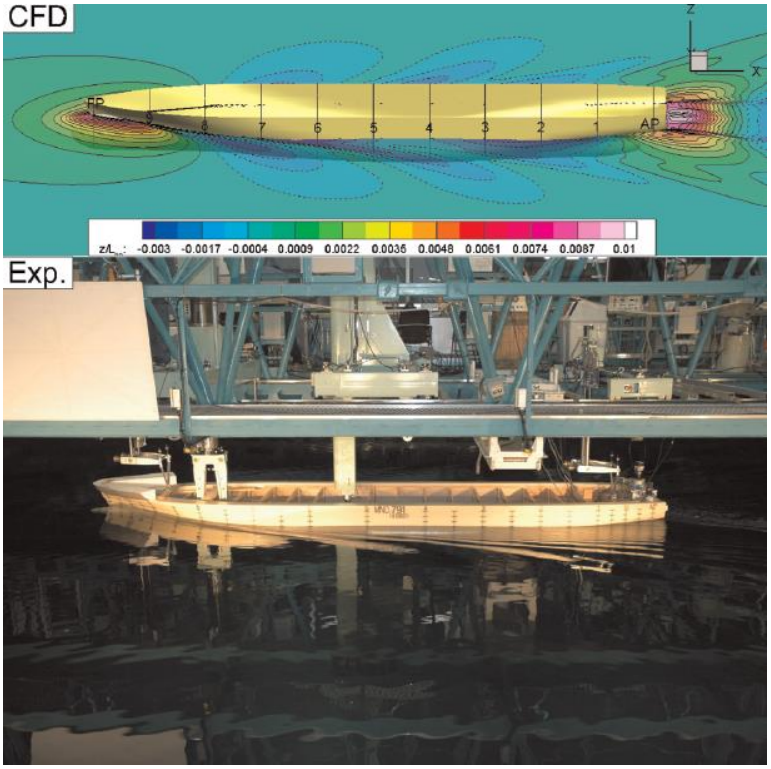

[a]

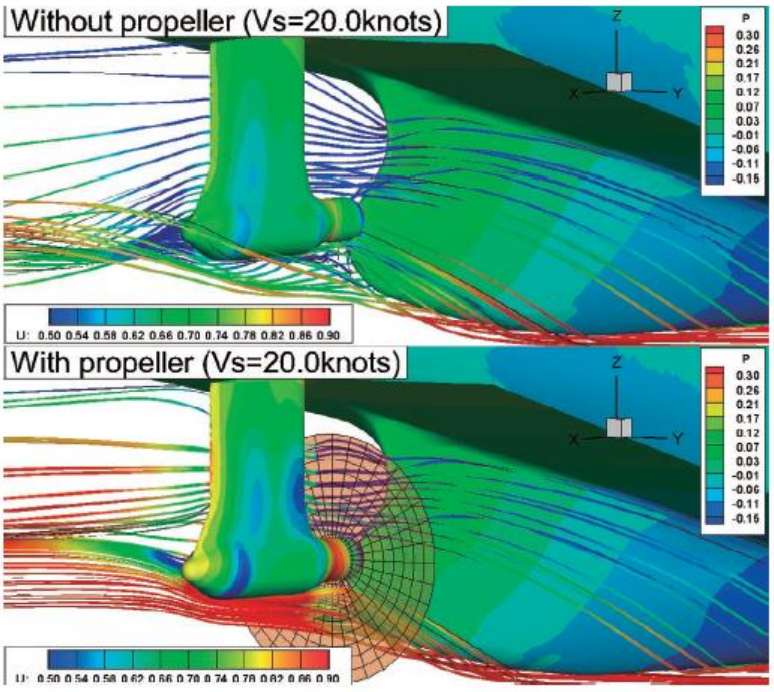

[b]

Figure 2.7: [a] Comparison of free surface wave pattern at Fn = 0.235 between experimental and computational results [b] Computational results of streamline and pressure distribution in the stern vicinity without (top) and with (bottom) propeller (Sakamoto et al., 2013).

2.3.2 Numerical prediction of ship stern and wake flows

The appeal of numerical methods in predicting ship hull flow is to seek the 'ideal' solution from a variety of shapes. Such hull design optimisation procedure has potential to find better solutions more rapidly than towing tank tests (Molland et al., 2011). In solving the ship flow problem, particularly high speed flows, the boundary layer is confined to a very thin region near the wall. Outside of that region viscosity is negligible. Inviscid, potential flow based approach were initially used in ship flows, with good prediction of wave resistance (Bertram, 2000). For ship resistances, inviscid free-surface methods based on the boundary element approach are also used in the analysis of fore bodies such as bulbous bow (Bertram, 2000). The use of inviscid methods for ship propulsion has also been around for some time. For example, in propeller analysis, lifting surface methods allows the three dimensional modelling of the propeller to be made yielding comparable results to experiment. According to Beck et al. (1996), inviscid flow codes are ready to be used by industry for wave resistance problems and offer advantages such as cost and time. However, such methods cannot provide detailed flow field information at the stern especially in the presence of an operating propeller. For surface vessels, viscosity is important in the thin boundary layer around the ship. Since propellers act in the wake of ships, velocity distribution in the near wake of the boundary layer is important to the performance of the propeller. Viscous methods are arguably the most widely used CFD analysis of ships stern and wake flow (Gorski, 2001). The viscous methods are based on the numerical solution of the Navier-Stokes and the continuity equation. Equation 2.5 is the incompressible continuity equation for the conservation of mass within a fluid presented in Cartesian tensor form.

$$\frac{\partial u_i}{\partial x_i} = 0 \tag{2.5}$$

The incompressible momentum equation for a Newtonian fluid can be written in the form:

$$\rho \frac{\partial u_i}{\partial t} + \rho \frac{\partial u_i u_j}{\partial x_j} = - \frac{\partial p}{\partial x_i} + \frac{\partial}{\partial x_j} \left(\mu \left(\frac{\partial u_i}{\partial x_j} + \frac{\partial u_j}{\partial x_i} \right) \right) + f_i \tag{2.6}$$

where i and j =1, 2, 3, ρ is the density of the fluid, p is pressure and μ the dynamic viscosity.

Appropriate boundary and initial conditions must be imposed on the equations given above. Ship flows become turbulent depending on the Reynolds number[4]. With the advent of super computers, numerical solution of the equations under turbulent conditions can be made. There are three possible approaches to the numerical solution of turbulent flows. The first and most intuitive one is by directly numerically solving the set of governing equations. Other approaches are the Large Eddy Simulation and the Reynolds Averaged Navier-Stokes (RANS) equation approach.

- **Direct Numerical Simulation (DNS) -** In direct numerical simulation, the Navier-Stokes equations are numerically solved without any turbulence modelling. This means that the whole range of spatial and temporal scales of the turbulence must be resolved. All the spatial scales of the turbulence must be resolved in the computational mesh, from the smallest dissipative scales (Kolmogorov microscales), up to the integral scale, L, associated with the motions containing most of the kinetic energy (Hatay and Biringen, 1995). Computational cost imposed by the mesh and time-step requirements using this approach makes it unsuitable for ship flow problems.

- **Large Eddy Simulation (LES) -** Large eddy simulation operates on the Navier-Stokes equations to reduce the range of length scales of the solution. The principal operation in large eddy simulation is low-pass filtering. This operation is applied to the Navier-Stokes equations to eliminate small scales of the solution. The governing equations are thus transformed, and the solution is a filtered velocity field. Large eddy simulation resolves large scales of the flow field solution. It also models the smallest scales of the solution, rather than resolving them as direct numerical simulation does (Henn and Sykes, 1999). To perform accurate LES computations for ship flow, a very fine mesh has to be used near the wall. This result in significantly larger cost in computations, however it has proved to be a good prediction model (Bensow and Bark, 2010).

- **Reynolds Averaged Navier-Stokes approach (RANS) -** The final approach is the decomposition of flow variables of the governing equation (Equation 2.5&2.6) into time mean and fluctuating components and then time averaging the entire equation. This approach is most widely used for ship flows. This was realised during the Gothenburg 1990 workshop on ship hydrodynamics (Larsson et al., 1991) when a more advanced method was required to effectively model the ship

[4]For external flow over ship hulls, typical Reynolds number magnitudes are as follows: Laminar flow: $Rn < 5 \times 10^5$; Turbulent flow: $Rn > 1 \times 10^6$. Values of Rn between these numbers represent transition from laminar to turbulent flow.

stern flow, after the failure of the boundary layer method[5] at the Gothenburg 1980 workshop (Larsson, 1981). Breakthrough was made in the ability to predict the stern flow. In contrast to the Gothenburg 1980 workshop, all the methods used except two were based on the solution of the Reynolds Averaged Navier-Stokes (RANS) equation. RANS was able to predict better the wake distributions at the stern as compared to the boundary layer method and the large eddy simulation (LES) method. The only drawback was its inability to predict the detailed shape of the velocity contours (hook shape created by the bilge contours). Deng et al. (1993) later showed that, the inability to predict these "hook shape" was due to inadequate turbulence modelling. Since then, RANS code has adopted models such as the k-ω turbulence model and Reynolds stress models to address the problem.

2.4 Reynolds Averaged Navier-Stokes (RANS) equation

By time averaging the equations 2.5 and 2.6, new terms are introduced which must be related to the mean flow variables through turbulence modelling. Detailed derivation of the RANS equation can be found in Versteeg and Malalasekere (2007).

Decomposition of the flow variables (instantaneous flow quantity $\boldsymbol{\phi}$) into sum of the mean, $\bar{\phi}$, and time dependent fluctuating component, $\boldsymbol{\phi}'$, can be expressed mathematically as:

$$\boldsymbol{\phi}\,(\mathbf{x},\,t) = \bar{\phi}\,(\mathbf{x},\,t) + \boldsymbol{\phi}'(\mathbf{x},\,t) \tag{2.7}$$

where $\mathbf{x}$ is the vector containing the Cartesian co-ordinates x, y and z in three spatial dimensions.

Mean value $\bar{\phi}$ in (2.7) can be obtained using three different forms of Reynolds averaging.

- Time averaging: suitable for stationary turbulence where a turbulent flow on average does not vary with time.

$$\bar{\phi}\,(\mathbf{x}) = \lim_{T\to+\infty} \frac{1}{T}\int_t^{t+T} \phi(\mathbf{x},t)dt \tag{2.8}$$

t is the time and T is the averaging interval. $\bar{\phi}$ does not vary in time, but only in space.

[5] Boundary layer method is where boundary layer equations are used to simplify physical model: diffusion in the predominant flow direction is neglected, the thickness of the boundary layer is taken to be small, and pressure is constant over the thickness. These assumptions are violated near separation boundary layers. As such separation cannot be properly predicted. According to Bertram (2000), it is the area of interest for improving aft bodies and designing the propeller.

- Spatial averaging: suitable for homogeneous turbulence.

$$\bar{\phi}\ (\mathrm{t}) = \lim_{cv\to\infty}\ \frac{1}{cv}\int_{CV}\ \phi(\mathbf{x},t)dcv \tag{2.9}$$

cv is the control volume. $\bar{\phi}$ is uniform in space and also varies in time.

- Ensemble averaging: suitable for unsteady turbulence.

$$\bar{\phi}\ (\mathbf{x},\ t) = \lim_{N\to\infty}\frac{1}{N}\quad \sum_{i=1}^{N}\bar{\phi}(\mathbf{x},\ t) \tag{2.10}$$

N is the number of experiments ensemble (usually large enough to eliminate fluctuation effects). $\bar{\phi}$ is a function of both time and space.

By substituting equation (2.7) into (2.5 &2.6) the incompressible RANS equation is obtained and expressed as:

$$\frac{\partial\overline{U_i}}{\partial x_i} = 0, \tag{2.11}$$

$$\rho\frac{\partial\overline{U_i}}{\partial t} + \rho\frac{\partial\overline{U_J}\,\overline{U_i}}{\partial x_j} = -\frac{\overline{\partial P}}{\partial x_i} + \frac{\partial}{\partial x_j}\left\{\mu\left(\frac{\partial\overline{U_i}}{\partial x_j} + \frac{\partial\overline{U_J}}{\partial x_i}\right)\right\} - \rho\frac{\partial\overline{u'_i u'_J}}{\partial x_j} + \bar{F}_i \tag{2.12}$$

It can be seen that equation (2.12) has the same format as the (2.6) with the exception of additional term known as the Reynolds stress tensor, $\frac{\partial\overline{u'_i u'_J}}{\partial x_j}$. This represents a transfer of momentum due to turbulent fluctuations. The Reynolds stress tensor forms a symmetrical second order tensor containing six independent components, three normal stresses-

$$\tau_{xx}\ = \text{-}\overline{\rho u'^2}\ ,\qquad \tau_{yy}\ = \text{-}\overline{\rho v'^2}\ ,\qquad \tau_{zz}\ = \text{-}\overline{\rho w'^2}\ , \tag{2.13}$$

and three shear stresses:-

$$\tau_{xy} = \ \tau_{yx}\ = \text{-}\overline{\rho u'v'}\ ,\qquad \tau_{xz} = \ \tau_{zx}\ = \text{-}\overline{\rho u'w'}\ ,\qquad \tau_{yz} = \ \tau_{zy}\ = \text{-}\overline{\rho v'w'}\ , \tag{2.14}$$

These six additional terms represent a system which is not closed, hence a fundamental problem of turbulence modelling based on the RANS equation is to find six additional equations in order to close the system of equations (2.12).

2.5 Estimation of ship resistance and powering using RANS

After the failure of the boundary layer method in the prediction of ships stern flow (Larsson, 1981), attempts to develop a more comprehensive approach to the problem were outlined. Several numerical methods were developed (Table 2.1). Most of these methods were characterized by the solution of the Reynolds Averaged Navier Stokes-equations and huge improvements were observed in the prediction of ship stern flow. One of the most important questions in the use of RANS as a numerical tool for ship hydrodynamics is how well it can predict ship resistances and powering. Table 2.2 provides successful RANS resistance and powering computations and the numerical parameters adopted. The use of RANS to predict the resistance and powering characteristics of a ship follows the same trend as that of experiments. This requires computations at towing and self-propulsion conditions similar to resistance and self-propulsion model tests respectively. In the case of resistance tests, several double body approximations and free surface flows around ship models have been reported in literature with improvements in predictions (Phillips et al., 2010; Tahara et al., 1996; Zhang et al., 2010; Sakamoto et al., 2013).

For self-propulsion computations analysis is made on the flow around the hull with propulsor and appendage. The most interesting and challenging aspect is the influence of the propeller action and the unsteady hydrodynamics of the appendage (rudder) working in the propeller wake. Methods to model the propeller action behind the hull include the moving reference frame approach (MRF). It is a steady state approximation where the fluid zone in the propeller region is modelled as a rotating frame and the farfield, hull and rudder are modelled as a stationary frame. This approach ignores the transient effects at the interface so the propeller race, tip vortices and hub vortices are fixed in space downstream of the propeller. Consequently, the transient interactions between the propeller and rudder are not modelled. The computational cost of this method is lower since it is a steady state simulation.

Another method is the transient approach where the propeller and farfield domains are joined using a 'rotor-stator method'. The propeller is rotated at each time step and the interface between the two domains is achieved using an sliding mesh interface. To ensure the flow structure generated around the propeller are correctly transferred to the stationary domain, a fine mesh is required at the interface. The computational cost involved in this approach is very high since the full transient flowfield has to be resolved.

Last but not the least is to use a representative propeller model or body force method. The levels of complexities in the body force propeller approach varies from prescribing the body forces (Simonsen, 2000; Phillips et al., 2010; Choi et al., 2010), through to coupling a more complex propeller performance code which accounts for the non-uniform inflow at the propeller plane (Phillips et al., 2009).

Table 2.1: State of the art in CFD ship resistance and powering prediction

Study	Workshop	Test cases	Methods
Larsson et al. (1981)	Gothenburg 1980	HSVA tankers	boundary layer methods (16) and 1 RANS method
Larsson et al. (1991)	Gothenburg 1990	HSVA tankers	1 LES, 1 boundary layer method and the rest RANS
Kodama et al. (1994) Tahara et al. (1996)	Tokyo 1994	HSVA tankers Series 60	Viscous and inviscid free-surface methods
Larsson et al. (2003)	Gothenburg 2000	KVLCC2, KCS DTMB5415	RANS with/without free-surface methods
Hino, (2005)	Tokyo 2005	KVLCC2, KCS DTMB5415	RANS with self-propelled at drift and in head seas
IWWWFB, (2012)	IWWWFB 2012	General	RANS with free surface
Larsson et al. (2013)	Gothenburg 2010	KVLCC2, KCS DTMB5415	RANS, heave and trim
SIMMAN, (2014)	SIMMAN 2014	KCS, KVLCC2, DTMB5415	RANS with PMM and CMT test in deep water

Han et al. (2008) presented a RANS simulation on the three-way coupling between the hull, propeller and rudder using the academic CFD code SHIPFLOW. The flow around hull and rudder was computed using a steady RANS method with an algebraic stress turbulence model, while the propeller was replaced by a body force model based on the lifting line method. They computed the total resistance of four Froude numbers at model scale and conducted self-propulsion tests of the hull and propeller with and without the rudder. For the propeller and rudder in open water, it was shown that the numerical method was able to simulate at reasonably good accuracy the effect of axial spacing between propeller and rudder. In the self-propulsion predictions the thrust deduction was slightly under-predicted compared with experimental results, while the wake fraction agreed well with the measured ones. The delivered efficiency was about 5% underestimated mainly because of an overestimation of the propeller torque. The influence of rudder location on local flow was investigated numerically by comparison of limiting streamlines on the hull and rudder, axial and cross-flow velocities at the propeller plane and axial velocities in four transversal cuts along the rudder and behind. According to Han et al. (2008), by moving the rudder backward the effect of the distance between the rudder and propeller behind the hull is effectively captured and showed the same tendency as the experiment.

Carrica et al. (2010), introduced a self-propulsion simulation using overset grids. A speed controller was used to control the propeller rpm and find the self-propulsion point when the target Froude number is reached. The method was applied to the KRISO container

ship (KCS) where the propulsion parameters agreed well with the experiments with the largest error less than 3.7%.

Muscari et al. (2010), presented a study of the flow around a propeller behind a fully appended twin screw hull using a RANS solver. A transient propeller approach using the was adopted. A comparison of numerical and experimental result was shown for a navy patrol vessel propelled by four-bladed twin controllable pitch propeller in a straight course, at Rn $=1.18\times10^7$ and Fn = 0.348 for the hull. The flow around port side half of the model was calculated and measured. The simulation was conducted with a 12.7M fine grid and a 1.6M coarse grid respectively. About 50% of the cells were dedicated to modelling the propeller. The main features were correctly captured by CFD of the tip vortex interacting with the rudder. The CFD and experimental results agreed well for the axial velocity and transversal vorticity along the vertical mid-plane of the rudder and for the axial velocity in two transversal cuts behind the propeller and rudder respectively. Along the trajectory of the tip vortex in the vertical mid-plane of the rudder, the axial velocity simulated with both fine and coarse grids was quite close to those measured, while the transversal vorticity was over-predicted especially with the fine grid.

Sakamoto et al. (2013) conducted a resistance and self-propulsion study for a low L/B twin-skeg container ship model of dimensions, 5.43m length, 1.185m breadth and 0.296m depth for twelve Froude numbers ranging from 0.139 to 0.299. Assumptions were made between the experiments and simulations prior to the calculations. Firstly, the hull used for the simulations did not have bilge keels. According to Sakamoto et al. (2013), it was not considered to have any significant effect on the resistance prediction, since their effect to resistance was mainly between 1% to 3% of the main hull. Secondly the ship was fixed at even keel for the simulations whilst it was free to sink and trim in the experiment. The experiment showed the sinkage to be $0.2\%L_{PP}$ downward to the bottom of the ship whilst the trim was 0.06^{o} downward to the bow. Both values were considered small and were ignored up to medium speed. Results of the resistance computations showed good agreement for the form factor, total resistance coefficient and effective power at the various Froude numbers compared with the experimental data. At Froude number of 0.299, the form factor and total resistance coefficient were underestimated by 2.5%. The self-propulsion computations predicted the thrust and torque coefficient with average error of 6% and 8% of the experimental data respectively. Parametric studies were also conducted in search of optimal propeller local to increase w_T. Twelve locations were considered and the optimal location was found at y/D and z/D of -0.1 and 0.05 respectively.

Although RANS computational prediction of ships total calm water resistance and powering to replace model testing is desirable, there are still uncertainties that needs to be addressed. A statistical analysis of computed ship's total resistance coefficient was reported at the Gothenburg 2010 workshop (Larsson et al., 2013) for a container ship

with scaling ratio of 1:31.6, (a) fixed in sinkage and trim and (b) free to sink and trim. A substantial reduction in standard deviation was observed for the fixed condition with mean comparison error below 2% indicating that all predictions for that particular condition were quite accurate even though they were still not within the experimental accuracy. The standard deviation for the self-propelled case was 3% for fixed condition with small comparison error. However for the free condition the mean comparison error was 7.2%. One obvious question was how dependent the results were on grid size. About 90% of all the model scale computations were made with grids below 10 million cells. By excluding the self-propulsion submissions, the towed conditions were predicted accurately with cells size in excess of 3 million. Even the largest grid of approximately 300 million cells showed the same improvement compared to that of the 3 million cells with comparison error of about 3%. However for cell sizes below 3 million, comparison errors increased to about 8%.

Another lesson learnt from the study was how dependent the results were on turbulence model. The simple two equation models performed reasonably well with the Menter (1994) model showing very good results; however the explicit algebraic stress model and the Reynolds stress model showed poorer results with grid coarsening and the self-propulsion condition.

Application of RANS to simulation of a complete hull in order to gain an understanding of the complex hydrodynamics occurring at the stern for performance improvement, where the hull, propeller and other appendages are combined in one model, is limited, and so far most of the work has been focused on modelling one or two of the components at a time.

Apart from resistances and powering, the use of RANS has also been applied to ship manoeuvring. Workshops such as SIMMAN (2008), were setup to benchmark the prediction capabilities of different ship manoeuvring simulation methods. The workshop was the first of its kind since manoeuvring simulations were not yet benchmarked for their prediction capabilities through systematic quantitative validation against Experimental Fluid Dynamics (EFD).

Although the Reynolds-averaged Navier-Stokes (RANS) approach has been used for some time now, its full capabilities are still yet to be exploited. In the report from the 26th International Towing Tank Conference (ITTC, 2011), the Committee on Propulsion concluded that remarkable progress had been made using numerical computations especially those of RANS on previously known technologies to improve propulsive efficiency, and that has enabled some previous technologies that only produced marginal or inconsistent improvements to improve efficiency more reliably. But it also concluded that there are still large amount of uncertainties in results of such computations especially in areas of grid dependency of different solvers, turbulence modelling, farfield boundary conditions and grid resolution.

2.6 Propeller analysis

Propellers produce thrust as each blade experiences local lift forces. Ship propellers can therefore be analysed as a lifting surface with shorter span-to-chord ratio. However unlike other foils, (e.g. aeronautical foils) the smaller span-to-chord ratio makes the ship propeller flow very complex (Bertram, 2000). Initial two-dimensional methods used to analyse the action of the marine propeller like the lifting-line theory introduced considerable errors, which needed to be corrected afterwards. However with the advent of highly skewed propellers, the use of three-dimensional flow method is obvious. Corrections made based on the use of lifting line theory cannot be applied. Three-dimensional methods used today include lifting surfaces, vortex-lattice methods etc. Below is an overview of the various approaches for propeller analysis in increasing order of computational cost. The computational cost of each technique is normalised to the baseline blade element momentum theory which has a cost of one as presented by Phillips (2009) and Bertram (2000).

- **Momentum theory -** Propeller is modelled as an actuator disk creating a pressure jump in the flow. Thrust, torque and corresponding power are attributed to changes in fluid velocity within the slipstream surrounding propeller disc.
  Pros: Simple and fast and yields ideal efficiency.
  Cons: Rotative and viscous losses not modelled.
  Cost:< 1.
  Used by: Phillips et al. (2010).

- **Blade element theory -** Forces and moments acting on blade derived from several sections represented as two dimensioned foils at an angle of attack to the flow.
  Pros: Can be used to perform a fairly detailed local analysis of the propeller in a shorter time.
  Cons: Induced velocities in the fluid due to propeller action are not accounted for.
  Cost:< 1.
  Used by: Benini (2004).

- **Blade element momentum theory -** Combination of momentum and blade element theory.
  Pros: Corrections for finite number of blades and strong curvature effects. Good for estimation of power loss for which the exact "mirroring" of the flow is not essential as long as the required conditions of the flow (head) are adequately captured.
  Cons: Resulting flow looks very different to that induced by a rotating propeller.
  Does not account for wake expansion.
  Cost: 1.
  Used by: Badoe et al. (2013); Phillips et al. (2009).

- **Lifting line method -** Propeller blade reduced to radially aligned straight vortices with strength varying over the radius.
  Pros: Rotative losses reflected in model. Good for initial design of propeller.
  Cons: Does not account for camber corrections and skewness. Unable to capture stall behaviour.
  Cost: ~ 10.
  Used by: Epps et al. (2010); Flood (2002).

- **Lifting surface method -** Propeller blade represented as infinitely thin surface fitted to blade camber line. Vorticity distribution accounted for.
  Pros: Three–dimensional blade model with corrections only for viscous effects.
  Cons: Pressure distribution corrections needed at hub. Complex method to program.
  Cost: ~ 10^2.
  Used by: Pien (1961).

- **Panel method -** Similar concept to lifting surface method but corrections for blade thickness and hub accounted for.
  Pros: blade thickness and hub corrections made.
  Cons: Complex method to program.
  Cost: ~ 10^3.
  Used by: Kewin (1979); Seol et al. (2002).

- **Reynolds Averaged Navier-Stokes method (transient method)-** Fully three dimensioned viscous flow method using finite volume or finite element approach to solve the average flow.
  Pros: Effective wake easily incorporated, flow field well captured and also near hub and tip of propeller.
  Cons: Computationally expensive approach.
  Cost: ~ 10^6.
  Used by: Stainer (1998); Stern et al. (2010),

- **Large Eddy Simulation method -** Pros: Ability to simulate unsteady behaviour of the propeller flow, in particular the size and frequency of turbulent structures, examples include evaluating the structural safety of the propellers at crash stop, crash back and crash ahead conditions where the use of RANS cannot cope due to the large scale unsteadiness.
  Cons: Most computationally expensive approach.
  Cost: ~ 10^8.

Used by: Bensow and Bark (2010).

The design aim of a propeller optimisation is to reduce power for delivered thrust with a propeller that avoids cavitation at design and off-design conditions. However as seen from the computational cost above and depending on one's objectives, the physical fidelity of simulation can be traded against computational cost if suitable empiricism is included in interpreting the results of the analysis (Molland et al., 2011). A brief description of the methods used for the analysis of the propeller in the current study is presented below.

2.6.1 Momentum theory

The momentum theory or actuator disk theory was first proposed by Rankine (1865) as a mathematical model for propeller action, where the rotor is modelled as an infinitely thin disc, inducing a constant velocity along the axis of rotation. This disc creates a flow around the rotor and a mathematical connection exists between the radius of the rotor, torque and induced velocity neglecting friction.

Consider an actuator disc working inside a stream tube, (Fig 2.8) with the flow moving from left to right. The action of the propeller can be assumed to accelerate the flow uniformly over the disc area from V_1, far upstream, to V_2, at disc and V_3, far downstream. Static pressure in the slipstream at station 1 and 3 is p_0. Pressure increase immediately behind disc is Δp. Thrust generated by the propeller is equal to the increase in axial momentum of the slipstream.

$$T = \dot{m}\ (V_3 - V_1) \tag{2.15}$$

where $\dot{m}$ is the mass flow rate per unit time through the disc.

The power P_D, absorbed by the propeller equals the increase in kinetic energy of the slipstream.

$$P_D = \frac{\dot{m}}{2}\ (V_3^2 - V_1^2) \tag{2.16}$$

From equation 2.15 and 2.16, it can be shown that

$$P_D = \frac{T}{2}\ (V_3 + V_1) \tag{2.17}$$

Power can also be equated to the work done by the thrust force of the propeller.

$$P_D = TV_2 \tag{2.18}$$

By equating (2.17) to (2.18), it can be shown that

$$V_2 = \frac{V_3+V_1}{2} \tag{2.19}$$

If *a and a1* represents the axial inflow factor at the propeller disc and wake respectively, then

$$V_2 = V_1(1+a) \tag{2.20}$$

$$V_3 = V_1(1+a1) \tag{2.21}$$

From equations (2.19) to (2.21), half the acceleration of the flow occurs before the propeller disc and the other half after the propeller disc therefore contraction of the slipstream is important between conditions far upstream and downstream in order to satisfy continuity equation.

2.6.2 Blade element theory

An alternate method for the propeller action was also developed by Froude (1878) which takes into account the propeller geometry known as the blade element theory. In the blade element theory, (see Figure 2.9) the blade is broken down into smaller sections or strips with width '*dr*' connected from tip to tip. Each of the strips can be regarded as an aerofoil with resultant incident velocity U, which comprises of an axial velocity V and a rotational velocity Ωr, which varies linearly up the blade. In the normal operating conditions, the blade pitch angle ϕ at the section is greater than the advance angle and this results in the section having an angle of incidence α. From the combination of angle of incidence α and the section zero lift line the elemental thrust and torque can be deduced from:

$$dT = 0.5\rho NcU^2 (c_l \cos\phi - c_d \sin\phi)\mathrm{d}r \tag{2.22}$$

$$dQ = 0.5\rho NcU^2 (c_l \sin\phi + c_d \cos\phi)\, r\mathrm{d}r \tag{2.23}$$

where N and c are the number of blades and the chord length of section respectively.

Table 2.2: Physical modelling and numeric for resistance and self-propulsion studies

Study	Test case	Code	Turbulence model	Grid size	Grid Type	Free-surface	Propeller	Velocity Pressure	Scale
Simonsen and Stern (2003)	ESSO Osaka	CFDSHIP-IOWA	*k-ω*	2.1M	M	-	-	PISO	1:43.478
Chao (2005)	KCS	COMET	RNG *k-ε*	-	-	-	BF	-	-
Lübke (2005)	KCS	CFX	-	2.2M	-	-	A	-	-
Phillips et al. (2009)	KVLCC2	CFX	SST*k-ω*	2.1M	S	Double body	BF	FC	1:58.000
Stern et al. (2010)	KCS	CFDSHIP-IOWA	*k-ε*/*k-ω*	20.3M	M	Level set	A	-	1:31.600
Stern et al. (2010)	DTMB	CFDSHIP-IOWA	*k-ε*/*k-ω*	10.3M	M	Level set	A	-	1:48.900
Larsson and Zou (2010)	KVLCC2	SHIPFLOW	EASM/SSTk-ω	4.7M	S	-	-	-	-
Stern et al. (2010)	KVLCC1	CFDSHIP-IOWA	*k-ε*/*k-ω*	5.6M	M	Level set	A	-	1:58.0
Zhang et al. (2010)	KCS	FLUENT	SST*k-ω*	-	M	VOF	A	SIMPLE	-
Carrica et al. (2011)	KCS	CFDSHIP-IOWA	*k-ε*/*k-ω*	23.2M	M	-	A	PISO	-
Sakamoto et al. (2013)	Twin-skeg	SURF	SA, *k-ω*	3.6M	M	Level set	BF	AC	1:36.126

A Actual propeller mode; AC Artificial compressibility; BF Body force propeller model, M Multiblock grid; S Single block grid; SA Spallart Allmaras; FC Fullycoupled.

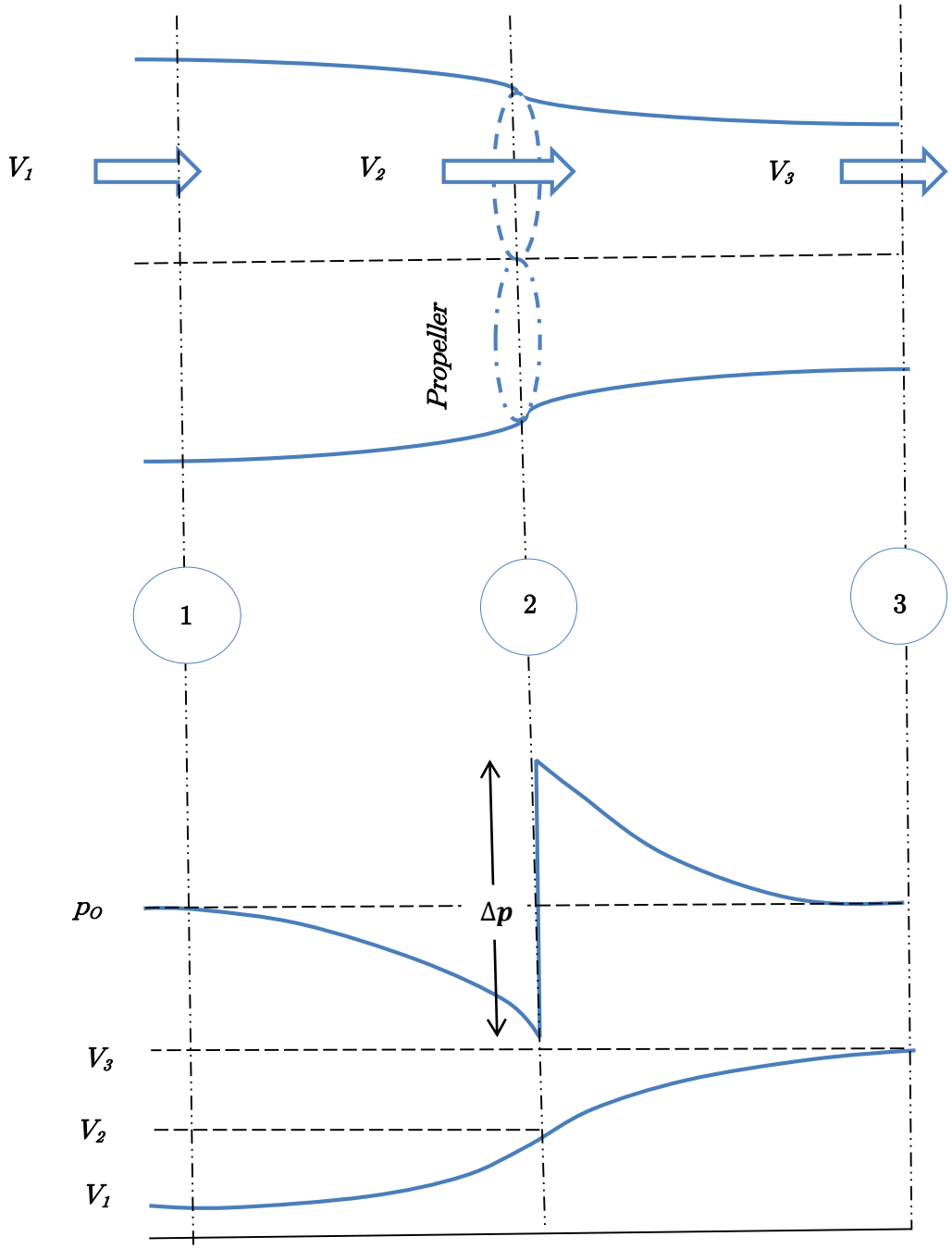

Figure 2.8: Basic momentum theory Carlton (2007).

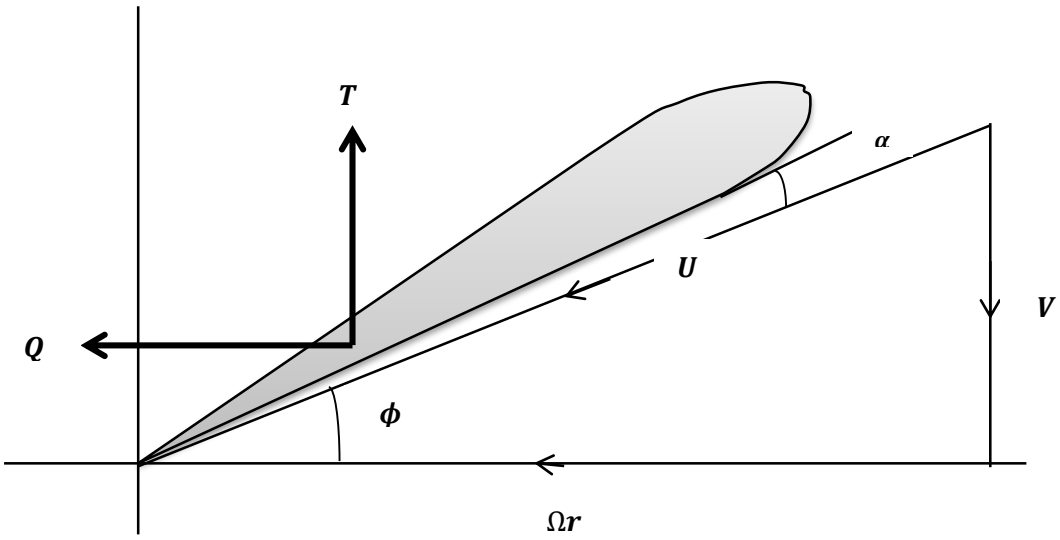

Figure 2.9: Blade element theory.

Section efficiency is given by:

$$\eta = \frac{V\,dT}{\Omega dQ} \tag{2.24}$$

By writing $\gamma = c_d/c_l$ and substituting equations 2.22 and 2.23 into 2.24 the local efficiency can be derived as

$$\eta = \frac{\tan\phi}{\tan(\phi+\gamma)} \tag{2.25}$$

The difference between the blade element theory and the momentum theory is that the blade element theory does not provide information on the momentum changes (a, $a1$) whilst the momentum theory does. These two theories can be combined to evaluate a field of induced velocity around the propeller, and therefore correct the inflow conditions assumed in the basic blade element theory. The induced velocities are not known until the blade loads are computed. With the loading available one can re-compute the field of induced velocities. This is usually an iterative method. Details of the combination of the blade element and the momentum theory have been used as part of the work presented in this thesis and will be presented in detail in chapter 3.

2.7 Chapter summary

This chapter discusses the assessment of the propulsive performance of LNG carrier ships. To be able to accurately predict them, the LNG carrier stern flow needs to be understood as well as the interaction between the ship, propulsor and appendage. The chapter outlined background regarding the stern and wake flow predictions. Key theories, both numerical and experimental were presented for such predictions. Conclusions drawn from the chapter show that, the prediction of the stern flow is very complex, mainly due to the change in cross-sectional shape of the hull and this influences the inflow to the propeller and rudder. Both experimental testing and numerical computations are used to aid in understanding the flow features at the stern in more detail so as to accurately predict them. The use of experimental testing as seen from the literature has much uncertainties and also it is time consuming and costly. Numerical methods on the other hand are considered a cheaper option. A key advantage of using numerical method is its ability to provide local flowfield details especially close to the ship hull which experimental testing does not offer. The evolution of numerical methods to predict the stern flow showed the solution of the Reynolds-averaged Navier-Stokes equation (RANS) as the most widely used design tool for ships stern and wake flows.

In the use of numerical methods for ship stern flow prediction the presence of the propeller at the stern and the downstream rudder complicates the stern flow phenomena. The propeller flow usually involves tip and hub vortices which are developed at the blade tips and hub respectively. The boundary layers on each blade and the pressure gradients due to the load on the propeller makes it even more difficult to understand the propeller flow, hence to predict them. The rudder downstream of the propeller also experiences tip vortices which usually develop at the rudder tip and strong pressure gradients when an angle of drift is applied to it. A region of the rudder also works in the slipstream of the propeller; due to the rotation in the slipstream the part of the rudder in the slipstream also experiences complicated pressure and velocity fields. Within the literature, theoretical approaches used in predicting the action of the propeller and the associated cost involved were discussed. Two of the most widely used are the blade element theory and the momentum theory approaches. The main difference between them is that the blade element theory does not provide information on the momentum changes (a_I, a) whilst the momentum theory does but not the actual action of the blade element. Blade element theory can be used to perform a fairly detailed local analysis of the propeller in a shorter time. In contrast the momentum theory provides useful results but cannot be used as a stand-alone tool to design the propeller. These two theories can be combined or used as stand-alone within a CFD environment to replicate the action of the propeller, by representing its action as a series of momentum sources.

The momentum theory based propeller analysis can be incorporated into RANS. Promising results compared to experiment for momentum theory based propeller flow

behind a hull have been demonstrated by Phillips et al. (2010) for a uniform thrust model. This approach neglects swirl and gives good estimates of a downstream rudder's lift characteristics, but is unable to predict rudder drag. The approach may be best suited for ship flows where requirements for blade effects, vortex shedding, swirl influence and cavitation analysis are not of prime importance.

Another means of predicting the propeller is by fully discretizing the propeller geometry. This is the only suitable approach used for detailed study of local flow around the blade, vortex shedding and cavitation analysis. However the time stepping involved in capturing the detailed blade and hub effect makes it resource intensive. This approach also requires a high level of refinement in the wake region as the predicted performance is also sensitive to capturing the wake and tip vortices (Molland et al., 2011).

Chapter 3

3 Numerical approach

3.1 Introduction

A fully appended LNG ship stern flow as seen in chapter 2 and the hydrodynamic interaction between all components of hull-propeller and rudder is a complex task which has to be well and clearly understood to effectively predict them and subsequently predict its resistance and powering performance. This makes an initial investigation using a combined LNG rudder, propeller and hull complicated. It was therefore decided to reduce the complexity by modelling one or two of the components at a time, to enable effective understanding of the interaction effect to be made and also gain experience with the modelling techniques. The experience gained can then be used to investigate the powering performance of a future twin skeg LNG ship.
As such this stepwise procedure has been adopted:-

1. Study of the propeller flow and its interaction with the upstream skeg and downstream rudder.

2. Study of the resistance and self-propulsion prediction of a fully appended ship.

3. Application of methods used in (1) and (2) to investigate the powering performance of a novel twin-skeg LNG carrier ship.

The subsequent sections are dedicated to developing a suitable numerical model to aid in the understanding of the stepwise procedure above.

Section 2.5 of the literature showed that the RANS methods perform well for ship flows. The order of CPU reduction of RANS methods makes it more suitable for understanding the stepwise procedure and as such will be used in this study.

3.2 Numerical towing tank

The set-up of numerical towing tank to study the stepwise procedure begins with the selection of a suitable RANS solver. Several commercial and academic solvers are available for solving ship flows, examples of which are ANSYS CFX, ANSYS Fluent, CD-Adapco StarCCM and OpenFOAM. For this work, OpenFOAM was selected over other commercial codes due to the reasons outlined below:

Commercial CFD vendors:

- Do not offer complete flexibility for customisation and add-on development to answer the need for research use.

OpenFOAM offers:

- Complete open software platform using object-oriented design.
- Extensive modelling capabilities in library form.
- State of art complex geometry handling and on target driven model development.
- No licencing restriction, unlimited number of users, jobs and cores.
- Commercial support and training which are provided by the developers.

The drawbacks with the use of OpenFOAM are that:-

- There is an absence of an integrated graphical user interface (stand-alone Open Source and proprietary options are available).
- The programmers guide does not provide sufficient details, making the learning curve very steep.
- Lack of maintained documentation makes it difficult for new users.
- Code lacks extensive verification.

3.2.1 The OpenFOAM approach

OpenFOAM (Open Field Operation and Manipulation, (hereafter OpenFOAM)) is a highly customisable set of C++ libraries for solution of problems in continuum mechanics (Jasak et al., 2007). The C++ class libraries make it possible to implement complicated mathematical and physical models as high-level mathematical expressions. This is facilitated by making the high levels of code resemble standard vector and tensor notation as closely as possible. The code is executed through applications, which consist

of *solver*s and *pre* and *post-processing* utilities. It is gaining considerable popularity in academic research and among industrial users because of its flexibility, accessibility, automatic parallelization of applications written using high-level syntax and good control over configurations (Weller et al., 1998). It solves the Reynolds-averaged Navier-Stokes (RANS) equations using a cell centered finite volume method. The code is fully open-source, which allows significant user modification and massive parallelisation. Parallelisation is achieved using the OpenMPI message passing interface.

3.2.2 OpenFOAM Finite Volume Discretization approach

Discretization process can be grouped into two categories:

- Solution discretization: where a numerical description of the computational domain is defined and the space is divided into control volumes or cells.
- Equation discretization: produces specific terms of the governing equations into discrete algebraic equations that are needed to be solved iteratively.

A complete description of the OpenFOAM solver and discretization approach is beyond the scope of this report but can be found in the OpenFOAM programmer's guide. The finite volume discretization is briefly presented with the following considerations:

- Method applicable to steady state and transient calculations
- Spatial dimensions, 1, 2 or 3 dimension
- Control volume is of any shape
- Method is based on discretizing the integral form of the governing equations over control volume of the discrete domain

3.2.3 Solution approach

OpenFOAM's finite volume method uses co-located methodology on unstructured polyhedral grids with arbitrary grid elements. Solution methodology for implicit equations (finite volume method (fvm)) differs from that of an explicit equation (finite volume calculus (fvc)) since the fvm equations are solved iteratively, rather than producing an immediate solution as in the fvc. The key feature of the finite volume method is the discretisation of the governing equations in integral form, thereby enforcing conservation of basic variables such as mass. Figure 3.1 shows a typical polyhedral control volume constructed around the centroid, P. The control volumes face has a centre f_c. By integrating the transport equation[6] (3.1) in space over an arbitrary control volume (3.2) and using the Gauss's theorem (3.3) to convert the volume integrals into surface integrals and integrating in space, each term of the general transport equation yields (3.4a -d).

[6] assuming that the discretization is second order accurate in space and time

$$\frac{\partial \rho \phi}{\partial t} + \nabla.(\rho \mathbf{u}\phi) - \nabla.(\rho \Gamma_\phi \nabla_\phi) = \rho S_\phi(\phi) \tag{3.1}$$

$$\underbrace{\int_{V_P} \frac{\partial \rho \phi}{\partial t} dV}_{\text{Temporal derivative}} + \underbrace{\int_{V_P} \nabla.(\rho \mathbf{u}\phi) dV}_{\text{convective term}} \underbrace{- \int_{V_P} \nabla.(\rho \Gamma_\phi \nabla_\phi) dV}_{\text{diffusive term}} = \underbrace{\int_{V_P} \rho S_\phi(\phi) dV}_{\text{source term}} \tag{3.2}$$

$$\left.\begin{aligned} \int_{V_P} \nabla.\mathbf{a} dV &= \oint_{\partial V_P} d\mathbf{S}.\mathbf{a} \\ \int_{V_P} \nabla \mathbf{a} dV &= \oint_{\partial V_P} d\mathbf{S}\mathbf{a} \\ \int_{V_P} \nabla \phi dV &= \oint_{\partial V_P} d\mathbf{S}\phi. \end{aligned}\right\} \tag{3.3}$$

where ∂V_P is a closed surface bounding control volume V_P and dS an infinitesimal surface element with associated out pointing normal on ∂V_P.

Convective term:-

$$\int_{V_P} \nabla.(\rho \mathbf{u}\phi) dV = \int_{\partial V_P} d\mathbf{S}.(\rho \mathbf{u}\phi) = \sum_f S.(\rho \mathbf{u})_f \, \phi f = \sum_f F\phi f \tag{3.4a}$$

where the face field ϕf can be evaluated using a variety of schemes examples of which are central differencing and upwind differencing.

Diffusive term:-

$$\int_{V_P} \nabla.(\rho \Gamma_\phi \nabla \phi) dV = \int_{\partial V_P} d\mathbf{S}.(\rho \Gamma_\phi \nabla \phi) = \sum_f (\rho \Gamma_\phi)_f \, \mathbf{S}.(\nabla \phi)_f \tag{3.4b}$$

Source term:-

$$\int_{V_P} \rho S_\phi(\phi) dV = \rho S_\phi V \tag{3.4c}$$

Gradient:-

$$\int_{V_P} \nabla \phi dV = \int_{\partial V_P} d\mathbf{S}.\phi = \sum_f S\phi f \tag{3.4d}$$

Using this equation to evaluate (3.1) over all control volumes a semi-discrete equation is obtained which when evaluated in time yields:

$$\int_t^{t+\delta t} \left[\left(\frac{\partial \rho \phi}{\partial t} \right)_P V_P + \sum_f F\phi f - \sum_f (\rho \Gamma_\phi)_f \, \boldsymbol{S}.(\nabla \phi)_f \right] dt = \int_t^{t+\delta t} (\rho S_\phi V) dt \tag{3.5}$$

where $F = \boldsymbol{S}.(\rho \mathbf{u})_f$ is the mass flux through the face *f*.

After spatial and temporal discretization using (3.4) in all control volume of the domain, a set of equations for the field variable ϕ is obtained which is solved using any iterative method.

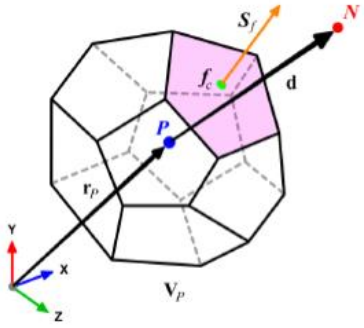

Figure 3.1: Finite volume discretisation schematics, where the vector from cell point P to the neighbouring cell centre point N is d. Face area vector S_f points outward from V_p, (OpenFOAM, 2011).

3.2.4 Pressure-velocity coupling

The Semi-Implicit Method for Pressure-Linked Equations, SIMPLE (Pantankar and Spalding, 1972) is a guess and correct methodology that allows to couple the Navier-Stokes equations with an iterative procedure. It is a steady state solution and uses under-relaxation of the variables instead of pressure correction to maintain stability of the solution. Courant number limitations do not apply. It is implemented in OpenFOAM and can be summed up below:

- Specified boundary condition
- Solves the discretized momentum equation to compute the intermediate velocity
- Mass fluxes are computed at cell faces
- Solves pressure equations and applies under-relaxation
- Corrects mass fluxes at cell faces
- Corrects velocities on basis of new pressure fields
- Updates boundary conditions
- Repeats all steps until convergence

Alternatively the Pressure Implicit with Splitting of Operators, PISO, (Issa, 1986) solves the Navier-Stokes equation in an unsteady problem. The main difference from the SIMPLE algorithm is outlined below:

- No under-relaxation is performed
- Momentum corrector step is performed more than once

Full details can be found in the icoFoam standard solver provided with OpenFOAM.

In addition, OpenFOAM has the option to use the PIMPLE algorithm, which is a combination of SIMPLE and PISO. This method includes both under relaxation and velocity correction, and thus may be used for transient flows but without the Courant number constraint of the PISO algorithm. In particular, the PIMPLE algorithm is used in combination with dynamic meshing within OpenFOAM.

3.2.5 Geometry

For validation of the stepwise study the geometry of the domain is selected to match as closely as possible, the experimental conditions. The positioning of the inlet and exit is necessary to ensure flow dynamics are sufficiently developed across the length of the domain. In a rudder-propeller simulation (stepwise steady 1), the inlet is placed 8 rudder chord lengths upstream and 12 rudder chord lengths downstream. For a complete steady hull-propeller-rudder simulation (stepwise steady 2), the boundaries are placed 1.2 ship lengths upstream and 2.5 ship lengths downstream of the hull whilst unsteady hull-propeller-rudder simulations extend the outlet to about 3 ship lengths downstream to prevent wave reflections. This conforms to ITTC recommended procedures and guidelines for ship CFD applications (ITTC, 2011). Figure 3.2 illustrates an example of a numerical towing tank. Table 3.1 also shows domain particulars used for stepwise study 2.

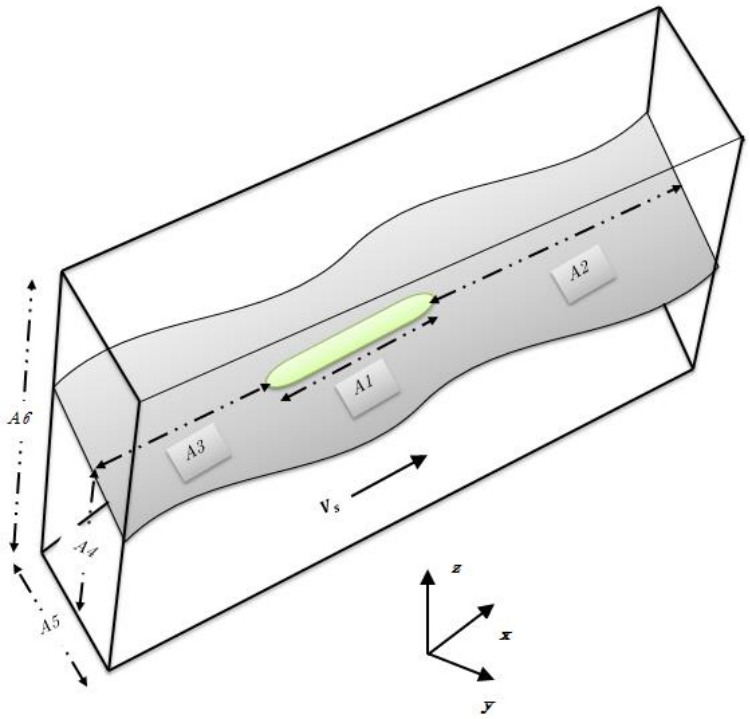

Figure 3.2: Geometrical representation of numerical towing tank adapted for unsteady complete hull-propeller-rudder computations.

Table 3.1: Numerical towing tank domain particulars.

Parameter	Dimensions
A1(hull length)	L (m)
A2 (exit)	$3L_{pp}$ (m)
A3 (inlet)	$1.2L_{pp}$ (m)
A4 (water column)	experimental tank depth, D/2 (m)
A5 (tank width)	experimental tank width, B (m)
A6 (air&water column)	experimental tank depth, D (m)

3.2.6 Choice of turbulence model

The Shear Stress Transport-SST k-ω turbulence model (Menter, 1994) is utilised for all calculations. The model has shown to be able to give accurate predictions in ship hydrodynamics, (80% of the submissions for the Gothenburg 2010 Workshop). An advantage of the SST model is its ability to predict more accurately non–equilibrium regions in boundary layer with adverse pressure gradients. The only drawback with this model is that it produces too large turbulence levels in stagnation regions and regions with strong acceleration. Previous investigation for ship flow has shown it to be better at replicating flow around ship hull forms, notably in capturing hooks in the wake contour at the propeller plane (Larsson et al., 2010). A complete description can be found in Versteeg and Malalasekere (2007). In brief, it combines both the k-ε model and the k–ω model. The use of k–ω in the inner parts of the boundary layer makes the model usable all the way down to the wall through the viscous sub layer; therefore the SST model can be used as low Re-turbulence model without any extra damping functions. It also switches to the k-ε in free stream and avoids the common problem of k–ω which is sensitive to the inlet free stream turbulence properties.

3.2.7 Choice of free-surface model

Free-surface is captured using the Volume of Fluid (VOF) method. The VOF is a fixed grid technique which is designed for two or more immiscible fluids whereby the interface position is usually part of the unknown to be solved. The volume fraction α is governed by:-

$$\frac{\partial \alpha}{\partial t} + \nabla . (\alpha u_i) = 0 \tag{3.6}$$

The Multidimensional Universal Limiter with Explicit Solution (MULES) algorithm (Ubbink and Issa, 1999) is used to ensure a sharp resolution of the free surface.

3.2.8 Meshing Approach

Unstructured meshes are used for all computations in this thesis. Using structured grid for complex geometries like fully appended ship requires expertise in laying out an optimal block structure for the fully appended ship. This particularly becomes time consuming. Unstructured grids on the other hand are automated and require little user time and effort. They also enable the solution of very large and detailed problems in a relatively short period of time as compared to structured grids.

Mesh generation used in OpenFOAM is either from an input file (blockMesh) or from generic geometry specified as STL[7] file which is meshed automatically with hex-dominant grids known as snappyHexMesh. Both blockMesh and SnappyHexMesh utility have been used for this work. An example of the mesh generation procedure is illustrated in Figure 3.3. Mesh generation utilizing snappyHexMesh utility begins with an initial mesh density set by creating a structured background mesh (blockMesh) of hexahedral cells which covers the entire domain, (step 1). The mesh refinement level for the background mesh is level 0. The cell aspect ratio should be approximately 1 and there must be at least one intersection of the cell edge with the STL. The maximum length, breadth and height of a cell size used for the stepwise study was 0.2m x 0.2m x0.2m respectively. The next step is the cell splitting stage which is performed according to specifications a user supplies in a dictionary (step 2). Cell removal and snapping to surfaces are then performed with the user specifying the inputs also through a dictionary (step 3). The snapping stage involves displacing the vertices in the castellated boundary onto the geometry surface and solving for relaxation of internal mesh with the latest displaced boundary vertices. Vertices that cause mesh quality parameters to be violated are found and their displacement reduced from their initial value and the snapping process repeated until mesh quality is satisfied. It should be noted that refinement levels for surface areas can be set either as a whole or separately for different surface components. The refinement levels range from 0 to 9. The final stage of the snappyHexMesh process is the layer addition (step 6). This process is optional but useful when computing boundary layer effects or flow separation. The whole meshing process is automatic and may take a couple of minutes depending on the geometry and problem to tens of minutes. One notable drawback with the use of snappyHexMesh is its difficulty in following sharp edges and corners around geometries.

[7] STereoLithography also known as Standard Tessellation Language is a file format native to the stereolithography CAD software created by 3D systems and the format is supported by several software packages.

3.2.8.1 Mesh strategy for numerical towing tank

In creating meshes for the stepwise study, several factors were considered:-

- Mesh distribution around geometries to capture the boundary layer.
- Mesh distribution to capture viscous wake.
- Refinement of the free surface region to avoid numerical damping.
- For rotating geometries, the mesh should allow smooth rotation without conflicting with meshes in stationary regions.
- Mesh cells should be kept as low as possible to reduce computation time.

In free surface computations a procedure was adopted to ensure the near-hull refinement blended smoothly with the free surface refinement. The process uses two zones, namely the near hull-region and the free surface region. The process is also illustrated in Figure 3.3 and is outlined below.

1. OpenFOAM's mesh processes steps 1-3 are performed for the hull model whilst ensuring the layer addition is disabled.

2. OpenFOAM utility toposet is used to select the near-hull region and then cut away from the mesh (step 4).

3. The refine mesh utility is then used to refine the free surface region in both longitudinal and vertical direction (step 5). Importance is placed on the vertical direction to better capture the wave elevation.

4. The near-hull region is stitched back to the main mesh and then the layer addition is enabled to grow boundary layers around the hull (step 6).

This process is implemented through scripting which can be called upon to control the input data of all the utilities.

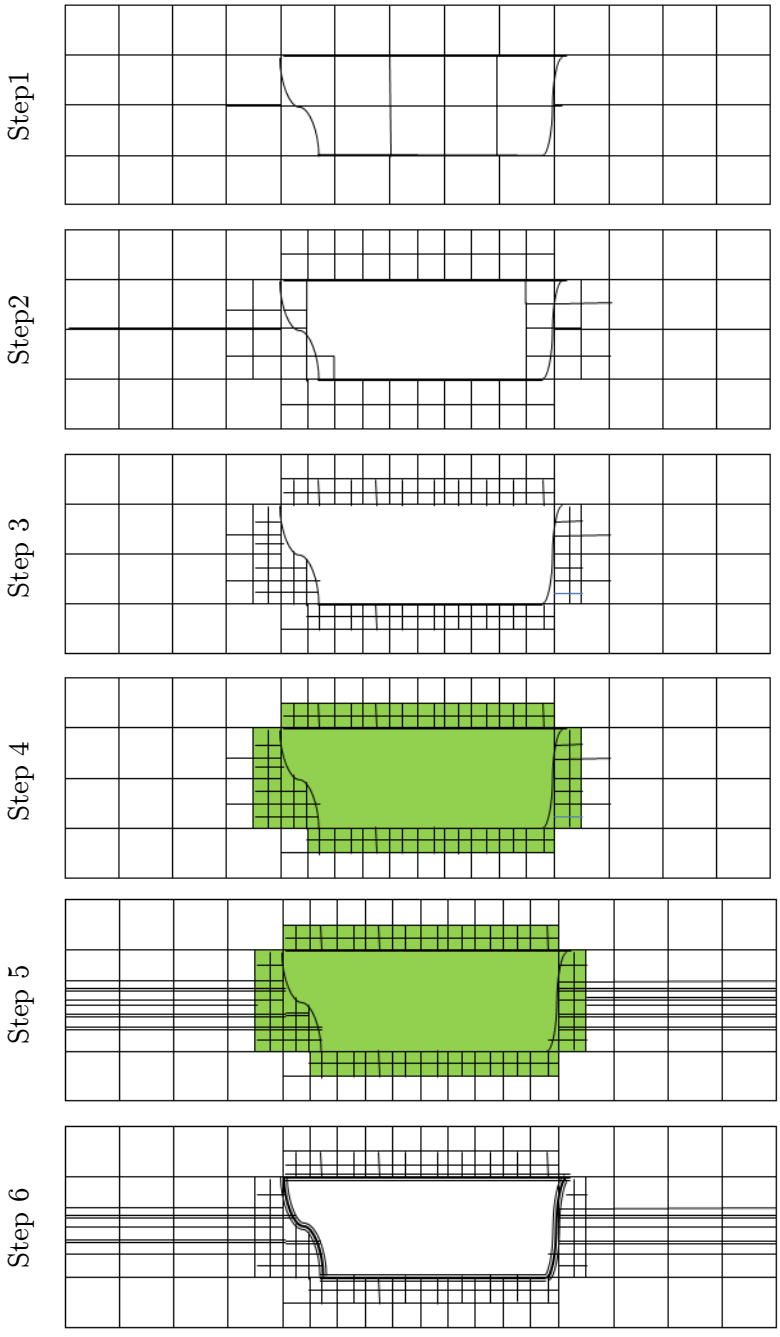

Figure 3.3: Schematics of mesh generation strategy for numeral towing tank.

3.2.9 Mesh sensitivity studies

Errors and uncertainties are unavoidable in CFD methodologies. In a case where a complex problem is being solved using CFD, it is advisable to compare the numerical results with the experiments to enable the user to assess how well the solution of the problem compares to reality. This thus gives an indication of the level of trust that needs to be placed on the results. The terminologies widely accepted (ITTC, 2008) in CFD are:

1. Verification: process of determining that a model implementation accurately represents the developer's conceptual description of the model and the solution to the model.
2. Validation: process of determining the degree to which a model is an accurate representation of reality from the perspective of the intended uses of the model.

The verification process involves quantification of the errors. This is usually the estimation of round off, iterative convergence and discretization errors. The validation involves quantification of the input uncertainty and physical model uncertainty. There are several available public access data banks to support CFD validation work but for credible validation one may limit itself to data from trusted source.

The concept of verification presented below is applied to this work and was proposed by Stern et al. (2001). The methodology has been adopted as one of the recommended procedures by the International Towing Tank Conference (ITTC) Resistance Committee (ITTC, 2008). The analysis is widely used for ship flow studies.

When a grid is generated it is advisable to perform calculations to investigate if the grid results in a stable solution. This requires at least three grids. This is refined systematically in all directions using the same refinement ratio r_G. Grid convergence can then be determined from the ratio of solution changes in the three grids.

$$R_G = \frac{\varepsilon_{21}}{\varepsilon_{32}} = \frac{S_2 - S_1}{S_3 - S_2} \tag{3.7}$$

where $S_2 - S_1$ and $S_3 - S_2$ represents solution changes between medium-fine and coarse-medium grids respectively. The following cases may be observed depending on the values of R_G.

- Converging results: $0 < R_G < 1$;
- Oscillatory results: $R_G < 0$; $|R_G| < 1$
- Diverging results: $|R_G| > 1$

3.2.9.1 Converging results

Based on Taylor expansion of the solutions of the three grids around the grid – independent solution S_C, the first order error estimate for the fine grid can be made by

$$\delta_{RE,G1} = \frac{\varepsilon_{21}}{-1 + r_G{}^{P_G}} \tag{3.8}$$

The estimated order of accuracy is given by

$$\mathrm{P_G} = \frac{\ln {}^{\varepsilon_{32}}/_{\varepsilon_{21}}}{\ln r_G} \tag{3.9}$$

where r_G is the grid refinement factor. A correction factor, $\mathrm{C_G}$ is introduced based on the P_{th}, which is the theoretical order of accuracy of the method which is applied:

$$C_G = \frac{-1 + r_G{}^{P_G}}{-1 + r_G{}^{P_{th}}} \tag{3.10}$$

If C_G turns close to one then the mesh uncertainty can be estimated using:

$$\mathrm{U_G} = \left|(1 - C_G)\delta_{RE,G1}\right| \tag{3.11}$$

else the mesh uncertainty can be estimated using:

$$\mathrm{U_G} = \left|(1 - C_G)\delta_{RE,G1}\right| + \left|C_G\delta_{RE,G1}\right| \tag{3.12}$$

3.2.9.2 Oscillatory results

For oscillatory results, it is only possible to estimate the uncertainty by preforming calculations enough to determine the upper and lower bounds of the oscillating solutions. This requires more than three grids.

$$\mathrm{U_{G1}} = \frac{1}{2}(S_U - S_L) \tag{3.13}$$

3.2.9.3 Diverging results

For divergence, it is not possible to estimate the uncertainty and error hence the grid quality needs to be improved to obtain a converging or oscillatory condition.

3.2.10 Solver settings

The following OpenFOAM solvers are used as part of the numerical towing tank implementations:-

- simpleFoam solver :- a steady-state solver for incompressible, turbulent flow.

- pimpleDyMFoam solver:- is an implementation of the pimpleFoam solver, which is a large time-step transient solver for incompressible flow using the merged PISO-SIMPLE algorithm. In addition the pimpleDyMFoam solver allows for dynamic meshes, it is transient and also allows for relatively large time steps.

- LTSInterFoam solver:- is a local time stepping (LTS, steady-state) solver for two incompressible, isothermal immiscible fluids using a VOF (volume of fluid) phase-fraction based interface capturing approach. The solver first maximises the time-step according to the local Courant number. It then processes the time-step field by smoothing the variation in time step across the domain to prevent instability due to large conservation errors caused by sudden changes in time step; spreading the most restrictive time step within the interface region across the entire region to further reduce conservation errors.

3.2.11 Boundary condition

Boundary conditions prescribed in OpenFOAM falls into two categories: Dirichlet or fixed value; which prescribes values of dependent variable on the boundary, and Neumann or fixed gradient; which prescribes the gradient of the variable normal to the boundary. Whilst the specific boundary conditions used for each case will be presented in the appropriate chapters, some general description of the boundary conditions used is provided here.

- **Inlet:** Velocity is prescribed at the inlet and the pressure assumes a zero gradient for consistency.
- **Outlet:** Pressure at the outlet is set to fixed value whilst the velocity is set to zero gradient. Boundary is usually placed at a distance which is free of geometrical disturbance to ensure a fully developed flow.
- **Symmetry:** A symmetry plane applies a constraint which mirrors fluid flow on the other side. This condition defines that component of solution gradient normal to this plane should be fixed to zero. Parallel components are extrapolated from interior cells.
- **Wall:** The most common boundary condition in fluid flow problems is the wall. This is commonly known as the no-slip boundary condition and it is appropriate condition for the velocity component at the wall. The normal component is set to zero whilst the tangential component is set to the velocity of the wall.
- **Cyclic (or periodic):** For two boundaries of the same face description, values of the flow variables are set equal to those on the face of the coupled boundary. Thus there is no restriction on the direction of flow at the boundaries.

3.2.12 Near wall treatment methods

The presence of the geometries (wall) in the gridwise study makes the flow behaviour and turbulence structure different from freestream turbulence. Around a thin region on the wall known as the boundary layer, viscosity plays an important role. Velocity components normal to the surface is much smaller than that parallel to the surface. Mean flow depends on the y distance from the wall, fluid density, viscosity and wall shear stress. As a result of dimensional analysis,

$$U_\tau = \frac{U}{\sqrt{\tau_w/\rho}} \tag{3.14}$$

where U_τ is the friction velocity, τ_w is the wall shear stress, ρ is the density and U is the velocity at y.

A Reynolds number based on the distance to the wall using the friction velocity can be defined as

$$y^+ = \frac{yU_\tau}{\upsilon} \tag{3.15}$$

where υ is the kinematic viscosity and y is the distance from the wall.

Experiments shows that the boundary layer structure, Figure 3.4, comprises of four regions:

- **Linear sublayer**: - Is a thin region, $y^+ < 5$, close to the wall and fully dominated by viscous effects.
- **Blending region**: - Is the zone that the laminar wall law blends to the turbulent wall law. Typically $5 < y^+ < 15$.
- **Log law region**: - Fully turbulent region where shear stress varies slowly with distance from the wall. Typically, $15 < y^+ < 500$.
- **Outer layer**: - Where inertia dominates the flow far from the wall and free from direct viscous effect.

The objective is to account for the boundary layer without having to use a mesh which is so fine that the flow pattern in the layer can be calculated explicitly. Standard wall functions are based on the assumption that the first grid point be placed away from the wall, typically in the log layer and the flow in the linear and blending region do not have to be resolved. Once a value of the boundary layer thickness is calculated and a y^+ is specified, the number of points inside the boundary layer has to be determined. This depends on the level of accuracy required and the Shear Stress Transport-SST k-ω turbulence model.

In the treatment of the wall boundary layer for the numerical towing tank, the ANSYS (2010) suggestion of 10-15 nodes were used whilst the distance between vertical nodes were estimated as a function of growth rate. It should be pointed out that it is not always possible to place 10-15 nodes in the boundary layer. For example, for complex hull and propeller shapes, due to strong curvatures and depending on the blade thickness, the mesh approach discussed in section 3.2.8 makes it possible for only 1-3 nodes to be placed in the boundary layer. Placing more than 3 nodes will result in achievement of less than 65% of near wall cells. This results from near sharp corners as the layers is collapsed to reduced skewness and non-orthogonality of the mesh. In such cases the surface refinement level on the walls can be increased (≥ 5) to make the mesh on the walls finer.

Wall functions approach relies on empirical correlations and have provides reasonably good predictions for high Reynolds number flows (Bakker, 2006). For low Reynolds number flow[8] a two layer zonal model may be used where only k equation is solved in the viscosity-affected region and ε is computed using a correlation for turbulent length scale. Table 3.2 developed by Bakker (2006) compares strengths and weaknesses of three near wall treatments approaches.

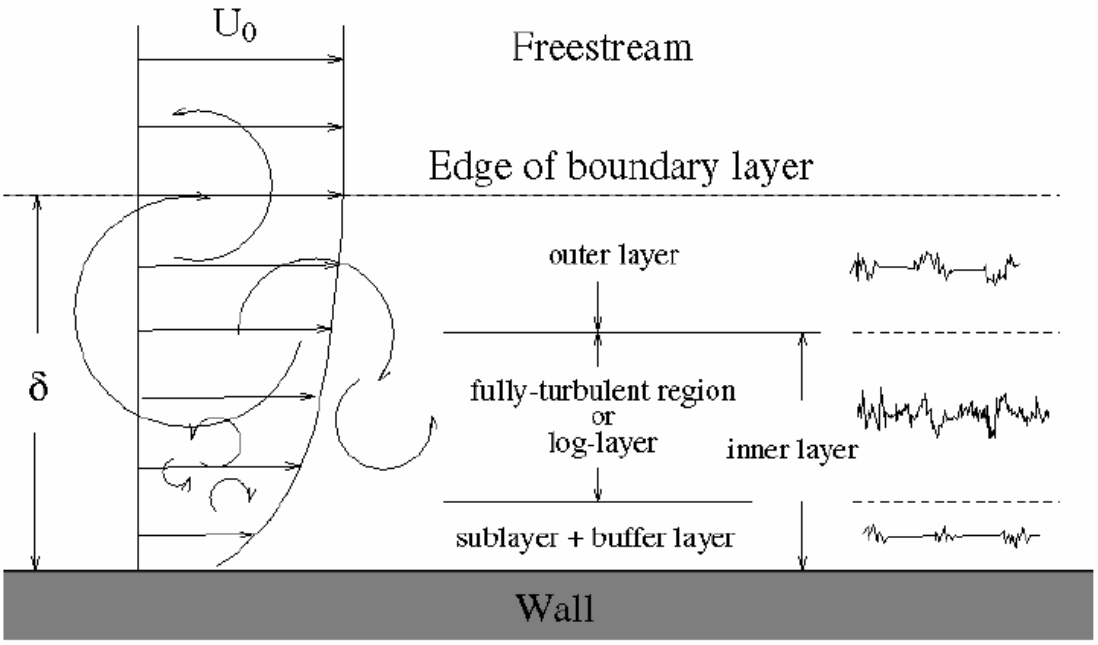

Figure 3.4: Turbulent boundary layer (Bakker, 2006).

[8]zones distinguished by a wall distance-based turbulent Reynolds number $Re_y = \frac{\rho\sqrt{k}y}{\mu}$

Table 3.2: Comparison of near wall treatments.

Approach	Strengths	Weaknesses
Standard wall-functions	Robust, economical, reasonably accurate	Poor for low-Re flows, strong body forces, highly 3D flows
Non–equilibrium wall functions	Accounts for pressure gradient effects, improved prediction for separation	Poor for low-Re flows, strong body forces, highly 3D flows
Two-layer zonal model	Does not rely on empirical law of the wall relations, good for complex flows and applicable to low-Re flows	Requires finer mesh resolution and therefore larger CPU and memory resources

3.3 Propeller modelling within a RANS Environment

Computation of the flow of a propeller behind a hull is highly complex and transient as it requires the use of high level of mesh cells around the blades coupled with small time steps and adequate turbulence modelling to resolve the complex flow features. The mesh quality and whether it captures all flow features thus determine the accuracy of the solution, likewise the viscous wake and its downstream propagation along with the tip vortex have a strong influence on the accurate prediction of propeller forces (Molland et al., 2011). In the setting up of a numerical towing tank to study the stepwise procedure, the objective is to be able to mimic the unsteady propeller flow behind the ship hull. This can be addressed using a hierarchy of techniques. A direct approach is to explicitly model the rotating propeller flow. Examples include the use of multiple or moving reference frame (MRF) as explained in section 2.5 and a sliding mesh to fully discretize the ship and propeller as presented in Lübke (2005) and Carrica et al. (2011), where a part of the mesh containing the propeller (rotor) rotates within the main mesh which contains the ship (stator) and a connection (interface) applied between both meshes. This approach theoretically offers the highest degree of fidelity but requires small time steps due to restrictions imposed by explicitly solving the propeller flow, thus placing a high demand on computation. An indirect approach is to u a body force model.

Both the direct approach using a sliding grid and the indirect approach using bodyforce models are available in OpenFOAM and are adopted in this study to account for the action of the rotating propeller flow. These approaches are described below.

3.3.1 Arbitrary mesh interface model (AMI)

The direct approach of modelling the propeller flow used in this study employs the arbitrary mesh interface (AMI) technique as implemented in OpenFOAM version 2.2.0. This technique allows flow data to be exchanged across disconnected mesh domains which can either be stationary or moving relative to one another. In the discussed context, it operates by projecting one of the sides of the interface on to the other and is used for handling rotating meshes. The AMI idea is based on a set of weighting factors that balances the fluxes at the region interface. An example of the AMI interface for a propeller is shown in Figure 3.5. The drawback to this approach is that it is computationally much more expensive since the full transient flow field needs to be resolved. Moreover the cell count required also increases as the fine detail of the propeller needs to be resolved. This becomes particularly limiting as one considers the difference of the significant flow feature scales for the hull and propeller.

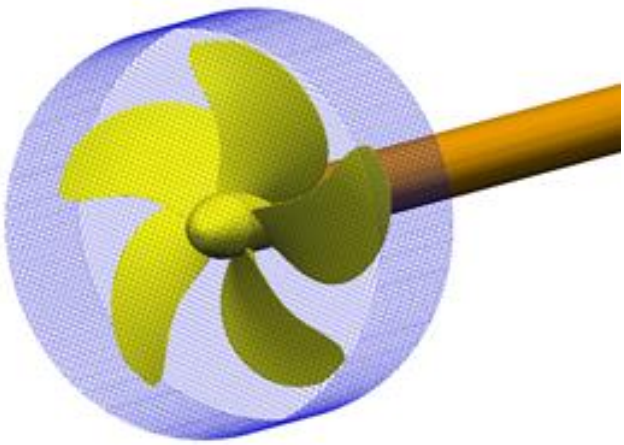

Figure 3.5: Example of an AMI boundary for a marine propeller.

3.3.2 Body Force propeller models

For simulations involving the interaction between the propeller, rudder and hull and not directly concentrating on the propeller, direct mirroring of the propeller flow is not essential. Instead the propeller can be neglected and its effect on the flow can be modelled by representing the propeller as a series of axial and momentum source terms. This is the idea behind the body force model. Several approaches to calculating the distribution of the momentum source terms exist and two prominent ones are mentioned below as:-

- Models which calculate the body force by explicitly introducing a pressure jump as a boundary condition.
- Models which add a localised momentum source as a body force.

For complex geometries the latter is ideal, within the OpenFOAM solver a dictionary exists where the swept volume of the propeller including the hub radius, tip radius and chord can be specified. Cells which lie within this volume can be searched and a load distribution be specified. Two different body force approaches will be considered for this study.

- Hough and Ordway (1965) prescribed thrust and torque distribution.
- An implementation to determine the magnitude of thrust and torque distribution from a Blade Element Momentum Theory (BEMt).

3.3.2.1 Hough and Ordway prescribed thrust and torque distribution

The radial distribution of thrust and torque is based on the Hough and Ordway (1965) circulation distribution; this has no loading at the tip and root. The distribution closely matches Goldstein (1929) optimum distribution. It has been used by others such as Stern et al. (1988), Simonsen (2000), and Phillips et al. (2009) to replicate the action of the propeller in several marine applications.

The non-dimensional thrust distribution f_{b_x} has the form:

$$f_{b_x} = A_x r^* \sqrt{1 - r^*} \tag{3.16}$$

where the non-dimensional radius r^* is defined as $(r' - r'_h)/(1 - r'_h)$, $r'_h = R_h/R_p$, $r' = r/R_p$, R_h = radius of hub and R_p = radius of propeller.

Similarly the non-dimensional torque distribution f_{b_θ} can be written as:

$$f_{b_\theta} = A_\theta \frac{r^* \sqrt{1-r^*}}{r^*(1-r'_h)+r'_h} \tag{3.17}$$

Since the volume force added over the actuator disc region must sum up to the total thrust and torque, it is fulfilled if the constants A_x and A_θ are computed as

$$A_x = \frac{C_T}{\Delta} \frac{105}{16(4+3r'_h)(1-r'_h)} \tag{3.18}$$

$$A_\theta = \frac{K_Q}{\Delta J^2} \frac{105}{\pi(4+3r'_h)(1-r'_h)} \tag{3.19}$$

$$C_T = \frac{2T}{\rho U^2 \pi {R_P}^2} = \frac{K_T}{\pi/J^2} \tag{3.20}$$

where K_Q and K_T are the torque and thrust coefficients respectively, T is the thrust, J is the propeller advance coefficient and Δ is the mean chord length projected into the x-z plane or actuator disk thickness. For numerical stability the length of the subdomain should be at least 0.1% of the propeller diameter (Phillips et al., 2009).

In the computational domain, the force f_{b_x} is aligned with the x-direction and can therefore be used directly. The tangential component is resolved in the y and z direction and the forces are imposed on the RANS grid at various points which lie within the propeller disk. By adopting this approach not all the interaction mechanisms are captured. This approach is good for modelling the interaction of propeller on hull and propeller on rudder. Since the forces are prescribed, and are independent of the current propeller flow field, interaction effects like hull on propeller and rudder on propeller cannot be captured. The effect of the hub is not captured. An introduction of a physical hub can aid in capturing flow effects as a result of the hub.

The full implementation of this method in OpenFOAM by coupling with the simpleFoam solver is presented in appendix 1. It has been used for a preliminary investigation for a propeller-rudder study which is detailed in appendix 2. Aside the simpleFoam solver the method has also been coupled to the LTSInterFoam solver for use in the stepwise study.

In brief the coupling procedure with simpleFoam solver used for the stepwise investigation (2) is presented as follows:-

1. First a steady state RANS computation is performed by setting the propeller revolutions (rps) to zero. The resulting nominal wake fraction is determined once a converged solution is achieved by sampling the velocities entering the propeller plane.

2. The momentum sources are then calculated based on the given propeller rps and the open water propeller characteristics. This procedure fails to capture the influence of the rudder and hull on the flow through and across the propeller disc.

3. The simulation is then started from the naked hull and rudder solutions but now with the added momentum sources (both axial and tangential momentum terms) and run until convergence is achieved.

An extra step can be added when considering self-propelled computations by varying the rps and adjusting the momentum sources in an iterative manner (each time convergence is achieved) until the thrust equals the self-propelled drag.

3.3.2.2 Blade element momentum theories (BEMt) coupling

This method couples the RANS solver with a blade element propeller code to determine the thrust and torque as well as their distribution. BEMt is a method of modelling the performance of tidal turbines (Mikkelsen, 2003) and ship propellers (Phillips et al., 2009). Blade element momentum theory combines both the blade element theory (Froude, 1878) and the momentum theory (Rankine, 1865) as described in chapter 2. The combination of these two theories alleviates some of the difficulties in calculating the induced velocity of the propeller. Solution to this problem can be achieved if the part of the propeller between r and $(r + \delta r)$ is analysed by matching forces generated by the blade elements, as 2D lifting foils to the momentum changes occurring through the propeller disc between these radii. An actual propeller is not uniformly loaded as assumed by Rankine and Froude actuator disc model, thus to analyse the radial variation of loads along the blade the flowfield is divided into radially independent annulus stream tube. The advantage of BEMt over more advanced methods is its low computational cost and the ability to tune the lift and drag properties of the two dimension section to the local Reynolds number, incorporating viscous effects such as stall or the effect of laminar separation at low Reynolds number (Phillips et al., 2009).

The implementation of the BEMt used here follows the procedure by Molland and Turnock (1996) but is explained here for better readability.

Consider the flow through an annulus of radius r and thickness δr at the propeller disc (Figure 3.6). From momentum theory the thrust and torque on the corresponding blade per unit span can be deduced and written as: -

$$\frac{\partial T}{\partial r} = 4\pi\rho r V^2 K a (1+a) \tag{3.21}$$

$$\frac{\partial Q}{\partial r} = 4\pi\rho r^3 \Omega K a' V (1+a) \tag{3.22}$$

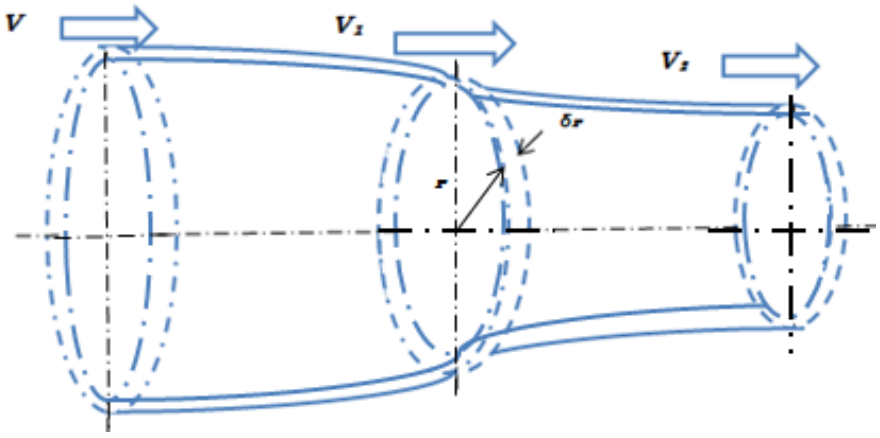

Figure 3.6: Stream annulus through a propellers disc.

where the axial inflow factor, a and the circumferential inflow factor a' are the values at the blade location. K is the Goldstein factor (Goldstein, 1929) to account for a propeller having finite number of blades. Ω is the angular velocity of the propeller. The local section efficiency can be obtained shown as:-

$$\eta = \frac{V\frac{\partial T}{\partial r}}{\Omega\frac{\partial Q}{\partial r}} = \left(\frac{V^2}{r^2\Omega^2}\right).\frac{a}{a'} \tag{3.23}$$

Non-dimensionalising (3.21), (3.22) and (3.23), using $r = xR$, $\Omega = 2\pi n$ and $J = \frac{V}{nD}$, $\partial T = \rho n^2 D^4 \partial K_T$, $\partial Q = \rho n^2 D^5 \partial K_Q$, $\partial r = \mathrm{R}.\,\partial x = (\mathrm{D}/2)\,\partial x$ results in:-

$$\frac{\partial K_T}{\partial x} = \pi x J^2 K\, a\,(1+a) \tag{3.24}$$

$$\frac{\partial K_Q}{\partial x} = 0.5\pi^2 x^3 J\, K\, a'\,(1+a) \tag{3.25}$$

$$\eta = \left(\frac{J}{\pi x}\right)^2.\frac{a}{a'} \tag{3.26}$$

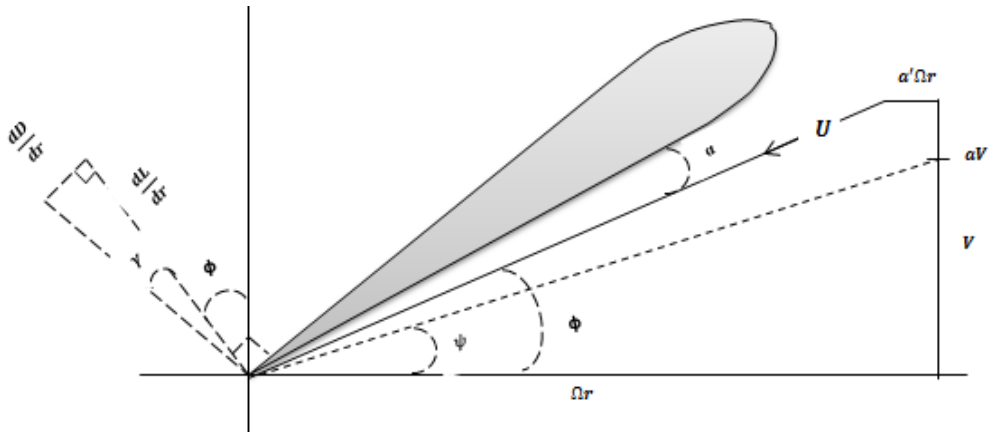

Figure 3.7: Cross–sectional blade element showing velocity and force vectors.

These momentum changes represented by the above equations can be balanced with hydrodynamic forces on the blades which can be analysed by considering an unfolded stream surface at a particular radial position. This appears as in the velocity vector diagram in Figure 3.7. The local lift and drag acting on a 2D blade section can be expressed as: -

$$\frac{\partial L}{\partial r} = 0.5\, N\rho c U^2 C_l(\alpha) \tag{3.27}$$

$$\frac{\partial D}{\partial r} = 0.5\, N\rho c U^2 C_d(\alpha) \tag{3.28}$$

where N = number of blade, c = blade chord and the lift and drag coefficient of the 2D section is C_l and $C_{d,}$ which depend on the angle of attack, α. From equations (3.27) and (3.28), $\tan\gamma = \frac{C_d}{C_l}$.

From the velocity vector diagram, ϕ is the hydrodynamic blade pitch angle of blade, ψ, is the undisturbed flow angle and α is the local angle of attack. The section lift and drag can be resolved to give the section thrust and torque as:-

$$\frac{\partial T}{\partial r} = \frac{\partial L}{\partial r}.\cos\phi - \frac{\partial D}{\partial r}.\sin\phi = \frac{\partial L}{\partial r}.\cos\phi(1\text{-}\tan\phi\ \tan\gamma) \tag{3.29}$$

$$\frac{\partial Q}{\partial r} = r\left(\frac{\partial L}{\partial r}.\sin\phi + \frac{\partial D}{\partial r}.\cos\phi\right) = r\frac{\partial L}{\partial r}.\cos\phi(\tan\phi + \tan\gamma) \tag{3.30}$$

Combining (3.27) and (3.29) and non-dimensionalising results in: -

$$\frac{\partial K_T}{\partial x} = \frac{\pi^2}{4}\left(\frac{Nc}{D}\right) C_l\,(1-a')^2\, x^2 \sec\phi(1\text{-}\tan\phi\ \tan\gamma) \tag{3.31}$$

Similarly combining (3.28) and (3.30) and non-dimensionalising results in: -

$$\frac{\partial K_Q}{\partial x} = \frac{\pi^2}{8}\left(\frac{Nc}{D}\right) C_l\,(1-a')^2\, x^3 \sec\phi(\tan\phi + \tan\gamma) \tag{3.32}$$

An alternate equation for local efficiency can be deduced from equations (3.31) and (3.32) as:-

$$\eta = \frac{1-a\prime}{1+a}.\frac{\tan\phi}{\tan(\phi+\gamma)} \tag{3.33}$$

By combining the ideal efficiency from momentum theory with the local efficiency from the blade element theory, the circumferential and axial inflow factors can be found as:-

$$a' = 1 - \eta_i(1 + a) \tag{3.34}$$

$$a = 1 - \eta_i\ .\ \frac{\eta}{\eta\eta_i + \tan^2\psi} \tag{3.35}$$

An iterative approach as illustrate in Figure 3.8 is used to determine the unknown section angle of attack and hence the true inflow factors by assuming $C_D = 0$, $\gamma = 0$, (Molland and Turnock, 1996).

3.4 RANS-BEMt coupling

The BEMt is coupled with the RANS solver using a two way coupling. Since the propeller works behind the hull, the inflow to the propeller is not uniform, hence to account for the non-uniform propeller inflow, a sectorial approach is used. This divides the propeller plane behind the ship hull into a series of radial, nR, and circumferential, nC, slices as seen in Figure 3.9. Each radial, nR, and circumferential, nC, slice is then probed to determine its local advance velocity (v_a'). Each local nominal wake fraction (w_t') is calculated based on the ship's speed and the local advance velocity.

The BEMt code iterates to find the local thrust (∂K_T) and torque (∂K_Q) at each nR, and nC, location based on the local nominal wake fraction, the local inflow speed and the rps. The local thrust and torque (one value per radial, nR, and circumferential, nC, slice) represents the mean thrust and torque exerted on that slice by the sweeping blades. They are then converted into axial and tangential momentum sources and distributed over the nR radial and nC circumferential slices respectively.

The following modifications were made to the Molland and Turnock (1996) BEMt code:-

- The Goldstein factor used for the original code was based on a functional relation by Wellicome (Molland et al., 2011); K $= \frac{2}{\pi} \cos^{-1}\left(\frac{\cosh(xF)}{\cosh(F)}\right)$ where F $= \frac{N}{2xtan\emptyset}$ - $\frac{1}{2}$ for F $\leq$ 85, otherwise K = 1, and N is the number of blades. This relation assumes that the inner part of the propeller is lightly loaded. In practice this is clearly not the case. To account for the hub a correction was made based on Tachmindji and Milam (1957), who made calculations for propeller blades ranging from 3 to 6 blades with finite hub of radius 0.167R. Figure 3.10 shows one such plot for a 5 bladed propeller. The variation in 'K' can be observed at x< 0.5 compared with values from Wellicome.

- To account for the effect of tangential wake, a propeller race rotation factor a" was introduced which is a correction to the undisturbed flow angle (tan ψ). The race rotation factor modifies equation (3.34) and (3.35) to:-

$$a' = 1 - \eta_i(1 + a) + a'' \tag{3.36}$$

$$a = 1 - \eta_i + a''.\frac{\eta}{\eta\eta_i + tan^2\psi} \tag{3.37}$$

The empirical relations for lift and drag used satisfy the following range of geometries and operating conditions.

- Advance Coefficient, $0.3 \leq \mathrm{J} \leq 1.1$
- Pitch Diameter Ratio, $0.6 \leq \frac{P}{D} \leq 1.20$
- Blade Area Ratio, $0.4 \leq BAR \leq 0.8$
- Number of Blades, $3 \leq N \leq 5$

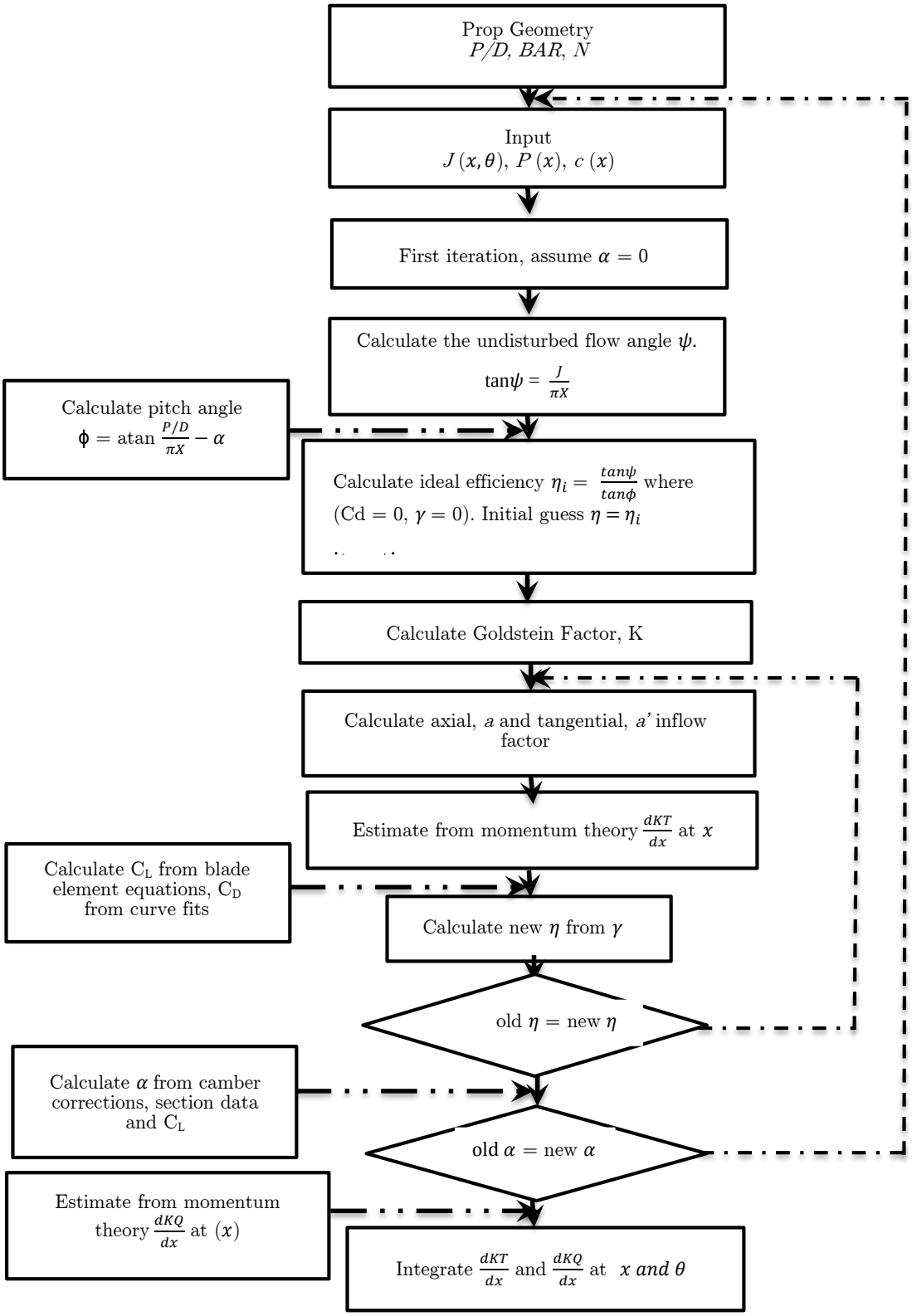

Figure 3.8: BEMT solution approach adopted by Molland and Turnock (1996).

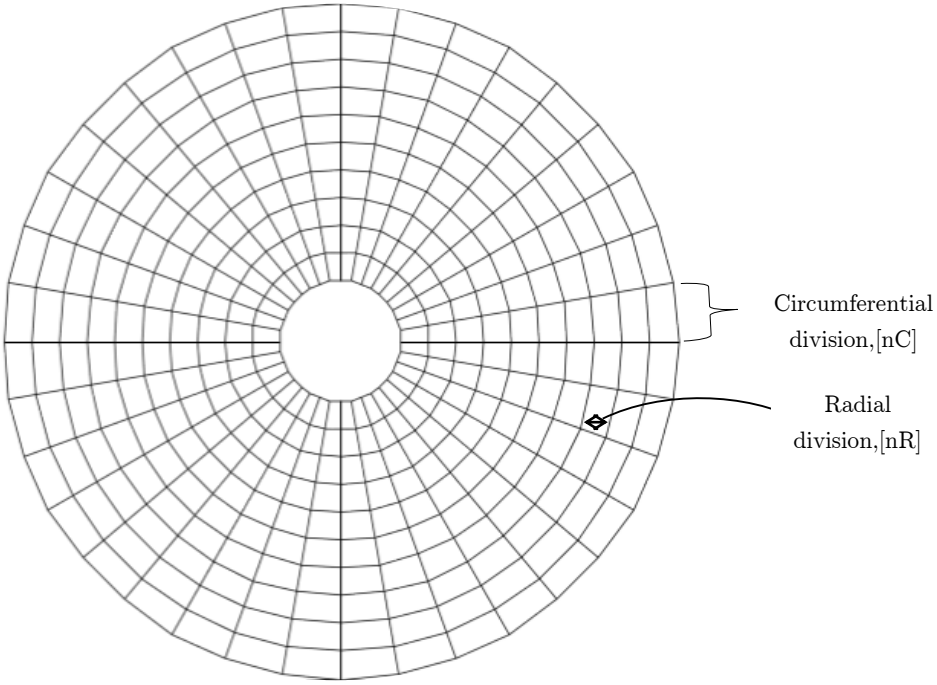

Figure 3.9: BEMt sectorial approach showing radial, nR, and circumferential, nC, subdivisions.

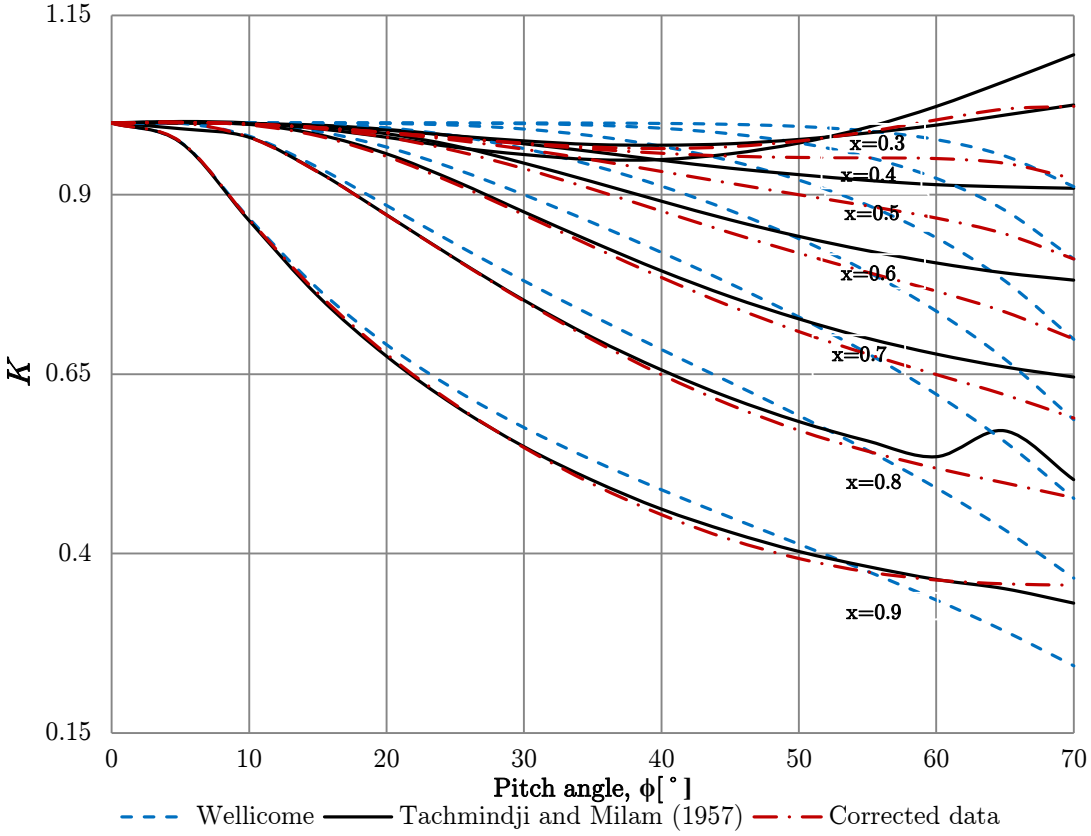

Figure 3.10: Comparison of Goldstein correction factor for a 5 bladed propeller.

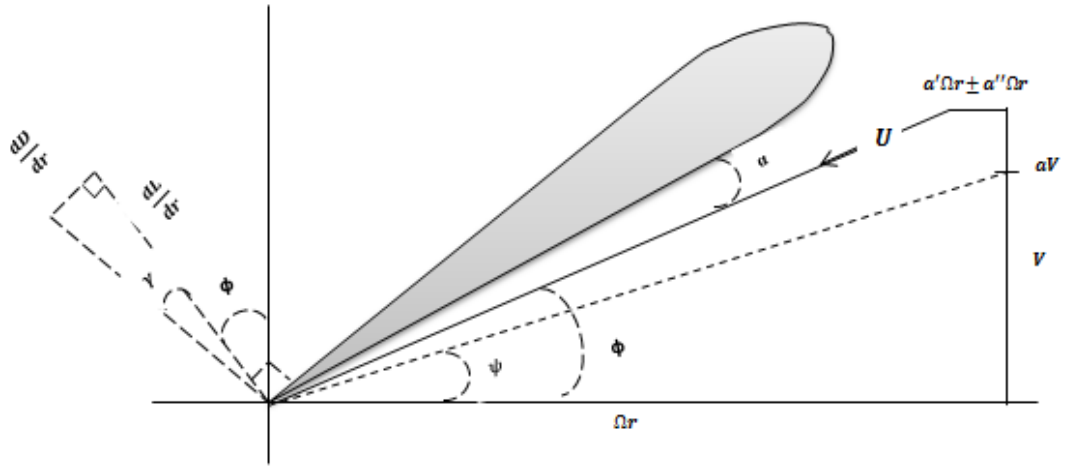

Figure 3.9: BEMt diagram including the influence of tangential wake.

3.5 Application of the numerical approach to LNG Ship Stern Design

Having established a RANS based numerical towing tank which will be used to replicate various aspect of the LNG carrier ships flow, this section discusses how best the stern arrangement may be designed and modelled. A Carlton (2007) ship design cycle is adopted here for LNG ships (see Figure 3.12). This design process will contain a preliminary estimate of the achievable target speeds and powers. Several propulsor, appendage and hull alternatives will then be reviewed. Next, the basic hull form is optimised from a resistance point-of-view for the two important draught conditions. This hull form forms the basis for the next step in the process: the study of the aft ship, the positions of the appendages, the study of the flow in the propeller field, as well as the creation and modification of possible stern skegs.

From Figure 3.12 it can be seen that the creation of a stern design for LNG carrier ship begins with an identification of the problem which in this case is a design aimed at enhancing the ship's propulsive performance. This initial block of defining the problem is important as it includes a complete definition of the inputs, outputs, limitations and constraints of the design. From the problem definition stage the next phase is to synthesize the design. This requires a formulation of the design from the inputs available. The design synthesis is usually conducted with the analysis and optimisation phase in the loop after which the evaluation of the design completes the stages of the design loop with an extra block for identification of future research needs. The following recommend the range of analyses that should be performed following the problem identification stage.

1. Stern hull design
2. Propulsor design
3. Control surface design
4. Scale effects

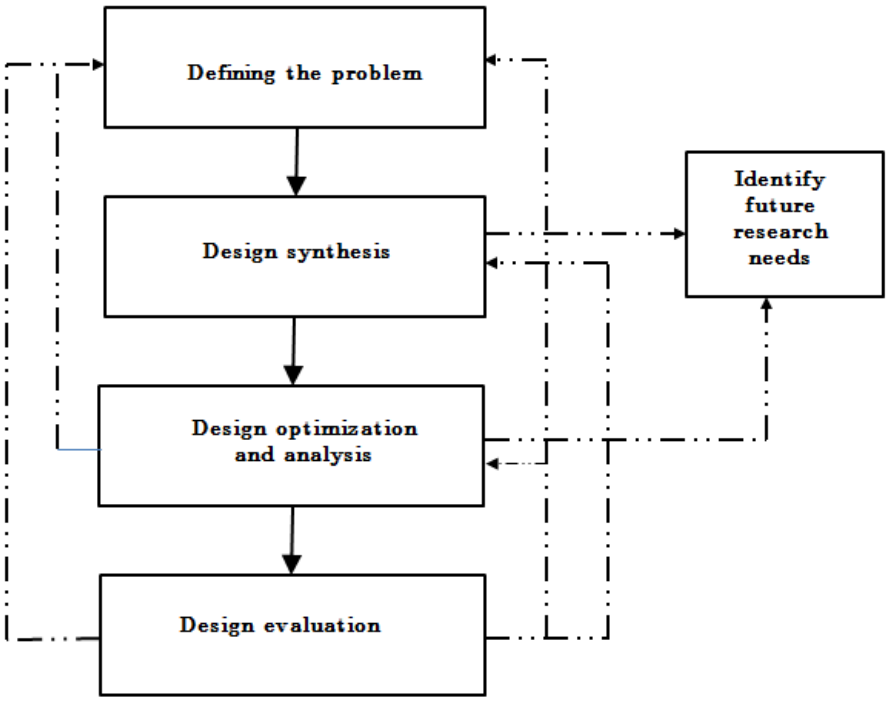

Figure 3.10: Phase of ship design (Carlton, 2007).

3.6 Stern hull design

The design of the LNG stern hull if not carefully chosen can have serious impact on the operating conditions. As a result of the operational requirements and draft restriction twin-skegs have become the choice for most LNG carrier ships. The pros and cons of employing a twin skeg stern design were outlined in chapter 2. An example from a hydrodynamic view point is to provide an improved flow to the propulsor. The skegs may however add to the total drag acting on the ship. Minimizing the additional drag may be key to successful stern design.

The skegs and hull flow may be characterised by complex vortex shedding which may require complex grid resolution in order to understand them. According to Eça et al. (2002) numerical simulation of such flows require grids with orthogonality at the ship surface where the no-slip condition is applied and high stretching of the grid towards that surface to resolve the flow in the near-wall region. It is not always easy to meet these requirements. For skeg geometries also, difficulties lie in ensuring the grids are not too skewed, whilst maintaining decent resolution in the regions of high gradients of flow variables.

3.7 Propulsor design

The propulsor design cycle for LNG ships begins with the choice of propeller. Various interesting propulsion plants are possible for LNG ships. Examples of these are

traditional twin screws, twin gondola propulsion, podded propulsors and hybrid propulsors (Quadvlieg et al., 2003). The choice of propeller for an LNG carrier ship can result from the consideration of a number of factors such as efficiency, noise reduction, cavitation and manoeuvrability. In practice it is important to aim for the highest possible level of propeller efficiency while keeping vibration and noise and hence cavitation at the lowest possible level. This places huge demand on the selection of suitable propulsor requirements. For example, if the requirement for the design is to reduce cavitation then the blade area ratio has to be increased, whilst the reverse is the case if the design is to obtain a high propeller efficiency (Van Beek, 2004). This thesis is mainly concerned with power reduction and the selection of parameters for the geometrical features of the propeller is vital if this is to be sought. This criterion is to be considered as the constraints for the LNG propeller design. Whilst there are several parameters to consider regarding the geometrical features of the propeller in terms of efficiency, this study will limit itself to key features which will have impact on the wake fraction, thrust deduction and hence delivered power. The key geometrical features are chosen such that the propeller gives the best overall performance over the LNG carrier's operational profile. Several studies need to be considered in order to establish the best combination of key features such as the pitch ratio, diameter and direction of rotation to satisfy the operational constraints of the LNG ship. In the selection of the optimum diameter, for instance for a propeller working behind the ship, Carlton (2007) suggested that the diameter be reduced than the optimum diameter found due to propeller-hull interaction effects. The pitch ratio is also vital. A high pitch usually results in increased power demand as the propeller becomes heavy whilst a low pitch means the propeller is light and would have issues absorbing power demands.

One of the most important parameters with the use of CFD for LNG propeller design is to simulate the wake field in the propeller plane, especially to give circumferential distribution of three components of the velocity. This is vital and serves as input condition for a propeller design. Section 3.2 outlined various approaches to LNG propeller modelling. Since the design must guarantee the best operational performance. It is important that the chosen design approach keep a subtle balance between several extremes, resulting in a compromise that depends on excessive computational cost and fluid dynamic fidelity and above all the experience of the propeller designer.

3.8 Control surface design

Due to the recent trend in LNG ship operation, the fore ship becomes slender whilst the aft ship full. Attention is therefore required on steering capability. This together with directional stability should therefore be judged as part of the total design process. The LNG aft ship design should therefore not only focus on the flow towards the propulsor but towards the control surface.

The role of the control surface is to provide course keeping stability for performance in straight ahead conditions. They have to be robust and reliable over the ship's lifetime. A fundamental requirement of the control surface is to produce the required lift with minimum drag. The rudder has to operate under the influence of the upstream skeg, hull and propeller. This makes the location of the rudder extremely important. According to Molland and Turnock (2007), it is advantageous to position the rudder in the slipstream of the propeller as it results in increased inflow velocities and rudder forces due to the acceleration and rotation of the flow by the propeller as described in appendix 2. The geometrical arrangement of the rudder in relation to the hull, skeg and propeller has consequences on the propulsive performance of the ship. The presence of the skeg and hull slows down the flow to the propeller. The propeller in turn accelerates and rotates the flow to a downstream rudder, affecting its performance. The location of the rudder will have influence on the upstream propeller and the overall propulsive performance effect of the rudder propeller combination (Molland and Turnock, 2007). It is therefore important that the LNG carrier stern arrangement satisfy its operational requirements and design draught conditions while it still maintains its course and manoeuvrability.

For the rudder design process, aside the geometrical parameter, attention has to be placed on its position. For twin skeg LNG ships a wide range of combinations has been outlined by Molland and Turnock (2007) for longitudinal separation, X/D, lateral separation, Y/D and vertical, Z/D position. These are summarized below.

- X/D:- values are typically in the range of 0.25-0.70. It is not known if the choice of this parameter has any influence on propulsive performance.
- Y/D:- values are typically between 0-0.25. Selection of these values usually have effect on the wake fraction (1-w_T). Another factor in the selection of a suitable value for this is to ensure removal of the propeller or tail shaft without removing the rudder.
- Z/D:- usually chosen such that the propeller tip is coincident with rudder tip.

If careful attention is given to a rudder design, then it may influence the ship's efficiency and performance. It is therefore paramount that the rudders are co designed with the propeller and the ship's hull form to enhance overall propulsive efficiency.

3.9 Scale effects

In reality LNG ship stern computations should be conducted in full scale, but it is not a straight forward task. The boundary layer in model scale is different from that of full scale (Castro et al., 2011). In full scale it is relatively thinner than in model test conditions. The wake fraction is therefore larger in model tests. Appendages which operate in the boundary layer also contribute to differences between model scale and full scale. High aspect ratio of grid cells is used to resolve the inner region of the boundary

layer model scale. This may increase when moving to full scale increasing the cost in computation. The high Reynolds number in full scale makes turbulent flow features smaller as compared to model scale, which also requires finer cells and lower time steps to resolve. It is not known how the turbulence model performs at full scale as they perform on model scale, since most parameters used in the turbulence models are tuned with or based on experimental data's at lower Reynolds number (Starke et al., 2006). According to Castro et al. (2011), it is not known if numerical computations for viscous flow around ships may be scalable.

The onset of flow separation is delayed in full scale as compared to model scale and vortices encounter higher damping (Visonneau et al., 2006). Ship's wake in the propeller plane therefore changes significantly. Vortices from bilge or struts are much weaker and vanish sometimes altogether in full-scale simulations.

Lastly, full scale wake scaling still poses a difficult task as addressed by the 26th ITTC specialist committee on scaling of wake field (ITTC, 2011). Detailed full scale wake measurements are relatively sparse. There is still ongoing research to shed more light on scale effects (Lübke and Maksoud, 2002). Understanding of the physical phenomena by comparing numerical simulations in model scale to experiments is the most practical option. In light of these model scale computations are considered for LNG carrier stern flows.

3.10 Chapter summary

This chapter has outlined a set up to a numerical approach for a stepwise study. A numerical towing tank including numerical techniques, uncertainty analysis and choice of propeller models were discussed. Conclusions drawn from the chapter are outlined below:-

- The solution of the RANS equation has been selected as a design tool to be used to conduct the stepwise study and eventually to assess the flow field around the LNG carrier hull. Capturing all aspects of turbulent flow around the stern of the ship hull form requires the use of a turbulence closure model to the RANS equation, however, to date, no unique turbulence model has successfully predicted all aspects of turbulence at the stern. The SST model has proven to be suitable in capturing some aspects of the stern flow, especially the hook shape created by the bilge contour.
- Boundary layer growth around a ship experiences cross flow due to the pressure difference around the bilge. This increases downstream, forming bilge vortices which make the stern flow very complex. To mirror this complex stern flow phenomena using RANS approach requires that the flow domain is properly discretised with appropriate grid distribution. The mesh resolution to be used around a ship hull was discussed. A procedure was adopted whereby the mesh refined around the ship hull is made denser in order to resolve the boundary layer

and in the free surface region to capture the wave elevation without affecting the mesh in the ship boundary layer.

- Prediction of the stern flow of the ship largely depends on how successful the propulsor action and unsteady hydrodynamics of the downstream rudder is replicated. Two existing methods of predicting the action of the an LNG carrier propulsor in OpenFOAM have been outlined, discretized propeller approach using AMI and Hough and Ordway model, and their implementation have been discussed.
- Another method of coupling a propeller performance code based on the blade element momentum theory (BEMt) for a ships propeller in OpenFOAM is discussed.
- Modifications were made to an existing BEMt code to include the effect of the hub when accounting for Goldstein corrections based on a finite number of blades and also the influence of tangential wake. To adopt the code to a ships wake, a sectorial approach was proposed to enable the code run at an arbitrary number of radial and circumferential locations based on the local inflow velocity. The coupling procedure of the BEMt code in an OpenFOAM environment is also discussed. This procedure includes an additional step to determine the effective velocity. The BEMt procedure assumes a curve fit for $C_l(\alpha)$ which is determined from empirical relations for foils as supposed to directly measuring them. This means that the code fails to capture viscous effects such as the stall point of the foil. This can be included as curve fit or from look up tables if this process is necessary in any investigation.
- Application of numerical method to LNG stern design has been outlined. The choice of stern hull fitting, propulsor and rudder is important to successful stern design.

The next two chapters are dedicated to reporting results of case studies using the numerical approaches presented in this chapter.

Chapter 4

4 Skeg-Rudder- Propeller Interaction

4.1 Introduction

The flow around a propeller and rudder has been discussed in detail in Appendix 2. The presence of an upstream skeg and its interaction with the propeller and rudder will alter the forces and the moments on the downstream rudder. The analysis of the flow and interaction effect between the skeg, propeller and rudder has significant importance due to the following reasons:-

i. the interaction of the skeg and propeller wake with the rudder is important for the performance of the rudder. Prior knowledge of the flow straightening, velocity and pressure fields on the downstream rudder can aid in designing a better coursekeeping ability of a ship.
ii. propulsive effects of the skeg, propeller and rudder flow could be important in the design of energy saving devices.
iii. computations of the flow around the skeg, propeller and rudder are necessary in order to understand the interaction with the hull and to determine the resistance and propulsive characteristics of a ship.
iv. data gathered from the computation of the interaction between the skeg, rudder and propeller would form a valuable set of data which can aid in the initial design of twin skeg ships or to maximize the propulsive efficiency of existing ones.

This chapter provides an understanding into the sensitivity in which the interaction between the skeg, propeller and rudder can be resolved with and without application of an angle of drift as well as the impact of varying the length of the upstream skeg on the

flow straightening, wake fraction and the thrust deduction fraction. Numerical results are compared with experiments by Molland and Turnock (1991, 1995, 2002, 2007), using the modified Wageningen B4.40 propeller and Rudder No.2.

4.2 Skeg-Rudder-Propeller Interaction Case Study

4.2.1 Details of experiment

Wind tunnel tests were performed by Molland and Turnock (1995) at the University of Southampton 3.5m x 2.5m wind tunnel. The experimental set-up comprises of a 1m span, 1.5 geometric aspect ratio rudder based on the NACA 0020 aerofoil section (Rudder No.2). A representative propeller based on the Wageningen B4.40 series was used. The propeller has a diameter of 0.8m. The rudder geometry and its arrangement with respect to the propeller are given in Figure 4.1. Dimensions of the different length of upstream skegs are also shown in Figure 4.2. Simulations were carried out for a constant wind speed of 10m/s and propeller revolutions of 2100, 1460 and 800 rpm, corresponding to propeller advance coefficients, J = 0.36, 0.51 and 0.94 respectively, which covers the operating conditions of most vessels. The propeller P/D at 0.7R is 0.95 and the rudder-propeller separation was fixed at X/D = 0.39. The rudder was mounted on the propeller centreline corresponding to Y/D = 0 with maximum height of the propeller tip coincident with the rudder tip at 1m.

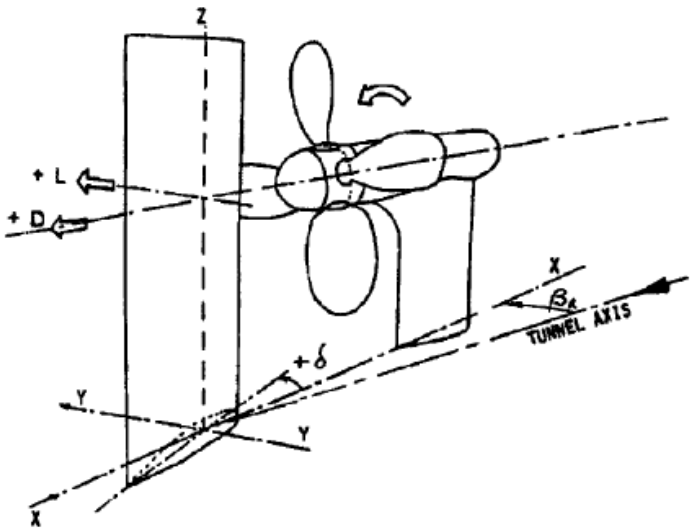

Figure 4.1: Rudder geometry and its arrangement in respect to propeller, source: Molland and Turnock (2007).

It has been argued by Molland and Turnock (1991, 2002) that for a propeller upstream of a rudder, a good approach to model the physics involved is to treat the rudder and propeller as a combined unit. The influence of drift angle can then be applied in the form

of velocity and flow straightening inputs to the basic isolated model of the rudder propeller combination. By using such approach, data for the rudder and propeller can be applied downstream of a hull, provided the hull wake fraction and hence the appropriate inflow velocity is applied to the rudder-propeller combination.

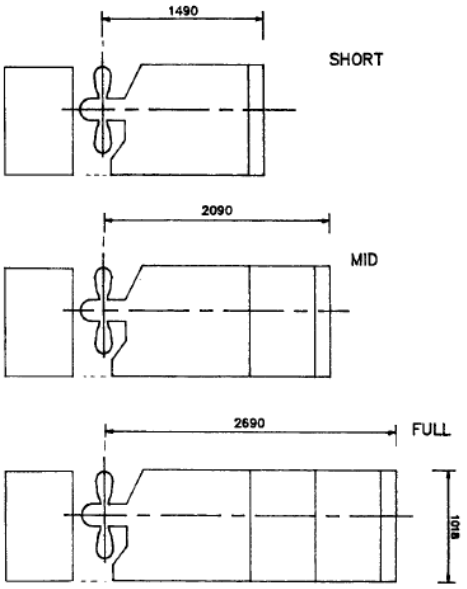

Figure 4.2: Overall dimensions of three centreboard configurations (mm), source: Molland and Turnock (2007).

The terminology applied to the flow straightening in the present study is illustrated in Figure 4.3, where δ is the rudder angle relative to ship axis, β_R is the geometric drift angle at the rudder which is larger than the ships drift angle β on a turn. For a model test in wind tunnel or towing tank β_R is the same as β.

With no flow straightening due to the propeller, the geometric rudder angle,α, is given by:

$$\alpha = \delta - \beta_R \tag{4.1}$$

With flow straightening due to the propeller, the effective rudder angle,α_E, is given by

$$\alpha_E = \delta - \alpha_0 = \delta - \gamma \beta_R \tag{4.2}$$

where γ is the flow straightening factor which depends on drift angle and propeller loading, and α_0 *is* the incidence for zero lift and can be obtained from basic lift and drag data (Molland and Turnock, 1995).

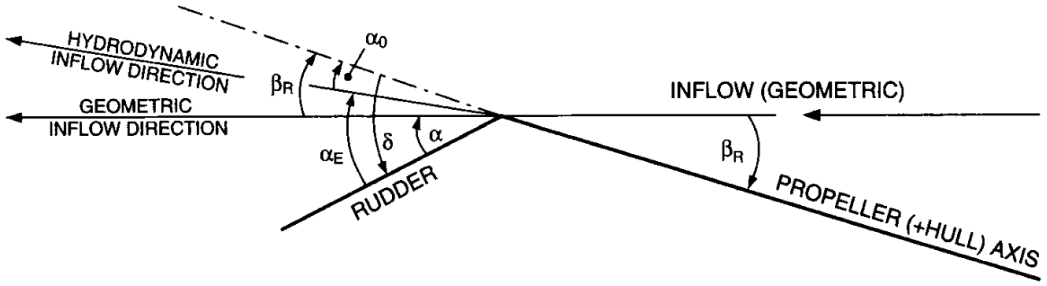

Figure 4.3: Flow straightening terminology adapted from, Molland and Turnock (1995).

4.2.2 Simulation conditions

Five sets of simulations were carried out in OpenFOAM version 2.2.0 using the pimpleDyMFoam solver:-

1. a propeller rudder combination in isolation at straight ahead conditions, that is without the application of drift angle for geometric rudder angles α = -10.4°, -0.4° and 9.6°.
2. a propeller rudder combination at drift angle of -7.5° for geometric rudder angles α =-10.4°, -5.4°, -0.4°, 4.6° and 9.6°. In relation to ship axis the geometric rudder angles will correspond to δ = -17.9°, -12.9°, -7.9°, -2.9° and 2.1°.
3. a short length skeg with propeller and rudder at drift angle of -7.5° for geometric rudder angles α = -10.4°, -0.4° and 9.6°.
4. a medium length skeg with propeller and rudder at drift angle of -7.5° for geometric rudder angles α = -10.4°, -0.4° and 9.6°.
5. a long length skeg with propeller and rudder at drift angle of -7.5° for geometric rudder angles α = -10.4°, -0.4° and 9.6°.

Full details of the geometrical parameters of the propeller, rudder and skegs and simulation flow conditions are presented in Tables 4.1 and 4.2 respectively. It should be noted that the drift angle simulations were carried out in propeller (+Hull) axis but the rudder results are presented in terms of wind tunnel axis (geometric inflow direction).

Table 4.1: Geometric parameters of propeller and rudder.

Parameter	Settings
Propeller diameter, D_p	800mm
Number of blades, N	4
Range of propeller revolutions r.p.m	0 to 3000
Blade area ratio, BAR	0.40
Boss diameter (max), D_h	200mm
P/D at 0.7R	0.95
Rake	0.0deg
Propeller blade root thickness ratio	0.050
Propeller section shape	Wageningen B series
Propeller blade outline shape	Wageningen B series with reduced skew
Rudder chord	667mm
Rudder span	1000mm
Rudder section shape	NACA 0020 aerofoil Section.
Rudder pivot point	30% of chord from leading edge
Rudder-Propeller separation, X/D	0.39 from propeller plane to rudder leading edge at 0^o
Short length skeg	1490mm
Medium length skeg	2090mm
Long length skeg	2690mm

Table 4.2: Simulation flow conditions.

Test	Free stream velocity (m/s)	Propeller advance ratio, J	Drift angles β_R (deg)	Geometric rudder angles α(deg)
Rudder&Prop alone	10	0.36, 0.51, 0.94	0	-10.4, -0.4, 9.6
Rudder&Prop alone	10	0.36, 0.51, 0.94	-7.5	-10.4, -5.4, -0.4, 4.6, 9.6
Short length skeg	10	0.36	-7.5	-10.4, -0.4, 9.6
Medium length skeg	10	0.36	-7.5	-10.4, -0.4, 9.6
Long length skeg	10	0.36	-7.5	-10.4, -0.4, 9.6

NOTE: Rudder angles selected to exactly match the wind tunnel experiments.

4.2.3 Model domain and boundary conditions

The entire flow field was considered as a result of asymmetry of the flow induced by the oblique motion and rotation induced by the propeller. A sliding grid approach which uses the arbitrary mesh interface technique (AMI) was used to account for the action of the rotating propeller (see section 3.3.1). Due to the complexity of the arbitrary mesh interface technique in handling propeller models at an angle, propeller drift angle was achieved by keeping the propeller fixed and rotating the wind tunnel and inflow as per the required drift angle as illustrated in Figure 4.4. This technique was automated by employing a script which, when called upon, allows rotation of the tunnel and inflow to the required propeller drift angle. For the straight ahead case the wind tunnel and inflow were not rotated. The inflow and outflow plane are located 8 rudder chord lengths upstream of the rudder leading edge and 12 rudder chord lengths downstream of the rudder trailing edge respectively. The domain size represents the wind tunnel dimensions. The origin of the co-ordinates is defined at 0.3 chords from the rudder leading edge at geometric angle of attack α=0°, the x-axis pointing downstream along the wind tunnel symmetry line. The nominal inflow velocity of 10m/s, turbulence intensity 0.04 and eddy length scale of 0.27m are set at the inlet. At the outlet boundary a zero gradient was applied. The skegs, propeller and rudder assumed a no slip boundary condition. Slip boundary condition was applied to the wind tunnel floor, walls and ceiling. As a result of the cost involved in computation it was not possible to mirror all geometric aspect of the experiments; as such the geometry was simplified. The gap between the rudder and wind tunnel floor was neglected, as was the support structure for the propeller. Table 4.3 summarizes the computational parameters adopted for this study. The straight ahead or no drift angle cases were started from rest and run for approximately 25 propeller revolutions whilst that of the drift angle cases were run for about 40 propeller revolutions due to the different flow patterns.

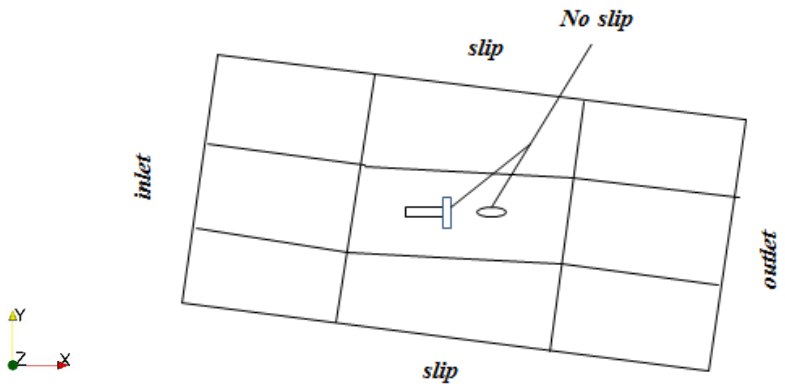

Figure 4.4: Applied boundary conditions and co-ordinate system for the drift angle computations.

Table 4.3: Computational parameters.

Parameter	Settings
Computing	Iridis 3 Linux Cluster
Mesh type	Unstructured hexahedral
Turbulence model	Shear Stress Transport, Menter, (1994)
Pressure-velocity coupling	PIMPLE
y^+ average (rudder)	30
Grad (U) Scheme	Gauss linear
Div (U)	Gauss linear upwind
Convergence criteria	RMS residual $< 10^{-8}$
Run type	Parallel (12 partitions run on 6x Dual core nodes)

4.2.4 Grid generation

All grids were created utilizing both blockMesh and snappyHexMesh in OpenFOAM version 2.1.0. Firstly, an initial structured hexahedral background mesh consisting of a multi-block topology structure was generated using blockMesh with nine blocks as shown in Figure 4.4. The centre block encompasses all the propeller, rudder and skeg geometries, with initial grid node distribution of around $n_\xi = 80$, $n_\eta = 18$ and in the wake $n_\zeta = 36$ of the rudder section making a total of about 50K cells (for the coarse grid). An unstructured, predominantly hexahedral mesh with local refinements around no slip walls was then created using snappyHexMesh utility. Specific areas within the domain were then specified for mesh refinement in progressive layers. For each layer of refinement each cell is split into eight equal parts, doubling the mesh density in all directions. Apart from the mid-block fitted around the geometries, most of the remaining cells were placed in the downstream block to capture both the propeller race and the rudder wake (Figure 4.5a). For the propeller mesh, the complexity of the propeller geometry especially around the blade tip with very small thickness and the difficulties associated with the use of snappyHexMesh in generating boundary layers on geometries with sharp corners and complex curvatures made it possible to place only two prism layer on the propeller. The surface refinement for the propeller was increased to ensure that most of the flow features were resolved. The average y^+ on the propeller was between 60-100. Ten elements were used to capture the boundary layer of the rudder with average y^+ of 30.

4.2.5 Grid sensitivity studies

A grid sensitivity study was conducted to provide insight into the impact of grid spacing on the overall performance prediction of the propeller and rudder at straight ahead conditions, that is drift angle, $\beta_R = 0^o$, propeller advance ratio, J = 0.36 and geometric rudder angle $\alpha = 10^o$. The methodology used was based on that presented by Stern et al. (2001). While this is applicable to structured mesh, it was assumed to be a suitable approach when using unstructured meshing strategy. In the present study of the grid, the contributions to the numerical uncertainty and error originating from iterations were not investigated, only the uncertainty introduced by the grids were investigated. Three grids referred to as coarse, medium and fine were generated based on the same geometry definition by a systematic $\sqrt{2}$ refinement of the background structured blockMesh. The number of points in all three directions of longitudinal, lateral and spanwise directions was varied. The grid system used for the sensitivity analysis is shown in Table 4.4. The total number of cells in the coarse, medium and fine grids was 1.4×10^6, 3.3×10^6 and 8.8×10^6 respectively.

Illustrations of the grids generated on the propeller are shown in Figure 4.5 for (b) coarse, (c) medium and (d) fine grid. Detailed grid parameters are also summarized in Tables 4.5 and 4.6, along with the comparison of predicted thrust coefficient and torque coefficient computed on each grid as well as viscous and pressure contributions to the total drag. The thrust and torque coefficient can be defined as:

$$K_T = \frac{T}{\rho n^2 D^4} \tag{4.3}$$

$$K_Q = \frac{Q}{\rho n^2 D^5} \tag{4.4}$$

where T and Q are the calculated thrust (force imparted by the fluid on the propeller blades in propellers axial direction) and torque (moment about the centerline of propeller) respectively, ρ is the density of air.

Rudder lift and drag values are also presented for Simonsen (2000) and Philips et al. (2010) who both performed similar investigations for straight ahead conditions (no applied angle of drift) using the CFDSHIP-IOWA and ANSYS CFX code respectively and using a body force propeller model with load distribution based on the Hough and Ordway (1965) thrust and torque distribution. From Table 4.5, by considering the R_G values, it can be observed that the rudder drag exhibited the diverging condition, hence uncertainty analysis was not estimated. The grid could have been improved especially around the tip region, hub, the leading edge of the rudder and root. According to Simonsen (2000) since the x-component of the normal to the rudder surface is large at the leading edge, the pressure contribution is dominant for the local drag coefficient in

this region, therefore if the leading edge pressure and suction peaks are not adequately resolved it could lead to discrepancies in drag coefficient. The grid quality was not improved further due to expense involved in computation (see Table 4.4). Although the detail local flow features such as the tip and hub vortices (which are useful for cavitation analysis) described above will not be captured by the level of grid used, for manoeuvring performance of the rudder exact "mirroring" of the flow field is not essential as long as the required condition of flow (head) are adequately captured. Another problem regarding the drag coefficient values might be attributed to insufficient turbulence model which may have influenced the frictional drag values. The numerical simulation assumed a fully turbulent boundary layer, while the flow over the experimental rudder was tripped from laminar to turbulent flow at a distance of 5.7% from the leading edge of the chord on both sides of the rudder using turbulence strips. This problem has been addressed by Wang and Walters (2012) who carried out studies to demonstrate the capability of transition sensitive turbulence models for three dimension turbulent flows around complex geometries to determine the relative importance of resolving the boundary layer transitional effect. According to Wang and Walters (2012) the SST is poorer at resolving the tip vortices and showed large discrepancies in propeller forces with increased propeller loads compared to transition sensitive models and this will have a significant effect on the forces of a rudder placed downstream of the propeller.

The R_G values for the other entire parameters aside the rudder drag exhibited the converging condition. This means that all parameters except rudder drag were converging as the grids were refined. Uncertainty estimates were then made based on the correction factor (C_G) of the propeller thrust coefficient, torque coefficient and rudder lift force (see Table 4.6). The uncertainty U_G introduced by using the fine grid was 7% , 21% and 29% of the numerical benchmark, S_C for the propeller thrust coefficient, torque coefficient and rudder lift force respectively. Investigations by Simons and Stern (2005) and Phillips et al. (2009) highlight the difficulties in the prediction of propeller torque and rudder forces with large uncertainties and comparison errors between calculated and experimental result unless significantly larger meshes are used. Wang and Walters (2012) indicated values in excess of 22M to resolve propeller forces, whilst Date and Turnock (2002) indicates values of 5-20M cells to fully resolve the ruder forces. However, a good level of understanding of the global forces required for rudder and propeller forces during manoeuvring may be obtained with this level of mesh resolution.

The time history for rudder and propeller forces for the medium grid presented in Figure 4.6 shows that the all the forces have converged at about 0.2secs, this correspond to approximately 8 propeller revolutions. However as stated earlier the simulation was run a little longer for about 25 propeller revolutions to obtain a fully converged solution.

Aside from the overall thrust and torque, the rudder lift and drag coefficient for geometric rudder angles α = -10.4°, -0.4°, and 9.6° are shown in Figures 4.7&4.8. Comparison is also made with Simonsen (2000) and Phillips (2010). Results show

improvement in the fine grid especially for drag coefficient. The calculated drag however is still greater than the experiment. This is due to the difficulties associated with replicating the influence of swirl on the local incidence angle. At high thrust loadings, swirl components increases, leading to a reduction in the drag experienced by the rudder, the mechanism is illustrated in Figure 4.9. Other reasons for the drag over prediction have been discussed such as grid resolution and turbulence model. Wall effects also plays a defining role in rudder drag prediction as has been addressed by Höerner (1965) who showed that due to root vortex the drag of wall mounted experimental rudder differs from that of numerical rudder. Because the propeller was working close to the wind tunnel floor, it could have influence the root flow, hence the root vortex and rudder drag prediction.

The medium grid was used for most aspect of this work unless otherwise stated. This is because of the high computational cost associated with using the fine grid (see Table 4.4). The medium grid results also compares well with the fine grid in terms of the rudder lift and propeller forces.

Table 4.4: Grid system used for sensitivity analysis.

Parameter	Coarse grid	Medium grid	Fine grid
BlockMesh refinement	80×18×36	113×24×51	160×36×72
Cells in rotating region	150K	300K	770K
Cells in stationary region	1.2M	2.9M	8.0M
Total no of cells (approx.)	1.4M	3.3M	8.8M
Computational expense	20-22hrs	60-65hrs	170-180hrs

NB: Computational expenses are based on parallel run of 12 partitions run on 6 core nodes for approximately 20 propeller revolutions. All times are in wall clock hours

Table 4.5: Grid sensitivity study for propeller and rudder forces, α= 10°, β_R= 0°, J = 0.36.

Grid	Coarse grid	Medium grid	Fine grid	Simonsen (2000)	Phillips (2010)	Data
K_T	0.305	0.294	0.286			0.283
ε	+7.77%	+3.89%	+1.06%			
K_Q	0.051	0.047	0.044			0.043
ε	+18.60%	+9.30%	+2.32%			
C_L	1.35	1.28	1.22	1.27	1.36	1.2505
ε	+7.96%	+2.36%	-2.44%	+1.56	+8.76	
C_D total	0.19	0.17	0.148	0.07	0.187	0.109
ε	+74.3%	+55.96%	+35.78%	-93.58	+71.56	
C_D viscous	0.075	0.072	0.069			
C_D pressure	0.115	0.098	0.079			

E = %Data (D)

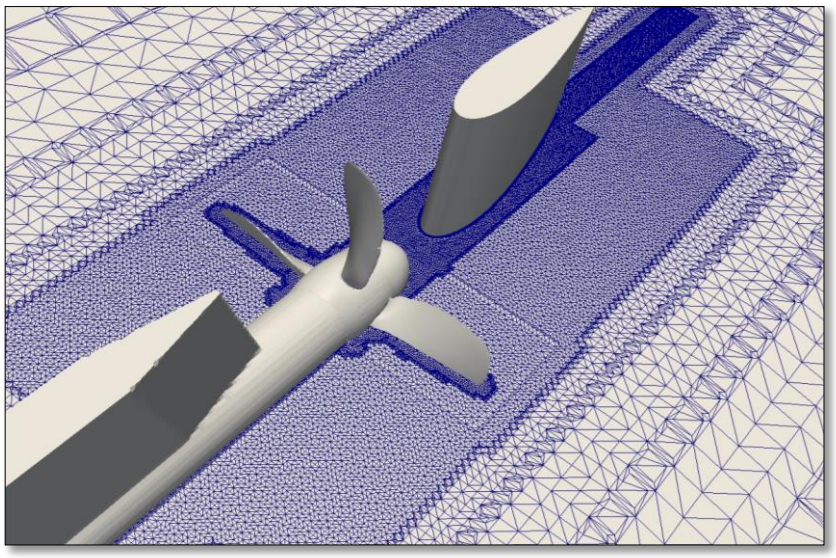

[a]

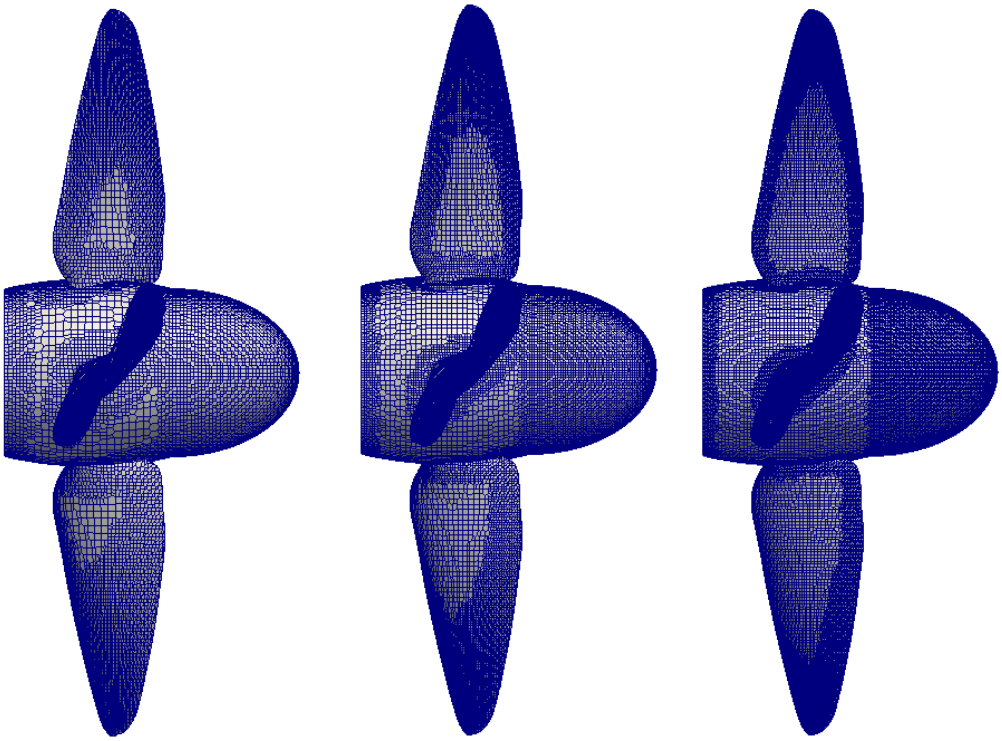

[b] [c] [d]

Figure 4.5: Mesh cut showing [a] horizontal plane through hub centerline (medium grid) [b] propeller coarse grid 1.4M, cells [c] medium grid 3.3M, cells and [d] fine grid 8.8M cells.

Table 4.6: Uncertainty analysis-propeller and rudder forces at α =10°, β_R = 0°, J = 0.36.

Study	R_G	P_G	C_G	U_G	δ^*_G	U_{G_C}	S_C
K_T	0.72	0.92	0.38	7.1%	2.8%	4.3%	0.283
K_Q	0.75	0.83	0.33	20.9%	6.9%	14.0%	0.043
C_L	0.86	0.44	0.16	29.0%	4.8%	24.0%	1.251

$\%S_C$

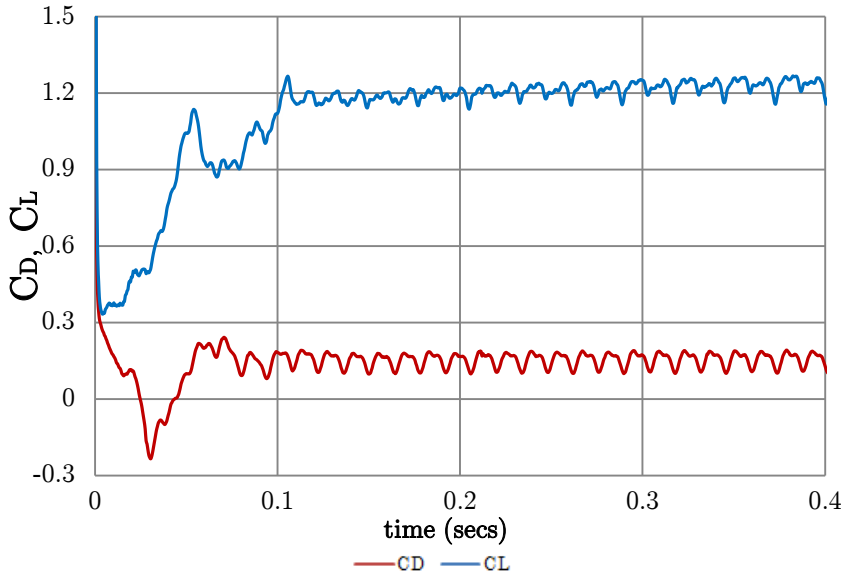

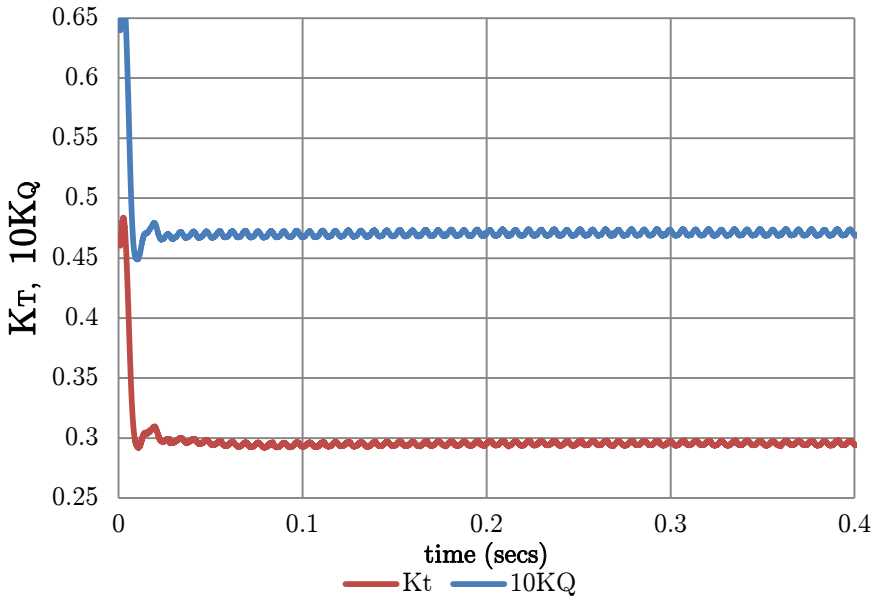

Figure 4.6: Time history of propeller and rudder forces with medium grid, α= 10°, β_R = 0°, J = 0.36.

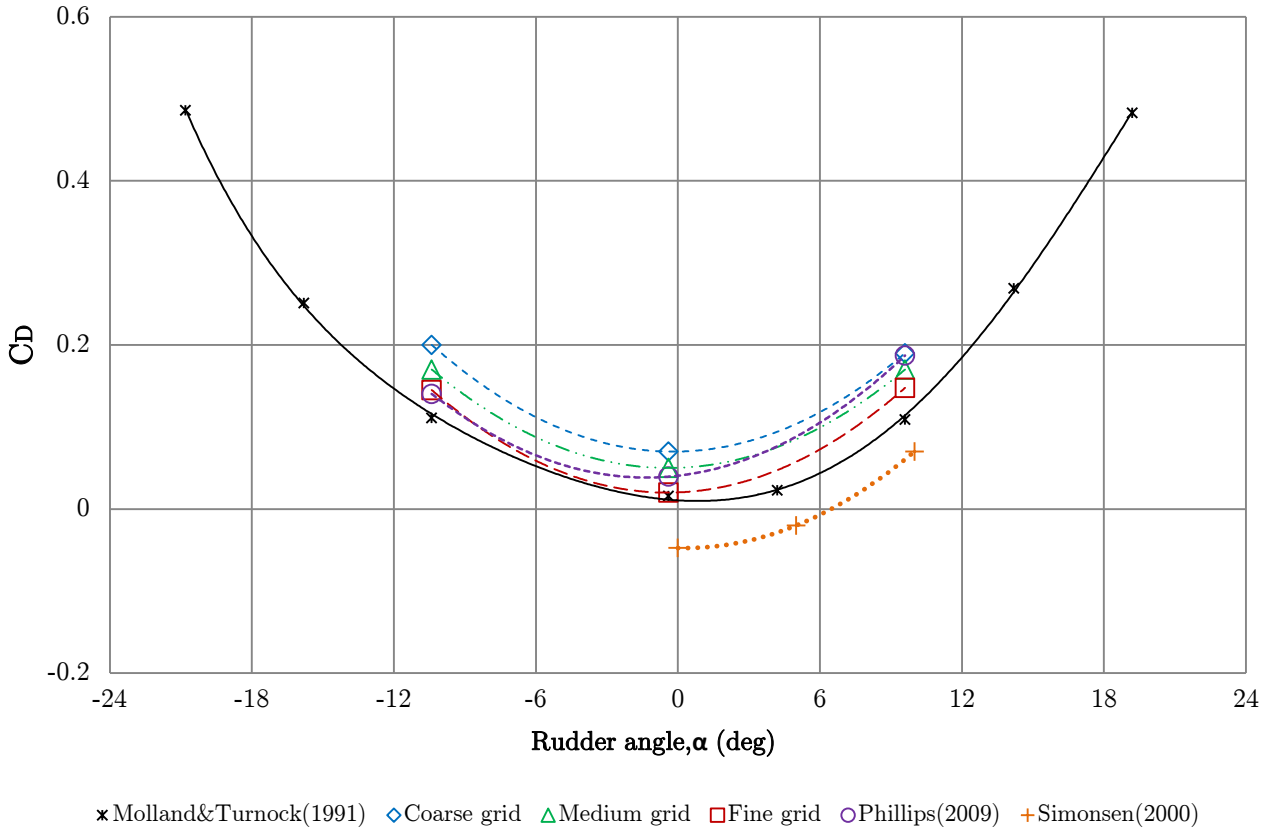

Figure 4.7: Rudder drag coefficient for grid resolution study, $\beta_R = 0^O$, J = 0.36.

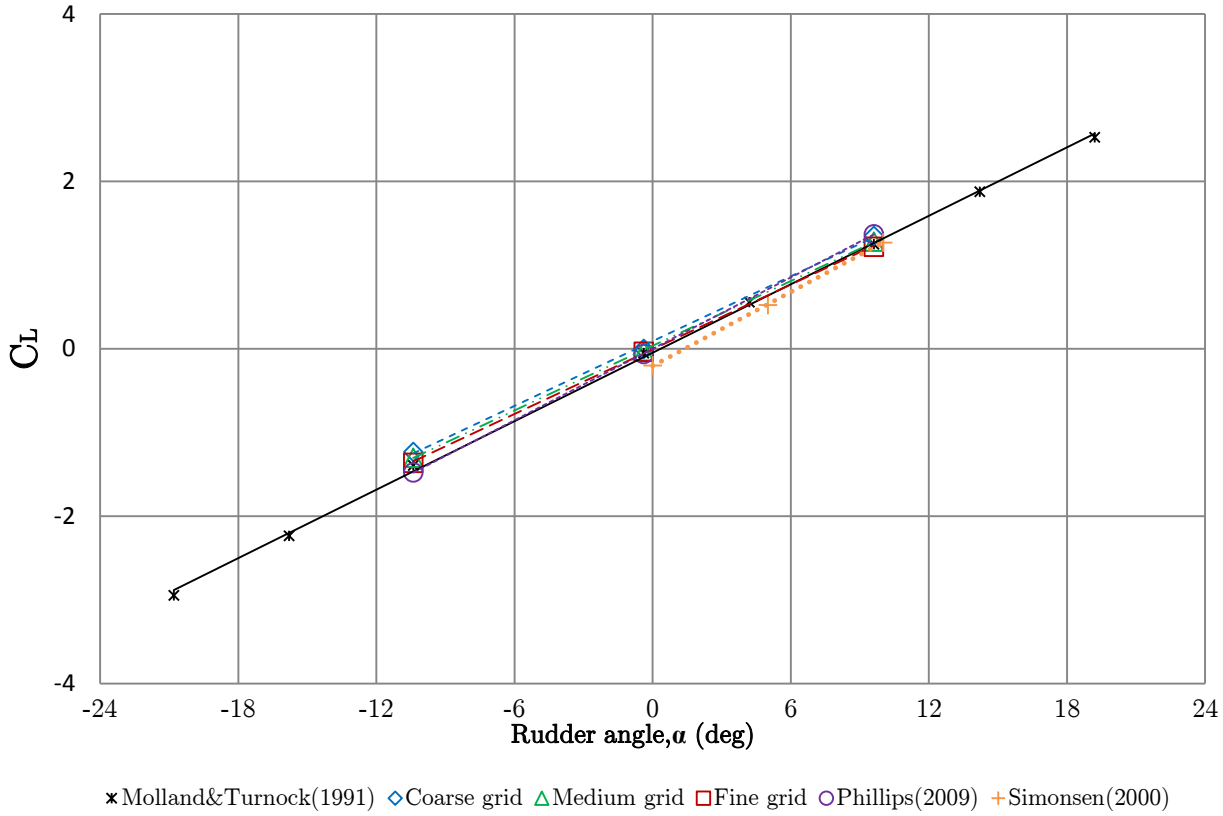

Figure 4.8: Rudder lift coefficient for grid resolution study, $\beta_R = 0^{\circ}$, J = 0.36.

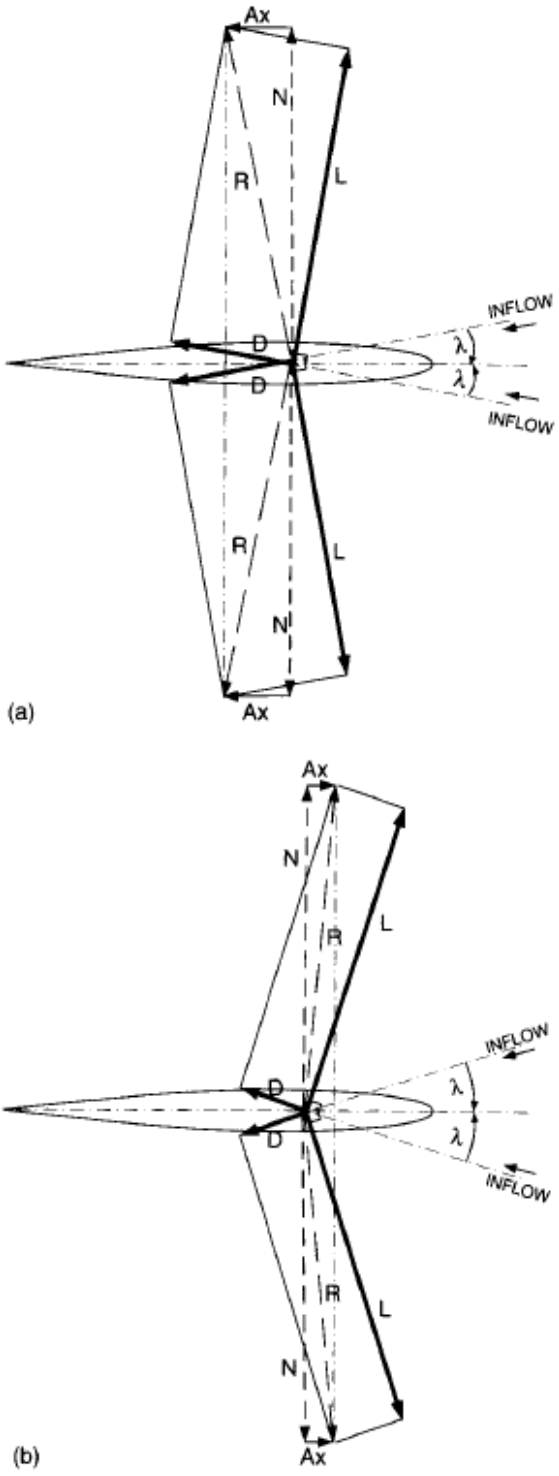

Figure 4.9: [a] Rudder angle zero degrees: forces due to propeller-induced incidence [b] Rudder angle zero: forces due to propeller-induced incidence - high thrust loading, source: Molland and Turnock (2007).

4.3 Results

4.3.1 Propeller open-water prediction

Figure 4.10 presents the computed open water performance of the model propeller at drift angles of 0° and -7.5° with corresponding experimental data (for β_R=0°) provided by Molland and Turnock (1990). The definition of the thrust and torque coefficient is given in equation 4.3 and 4.4. The propeller open water efficiency is defined as:

$$\eta_o = \frac{J}{2\pi}\frac{K_T}{K_Q} \tag{4.5}$$

where J is the propeller advance coefficient.

For most of the propeller advance coefficients, the agreement for the propeller forces and efficiencies with experiment was good. For example at J of 0.36 and 0.51 at β_R=0°, the agreement for K_T, $10K_Q$, and η was less than 5%. The trends with varying advance coefficients were also well predicted. The data for applied angle of drift (β_R= -7.5°) also follows the same trend as that of the zero angle of drift but with an upwards shift in propeller thrust and torque coefficient curves.

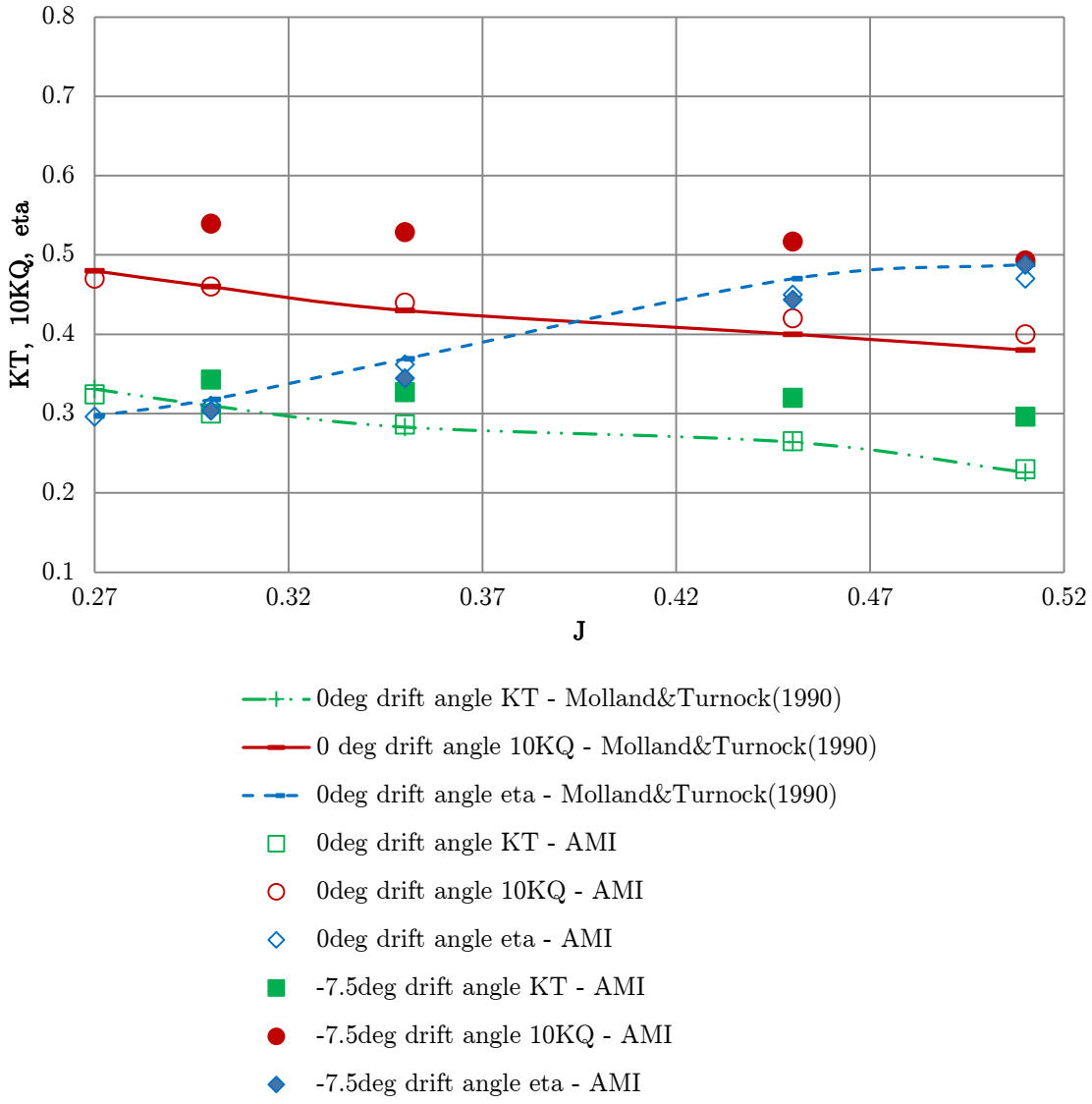

Figure 4.10: Comparison of measured and computed propeller open-water characteristics; β_R = -7.5^{O}& 0^{O}.

4.3.2 Rudder–propeller combination in isolation

The global forces for rudder and propeller in isolation, with and without applied drift angle are illustrated in Figure 4.11. For non–zero angles of drift, the rudder forces are calculated relative to ship body axis, not the wind tunnel centerline. The lift and drag coefficients are defined normal and parallel to the ship body axis respectively. Results for zero drift angle condition demonstrates that the wake field generated by the propeller compares well with experimental values of lift and drag on a rudder placed aft of the propeller at different angles of incidence. The influence of drift angle is well captured in terms of rudder lift and drag characteristics. The effect of the applied drift angle on the

rudder results in a downward shift of the lift curve and does not significantly change the lift curve slope as seen in Figure 4.11.

The applied drift angle also resulted in an over prediction of propeller torque (see Table 4.7), since rudder forces are dependent on the inflow conditions (propeller race) which in turn are dominated by the action of the propeller, slight over-prediction in propeller force will result in an increased inflow velocity to the rudder, causing an increase in rudder force, hence the upward shift in rudder lift curve observed for the -7.5deg drift angle as compared with experiment. At $\alpha =$ -10° (α_E of -23°), the predicted accuracy for rudder drag deteriorates. The reason is most likely that the rudder has stalled and the mesh count (of 3.3M) used to mirror entire flow field makes it difficult to capture the stall effect. The grid used, however is able to predict accurately the effective angle of attack (α_E) up to 18° ($\alpha =$ -5°). Also loss of lift can be observed at rudder angles >10°. The influence of advance ratio on the performance of the rudder and propeller at drift is also well captured (Figure 4.12). As propeller thrust loading increases the drag experienced by the rudder increases. From the lift curve plots it can be observed that a particular geometric rudder angle exist (4°< α <5°) where changes in propeller advance ratio does not have effect on the lift experienced by the rudder.

The overall results however provide reasonable initial estimates for rudder forces at drift angle $\beta_R = -7.5^0$ and 0°. Overall improvements in mesh resolution around the propeller, rudder and rudder tip vortices would improve the quality of the results.

4.3.3 Rudder–propeller with different length of upstream skegs

An upstream skeg at angle of drift slows down the inflow to the propeller. For a rudder downstream of the propeller at drift, accurate determination of the rudder forces is influenced by the axial and tangential wake flow (Figure 4.13). The investigated flow straightening effect in the presence of three upstream skegs as shown in Figure 4.14 follows the same trend as that of the rudder–propeller in isolation discussed earlier. In all quantities, i.e. lift and drag characteristics, the calculations compared well with the measured values. The lift curve slope, $\partial C_L/\partial\alpha$ (see Table 4.8) are also well predicted. It can be seen that the presence of the skegs tends to reduce the lift curve slope as a result of flow straightening and there is a downward shift in the lift curve compared to the rudder and propeller alone at drift. The calculated drag when approaching stall was not accurately predicted due to similar reasons outlined earlier.

The rudder drag at zero incidence C_{D_0} is highest for the rudder-propeller in isolation. Comparison of the plots to that of the non-zero drift angle case in Figure 4.11 shows that the asymmetry in the flow results in a shift in the performance of the rudder which increases with increasing upstream skeg length. This shift may depend on the angle of drift. The lift curves in Figure 4.14 also show that, most of the flow straightening was

achieved by the short length skeg. Further lengthening of the skeg resulted in little flow straightening. This is also shown in a combined plot which clearly illustrates flow straightening effects for all cases considered, Figure 4.15. From the plots, the propeller straightened the flow (i.e $\beta_R - \alpha_O$) by almost 13^O for the short skeg compared to experimental value of 12^O, leading to a significant increase in side force. The trend in flow straightening however was not accurately predicted from no-skeg to the short length skeg. This was expected due to the over-prediction in propeller forces explained earlier (in section 4.2.4) resulting in an upward shift in rudder lift curve for the rudder and propeller alone at drift. Differences in flow straightening (decrease in αo) predicted from the short-medium length skeg and medium-long length skeg was both 0.8 for the experiment compared to 0.9 for the calculations.

Table 4.7: Comparison of average propeller thrust and torque coefficients at drift, $\beta_R = -7.5^o$.

	K_T (average)		K_Q (average)	
	Molland&Turnock	AMI	Molland&Turnock	AMI
Rudder&Propeller alone	0.336	0.333	0.046	0.054
Short length skeg	0.306	0.314	0.051	0.051
Medium length skeg	0.325	0.322	0.051	0.051
Long length skeg	0.315	0.317	0.051	0.051

Table 4.8: Rudder lift curve slope, $\partial C_L/\partial\alpha$, and corresponding drag at zero incidence,C_{DO}.

	C_{DO}		$\partial C_L/\partial\alpha$	
	Molland&Turnock	Calculations	Molland&Turnock	Calculations
Zero drift angle	0.016	0.02	0.132	0.129
Rudder&propeller alone	0.083	0.06	0.146	0.144
Short length skeg	0.029	0.01	0.121	0.119
Medium length skeg	0.025	0.012	0.119	0.115
Long length skeg	0.0169	0.019	0.125	0.126

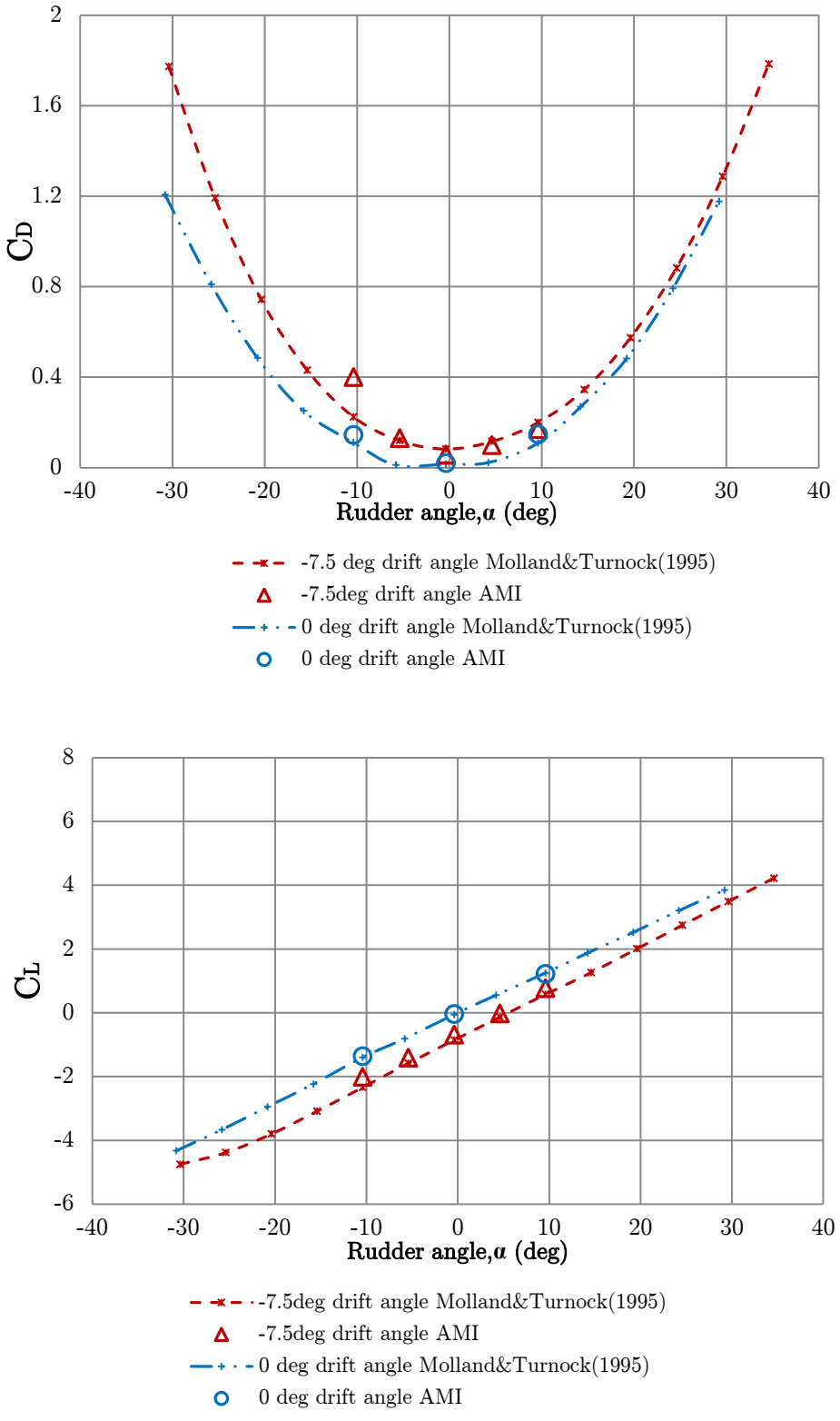

Figure 4.11: Effect of drift angle on the performance of a rudder and propeller combination in isolation at J = 0.36, β_R = -7.5^{O} (medium grid results) and $\beta_R = 0^{O}$ (fine grid results).

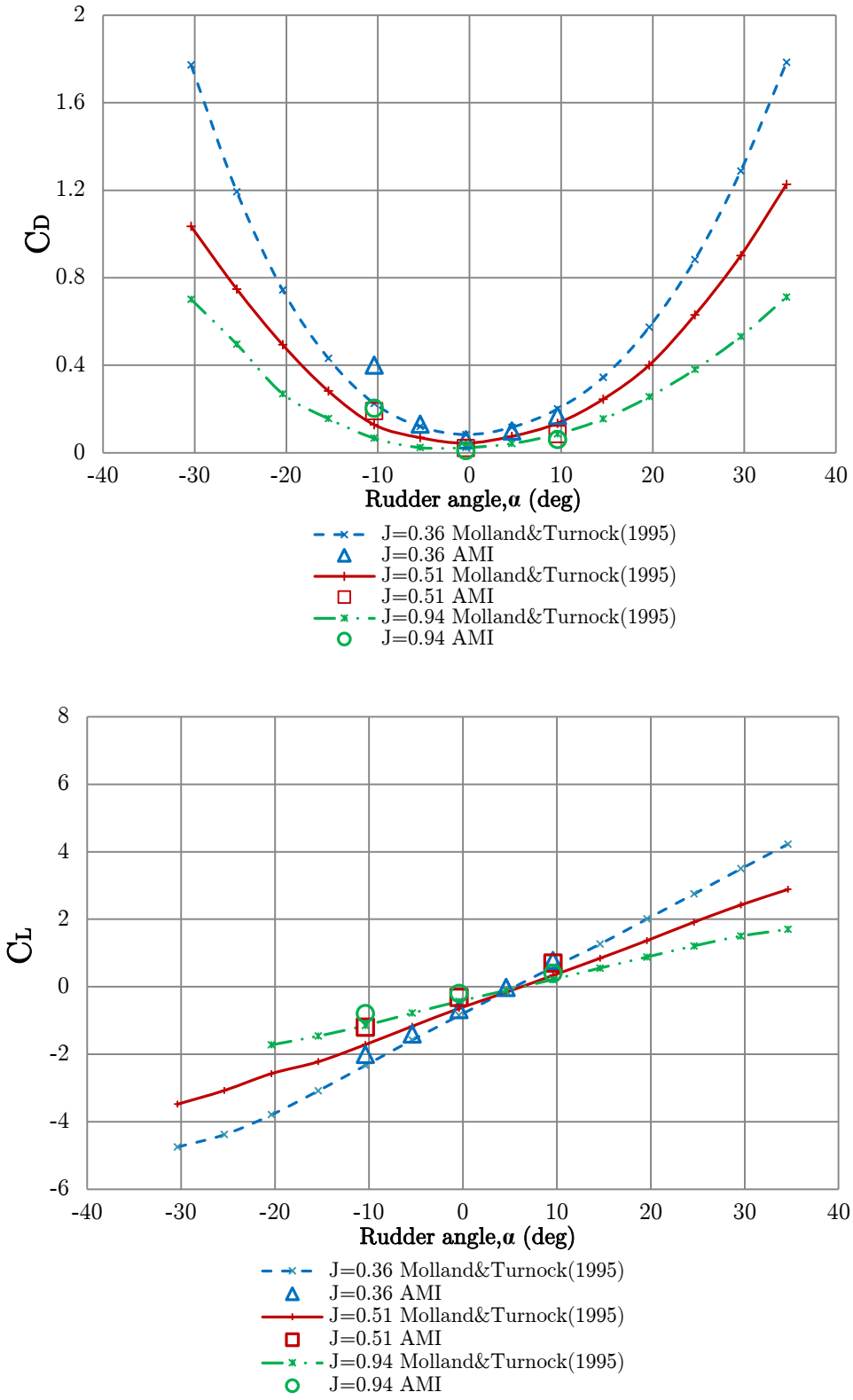

Figure 4.12: Effect of advance ratio on the performance of a rudder and propeller combination in isolation at drift angle, β_R = -7.5^{O}.

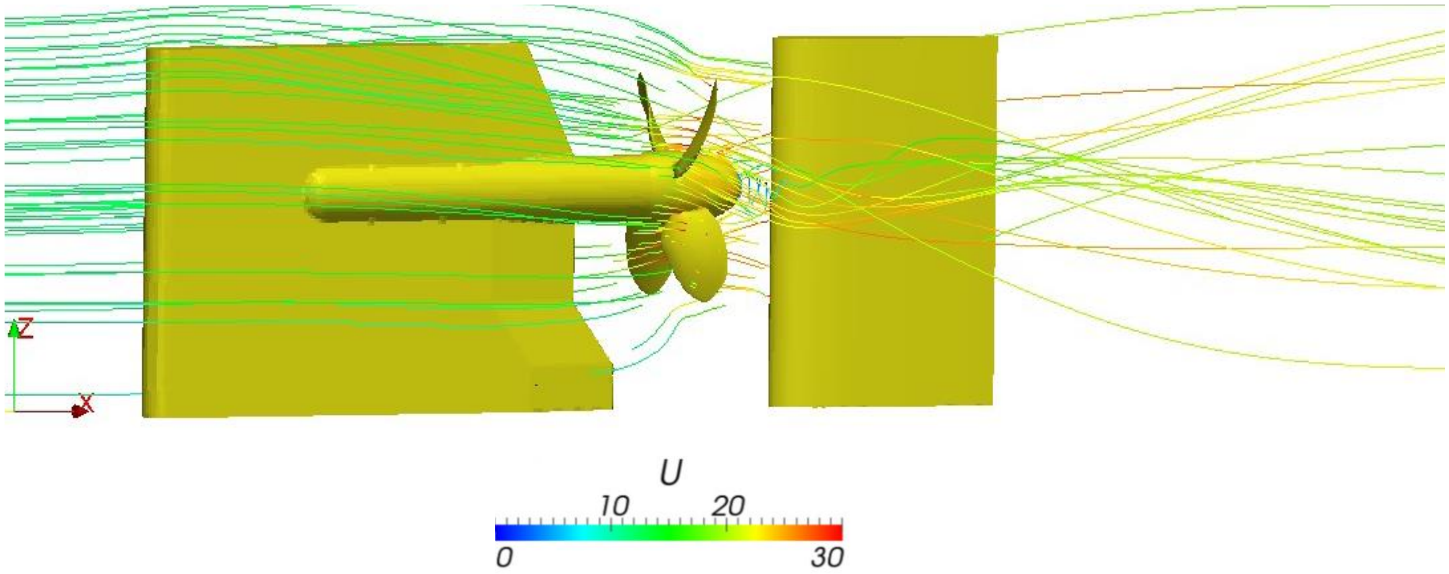

Figure 4.13: Streamlines passing through the shortboard, J = 0.36, β_R = -7.5^{O} at α = 10^{o}.

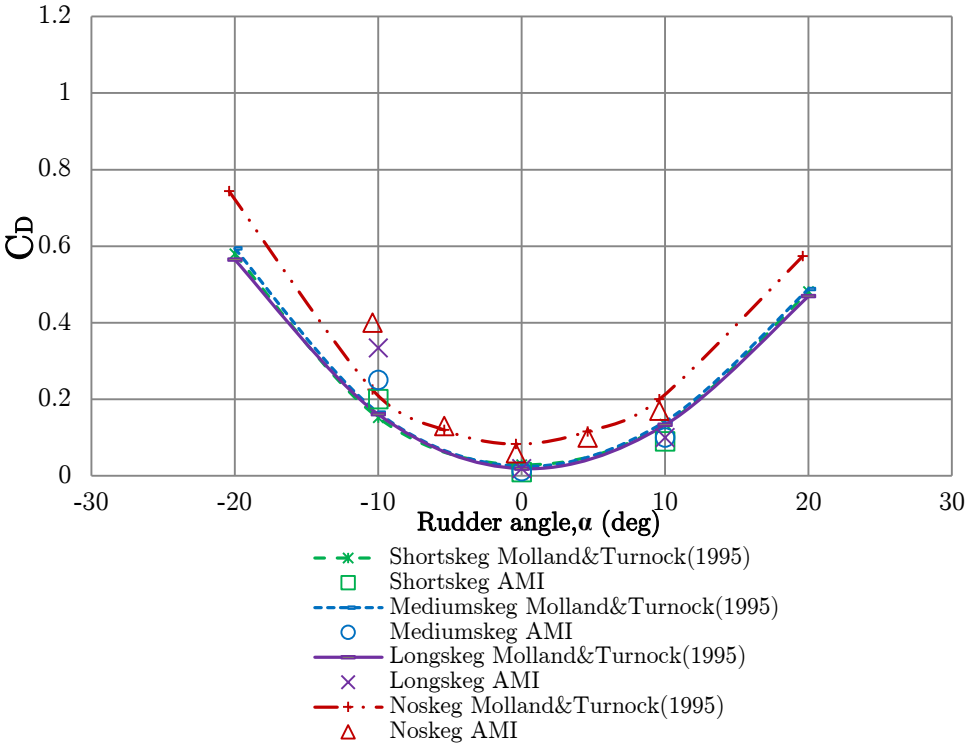

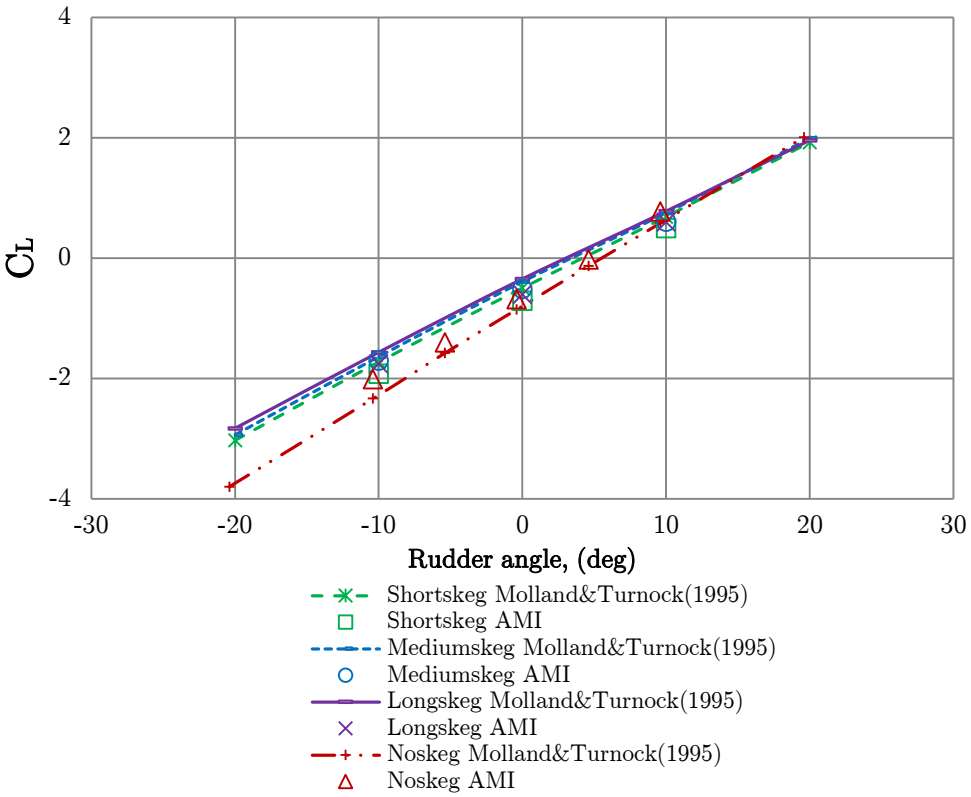

Figure 4.14: Effect of drift angle on the performance of a rudder downstream of three centreboard configurations at J = 0.36, β_R = -7.5^{O}.

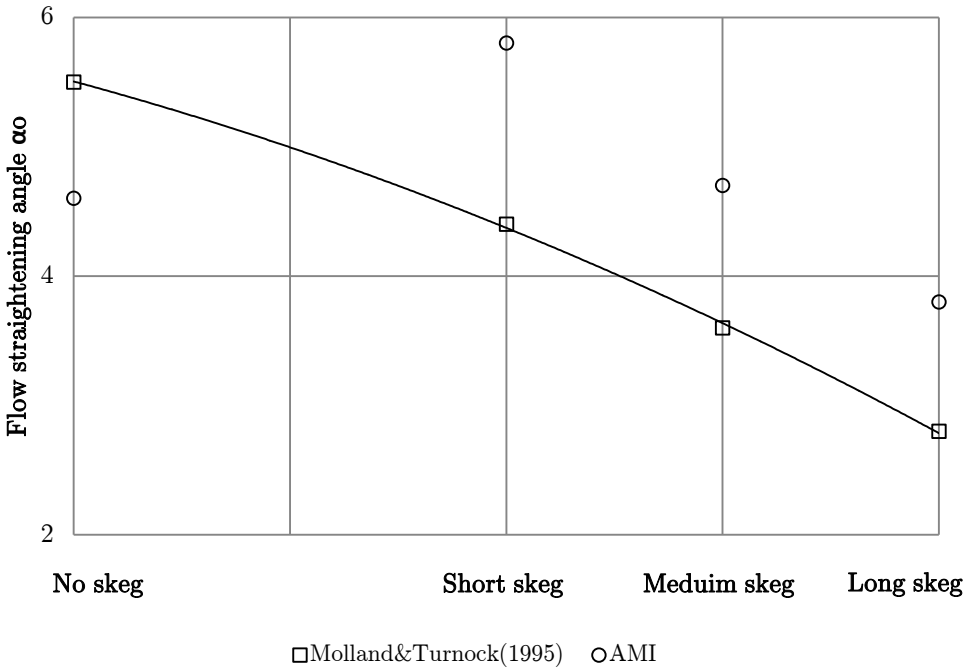

Figure 4.15: Effect of propeller and skeg length on flow straightening angle, α_0.

4.3.4 Drift angle influence on propeller performance

The action of a propeller accelerates the incoming flow onto a downstream rudder thus modifying the flow around the rudder. The rudder itself blocks and diverts the upstream flow onto and through the propeller, affecting the thrust produced and torque developed on the propeller. The influence of the rudder on the propeller thrust performance at drift and with different skeg lengths (Figure 4.16) was investigated by comparing the differences in the net thrust of the propeller and rudder combination and with different skeg lengths with the open water data for the propeller at J = 0.36, $\beta_R = 0^o$ (Figure 4.10). The presence of the skegs clearly has a marked change on the propeller thrust with the "*dkt*" curve highest for the medium skeg. The results show a good *dkt* prediction for the short and long length skegs compared with the experiment. At positive geometric rudder angle, the propeller thrust of the medium skeg was predicted to be the same as the longskeg. Figure 4.17 presents the instantaneous boundary layer profile for the short length skeg at drift. One may clearly see the velocity deficit at the propeller inflow caused by the skeg boundary layer. It is also interesting to note how the accelerated flow impinges on the rudder and the development of the rudder tip vortices.

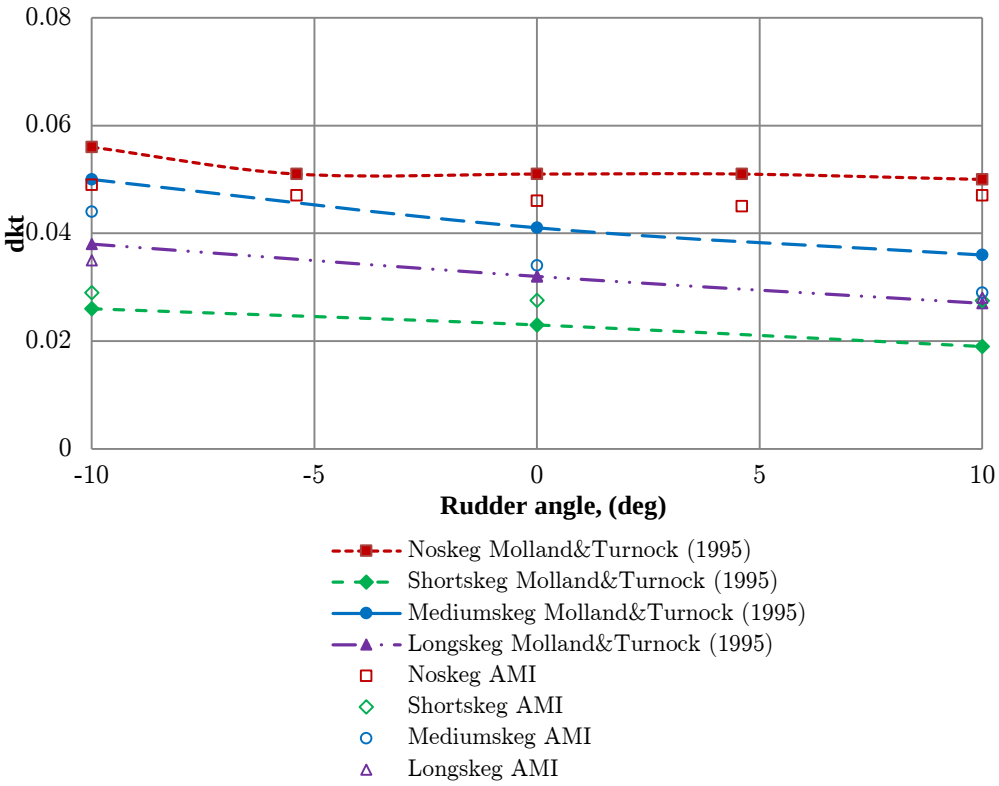

Figure 4.16: Effect of drift angle on propeller thrust augments for rudder and propeller alone and different board lengths, J = 0.36, β_R = -7.5°.

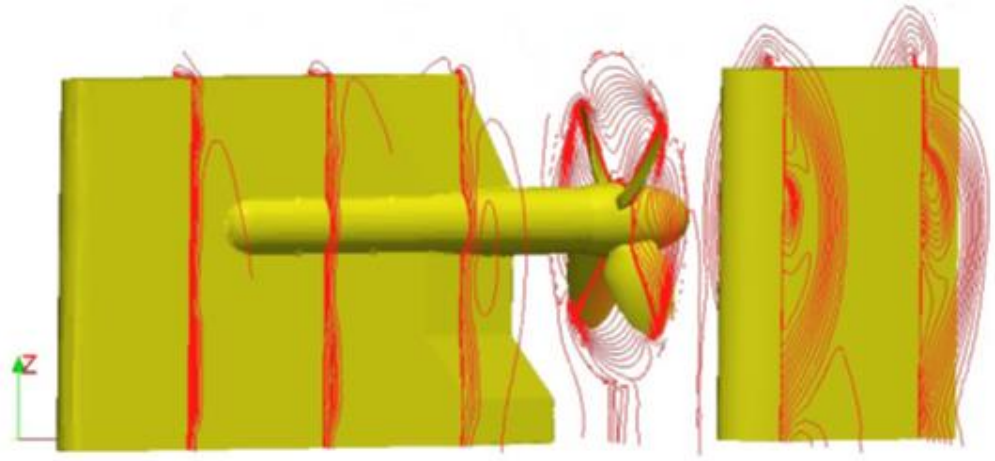

Figure 4.17: Instantaneous velocity profile for short length skeg at drift J = 0.36, β_R = -7.5°.

4.3.5 Comparison of propeller side forces with and without applied angle of drift

The net sideforce due to the propeller at drift is important in the prediction of ship manoeuvres. The propeller sideforce results from the rotational motion of the ship and is dependent on the inflow and angle of drift. Figure 4.18 presents the sideforce due to the propeller normalized with rudder lift force at an angle of drift of -7.5°. The sideforce (magnitude in this case) is the resultant of the fluid force component in the propeller plane and is defined as:

$$K_s = \frac{\sqrt{{F_y}^2+{F_z}^2}}{\rho n^2 D^4} \tag{4.6}$$

The results show that the sideforce increases with increasing rudder angle. At 10° rudder angle the presence of the shortskeg increased the propeller sideforce compared to the medium and longskeg. This is confirmed in the flow straightening plots in Figure 4.15 where the maximum flow straightening was achieved by the shortskeg. Comparison of the propeller advance ratios at 10° rudder angle (Figure 4.19) shows that as propeller thrust load increases the sideforce due to the propeller reduces. Values in Figure 4.20 of the propeller sideforces without application of drift compared to that at drift (Figure 4.19) shows the importance of the propeller sideforce especially in areas of ship manoeuvring.

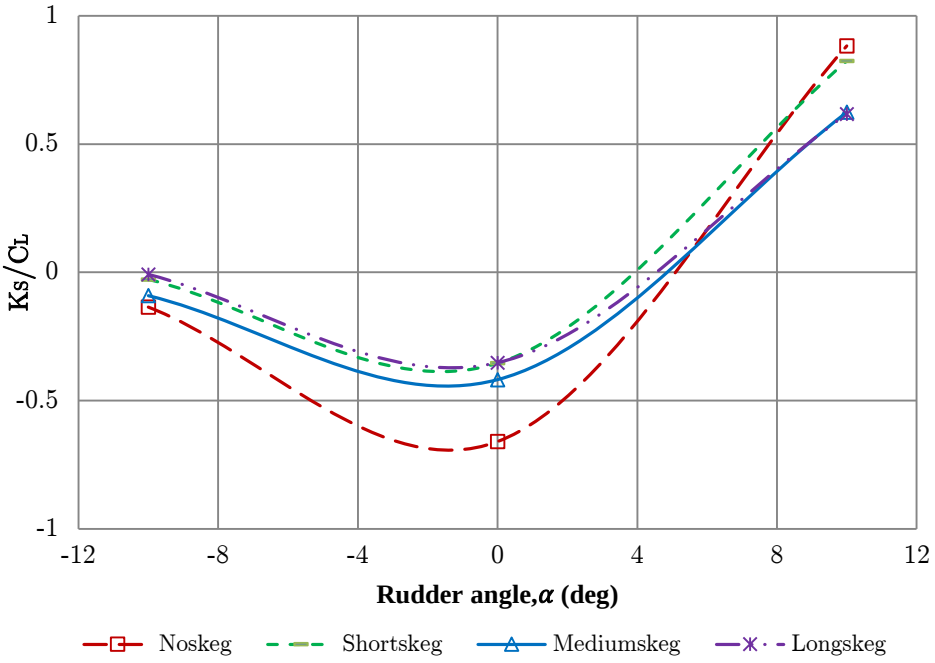

Figure 4.18: Effect of skeg length on propeller side force, at J = 0.36, β_R = -7.5°.

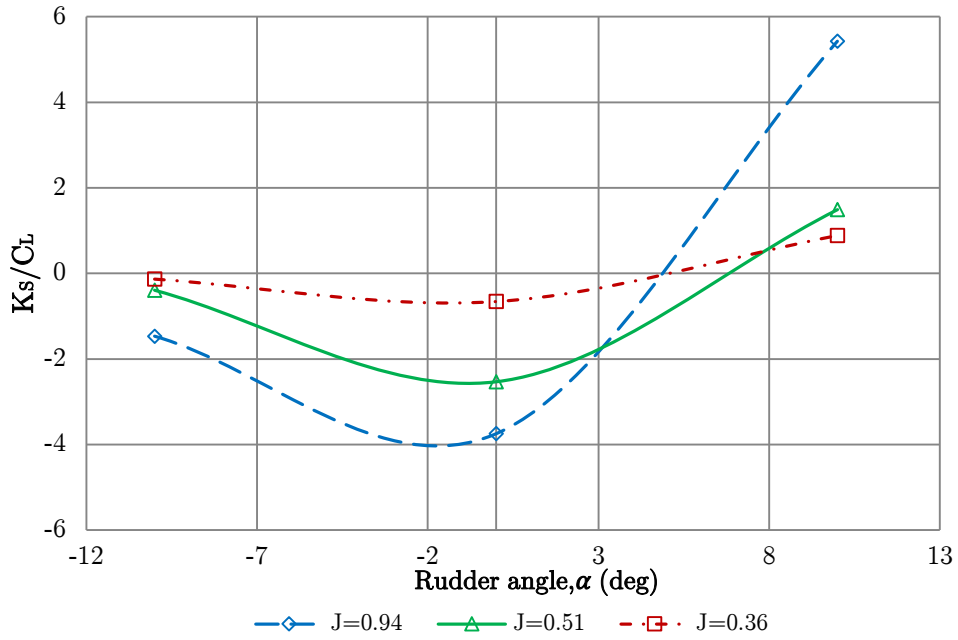

Figure 4.19: Effect of advance ratio on propeller side force, rudder and propeller combination in isolation, β_R = -7.5^{O}.

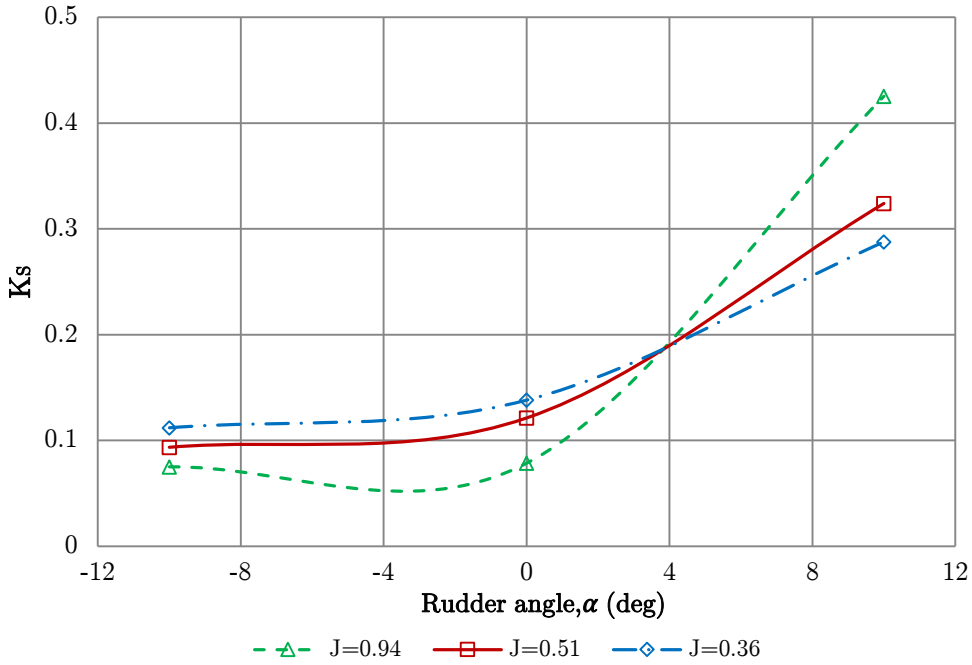

Figure 4.20: Effect of advance ratio on propeller side force, rudder and propeller combination in isolation, $\beta_R = 0^{O}$.

4.3.6 Skeg-rudder-propeller interaction propulsive performance data set

An overall table showing values of propeller sideforces, lift, drag and wake data's for all the cases considered is presented in Table 4.9. The effective wake fraction was obtained on the basis of thrust identity method. The results in Table 4.9 may provide initial estimates for the propulsive performance of skegs and the straight forward rudder force prediction including effects of drift angle and upstream skeg geometry, which is useful and can aid in the initial design of twin skeg ships or to maximize the propulsive efficiency of existing ones. The data set may also be found useful in other areas of ship manoeuvring such as the prediction methods of rudder forces during ship manoeuvring.

4.3.7 Wake plots

A wake plot was carried out (in wind tunnel axis) to observe the distribution of velocities arriving at the rudder. The results of such plots are shown in Figures 4.21-4.23 for zero and ten degrees rudder angle. Figure 4.24 presents the location of the wake plots. Differences in the velocity plots were observed for the propeller tangential velocities (v/U plots) in areas of the rudder below the propeller hub, increasing with increase in geometric rudder angle. At 10^{o} geometric rudder angle, the presence of the skegs also increased these velocities. The horizontal velocity plots in Figure 4.23 showed little difference in all the cases considered. In summary, the plots shows the importance of the tangential velocities for a propeller at drift and these need to be adequately captured to effectively predict the forces on a downstream rudder

4.3.8 Rudder pressure distribution

The chordwise pressure distribution of surface pressures for eight spanwise rudder locations from the root to tip with and without applied angle of drift and for different skeg lengths are compared in Figure 4.25. The computed chordwise pressure distribution represented by the local pressure coefficient Cp is given by:

$$Cp = \frac{P - P_{\infty}}{0.5\rho U^2} \tag{4.7}$$

where $P - P_{\infty}$ is the local pressure; ρ is the density of air and U is the free stream velocity. Drift angle influence can be observed for most areas of the rudder span below the center of the slipstream (below the hub). This was also observed in the velocity plots in Figures 4.21-4.23 where the tangential velocities of the propeller were dominant in areas below the rudder hub. Close to the slipstream, (span 230 & 390mm) local incidence resulted in the pressure peak increasing with increasing skeg lengths at the rudder leading edge. An area of interest was just around the hub where the unsteadiness in the flow introduced by the hub vortex can be observed for span 530mm as a bulge in the pressure

curve for the zero drift angle around the rudder trailing edge. This was not observed for the drift cases. In areas close to the tip (span 705mm-970mm) there were little or no differences in pressure curves for the drift cases. This is also seen in the streamlines passing through the short board at drift, Figure 4.13 where most of the flow changes occur in the rudder mid span, explaining why there was little difference in pressure curves for the drift cases around the rudder tip.

4.4 Conclusions

- A methodology of gaining valuable insight into the interaction between the skeg, rudder and propeller has been presented. Computational results for both global and local flow quantities were discussed and compared well with measured values. A mesh density of 3.3M cells proved inadequate to achieve a grid independent solution mirroring the entire flowfield and capturing all aspects of skeg, propeller and rudder flow and the interaction effect occurring between them. However, a good understanding of the flowfield and forces associated with the skeg, propeller and rudder can be obtained with the level of grid resolution used.

- The importance of the effective angle of drift and the sideforce due to the propeller on the performance of a rudder–propeller combination was demonstrated from the results obtained. When rudders are placed behind a propeller, lift force increases with increasing propeller load. Effect of drift tends to shift the forces associated with the rudder but does not change them totally. This shift is dependent on the angle of drift. The highest flow straightening occurred due to the presence of the short length skeg. It can be seen from this study that there is a significance expense associated with a time resolved propeller interaction (see Table 4.4). A body force method is far superior in terms of computational effort (Badoe et al., 2012; 2013).

- To relate this investigation to propulsive performance of ships which employ the use of skegs, since the lift curve slope was predicted within 2-3% accuracy the methodology used can be considered to be reasonable and the data for the skegs may be used to obtain initial estimates of the propulsive coefficients such as wake, thrust deduction, propeller thrust, torque and side force of a relatively thin skeg upstream of a propeller whilst that of that of the propeller-rudder combination alone might provide an idea for twin screw ships.

- Improvements to this methodology can still be made with important factors such as thorough verification and validation, improvements in grid resolution to accurately predict the propeller flow field hence accurate prediction of the rudder forces during stall.

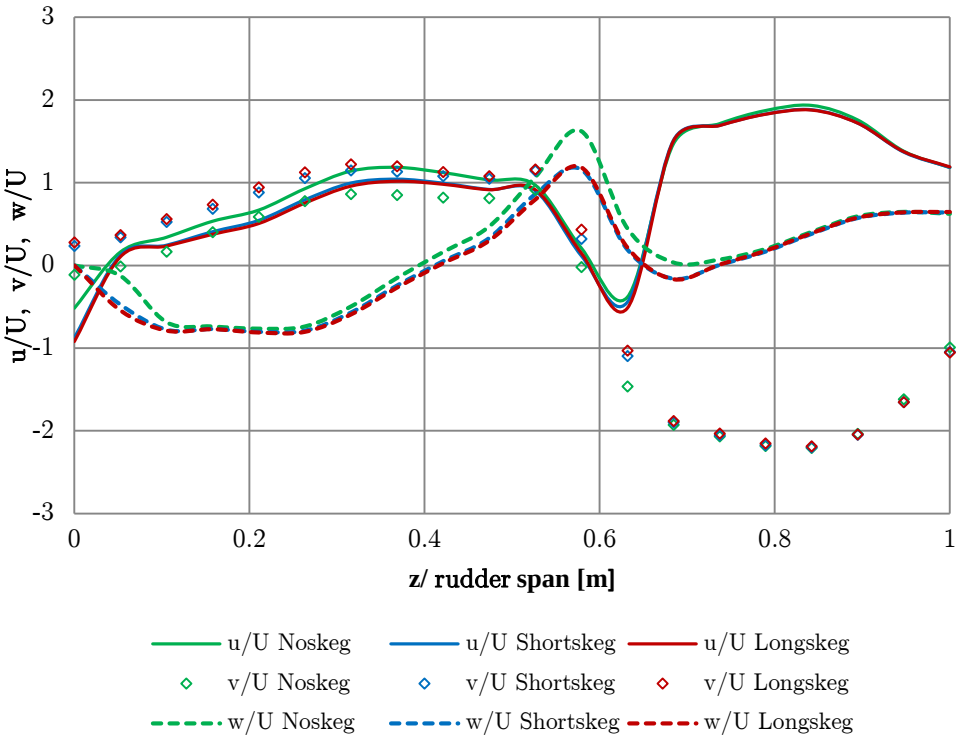

Figure 4.21: Velocity downstream of the propeller plane (X/D=0.374) at y=0, J = 0.36, β_R = -7.5^O, α = 0^O.

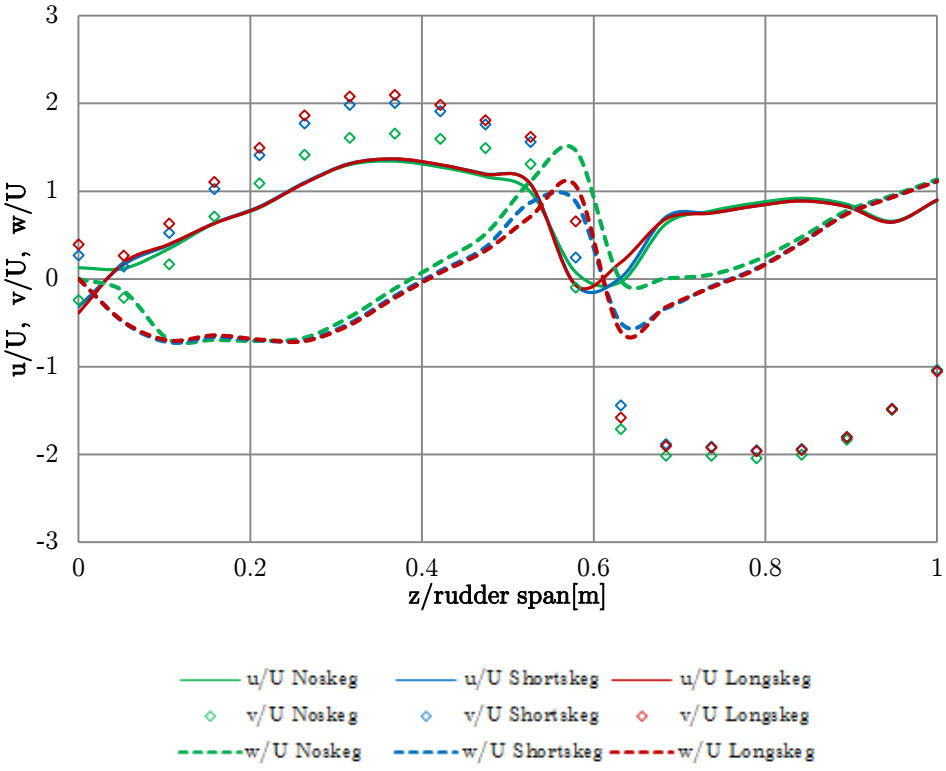

Figure 4.22: Velocity downstream of the propeller plane (X/D=0.374) at y=0, J = 0.36, β_R = -7.5^O, α = 10^O.

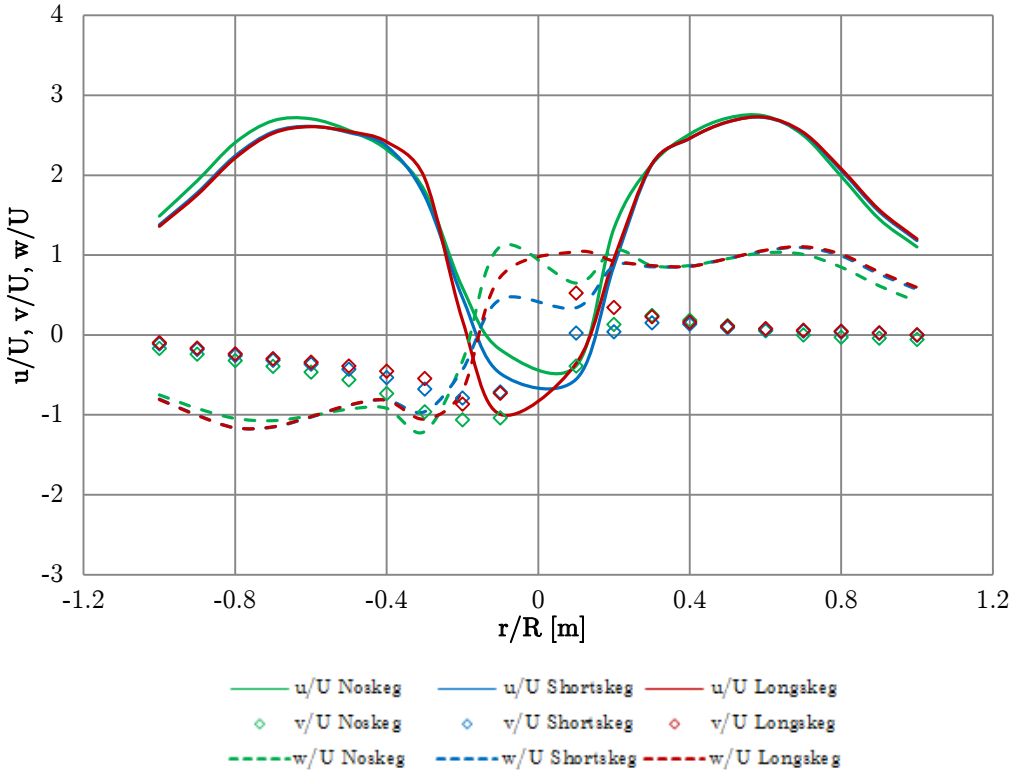

Figure 4.23: Velocity downstream of the propeller plane (X/D=0.374) at z=0.6, J = 0.36, β_R = -7.5^{O}, α = 10^{O}.

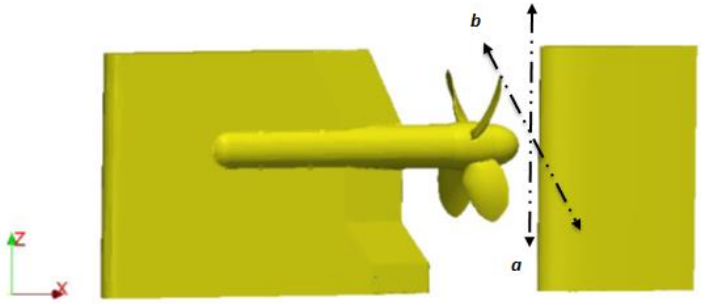

Figure 4.24: Wake cut location for plots of velocity downstream of the propeller plane (a) at y=0, (b) at z=0.6

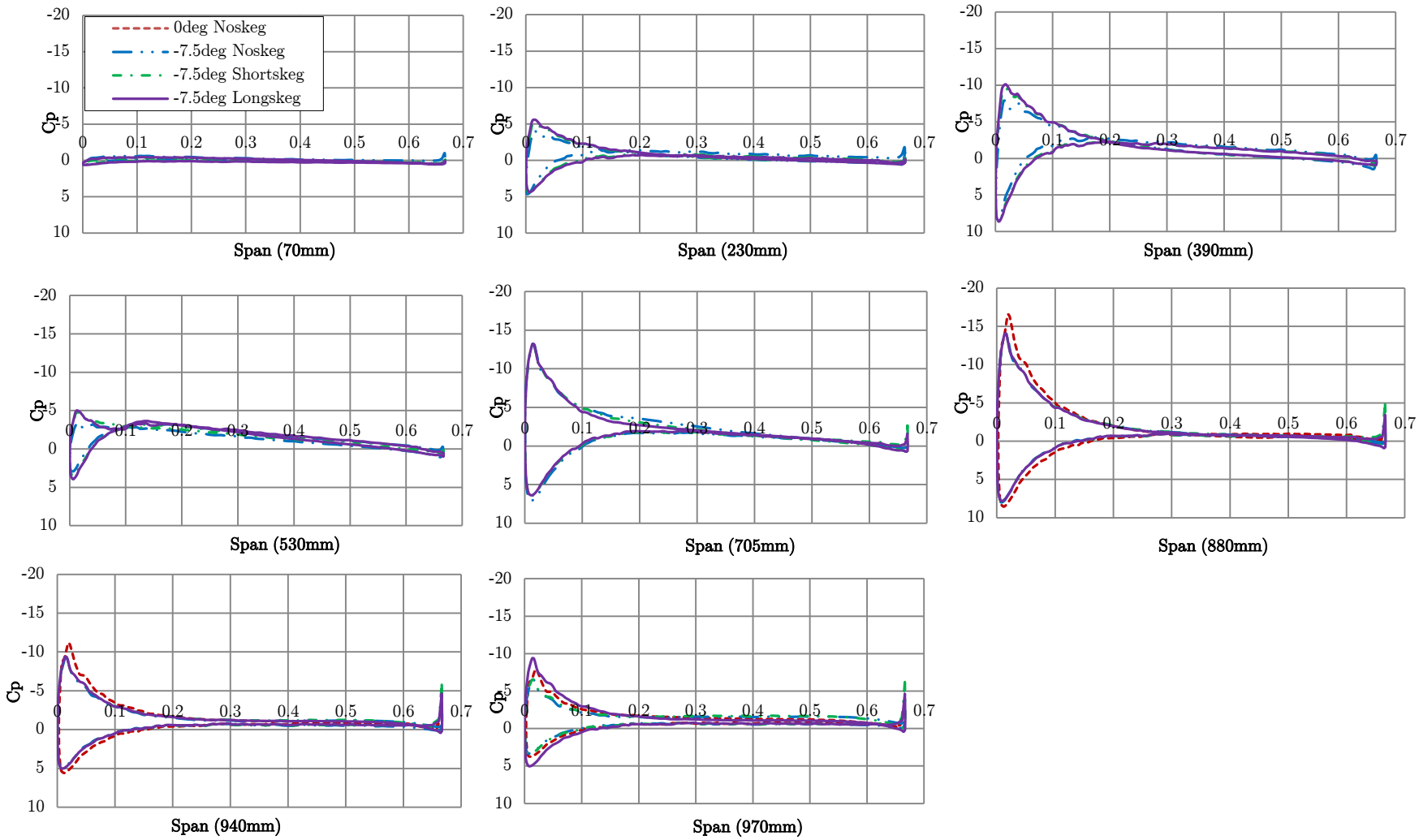

Figure 4.25: Chordwise pressure distribution at various rudder spanwise positions, J = 036, β_R = -7.5°& 0°, α = 10°.

Table 4.9: Data set for skeg-rudder-propeller interaction propulsive performance.

Rudder angle, β_R *[°]*	*[°]*	K_T	K_Q	K_S	η	t	w_T	∂Kt	∂Kq	C_L	C_D	*Skeg drag [N]*	*Skeg lift [N]*
Rudder&Propeller alone, J=0.36													
-10	0	0.397	0.054	1.12E-3	0.480			0.111	0.01	-1.360	0.145		
0	0	0.390	0.053	1.38E-3	0.486			0.104	0.90E-2	-0.034	0.020		
10	0	0.334	0.053	2.88E-3	0.476			0.048	0.90E-2	1.220	0.148		
Rudder&Propeller alone, J=0.51													
-10	0	0.304	0.041	0.94E-3	0.601			0.074	0.1E-2	-0.859	0.129		
0	0	0.300	0.040	1.20E-3	0.608			0.070	0.00	0.013	0.062		
10	0	0.330	0.041	3.20E-3	0.667			0.100	0.1E-2	0.796	0.138		
Rudder&Propeller alone, J=0.94													
-10	0	0.060	0.022	4.30E-3	0.408			-0.014	0.2E-2	-0.500	0.074		
0	0	0.111	0.022	0.80E-3	0.754			0.037	0.2E-2	-0.040	0.030		
10	0	0.116	0.022	4.30E-3	0.788			0.042	0.2E-2	0.500	0.070		
Rudder&Propeller alone, J=0.36													
-10	-7.5	0.335	0.054	2.73E-3	0.355			0.049	0.01	-2.010	0.400		
- 5	-7.5	0.333	0.053		0.359			0.047	0.90E-2	-1.400	0.130		
0	-7.5	0.332	0.053	4.88E-3	0.358			0.046	0.90E-2	-0.680	0.059		
5	-7.5	0.331	0.053		0.357			0.045	0.90E-2	-0.020	0.100		
10	-7.5	0.333	0.053	6.85E-3	0.359			0.047	0.90E-2	0.777	0.170		
Rudder&Propeller alone, J=0.51													
-10	-7.5	0.303	0.042	4.70E-3	0.585			0.073	0.2E-2	-1.200	0.190		
0	-7.5	0.302	0.042	8.10E-3	0.583			0.072	0.2E-2	-0.320	0.022		
10	-7.5	0.300	0.040	10.40E-3	0.608			0.070	0.00	0.700	0.085		
Rudder&Propeller alone, J=0.94													
-10	-7.5	0.146	0.031	11.70E-3	0.704			0.072	0.011	-0.800	0.203		
0	-7.5	0.147	0.030	7.50E-3	0.733			0.073	0.010	-0.200	0.010		
10	-7.5	0.148	0.030	21.70E-3	0.738			0.074	0.010	0.400	0.060		
Short length skeg, J=0.36													
-10	-7.5	0.315	0.051	0.53E-3	0.353	9.71E-3	0.217	0.029	0.70E-2	-1.920	0.200	1.542	21.155
0	-7.5	0.313	0.051	2.52E-3	0.351	9.77E-3	0.205	0.028	0.70E-2	-0.710	0.010	1.542	21.155
10	-7.5	0.313	0.051	4.12E-3	0.351	9.77E-3	0.205	0.028	0.70E-2	-0.500	0.090	1.542	21.155
Medium length skeg, J=0.36													
-10	-7.5	0.330	0.051	1.55E-3	0.370	0.022	0.259	0.044	0.70E-2	-1.700	0.250	3.427	26.382
0	-7.5	0.320	0.051	2.13E-3	0.359	0.021	0.240	0.034	0.70E-2	-0.510	0.012	3.427	26.382
10	-7.5	0.315	0.051	3.80E-3	0.353	0.022	0.217	0.029	0.70E-2	0.607	0.100	3.427	26.382
Long length skeg, J=0.36													
-10	-7.5	0.321	0.052	0.15E-3	0.353	0.016	0.244	0.035	0.80E-2	-1.754	0.334	2.534	32.634
0	-7.5	0.318	0.051	2.10E-3	0.357	0.016	0.232	0.032	0.70E-2	-0.600	0.019	2.534	32.634
10	-7.5	0.314	0.051	3.70E-3	0.352	0.016	0.211	0.028	0.70E-2	-0.600	0.100	2.534	32.634

Chapter 5

5 Hull-Propeller-Rudder Interaction

5.1 Introduction

The prediction of a ship's wake field and its resistance and powering performance is dependent on how well the three way interaction between the hull, propeller and rudder is understood and modelled. This is usually not an easy task especially at the stern of the ship where strong pressure gradients and curvature of the hull exist. This results in flow separation and both converging and diverging streamlines, which may have important consequence on the resistance and power of a ship.

The work presented in this chapter makes use of the modelling techniques and experienced gained from chapter 4 to investigate the three-way interaction between the hull, propeller and rudder by replicating experiments performed by MOERI and FORCE for the KCS operating at a Froude number of 0.26 and 0.202 respectively. The ability of three different propeller models and the coupling procedure in a RANS environment as described in section 3.3 namely; Hough and Ordway prescribed body force propeller, a propeller performance code based on the blade element momentum theory (BEMt) and a discretized propeller approach which employs the arbitrary mesh interface model, hereafter referred to as RANS-HO, RANS-BEMt and AMI respectively are compared for the study of resistance and propulsion capabilities of a container ship. This is validated against experimental data from the Gothenburg 2010 workshop (Larsson et al., 2010) and the SIMMAN 2014 workshop on verification and validation of ship manoeuvring simulation methods (SIMMAN, 2014).

The main focus here is a detailed analysis on the prediction of the hull and rudder performance resulting from the different levels of body force propeller approximations, the associated cost and the suitability of the various approaches for design evaluation purposes. Selected results from this study was presented to the SIMMAN workshop to allow comparison of the different modelling approaches with other organisations that also carried out similar studies.

5.2 Hull-Propeller-Rudder Interaction Case study

5.2.1 Details of experiment

The case considered is the well-known KRISO container ship, conceived to provide for both exploration of flow physics and for CFD validation as shown in Figure 5.1 and Table 5.1. Data are available experimentally such as Fujisawa et al. (2000) and Kim et al. (2001) and numerically from Larsson et al. (2010). Two different model scales were used for this study; the MOERI KCS hull 1:31.6 scale, designed at KRISO and tested at SRI (Fujisawa et al., 2000) was used for RANS-BEMt sensitivity studies in the prediction of local flow details. This is because of the availability of local flow data for the MOERI hull. The SVA hull 1:52.7 scale, tested at FORCE Technology (SIMMAN, 2014) was used mainly for the comparison of resistance and self-propulsion details.

Measurements of local velocity field on the MOERI KCS hull were carried out at SRI's towing tank (400m long x 18m breadth x 8m depth) at Froude number Fn = 0.26 under even keel conditions. The rate of the propeller model was set at 9.5rps and self-propulsion condition at "ship point". Full details of the experimental conditions and data can be found at Fujisawa et al. (2000).

The forces and moments data for the SVA hull were obtained as part of the SIMMAN 2014 Workshop on Verification and Validation of Ship Manoeuvring Simulation Methods (SIMMAN, 2014). Test No 2a-1 involving captive simulation in deep still water condition was considered. The self-propulsion test was carried out at Fn = 0.202 in the fully appended configuration and the propeller rps was set at 14.

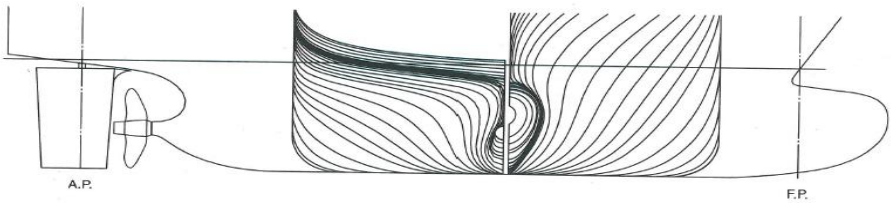

Figure 5.1: Body plan and side profile of the KCS ship model, source: Fujisawa et al. (2000).

5.2.2 Simulation conditions

Six sets of simulations were carried out with the SVA hull using a double body approach [NF] and considering the effect of free surface [F] (hereafter referred to as variants [F] and [NF] respectively) to enable a comparison to be made between [F] and [NF] on the prediction of hull, propeller and rudder forces and are outlined below:-

1. Static rudder KCS [F] computations at drift angle, $\beta = 0^{O}$, rudder angle, $\alpha = 0^{O}$ using a RANS-HO approach.
2. Static rudder KCS [F] computations at drift angle, $\beta = 0^{O}$, rudder angle, $\alpha = 0^{O}$ using a RANS-BEMt approach.
3. Static rudder KCS [NF] computations at drift angle, $\beta = 0^{O}$, rudder angle, $\alpha = 0^{O}$ using a RANS-HO approach.
4. Static rudder KCS [NF] computations at drift angle, $\beta = 0^{O}$, rudder angle, $\alpha = 0^{O}$ using a RANS- BEMt approach.
5. Static rudder KCS [NF] computations at drift angle, $\beta = 0^{O}$, rudder angle, $\alpha = 0^{O}$ using a discretize propeller, AMI.
6. Static rudder KCS [NF] computations at drift angle, $\beta = 0^{O}$, rudder angle, $\alpha = -20^{O}$, -10^{O}, -20^{O}, 10^{O}, 20^{O} using a RANS-BEMt approach.

Only one simulation was carried out with the MOERI hull using a double body approach for:-

1. Self-propelled KCS [NF] computations at drift angle, $\beta = 0^{O}$, using a RANS-BEMt approach.

Details of the simulation conditions for MOERI and SVA scales are presented in Tables 5.2 and 5.3 respectively.

Table 5.1: Principal dimensions of the KCS model, rudder and propeller.

		Model scale	
Dimensions	Full scale	SVA	MOERI
Scale	1.00	52.667	31.5994
Length between perpendicular, L_{PP} (m)	230.0	4.3671	7.2785
Breadth of water line, B_{WL} (m)	32.2	0.6114	1.0190
Depth, D (m)	19.0	0.4500	0.5696
Draft, T (m)	10.8	0.2051	0.341
Displacement (m^3)	52030	0.3562	1.6497
Rudder type	SB horn rudder	SB horn rudder	
Lat. area (m^2)	54.45	0.0196	
Propeller type	FP	CP	FP
Number of blades, N	5	5	5
Diameter (m)	7.9	0.150	0.250
P/D at 0.7R	0.997	1.000	0.9967
Ae/Ao	0.800	0.700	0800
Rotation	Right	Right	Right
Hub ratio	0.180	0.227	0.1800

where SB-semi balanced; FP-fixed pitch; CP-controllable pitch

Table 5.2: Self-propelled test case for container ship KCS at MOERI scale.

Parameter	Description
Test	Self-propelled at ship point
Condition	Fixed (even keel)
Fn	0.26
Rn	1.4×10^7
Propeller	yes
rps	9.5
Experimental data	resistance, local flow details
Experiments	MOERI

Table 5.3: Captive simulation for container ship KCS in deep still water at SVA scale.

Parameter	Description
Test	PMM simulation in deep water, static rudder
Condition	Fixed (even keel)
Fn	0.202
Rn	4.549×10^6
Rudder	yes (α = -20°, -10°, -20°, 0°, 10°, 20°)
Propeller	yes
rps	14
Experimental data	Forces/moments
Experiments	SVA

where PMM-Planar Motion Mechanism

5.2.3 Model domain and boundary conditions

The full geometry was considered hence the selected domain covered the entire flow field around the hull using a single block topology 10m wide and 5m deep for the SVA model whilst that of the MOERI version was 18m wide and 8m deep to match the tank dimensions. The inflow and outflow plane corresponds to that described in section 3.2.5 for both model scales. The hull and rudder were modelled using a no-slip condition whilst the free surface was modelled using the two phase volume of fluid technique (VOF) and

the double body approach. The computations are performed in OpenFOAM v2.2.0. Table 5.4 presents the computational parameters adopted.

Table 5.4: Computational parameters.

Parameter	Description
Steady state double body computations	
Computing	Iridis 4 Linux Cluster
Mesh type	Unstructured hexahedral
Turbulence model	Shear Stress Transport (Menter, 1994)
Convections terms	Gauss linear second order upwind schemes
Diffusion terms	Central differencing schemes
Pressure-velocity coupling	SIMPLE
Free surface and transient computations	
Computing	Iridis 4 Linux Cluster
Mesh type	Unstructured hexahedral
Turbulence model	Shear Stress Transport (Menter, 1994)
Convections terms	First to second order approach
Diffusion terms	Central differencing schemes
Pressure-velocity coupling	PIMPLE
Volume fraction	vanLeer scheme with interface compression

5.2.4 Grid generation

For all double body, [NF] steady simulations using RANS-HO and RANS-BEMt, the grids generation process as described in section 3.2.8 and implemented in OpenFOAM version 2.2.0 was used. Most of the grids were congregated in the regions of the stern, bow and near the hull surface. Ten to twelve elements were used to capture the boundary layer of the hull and rudder, yielding an approximate y^+ of 60 and 30 respectively. The total number of elements used was approximately 10 million.

In the free surface [F] computations using RANS-HO and RANS-BEMt, the grid strategy as described in section 3.2.8.1 was used. The total number of elements was about 18 million with around 4 million elements dedicated for the treatment of the free surface.

In the transient computations using AMI, since the propeller was close to the rudder extra care was taken with the AMI patches to allow smooth rotation without conflicting with the rudder grids and also keeping in mind the associated computational cost. As such the refinement level for the sides of the rudder was kept the same as the inflow (hull wake). Due to the difficulties with the use of snappyHexMesh to generate layers on geometries with sharp corners and curvatures only one prism layer was placed on the propeller. The surface refinement for the propeller was made finer to ensure that most of the flow features were resolved. The y^+ of the propeller, rudder and hull was 130, 40 and 60 respectively. The total number of cells was approximately 12.7 million. Figure 5.2(a)

shows the mesh resolution for the stern [NF] for RANS-HO&RANS-BEMt and 5.2(b) for AMI using the SVA hull.

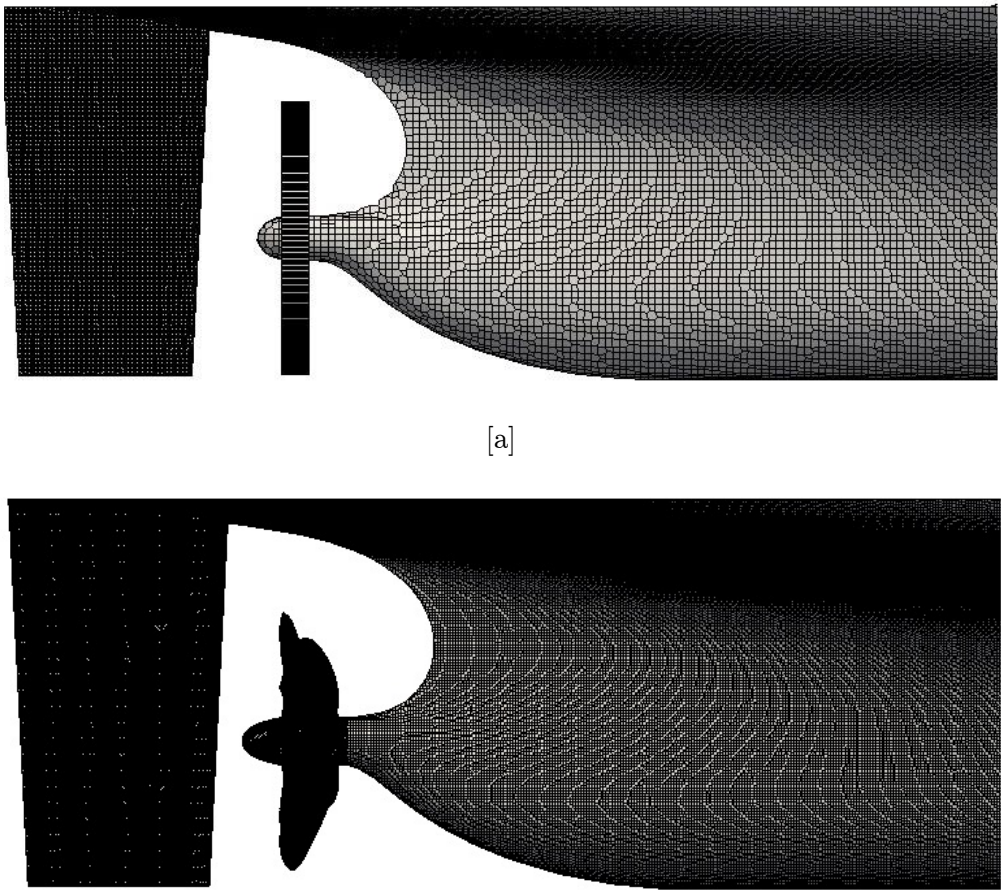

[a]

[b]

Figure 5.2: KCS stern mesh, NF: [a] RANS-HO&RANS-BEMt and [b] AMI using SVA hull.

5.3 Results

5.3.1 BEMt sensitivity studies (MOERI scale)

As discussed in section 3.3.2.2, the RANS-BEMt propeller was adapted to the ships wake using a sectorial approach which accounts for the non-uniform radial and circumferential inflow conditions. This procedure enables the BEMt code run at an arbitrary number of radial, nR, and circumferential, nC, locations based on the averaged inflow velocity over the propeller plane, $\overline{Va'}$ as seen in Figure 3.10. A sensitivity analysis was carried on the RANS-BEMt propeller to determine the number of radial nR, and circumferential, nC, subdivisions to effectively capture the MOERI hull wake field with the working propeller. A series of radial subdivisions, nR =10, 20, 40 and circumferential, nC subdivisions from 10-360 were used. It can be seen from the convergence plot in Figure 5.3 that nC converges at about 180 subdivisions. The plots in Figure 5.4 were then created by fixing nC to 180 and the varying nR. The plots were taken with the working propeller. It can be seen from the plots that the wake field is predicted reasonably well by using nR=20 and nC =180 (Figure 5.4b). It should however be noted that varying the number of circumferential subdivisions has little impact on the overall propeller K_T and K_Q.

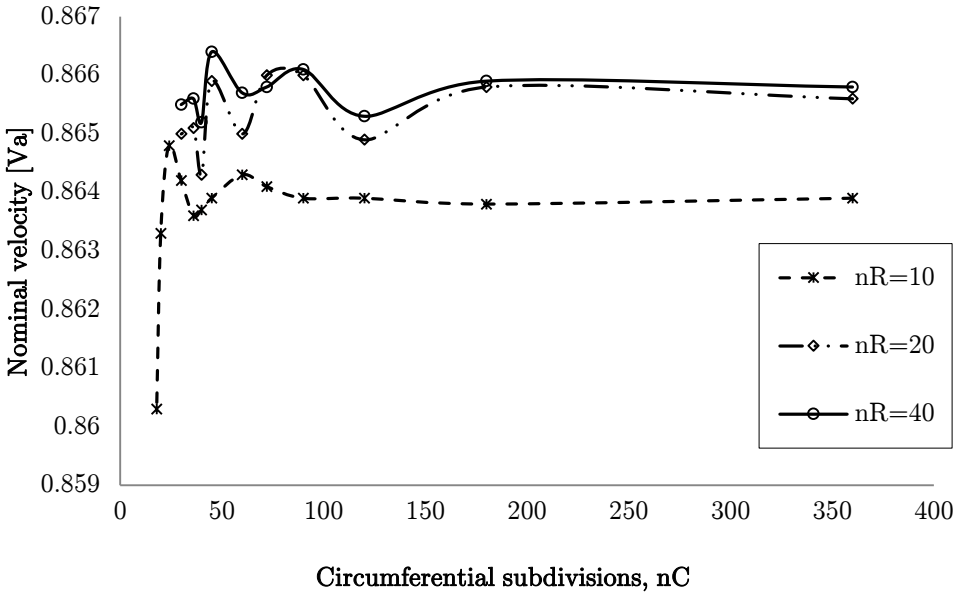

Figure 5.3: Convergence of nominal velocities for various radial, nR, and circumferential, nC, subdivisions.

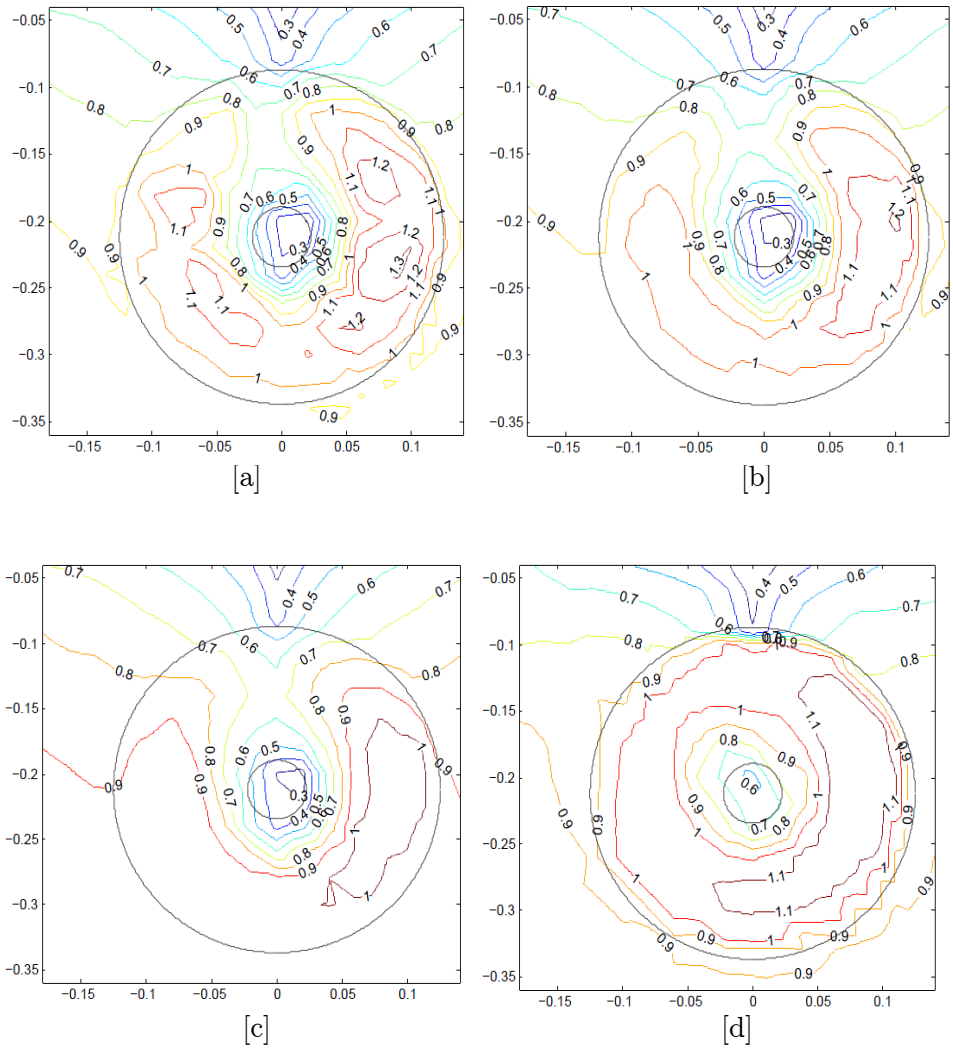

Figure 5.4: BEMt sensitivity studies for local velocity field (u/U contour) 0.25D behind propeller plane (x/L=0.491), Fr 0.26 with [a] nR =10 [b] nR =20 [c] nR =40 [d] Experiment, SRI, at n_p = 9.5rps.

5.3.2 Propeller open-water prediction

The open-water performance shown in Figure 5.5 calculated from the RANS-BEMt propeller and the AMI is compared with values from SVA. The results for the AMI were taken after ten propeller revolutions. The trend in K_T plots highlights the good agreement of the predicted thrust of the propeller for both propellers. For the effective advance speed of interest for this work (nominal J=0.6), the agreement for K_T and 10 K_Q was excellent using a RANS-BEMt propeller, with difference of less than 0.2% whilst that AMI propeller showed differences of 4%. The large variation in AMI prediction is attributed to insufficient mesh resolution around the blades and its boundary layer.

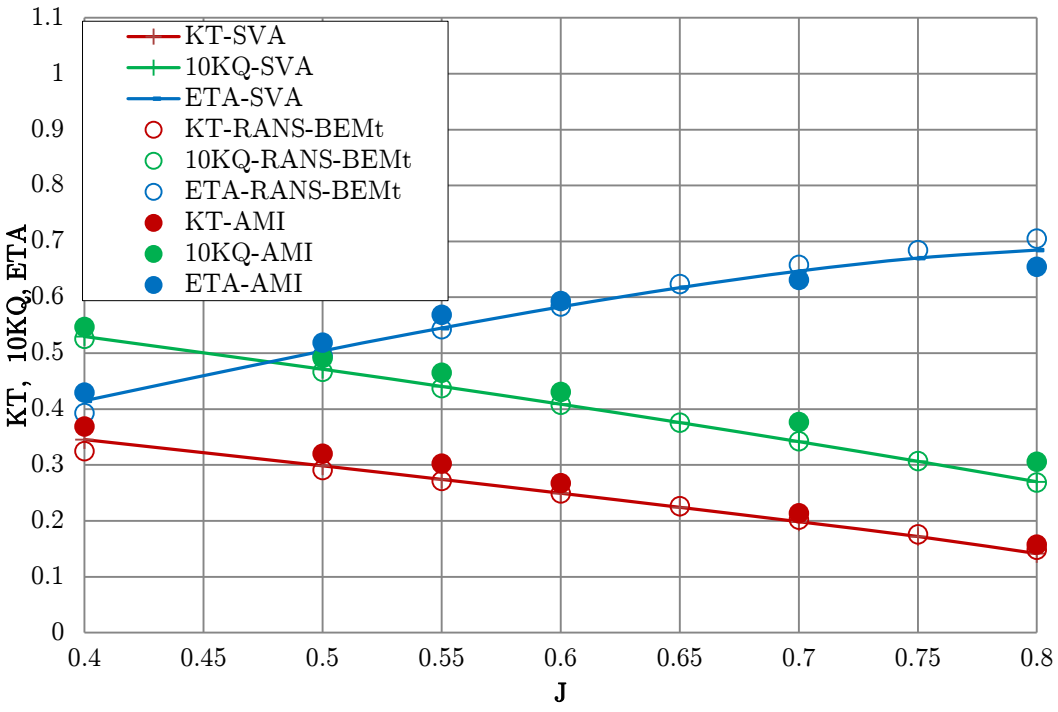

Figure 5.5: Comparison of propeller characteristics in open water. Experimental data made available as part of the SIMMAN 2014 workshop, Schiffbau-Versuchsanstalt Potsdam (SVA) scale, (SIMMAN, 2014).

5.3.3 Comparison of nominal wake field (MOERI scale)

The prediction of a ships nominal wake field is important since it provides a good initial estimate for the BEMt-RANS propeller model. The local velocity field without the working propeller model at an even keel 0.25D behind the propeller plane is compared with that of SRI in Figure 5.6. The symmetry with respect to the ships centreline is well predicted compared to experiments up to $u/U \approx 0.7$. The diffusive contour lines of

u/U ≈0.8&0.9 at the top part of the propeller outer radius (both port and starboard) are likely the result of insufficient mesh resolution around that region. The distortion in the velocity, i.e. the "hook shape" is very small compared to that of the experiment. Other distinct flow features such as the weak vortex flow found on both sides near the upper corner of the propeller boss and the downwards flow found near the centreline above the shaft were accurately predicted. The averaged nominal wake 1-w_t was 1% over estimated at 0.720 compared to SRI's value of 0.712.

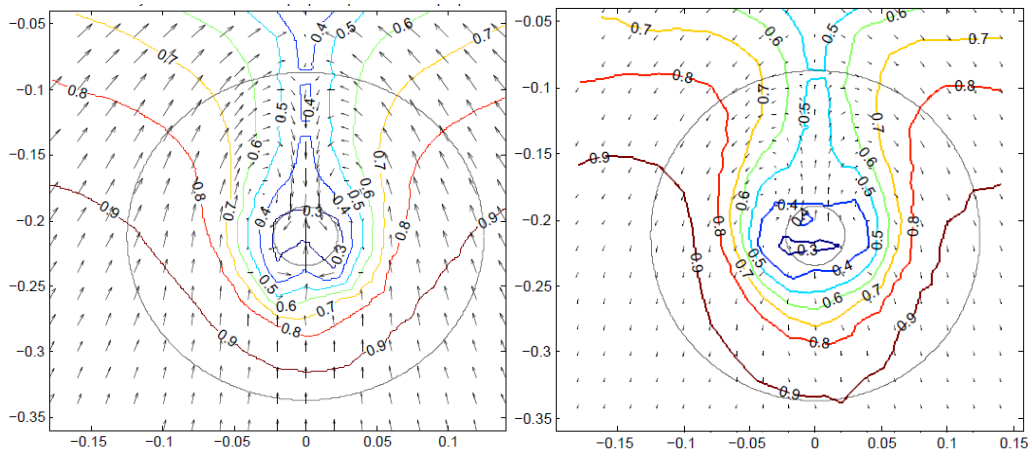

[a] [b]

Figure 5.6: Local velocity field (u/U contour & v/U-w/U vectors) 0.25D behind propeller plane (x/L=0.491), Fr 0.26 without propeller [a] Fine grid, [b] Experiment, SRI.

5.3.4 Impact of free surface on nominal wake field (SVA scale)

The nominal velocity field at the propeller location with the rudder for the towed condition is illustrated in Figure 5.7. No local flow field data was provided as part of the experiment and hence a comparison was made based on double body [NF] and free surface [F] simulations. Comparison of the two plots shows little variations. The double body plot shows a much smaller boundary layer around the hull and which thickens gradually, with a much smaller 'hook' like shape of the shape of the velocity deficit when compared to the plot with free surface included. It should be noted that the mesh count for the double body computation is slightly lower than that of the free surface computation as such might also introduced slight differences in the boundary hull boundary layer. A similar plot showing the circumferential distribution of the nominal wake fraction (w_t) at various r/R locations is presented in Figure 5.8. The wake peaks in the propeller top position (ϕ =180°) is similar for both plots. Slightly higher wake values are observed for the free surface conditions at the outer radii. The free surface conditions shows slight asymmetry. The reason may be due to slight variation in the meshing.

Table 5.5 compares the total resistance, frictional resistance and nominal wake fractions for the free surface and double body computations. The wave resistance components follow from an existing non-linear potential flow code (Couser et al., 1998), resulting in $C_w = 0.988\times 10^{-3}$ for the KCS (SVA scale) including rudder and hub in this condition. Variations between all the resistance components at this particular Froude number (Fn =0.202) are 2.5%, 7% and 0.6% for C_T, C_F and 1-w_t respectively.

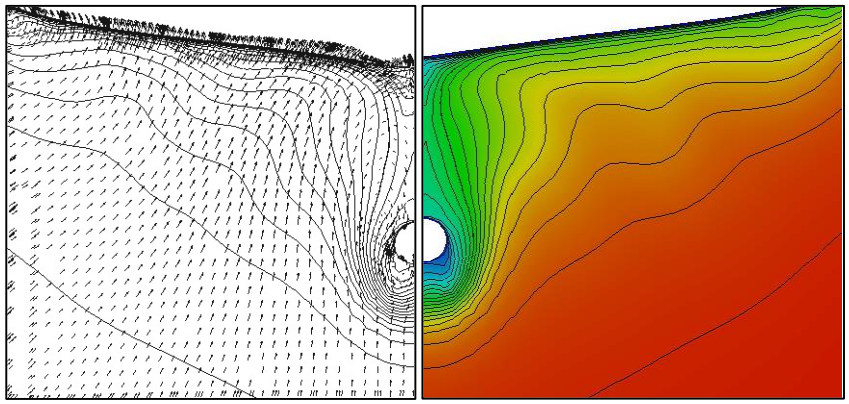

[a]

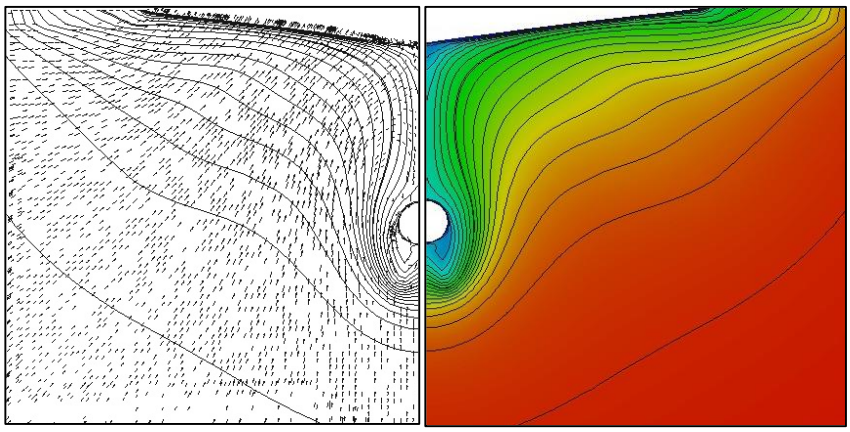

[b]

Figure 5.7: Local velocity field (u contour & v-w vectors) at the propeller plane, Fn = 0.202 without propeller [a] with free surface, F [b]double body, NF simulation using RANS-HO&RANS-BEMt.

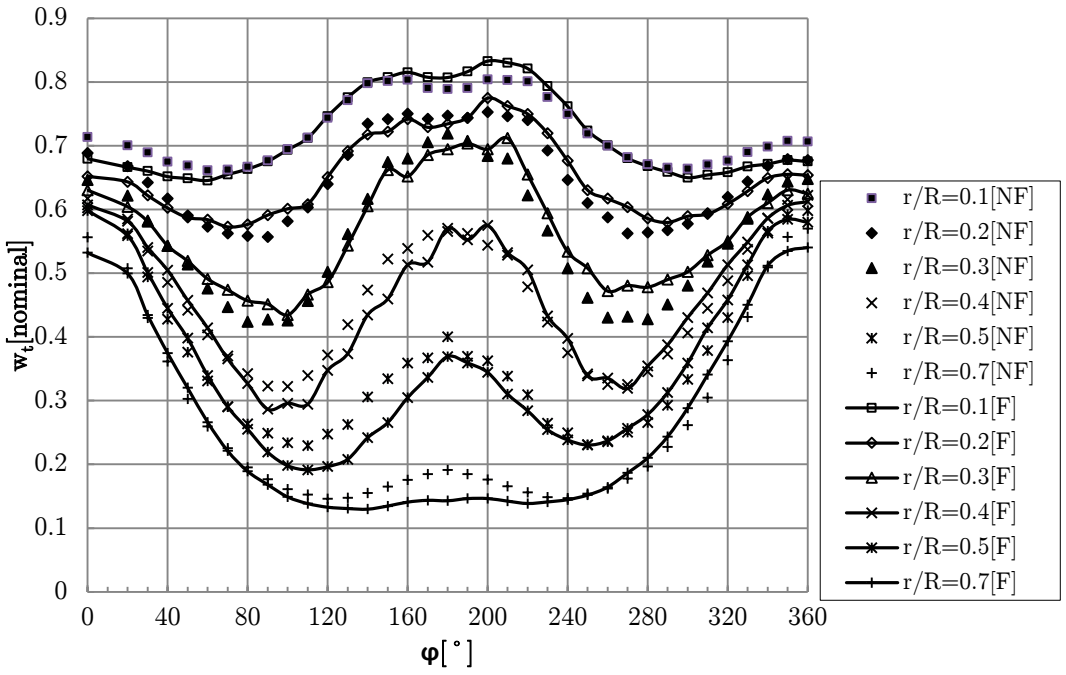

Figure 5.8: Circumferential distribution of nominal wake fraction, (w_t), at the propeller disc with free surface [F] and double body [NF] simulations using RANS-HO&RANS-BEMt.

Table 5.5: Resistance parameters for KCS in fixed condition (SVA scale).

Parameter	Free surface condition [F]	No-Free surface condition [NF]
C_T	5.23×10^{-3}	5.10×10^{-3}
C_F	3.71×10^{-3}	3.46×10^{-3}
1-w_t	0.661	0.657

NB: Resistance parameters are non-dimensionalized with $0.5\rho S{U_O}^2$.where S is the wetted surface area including rudder, ρ is the density of water at 10 degrees and U is the inflow velocity.

5.3.5 Axial velocity variation in front, at and behind the propeller plane (SVA scale)

The comparison of axial velocity contours at locations in front and behind the propeller plane is shown in Figure 5.9-5.11. The plots were taken from double body [NF] computations using RANS-HO, RANS-BEMt and AMI methods in order to compare their strengths and weaknesses. The AMI plots are time averaged. The upstream influence at 0.9 propeller diameter showed little difference for all methods as seen from Figure 5.9, which may be due to the fact that 0.9 propeller diameter may be far to locate any localised upstream effect of the propeller.

At the propeller plane (Figure 5.10) the differences in the various methods become more prominent. RANS-HO shows symmetry in the flow compared to the other methods. This is because the method assumes a constant circumferential distribution of thrust and torque which is not true in reality. RANS-BEMt is more consistent with the AMI, which shows the actual propeller hydrodynamic influence on the inflow and as such a different flow regime to that of RANS-HO can be seen. The differences result from the sectorial approach adopted for the propeller which unlike RANS-HO does not use an average circumferential distribution but rather takes into account the local thrust and torque at each radial and circumferential location in the propeller plane. This results in greater asymmetry in the flow field. The load on the port side of the propeller in RANS-BEMt is much greater compared to the AMI. Since no experimental flow field data was provided, an in depth flow field comparison between these two method proved difficult. However it should be borne in mind that a 4% increase in propeller force for J=0.6 was achieved using AMI with the level of mesh density used as such the large error might contribute to the reason for the differences in plots.

5.3.6 Global forces

Table 5.6 shows a combined result for resistance and propulsion parameters for RANS-HO, RANS-BEMt and AMI with [F]and without [NF] the influence of free surface effect. These are compared with experimental data by FORCE Technology.

By taking the free surface effect [F] into account RANS-BEMt predicted the propeller thrust within 1% of the experimental data whilst the torque was predicted within 12%. RANS-HO used a prescribed thrust and torque values from open-water data. The drag was predicted within 4% using a RANS-BEMt method whilst the RANS-HO predicted the drag within 23%. The reason for such high drag discrepancies using RANS-HO even though a prescribed thrust and torque values were used may be attributed to the inability to capture the interaction effect between the hull on propeller and rudder on propeller and vice versa. It should be recalled from the flow field data that the method was poor in replicating the swirl effect which resulted in a different flow field (i.e. symmetry in the flow field). This may have contributed to the poor prediction of the hull forces and subsequently on the forces associated with the rudder. Unfortunately, no experimental data set was available for the rudder forces, but it should be borne in mind that the rudder forces are dependent on its inflow conditions such as the hull wake and propeller race. As such a decrease or increase in any of them might affect the forces developed on the rudder. The hull forces using the RANS-HO were predicted within 15% of RANS-BEMt method.

Computations using a double-body approach show that the swirl effect was better predicted using an AMI at 4% whilst the RANS-BEMt showed values of 19%. RANS-BEMt however showed a much improved thrust at 4% compared to 13% using AMI. The

non-dimensionalised drag (X') was predicted by 2.4%, 5.8% and 28.5% using RANS-BEMt, AMI and RANS-HO respectively.

Results of the RANS-BEMt also show that by using a double body approach propeller thrust showed a difference of 3% compared to taking the free surface into account. Similarly for the torque a 7% difference was observed. With respect to the drag there was less than 2% difference in using a double body approach or by accounting for the free surface. An overall cost in computation is also shown in Table 5.6 which shows that there is still a significant computational expense associated with a discretized propeller and that body force based methods are still likely to be required with ship resistance and propulsion simulations.

Selected results from the above simulations were submitted to the SIMMAN workshop. Five groups produced RANS simulations of KCS hull with straight ahead condition in deep water. These are compared with experiments by FORCE Technology. Table 5.7 compares the predicted global forces and moments. The submitted are shown as SOTON (Method 1) using a RANS-BEMt. There is a significant scatter in the numerical solutions and significant variations between these values and the experiment.

Lastly the influence of the rudder on propeller δk_t was compared for various rudder angle (Figure 5.12). δk_t values were obtained by finding the difference in thrust of the bare hull-propeller and the fully appended hull computations. The high δk_t curve as compared to that of SVA may be attributed to the increased nominal velocities predicted using a double body approach. The results however show that the presence of the rudder increases the thrust produced by the propeller, with increased rudder angle.

5.4 Conclusions

To demonstrate the effectiveness of the proposed sectorial approach used for the RANS-BEMt, a simulation of the flow and interaction effect around the KCS hull was conducted with other existing approaches such as a discretise propeller approach, AMI and a body force approach with strength calculated using the Hough and Ordway thrust and torque distribution, (Hough and Ordway, 1965), RANS-HO. A mesh sensitivity quantified the number of radial, nR and circumferential, nC subdivisions which best captures the wake field after which simulations were conducted on a fully appended KCS using the optimum nR and nC. The following conclusions are drawn from the investigation.

5.4.1 Fluid dynamic fidelity

RANS-HO assumes a constant circumferential distribution of thrust and torque hence does not capture the interaction between the hull on propeller and rudder on propeller and vice versa. The method estimated the resistance with reasonable accuracy, but was

poor in replicating the swirl effect which resulted in a different flow field (i.e. symmetry in the flow field).

RANS-BEMt is best suited for capturing and predicting most aspect of the resistance and propulsion characteristics of a ship. The method calculates the thrust and torque as part of the simulation and is able to give estimates of the interaction between the hull on propeller and rudder on propeller. It is able to replicate the swirl effect much better than RANS-HO.

AMI theoretically offers the highest degree of fidelity even though the results shown using this method would have been improved with much finer mesh resolution especially around the propeller blades and in the boundary layer. The method however requires small time steps due to restrictions imposed by explicitly solving the propeller flow.

5.4.2 Computational cost

RANS-HO is the least costly as can be seen from Table 5.6 and can be used for quick resistance and self-propulsion estimations only if the flow field details are not of prime importance as long as the required conditions of the flow heads are captured.

RANS-BEMt follows on from RANS-HO as being less costly for ship resistance and propulsion simulations with less than 0.27% of the total simulation spent on propeller modelling.

AMI is the most computationally demanding approach since the full transient flow field needs to be resolved with a higher level of mesh cells in order to provide accurate estimates of resistance and propulsion parameters. The method does not only suffer from longer overall simulation time but also from increased computational time per time step.

Comparison of the double body and free surface computations showed little difference in the nominal velocities at various r/R locations of the propeller plane. The double body also resulted in an increase in thrust and drag by 3% and 1% respectively when using a RANS-BEMt approach for Froude number of Fn=0.202. Accounting for the free surface effect is time consuming and computationally demanding (especially if computations are to be conducted for a range of speeds and draught conditions) since smaller time steps and long runs are needed for the waves to settle before extracting the inflow velocities for the propeller and since the results are within the likely bounds of experimental error, an alternate and quicker option of predicting the resistance and propulsion parameters will be to run the simulation without the free surface and then use a linear potential flow code to predict the wave resistance.

5.4.3 Suitability for design purposes

RANS-HO reasonably predicted the global forces compared to the experiment but was poor in replicating the flow field as such the method may be used for initial assessment of

ships resistance and propulsion where requirement for exact mirroring of the flow fields are not essential.

RANS-BEMt was able to predict the resistance and propulsion parameters much better but the propeller influence has been averaged over one blade passage which neglects tip and hub vortices, this makes it unsuitable for cavitation analysis. The methods may however benefit from addition of tangential inflow conditions and coupled with the non–uniform inflow inputs may be suitable for transient manoeuvring simulations as well as resistance and powering computations.

AMI is more suitable for all the analysis described above but requires experience in the use and distribution of high mesh cells to capture detail flow features.

Overall these simulations provide initial estimates of resistance and propulsion parameters for the appended KCS hull form. The results would benefit from the following:-

- much finer mesh resolution in the boundary layer region, resolving the viscous sublayer would remove uncertainties in the use of wall functions.
- good resolution of the bilge vortices would facilitate much improved propeller inflow predictions and hull surface pressure.
- fine mesh density around the rudder and tip and root vortex would improve the rudder force prediction.

Having established the strengths and weaknesses in the numerical towing tank and methodology in the stepwise study, the experience gained is utilised to design the stern of a future twin skeg LNG ship and assess its powering performance.

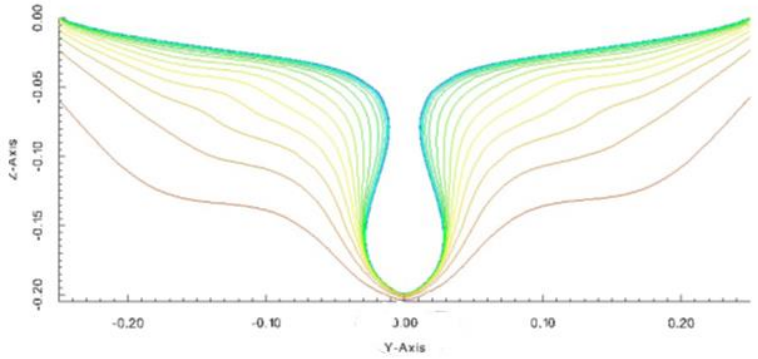

[a]

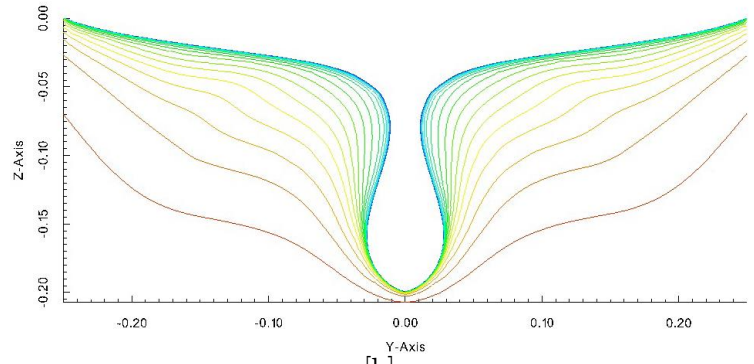

[b]

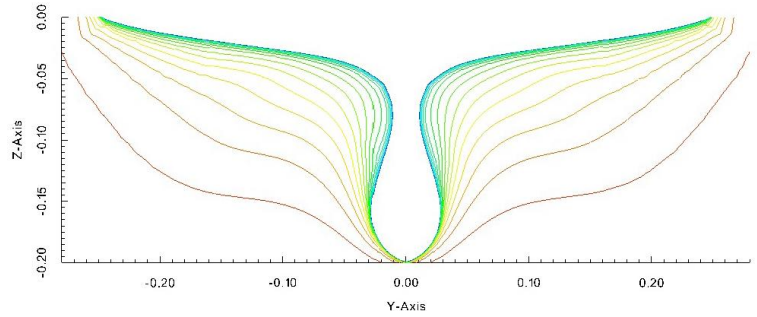

[c]

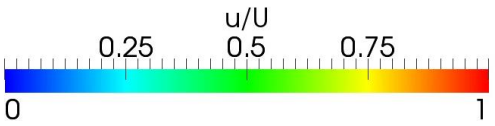

Figure 5.9: Axial velocity field (u contour) 0.9D upstream of propeller plane, Fn 0.202 from [a] RANS-HO [b] RANS-BEMt and [c] AMI, double body computations at n_p = 14.0rps.

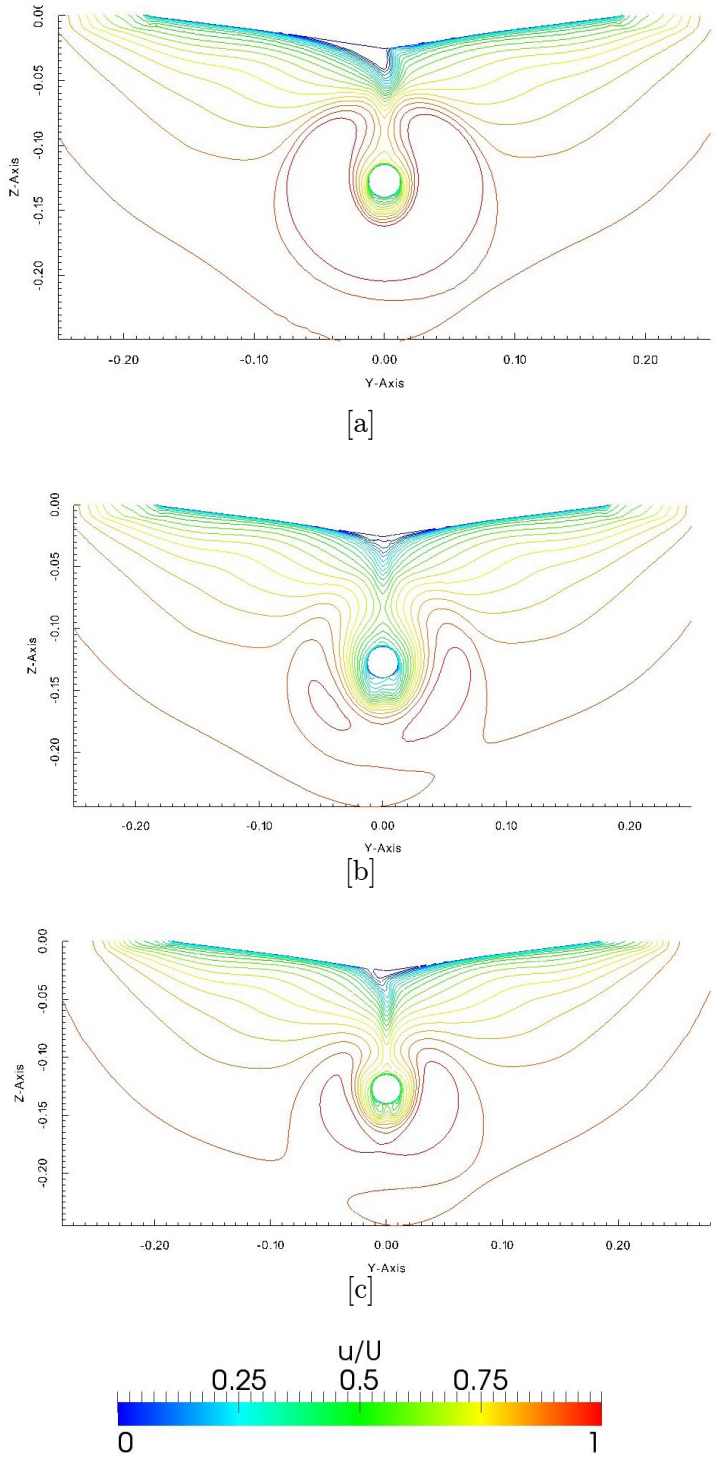

Figure 5.10: Axial velocity field (u contour) at propeller plane, Fn 0.202 from [a] RANS-HO [b] RANS-BEMt and [c] AMI, double body computations at n_p = 14.0rps.

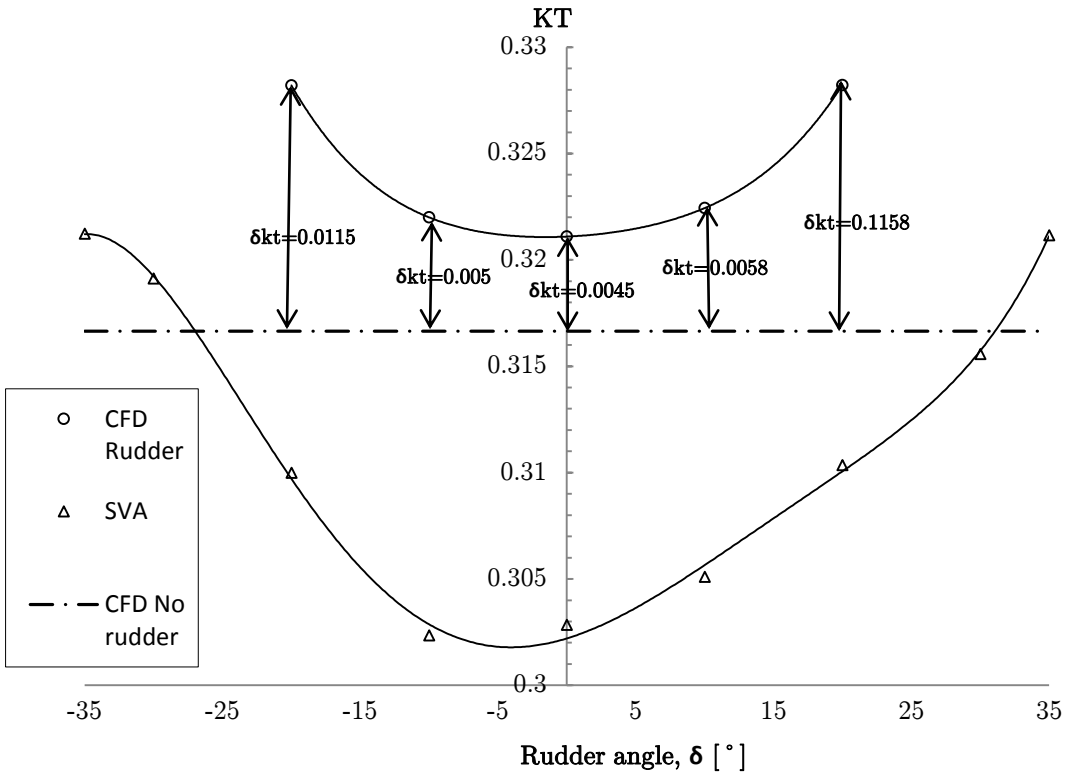

Figure 5.11: Comparison of BEMt propeller forces [KT] and rudder influence on BEMt propeller [δkt] for various rudder angle with experiments, Fn 0.202 and n_p = 14.0rp

Table 5.6: Resistance and propulsion parameters.

Parameter	RANS-HO		RANS-BEMt		AMI	Data
	F	NF	F	NF	NF	
Hull drag Total ($Fxt\times 10^{-2}$)	2.295	2.3747	1.938	2.160	1.530	-
$X'\times 10^{-2}$ (T'-(Fxt+ Rxt'))	1.417	1.314	1.922	1.795	1.732	1.840
$Y'\times 10^{-3}$	1.935	1.462	1.032	1.802	0.266	-0.064
$N'\times 10^{-3}$	- 0.973	- 0.708	-0.400	-0.560	-0.914	-0.280
Rud Force Total ($Rxt'\times 10^{-3}$)	1.504	1.738	0.466	0.684	0.863	-
Rud Force Total ($Ryt'\times 10^{-3}$)	1.896	0.852	0.743	1.485	1.648	-
Prop Thrust ($T'\times 10^{-2}$)	P	P	3.907	4.030	3.348	3.862
Prop Torque ($Q'\times 10^{-4}$)	P	P	2.160	2.240	1.810	1.880
Total simulation time[9]	30-60hrs	3-5hrs	30-60hrs	4-6hrs	>200hrs	
Cost on prop modeling[10]	-	-	$< 0.27\%$	$< 0.27\%$		

NB: X'-hydrodynamic longitudinal force; N'-hydrodynamic yaw moment; Rx'-rudder force in x direction; Ry'-rudder force in the y direction; T'-propeller thrust; Q'-propeller torque; P-prescribed thrust and torque (open-water data values), NF: - Freesurace surface effect not taken into account, F: - Freesurace surface effect taken into account; All parameters non-dimensionalised by ($0.5\rho V^2 L_{PP} T$) except N' and Q' which are non-dimensionalised by ($0.5\rho V^2 L_{PP}{}^2 T$).

[9] Simulation times are in wall clock hours using 64processors.
[10] Costs on prop modelling are in percentage of total simulation time and includes mapping and data handling.

Table 5.7: Test Case 2a-1: KCS, static rudder, β=0.0[deg], δ=0.0[deg], deep water. Results taken from SIMMAN 2014 website, (www.smmman2014.dk).

Organization	Code	Integral Values(x 10^{-3})						
		X'	Y'	N'	$R_X{}'$	$R_Y{}'$	T'	Q'
FORCE	EFD	18.39	-0.06	-0.28	-	-	38.56	0.19
HSVA	FreSCo+ (body force)	19.16 (4%)	2.85 (-4561%)	-0.00 (-99%)	1.17 -	-3.27 -	37.48 (-3%)	0.20 (6%)
SOTON (Method 1)	OpenFOAM (body force)	19.22 (5%)	-1.03 (1513%)	-0.40 (45%)	0.47 -	0.75 -	39.07 (1%)	0.22 (15%)
SOTON (Method 2)	OpenFOAM (actual prop)	26.52 (44%)	-2.27 (3448%)	-0.06 (-80%)	1.39 -	0.06 -	32.16 (-17%)	0.17 (-11%)
SOTON (Method 3)	OpenFOAM (body force)	15.08 (-18%)	-0.30 (363%)	-0.11 (-60%)	1.62 -	-0.27 -	35.81 (-7%)	0.20 (7%)
OSK Ship Tech	Star-CCM+ (actual)	23.53 (28%) *0.13	-0.85 (1235%) *0.22	0.42 (-251%) *0.01	0.74 - *0.32	0.87 - *0.52	42.18 (9%) *0.08	0.22 (19%) *0.03

	mean	29.70	-0.32	-0.03	1.08	-0.25	37.34	0.20
	std dev	3.96	1.71	0.26	0.42	1.56	3.33	0.02
	mean error	12.60%	399.77%	-88.77%	-	-	-3.15%	7.18%
	std dev of error	21.40%	2677%	94.99%	-	-	8.64%	10.13%

*Usn according to QM Section 4.9-04-01-01 and QM Section 4.9-04-01-02, see (www.smmman2014.dk)

(....%) error E of simulation relative to experiment D in percent (E=(S-D)/D)

Chapter 6

6 Estimating the Resistance and Self-Propulsion Characteristics of a Future Twin-Skeg LNG Ship.

6.1 Introduction

The numerical towing tank, stern design cycle outlined in chapter 3 and the experience gained from chapters 4 and 5 are applied here to model the self-propulsion characteristics of a future twin skeg LNG ship in order to investigate its propulsive performance. The twin skeg ship model (termed TSLNG hereafter) is an innovative geometry investigated and provided by Shell shipping as part of its growing interest to reduce fuel consumptions and emissions among its fleet. In TSLNG, both propeller shafts are enclosed by a part of the hull also known as skegs (Figure 6.1), this therefore provides a smooth flow to the propeller compared to ordinary twin screw ships. To take advantage of this circulatory flow and to further improve the flow to the propellers and rudders, four parametric studies were considered aimed at reducing thrust deduction (t) and increasing wake fraction (w_T) after which an improved design was chosen. The terminology improved design mentioned in this work is strictly defined as the best design from the parametric study for a range of design speed conditions.

The parametric studies to be conducted are outlined below:-

1. Investigate a range of propeller P/D ratios to assess its impact on thrust deduction.

2. Investigate a range of propeller diameters (D) to assess its impact on thrust deduction.
3. Varying the lateral separation (Y/D =0.1, 0.2 and 0.3) of the twin rudders (a) inwards (b) outwards and (c) both starboard.
4. Varying the direction of rotation of the twin propellers (i) inwards (ii) outward (iii) port inwards and starboard outwards to assess its impact on thrust deduction.

This poses a challenge since it requires a complete computation of resistance and self-propulsion test over a range of speed and design draught conditions with high level of accuracy that is capable of prediction any small differences in flow characteristics as well as changes in propulsive power resulting from small variations in design parameters listed above. Although a discretized propeller approach using the AMI would be more suitable for such computations, the RANS-BEMt method was chosen for this work due to lower computational cost compared to AMI and higher fluid dynamic fidelity over RANS-HO method (see chapter 5).

Based on the results of the parametric studies the second phase will be to select the most improved design for evaluation of the LNG ship's power performance for a range of speeds and draught conditions.

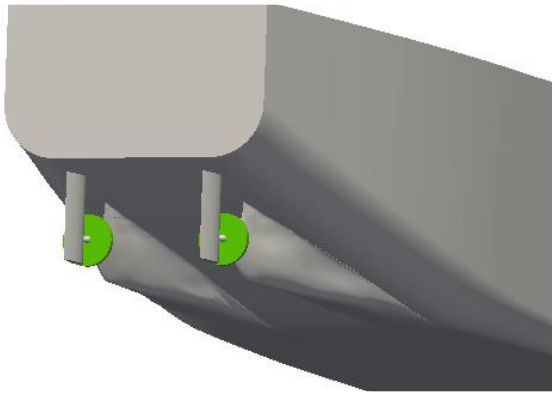

Figure 6.1: Stern view of TSLNG showing twin skegs, rudders and propeller.

6.2 The Twin-Skeg LNG carrier (TSLNG) Case study

6.2.1 Details of experiment

The dimensions of TSLNG ship are 292.17m in length, 44.15m in breadth and 12m in loaded draught. The model utilised for the computations has scaling ratio of 1:32.189. No rudder and propeller was provided as part of the investigation. It was therefore decided

to scale and adapt the rudder used in chapter 4 for the ship model. The area of the rudder conforms to Det Norske Veritas, (DNV 2001) recommendation of:-

$$A = \frac{TL}{100}\left[1 + 50{C_B}^2\left(\frac{B}{L}\right)^2\right]m^2 \quad (6.1)$$

where T is the draft of the ship, L is ship length, B is the breadth and C_B is the block coefficient of the ship.

The shorter stern of the ship hull did not provide much scope to examine the influence of longitudinal separation, hence the rudder was fixed at X/D=0.26. The vertical separation of Z/D coincided with the propeller tip. Only the variation in lateral separation, Y/D was investigated. Details of the rudder can be found in Table 6.1. The propeller used in chapter 5 was also scaled and adapted to the ship (see Table 6.1). The propeller tip to keel clearance was $\geq$ 0.07R (m) as recommended by DNV. Investigations were carried out for a range speeds (six speeds in loaded and six speed in ballast) in both loaded and lightly ballast conditions. Details of the simulation conditions can be found in Table 6.2. Figure 6.2 presents the stern arrangements in both fully loaded and ballast draught conditions. Noteworthy is the propeller diameter with respect to the waterline for both draught conditions.

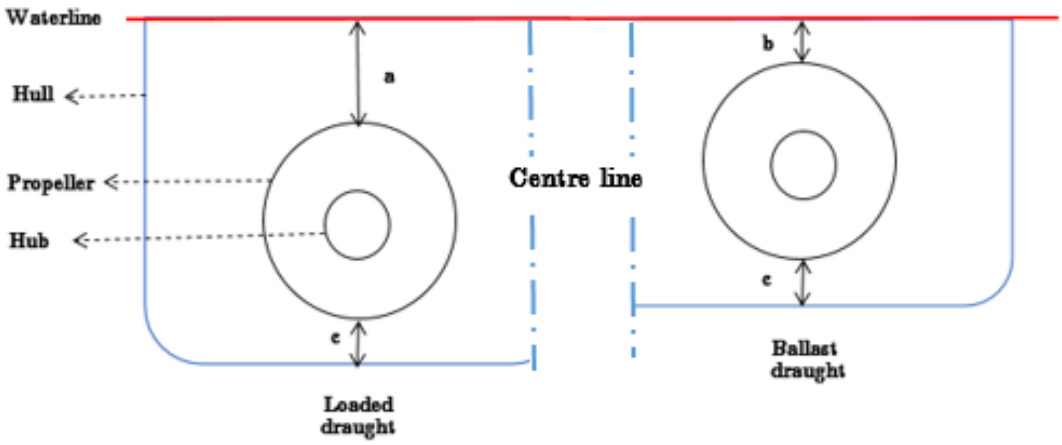

NB: propeller-hull clearance in loaded draught, a =0.13m, propeller-hull clearance in ballast draught, b = 0.01m, propeller tip to keel clearance, c =0.029m

Figure 6.2: TSLNG stern design draught details.

The simulated TSLNG stern flow field was compared to that of MS791 twin skeg's stern flow pattern (Sakamoto et al., 2013) to see if the tendencies in flow pattern existed for the simulation. This was as a result of lack of TSLNG experimental flow field data. The dimensions of MS791 are 196.2m in length, 42.809m in breadth and 10.7m draught, with a scaling ratio of 1:36.126.

6.2.2 Model domain and boundary conditions

The boundary condition and mesh strategy used are similar to that of the MOERI scale in chapter 5, but the domain width and depth were both extended by 2m to accommodate the bigger hull. Since the maximum Froude number for TSLNG was 0.2, it was decided not to include the influence of free surface in the computation. This assumption is supported by Bertram, (2000) and also finding from the chapter 5 which showed little difference in resistance parameters when using a double body approach and considering the effect of free surface for Fn = 0.202. It should be noted that comparison between double body approach and the use of free surface at Fn = 0.202 was not assessed for self-propulsion simulations in Chapter 5.

6.2.3 Grid generation

The grid generation process used exactly matched that as described in chapter 5, with most of the grid being clustered around the stern region, propeller plane and bow.

6.2.4 Grid sensitivity

Due to the lack of available experimental data, a grid based error and uncertainties based on Stern et al. (2001) is not applicable. However, table 6.3 shows the predicted total resistance coefficient, form factor and frictional resistance coefficient for the different grids at Fn = 0.197. The wave resistance used as part of the calculation to find the total resistance coefficient follows from an existing non-linear potential flow code (Couser et al., 1998). The form factor and total resistance shows oscillatory convergence whilst that of the skin friction demonstrates converging condition.

Table 6.1: Principal dimensions of TSLNG model, rudder and propeller.

Dimensions	Model scale
L_{PP} (m)	9.0767
B (m)	1.3716
D (m) loaded/ballast	0.3650/0.2485
C_B	0.7360
Rudder type	balanced rudder
Rudder profile	based on NACA0020
Lat. area (m^2)	0.0607
Longitudinal separation (X/D)	0.2600
Rudder aspect ratio (m)	1.8700
Propeller type	CP
Number of blades, N	5.0000
Diameter (m)	0.2000
P/D at 0.7R	1.0000
Ae/Ao	0.700
Rotation	inwards
Hub ratio	0.227

Table 6.2: Simulation flow conditions

Test	Loaded	Ballast
Base Design		
Resistance	Fn = 0.159-0.207	Fn = 0.162-0.211
Self-propulsion	Fn = 0.159-0.207	Fn = 0.162-0.211
Parametric studies		
Self-propulsion	Fn = 0.197	Fn = 0.201
Improved Design		
Resistance	Fn = 0.159-0.207	Fn = 0.162-0.211
Self-propulsion	Fn = 0.159-0.207	Fn = 0.162-0.211

Table 6.3: Grid sensitivity studies

Variable	Coarse Mesh	Medium Mesh	Fine Mesh
Total number of cells	1.8M	4.5M	9.0M
BlockMesh refinement	20×10×5	28×14×7	40×20×10
C_T	2.73×10^{-3}	3.08×10^{-3}	3.04×10^{-3}
C_F	3.13×10^{-3}	2.74×10^{-3}	2.64×10^{-3}
(1+k)	1.14	1.16	1.15

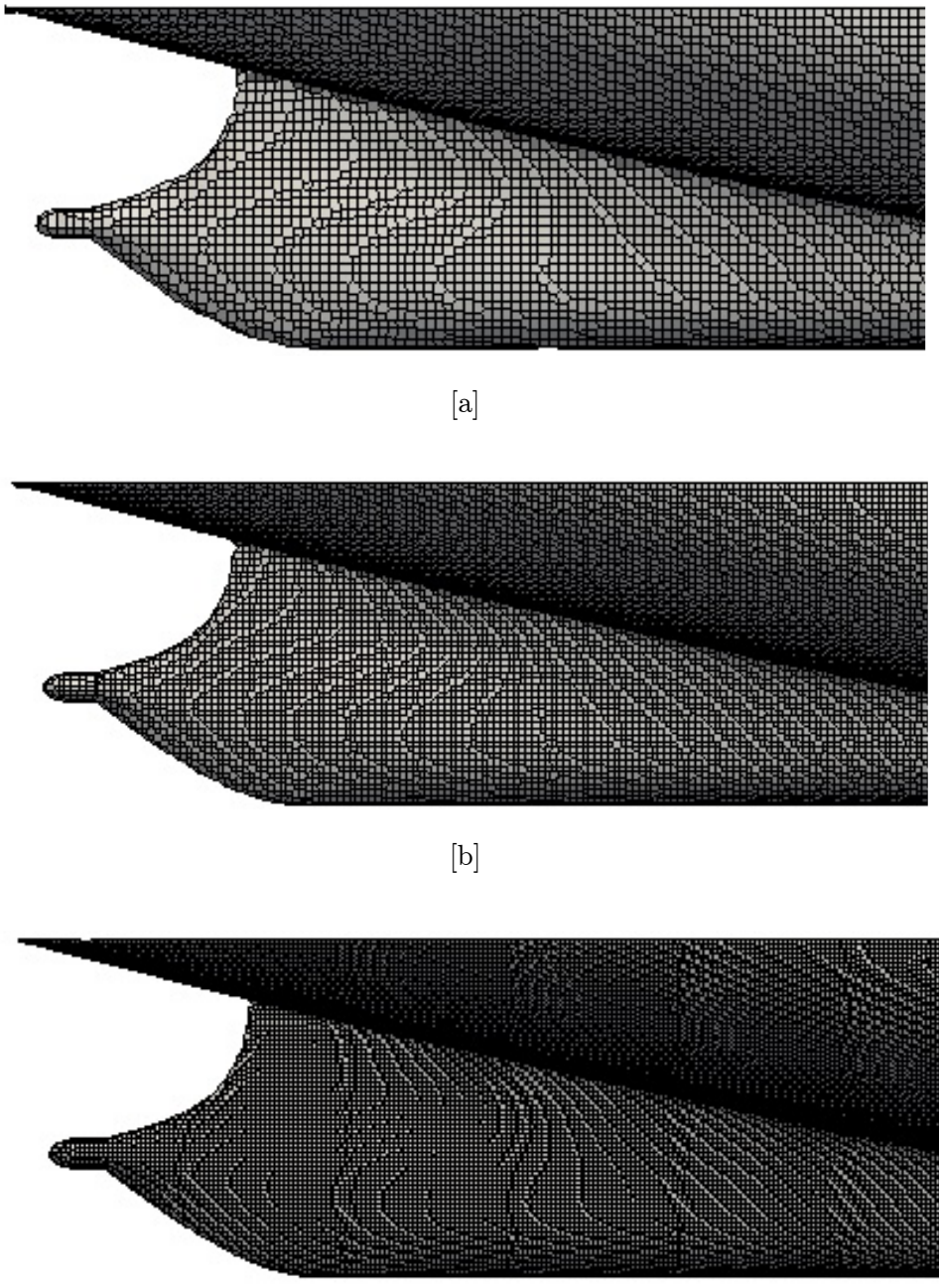

[a]

[b]

[c]

Figure 6.3: Mesh cut showing [a] coarse mesh stern, (1.8M cells overall) [b] medium mesh stern, (4.5M cells overall) [c]fine mesh stern, (9.0M cells overall).

6.3 Results of base case

6.3.1 Resistance predictions for barehull and rudder

Accurate modelling of the hull boundary layer and the circulatory flow around the skegs of a twin skeg ship in towed condition is of upmost importance since these features are used in predicting the inflow to the propeller plane. A long run was performed for TSLNG in the towed condition starting from rest with a time step $\delta t = 1 \times 10^{-3}$ to damp out any blockage due to the outer boundaries and to ensure a fully developed stern wake field. Here base case signifies all conditions before improvements were made. As mentioned in the beginning, the stern flow field was compared with MS791 twin skeg ship. Figure 6.4a presents the computed axial velocity distribution at the propeller ($x/L_{PP} = 1.2526$). For the axial velocity distribution, the computed results show the bent contour of low velocity region behind the skeg. This compares well with that of MS971, a twin skeg ship which employs a podded propulsor (Sakamoto et al., 2013). The contour is more rolled up inward than that of TSNLG. This is due to the differences in skeg geometries. By illustrating the propeller disc by a circle in Figure 6.4, it can also be observed that the axial velocity is approximately three quarters of the ships speed over greater portion of the propeller disc. This is very important from a propulsive efficiency point of view as this determines the propeller performance. The calculated frictional resistance coefficient, C_F, was 2.65×10^{-3} compared to the ITTC friction line[11] of 2.82×10^{-3}.

A disadvantage with the equipment of skegs is that they have high wetted surface area, hence increasing frictional resistance (see chapter 2). But as may be seen from the streamline plot in Figure 6.5a&b, the presence of the skeg provides pre swirl to the propeller. This is advantageous for the propeller performance as it can contribute to improve the propeller efficiency, thus compensating for the increase in friction resistance.

Table 6.4 shows the resistance components at Fn = 0.197 for bare hull and with rudder. It can be seen from the table that the inclusion of the rudders increases the total drag and the towed power by 1.1%. A combined plot of the total drag, viscous drag and the effective power for different speed range and operational draft is presented in Figure 6.6 where an increment of 20W (average) of power is consumed from one speed to another on full load. A detailed breakdown of the resistance test for other speed conditions can be found in Table 6.7 and Table 6.10 respectively.

[11] ITTC formula for frictional resistance coefficient, $C_F = \frac{0.075}{(\log_{10} Rn - 2)^2}$

Table 6.4: Resistance component for Fn = 0.197, Loaded draught condition

Variable	Barehull	Barehull and rudder
C_T	3.016×10^{-3}	3.049×10^{-3}
C_F	2.614×10^{-3}	2.647×10^{-3}
C_R	0.402×10^{-3}	0.402×10^{-3}
P_E (W)	154.246	155.960
(1+k)	1.12	1.15

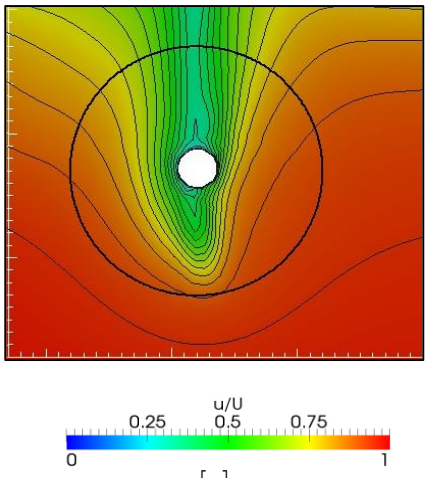

[a]

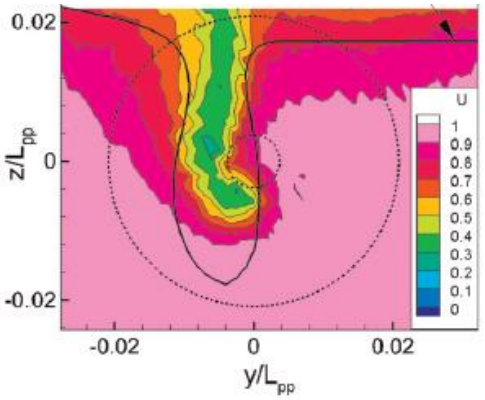

[b]

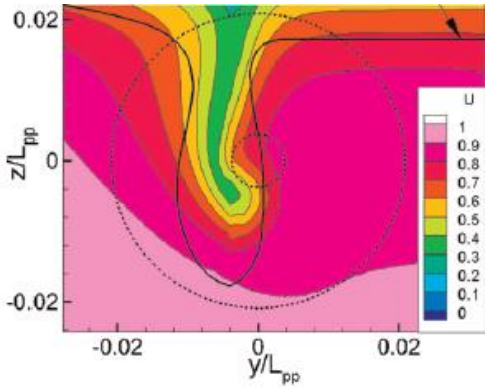

[c]

Figure 6.4: Comparison of velocity distribution at propeller plane for [a] fully loaded draught, Fn = 0.197 with rudder and [b&c] experiment and CFD computation respectively of MS971, Sakamoto et al. (2013), Fn = 0.235.

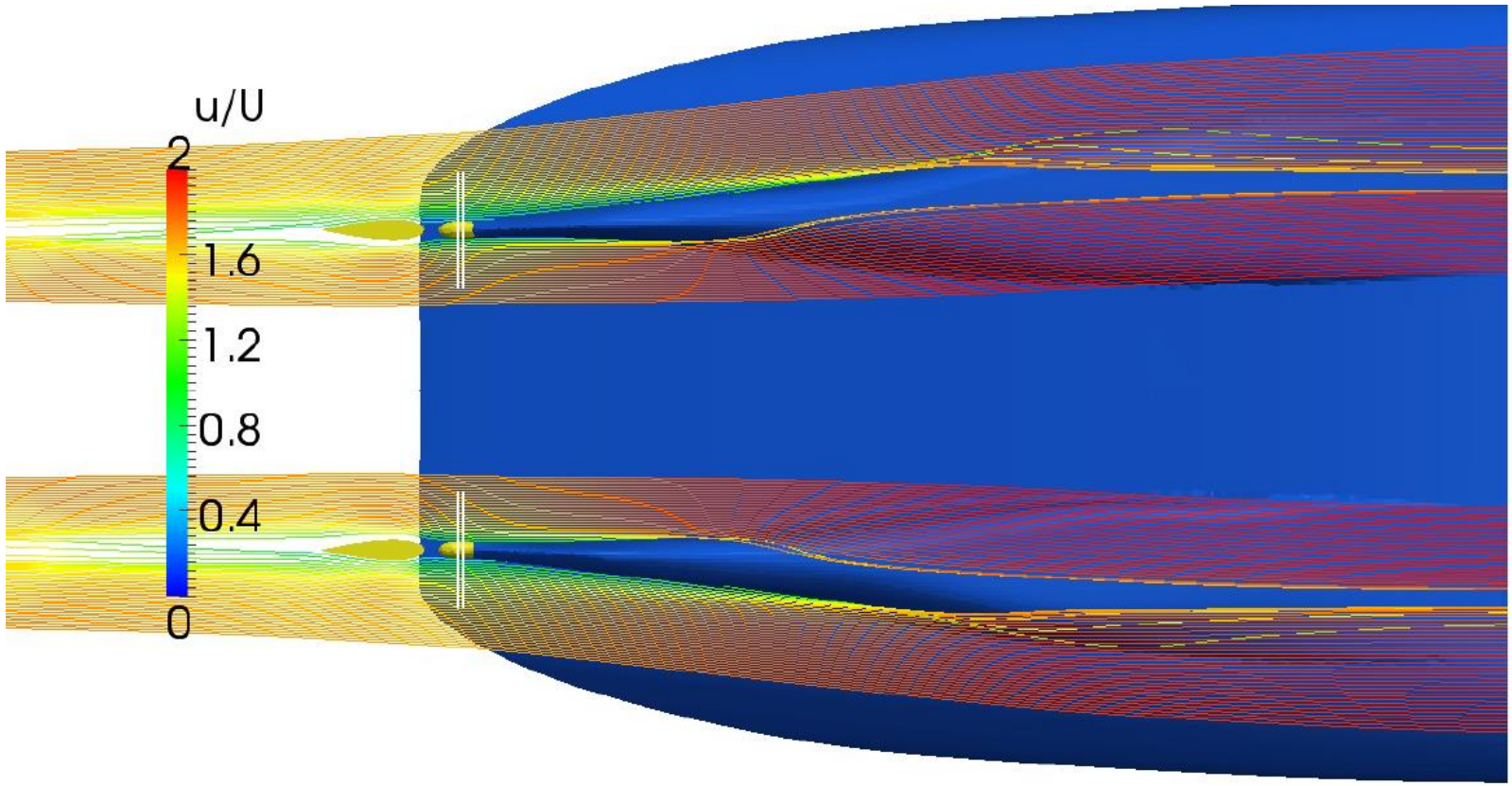

Figure 6.5a: Streamlines passing through twin skegs at loaded draught, Fn = 0.197 (view from bottom).

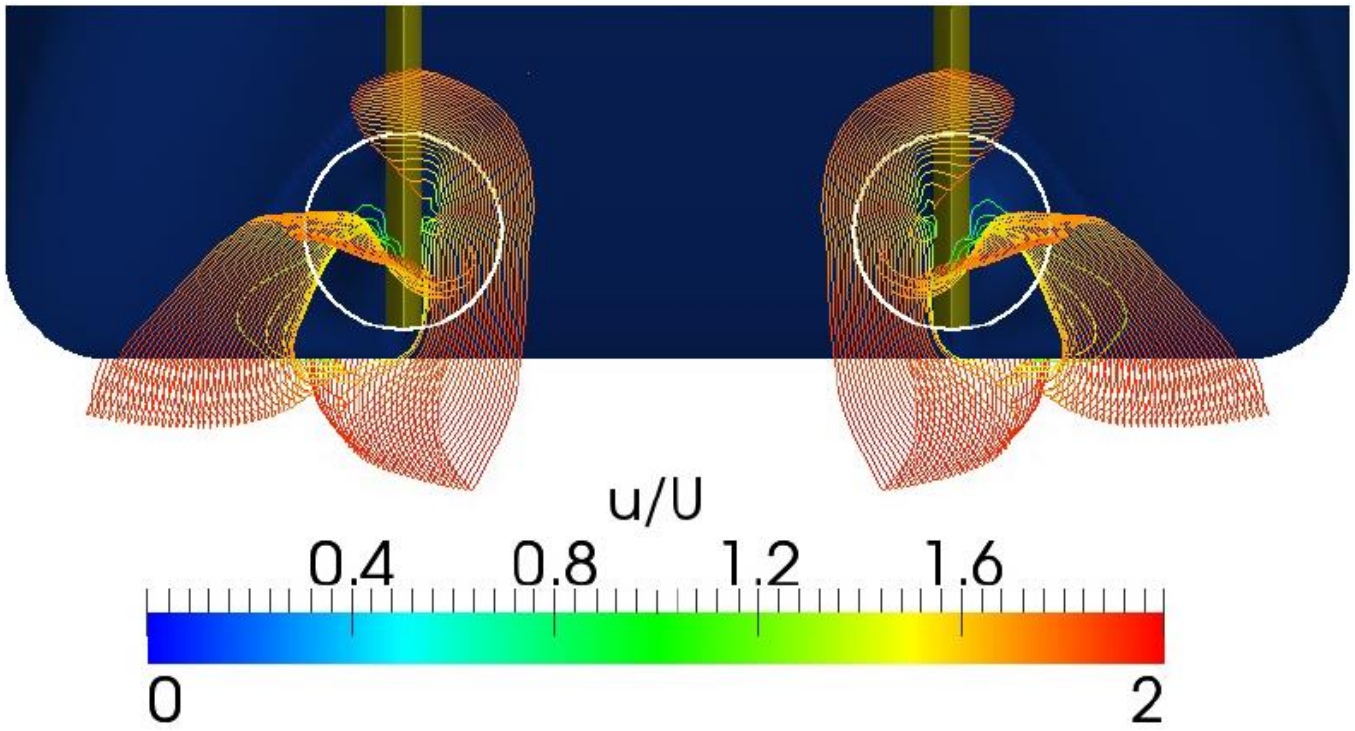

Figure 6.6b: Streamlines passing through twin skegs at loaded draught, Fn = 0.197 (view from stern).

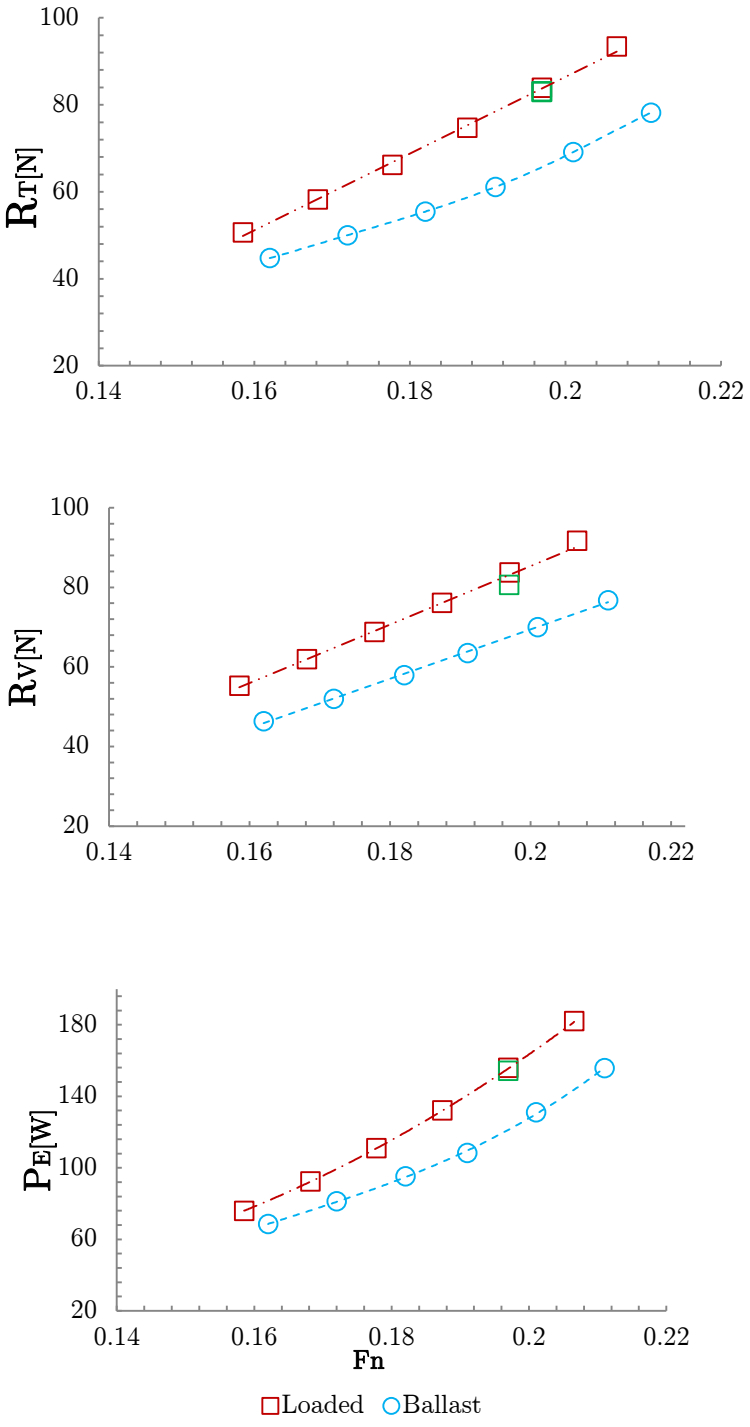

Figure 6.7: Comparison of resistance components, R_T, R_V and P_E, at various Fn range for loaded and ballast design draught conditions for hull and rudder. Green squares signify barehull only (no rudder) parameters for loaded condition at Fn = 0.197.

6.3.2 Self-propulsion simulations

The self-propulsion point is realised by repeating the RANS-BEMt (see chapter 3) iteration loop and manually adjusting the rpm until the self-propelled thrust is equal to the self-propelled drag or the difference between the self-propelled thrust and the self-propelled drag is less than 0.1. The thrust deduction can then be deduced at this point from:-

$$t = 1 - \frac{R}{T_{sp}} \tag{6.2}$$

A sensitivity studies was carried out to determine the impact on thrust deduction when the self-propelled thrust is over-predicted. This procedure was carried out by running self-propulsion simulations and manually adjusting the rpm until the self-propelled thrust (T_{sp}) is equal to the self-propelled drag (R_{sp}) or T_{sp} - R_{sp} = 0. The thrust deduction (t) is then deduced from equation 6.2. Thrust deductions were also deduced from different errors (T_{sp} - R_{sp} = 0.1, 0.4, 0.5, 0.7 and 2.7) and plotted. The combined plot is shown in Figure 6.7. From the plot, it can be seen that a linear relation exist between self-propelled thrust prediction and its impact on thrust deduction. For example from the results, an error of the self-propelled thrust by say 7% will result in an error in thrust deduction by approximately 7%. It should however be pointed out that this relation has been found based on constraints placed on the hull and the use of nominal wake values as input to the BEMt propeller code.

Existing empirical method of determining the thrust deduction of twin screw ship is by the use of Holtrop (1986) regression formula[12]. This was assumed applicable for twin skeg ship. Self-propulsion simulations were conducted at five different TSLNG ship draught of T = 0.249m, 0.364m, 0.437m, 0.583m and 0.729m corresponding to breadth-draught ratios of B/T = 5.520, 3.759, 3.136, 2.352 and 1.882 after which the thrust deductions were then deduced. The results were compared to the Holtrop thrust deduction regression formula. Figure 6.8 compares the trend in thrust deduction for TSLNG for the various draught conditions to that of Holtrop (1986). It can be seen from the results that depending on the breadth-draught ratio, Holtrop (1986) can overestimate the thrust deduction which is very useful to be borne in mind when using the Holtrop (1986) as first estimate in an initial design stage.

Axial velocity distributions along various locations of the hull in both loaded and ballast condition were taken at the self-propulsion point. Figure 6.9 shows one such plot at 0.9D

[12] $t = 0.325C_B - 0.18885D_P/\sqrt{(BT)}$ where B is the ship's breadth, T is the draught, D_P is the propeller diameter and C_B is the block coefficient.

and 1.0D upstream of the propeller plane for Fn = 0.197. It is interesting to note that on the loaded draught for 0.1D the rotation induced by the propeller leads to a slight symmetry. Tables 6.8-6.9 and 6.11-6.12 shows the self-propulsion parameters for TSLNG for different speed ranges in loaded and ballast condition respectively. The K_T and K_Q at self-propulsion point decrease with increasing Rn due to the reduction in local section drag coefficient. This is because K_Q is dependent on the local section drag coefficient C_D. Propeller efficiency therefore increases with propeller Rn.

In most single screw and twin screw ships an upward flow exists at the aft end which leads to an axial flow component plus a tangential flow component (Molland et al., 2011). The influence of tangential wake (see Figure 6.11) was investigated for TSLNG. The location of the cuts for the plots is shown in Figure 6.10. The results shows that by considering the upward flow the true axial velocity component, v_a, is slightly over-predicted, both the radial and tangential components of wake are modified. This can have effect on the thrust deduction and hence the propulsive efficiency. Tangential flow effects from the plots were found to be small hence was neglected for all subsequent computations.

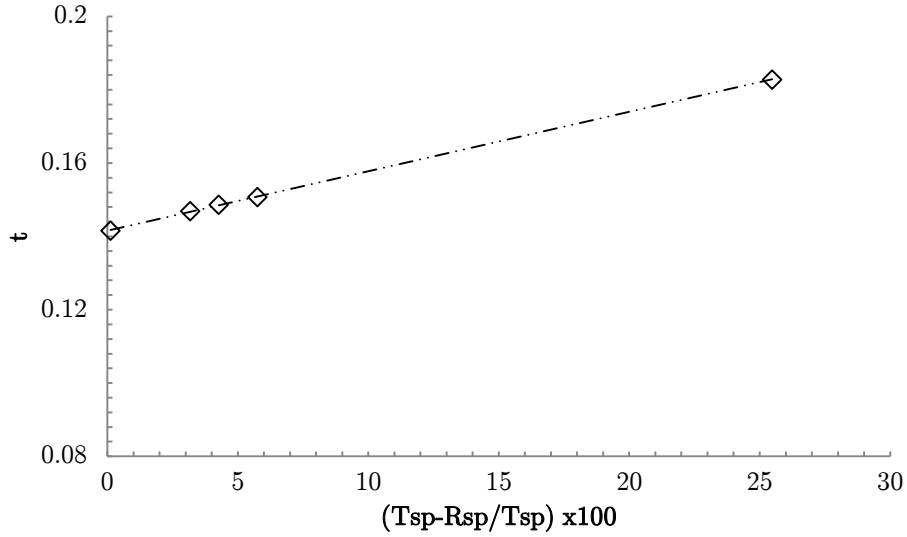

Figure 6.8: Error margin in thrust deduction prediction.

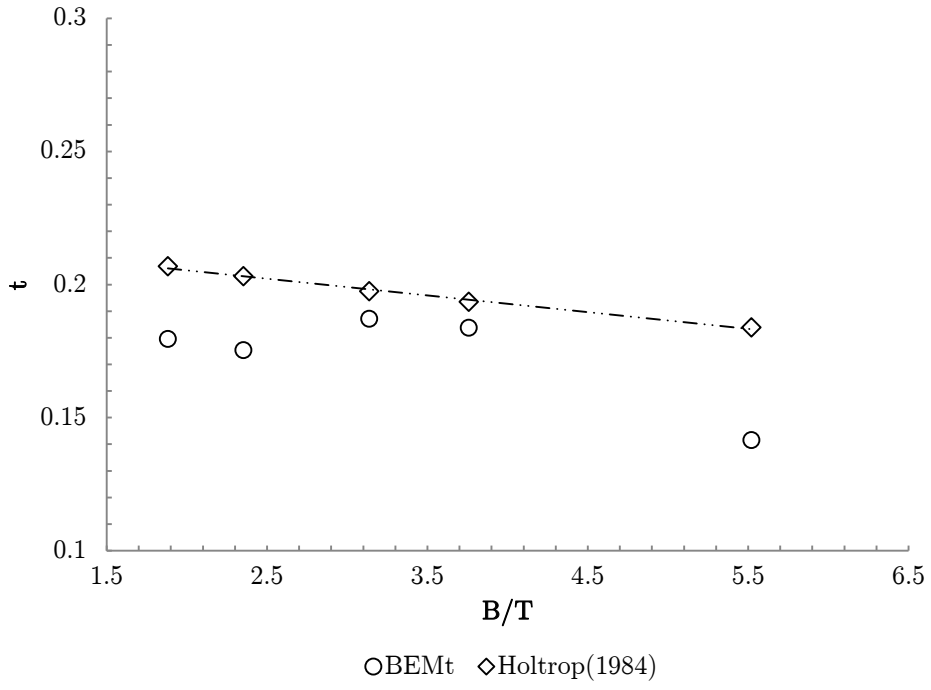

Figure 6.9: Comparison of calculated and empirical thrust deduction, (t) for different draft conditions, fixed hull and rudder at even keel

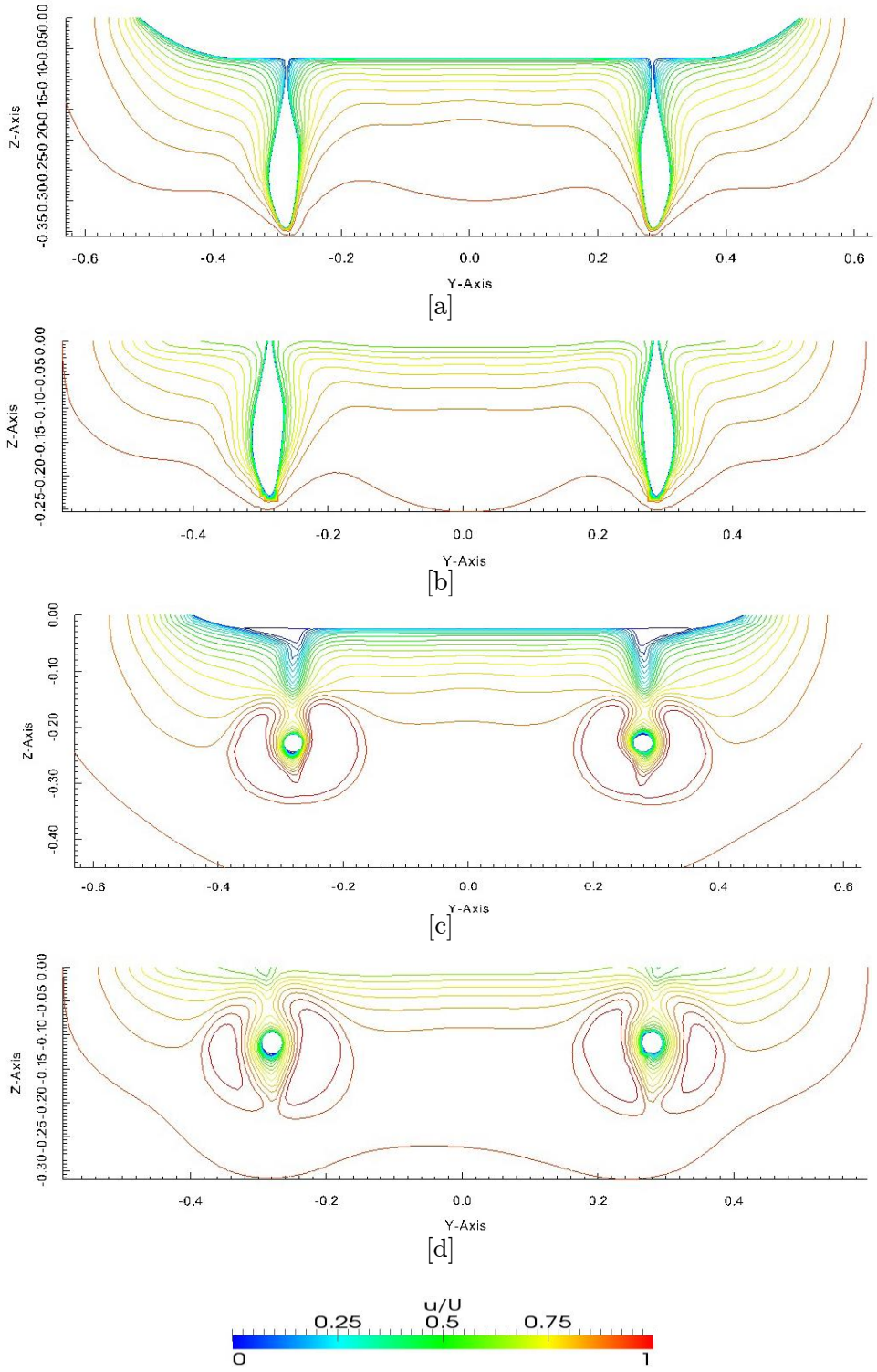

Figure 6.10: Axial velocity field (u contour) at self-propulsion point, 0.926D upstream of propeller plane, [a] loaded draught [b]ballast draught and 0.1D upstream of propeller plane, [c] loaded draught [d]ballast with inwards rotating propellers.

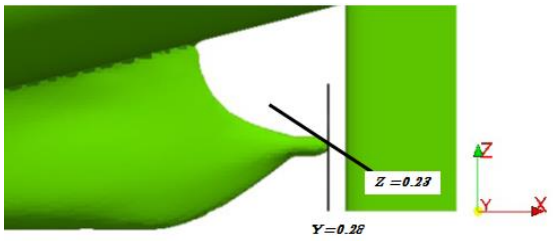

Figure 6.11: Wake cut location for plots of velocity at 0.18D behind propeller plane

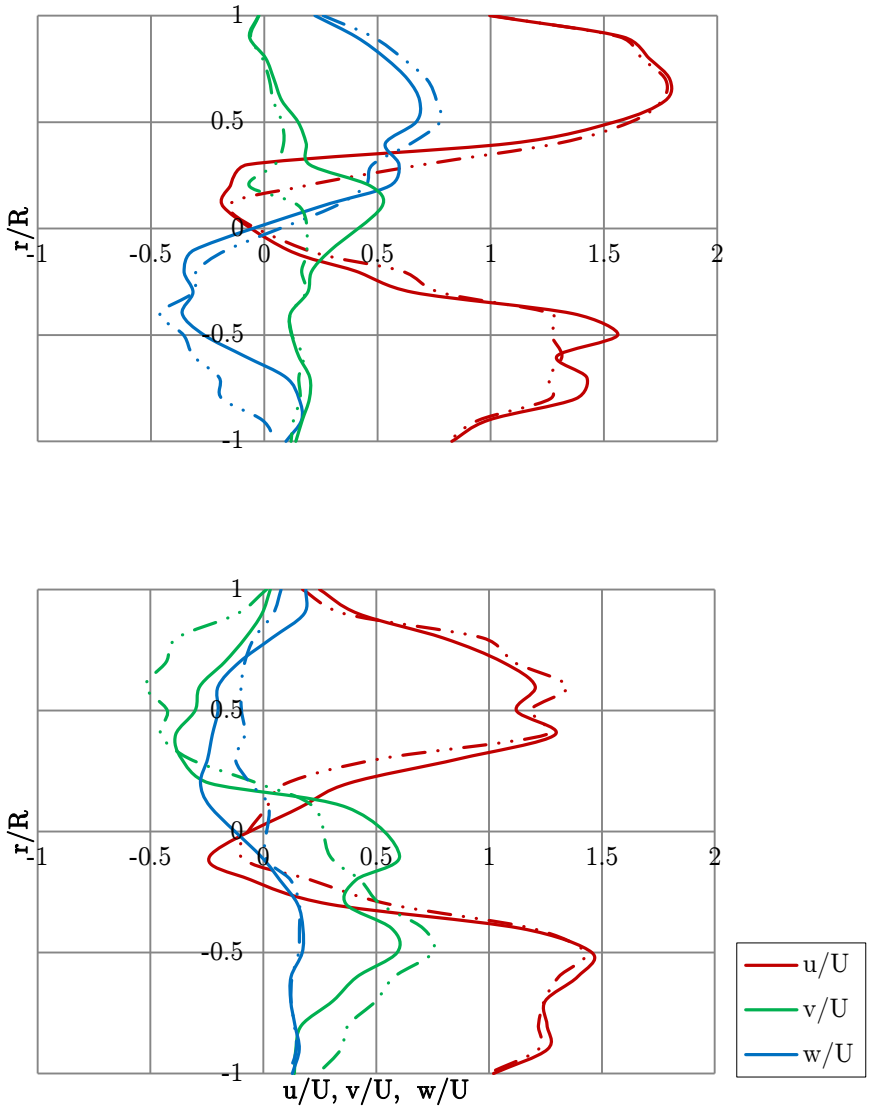

Figure 6.12: Wake cut at 0.18D behind propeller plane [top] fixed z and varied y [bottom] fixed y and varied z, for loaded draught condition, port side propeller. NB: solid lines represent the addition of tangential wake effect and dotted lines represent no addition of tangential wake effect.

6.4 Parametric studies

Parametric studies were conducted in order to establish the best combination of propeller diameter, pitch ratio, rudder location and rotational direction to satisfy the operational profile of the ship.

6.4.1 Pitch diameter ratio influence on thrust deduction

Different pitch ratios ranging from P/D of 0.6 to 1.2 were selected to determine their impact on thrust deduction. The studies were carried out both in the loaded and ballast condition at Fn = 0.197 and Fn = 0.201 respectively. Figures 6.12 and 6.13 shows the results from the study for loaded and ballast draught respectively. The red values in the plots indicate the base case pitch ratio of the propeller which is P/D=1.0. From the results it can be seen that there is not a significant change in thrust deduction when the pitch ratios are varied. The hull efficiency curve follow the same trend as the thrust deduction curve, however there is a significant variation in the behind efficiency curve which shows that the behind efficiency increases as the pitch ratio decreases until P/D = 0.8 after which further decreasing the pitch ratio has no impact on the behind efficiency. The reason for the variation in the behind efficiency plot is mainly driven by the open water efficiency as shown in Figure 6.14. As the pitch ratio is reduced the load distribution from one radius to another also reduces hence the propeller works in a smaller race and the operating point of the propeller shifts to a point of higher efficiency.

Figure 6.15 shows the axial velocity plot taken at various cuts (see Figure 6.10) behind the propeller plane for various pitch-diameter ratios. It is interesting to note how the hub vortices modify the shape of the curves, with the strength of the vortices increases as the P/D increases.

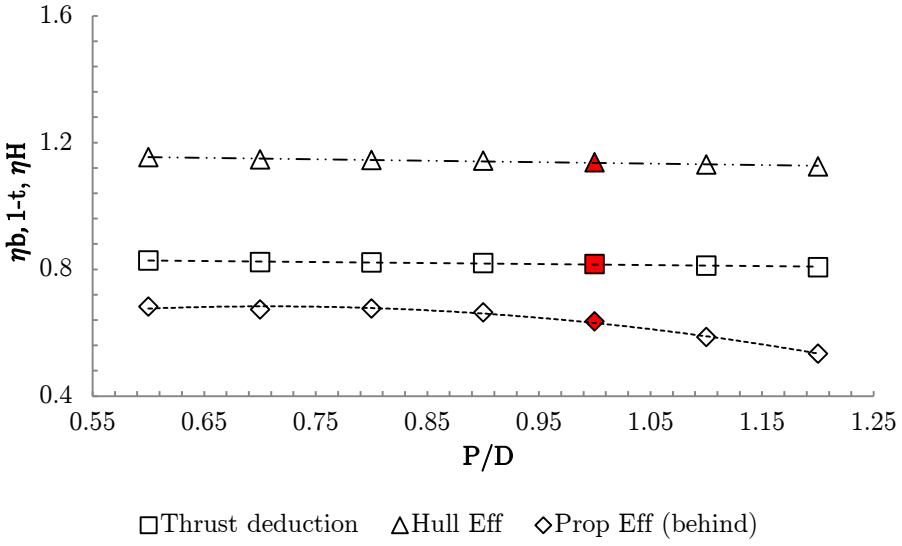

Figure 6.13: Effect of propeller model's pitch diameter ratio variation on self-propulsion coefficients, (analysis based on nominal wake values) for loaded condition, red values highlights base case, Fn = 0.197.

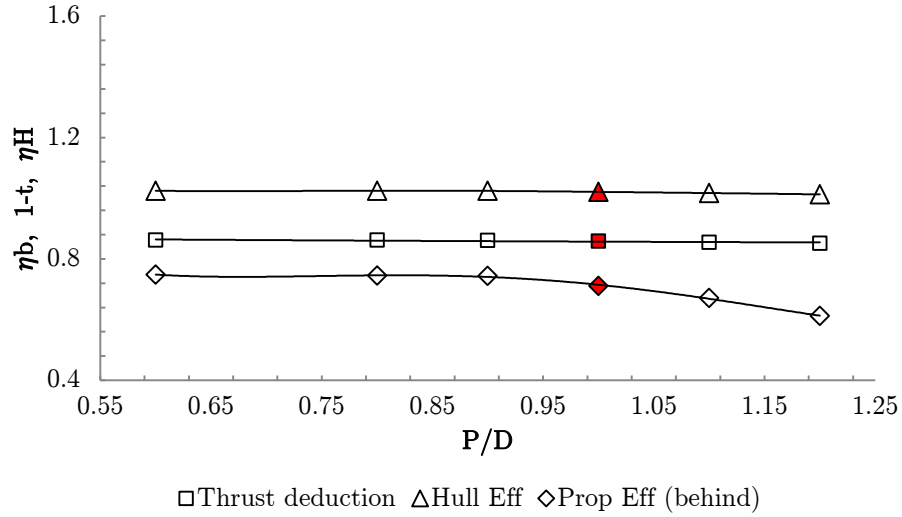

Figure 6.14: Effect of propeller model's pitch diameter ratio variation on self-propulsion coefficients (analysis based on nominal wake values) for ballast condition, red values highlights base case, Fn = 0.201.

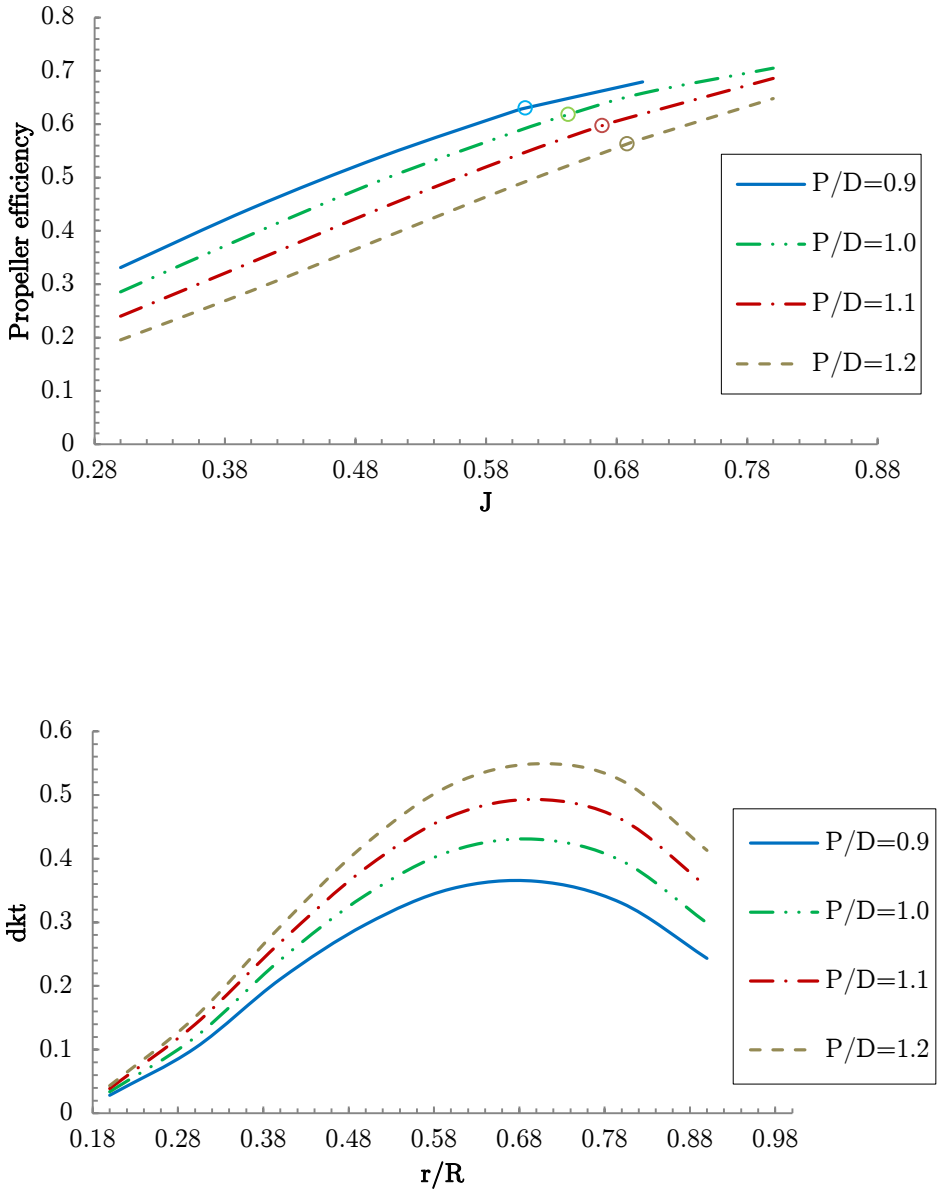

Figure 6.15: Effect of P/D variation on (top) propeller efficiency where the circles on plot are the propeller operating points and (bottom) thrust distribution along the blade at 0.7R, loaded condition.

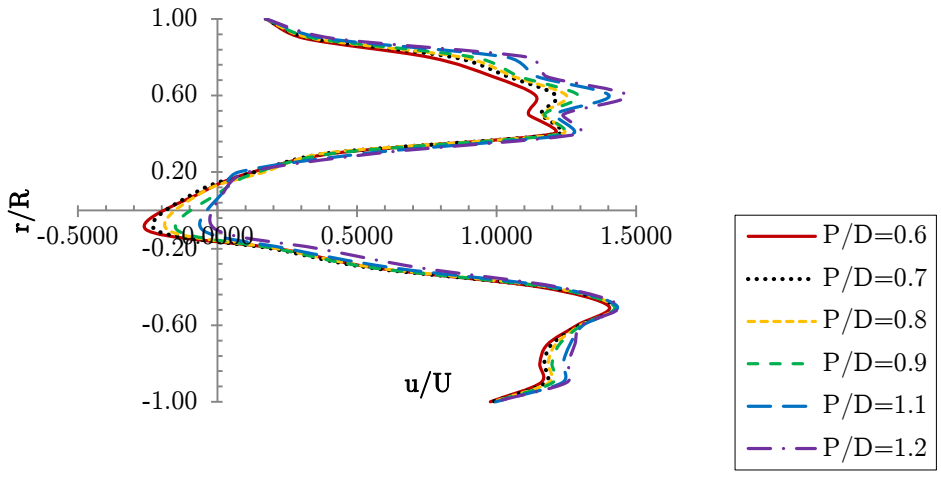

[a]

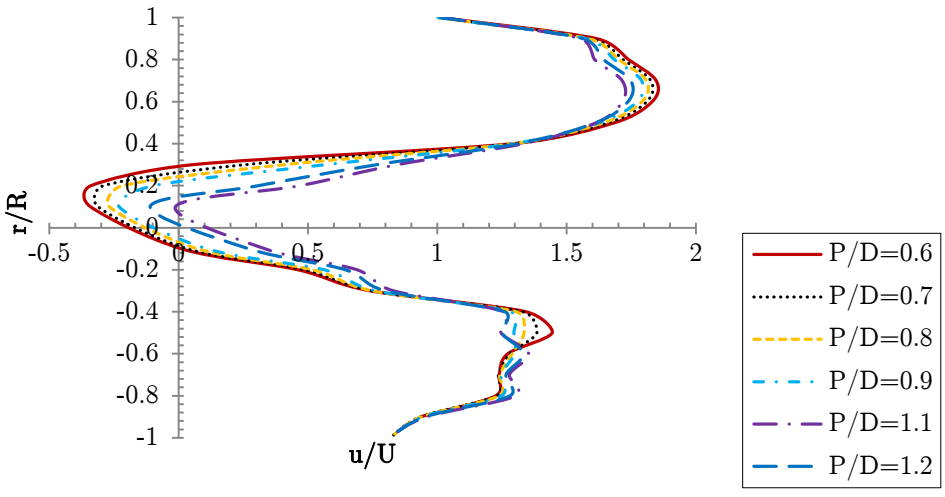

[b]

Figure 6.16: Axial velocity plot at 0.18D behind propeller plane for various pitch-diameter ratios at [a] fixed z and varied y [b] fixed y and varied z, port side for loaded condition.

6.4.2 Propeller diameter influence on thrust deduction

The choice of propeller diameter was made on the basis of optimum efficiency for the geometrical constraints. Four propeller diameters (D_p =0.18m, 0.19m, 0.20m and 0.22m) were chosen for this study. This was because due to the design draught conditions of TSLNG any increment in diameter above 0.22m will result in ventilation issues at level trim ballast draught. The studies were carried out at the same Fn as the P/D studies both in the loaded and ballast condition. If the wake of the hull is adapted to the propeller, then it can be said that circumferential average wake values tends to be higher near the boss and hence average η_H values increases as the propeller diameter is reduced. Likewise the η_B increases with increase in propeller diameter. This tendency can be seen in the plots in Figure 6.16-6.17. The average rps at self-propulsion point for the different propeller diameters in the loaded and ballast conditions 14.8 and 13. 6 respectively.

Figure 6.18-6.19 illustrates plots for propeller diameter against propeller efficiency for both loaded and ballast conditions. Figures 6.20a&b also illustrates the axial velocity distribution for the various propeller diameters, which shows that the propeller race reduces as propeller diameter increase.

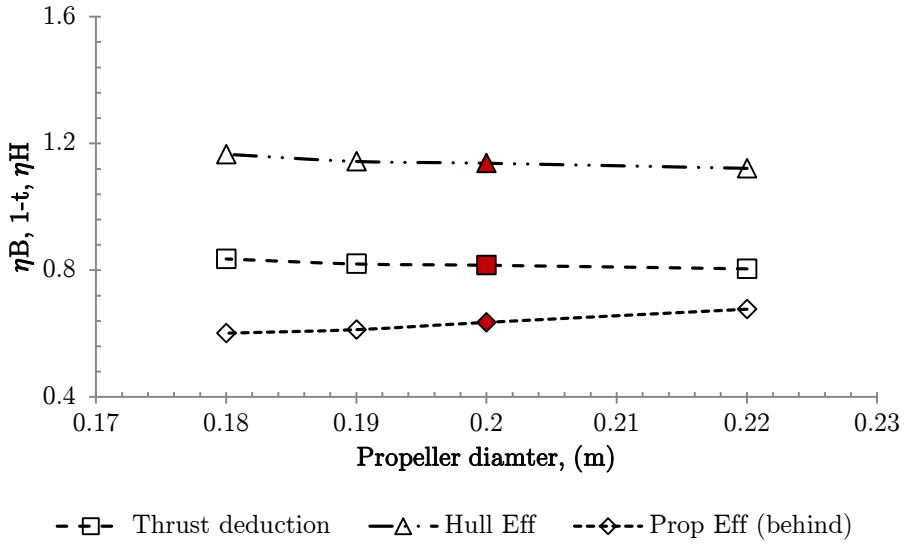

Figure 6.17: Effect of propeller diameter variation on self-propulsion coefficients, for loaded condition, red values highlights base case.

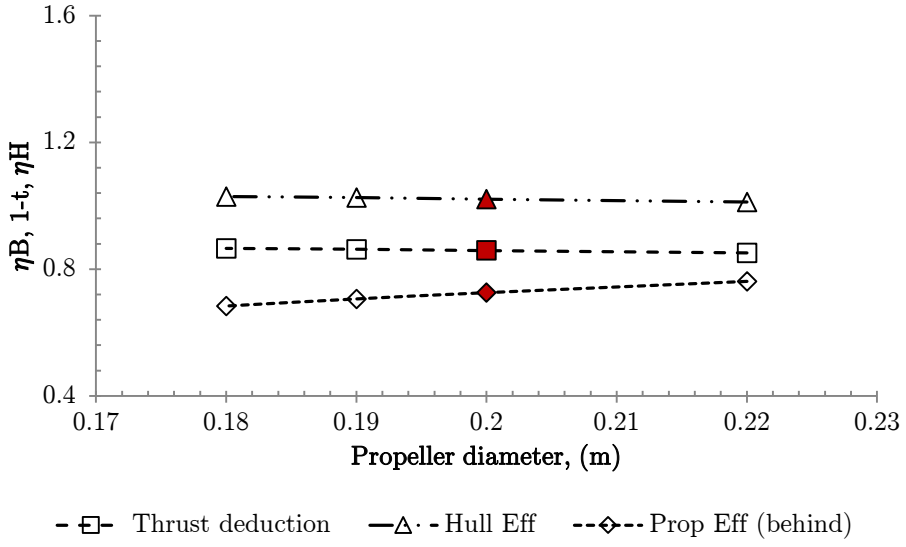

Figure 6.18: Effect of propeller model's diameter variation on self-propulsion coefficients, for ballast condition, red values highlight base case, red values highlights base case.

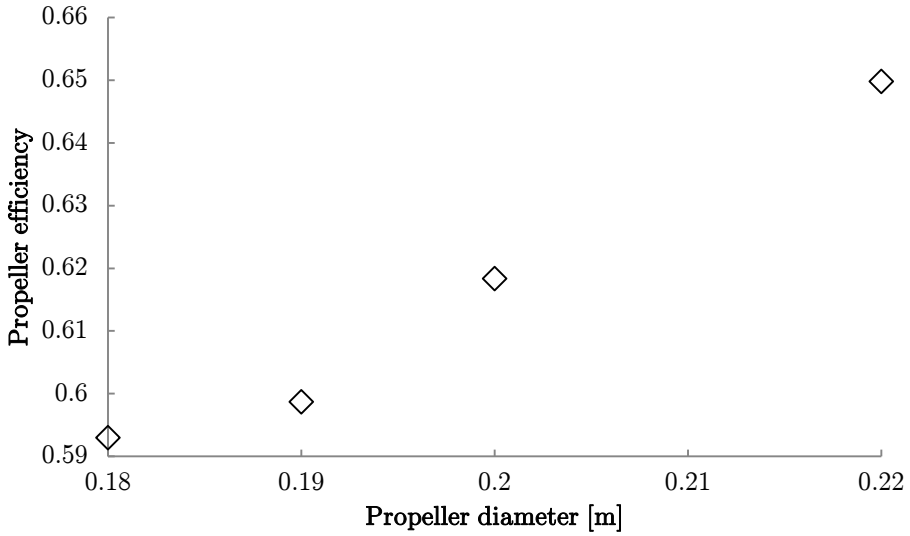

Figure 6.19: Effect of propeller diameter variation on propeller efficiency in fully loaded condition, Fn =0.197.

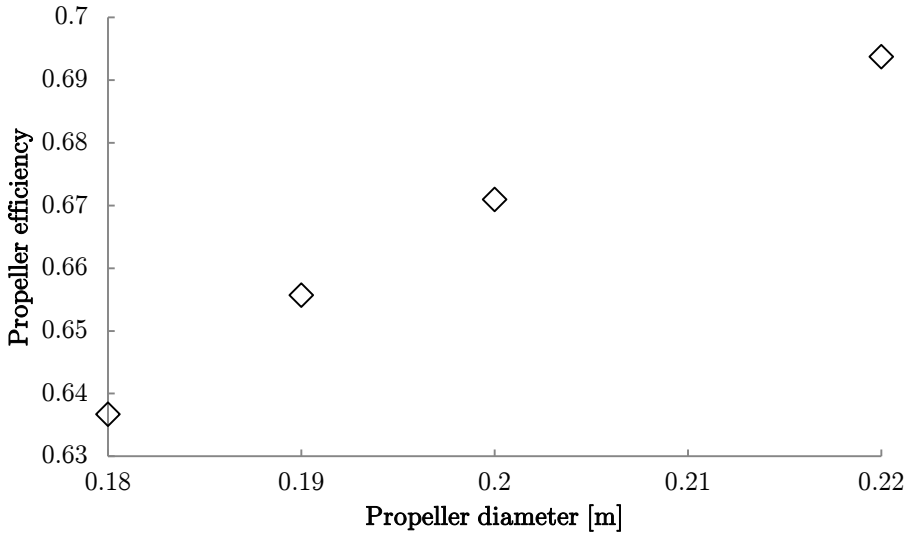

Figure 6.20: Effect of propeller diameter variation on propeller efficiency in ballast condition, Fn = 0.201.

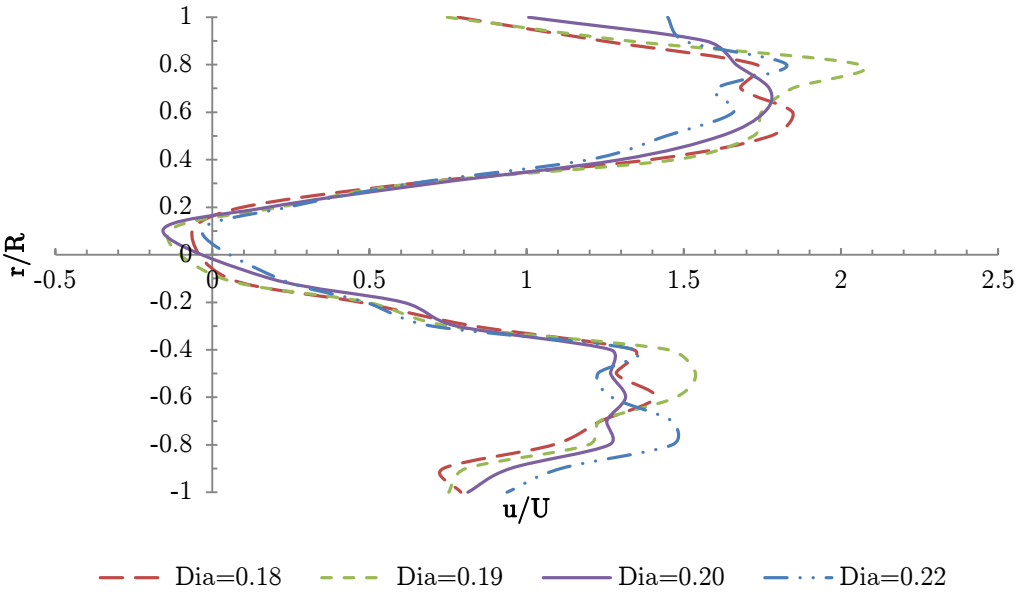

[a]

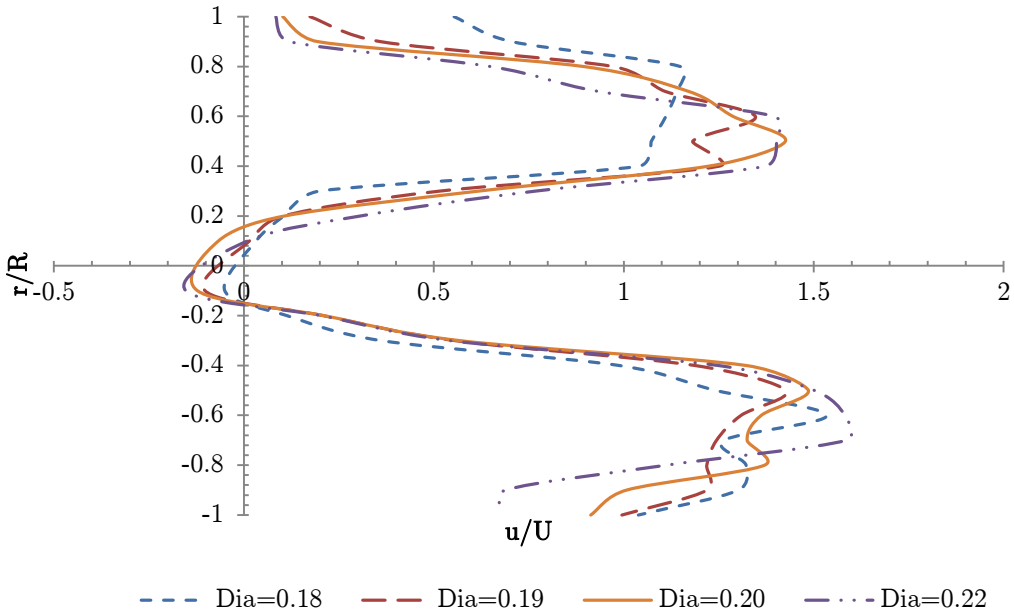

[b]

Figure 6.21: Axial velocity plot at 0.18D behind propeller plane for various propeller diameters (in metres) at [a] fixed z and varied y [b] fixed y and varied z, port side, for loaded condition.

6.4.3 Rudder lateral separation influence on thrust deduction

Studies carried out in Appendix 2 and chapter 4 shows that the geometrical arrangement of the rudder, propeller and the hull can have significant influence on both manoeuvring and propulsion performance. Usually the effect of the hull and skeg is to slow down the flow into the propeller, whilst the propeller accelerates and rotates the flow unto the rudder, affecting its performance. The rudder location also influences the upstream propeller skeg and hull and the overall-propulsive effect of the hull-skeg-propeller-rudder combination. It is therefore important that an overall rudder position is sought which satisfy propulsion, fuel and speed and also ensure that the vessel is manoeuvrable. For twin skeg arrangements there is normally more freedom in the siting of the rudders relative to the propeller and skeg. A wide range of X/D, Y/D and Z/D are usually employed. The design of TSLNG as already stated is such that the small space at the stern does not provide much scope for performing a longitudinal separation, X/D analysis. On twin screw ships it's been argued by Molland and Turnock (2007) that Z/D values should tend to 1.0 with the rudder tip, coincident with the propeller tip. For this study only Y/D was considered. Aside powering performance, the rudder is offset laterally from the skeg and propeller to enable the tail shaft to be removed from the propeller shaft centreline without removing the rudder. Three tests were carried out:-

1. offsetting both rudders starboard by Y/D = 0.1, 0.2 and 0.3
2. offsetting both rudders inwards by Y/D = 0.1, 0.2 and 0.3
3. offsetting both rudders outwards by Y/D = 0.1, 0.2 and 0.3

The studies were carried out at Fn =0.197 in the loaded draught condition. The results of the three test are shown in Figure 6.21 and Table 6.5 and compared to the base case of placing the rudder directly behind the propeller at Y/D=0. It can be seen from Figure 6.21 that minimum 1-w_t is favoured by placing the rudder directly behind the propeller at Y/D=0. The rudder drag is also reduced.

From Table 6.5 it can be also seen that maximum 1-t is achieved if the rudder is directly placed in the propeller slipstream at Y/D=0. For both starboard and outwards tests the table shows that as Y/D increases, 1-t reduces. There is not much change in 1-t when the rudders are offset inwards. This is confirmed by the wake plots shown in Figure 6.22 which shows a balance in load resulting from the rotation of the propeller for the inwards rudder offset. The direction of propeller rotation was inwards for this study.

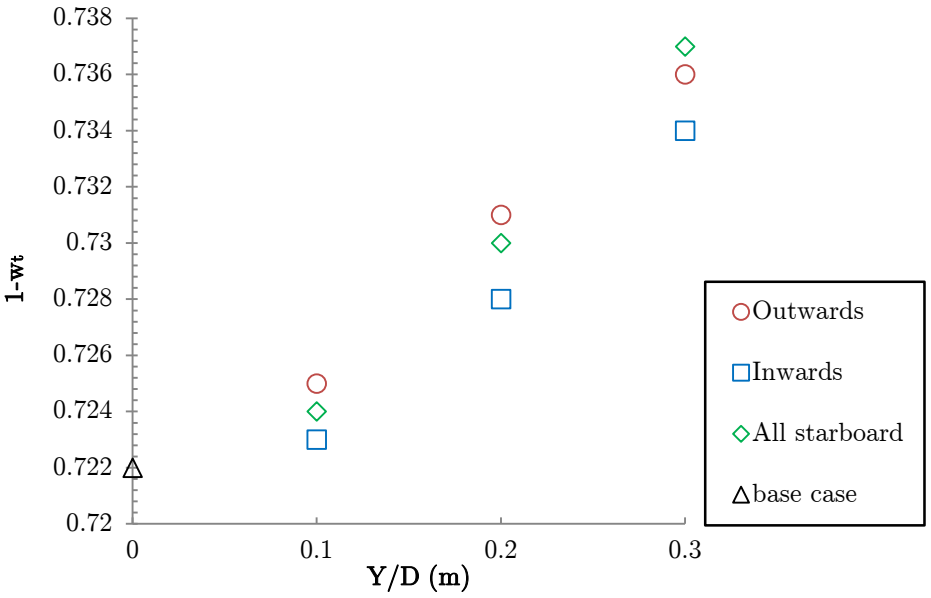

[a]

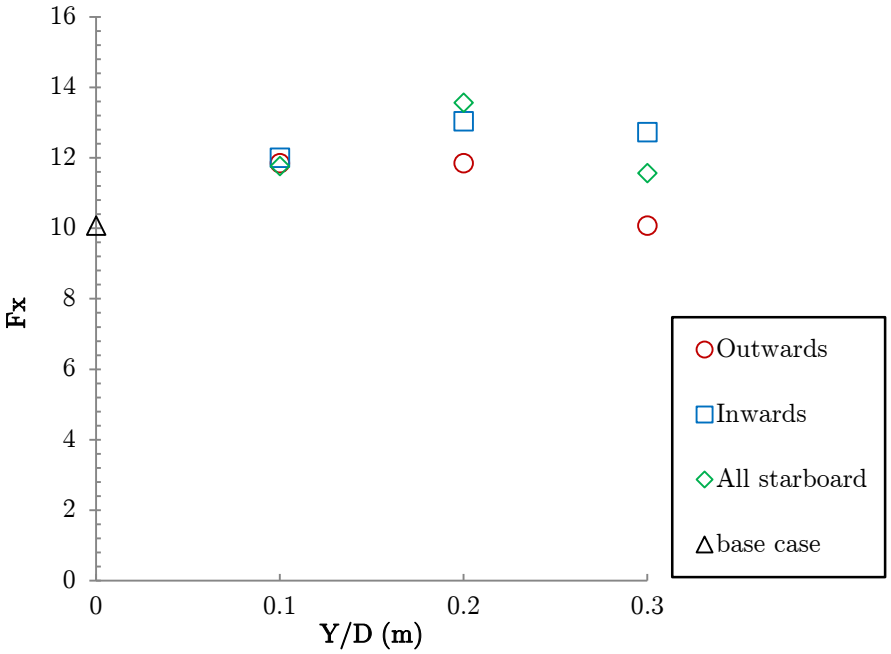

[b]

Figure 6.22: Effect of offsetting the rudder laterally from the propeller shaft centreline on [a] wake fraction and [b] rudder axial force.

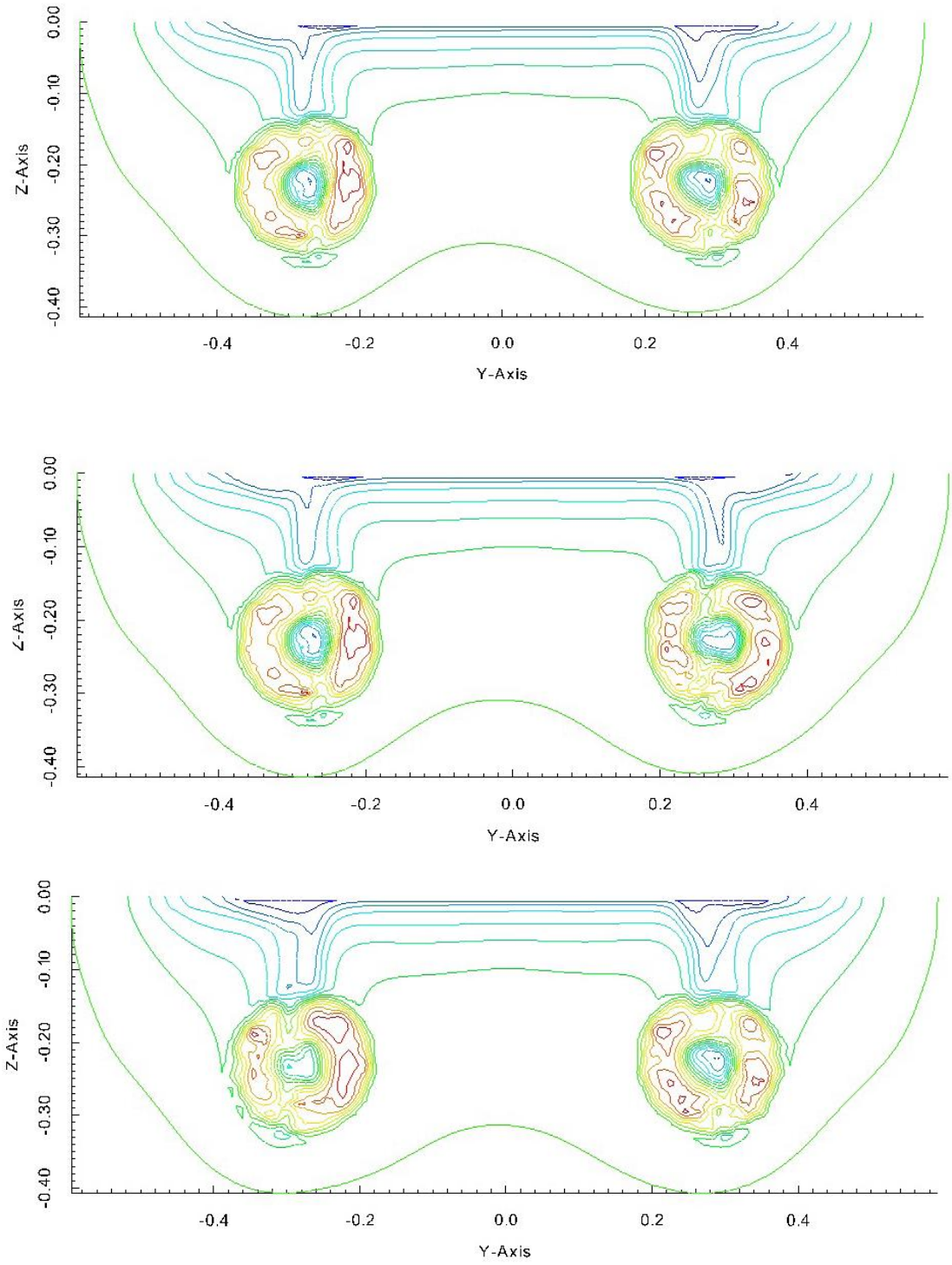

Figure 6.23: Axial velocity field (u contour) at self-propulsion point, 0.25D downstream of propeller plane, [top] both rudder starboard [middle] inwards [bottom] outwards for Y/D=0.2

Table 6.5: Resistance and propulsion parameter for rudder lateral separation (Y/D) studies.

Parameter	Both starboard			Inwards			Outwards			Directly behind propeller
	$0.1D_p$	$0.2D_p$	$0.3D_p$	$0.1D_p$	$0.2D_p$	$0.3D_p$	$0.1D_p$	$0.2D_p$	$0.3D_p$	
Hull drag	102.37	102.75	103.88	101.99	101.71	101.70	102.93	104.06	105.77	102.34
1-t	0.799	0.795	0.790	0.801	0.803	0.802	0.792	0.789	0.781	0.816
1-w_t	0.724	0.730	0.737	0.723	0.728	0.734	0.725	0.731	0.736	0.722

Influence of the direction of propeller rotation

Propulsion performance can be different depending on the direction of rotation of the propeller. To investigate this effect on the twin propellers of the LNG ship, three different tests were carried out as shown below:-

- inwards rotation of both propellers
- outwards rotation of both propellers
- inwards rotation of the port propeller and outwards rotation of the starboard propeller

Figure 6.23 shows that wake gain was made with inwards rotation of the propellers.

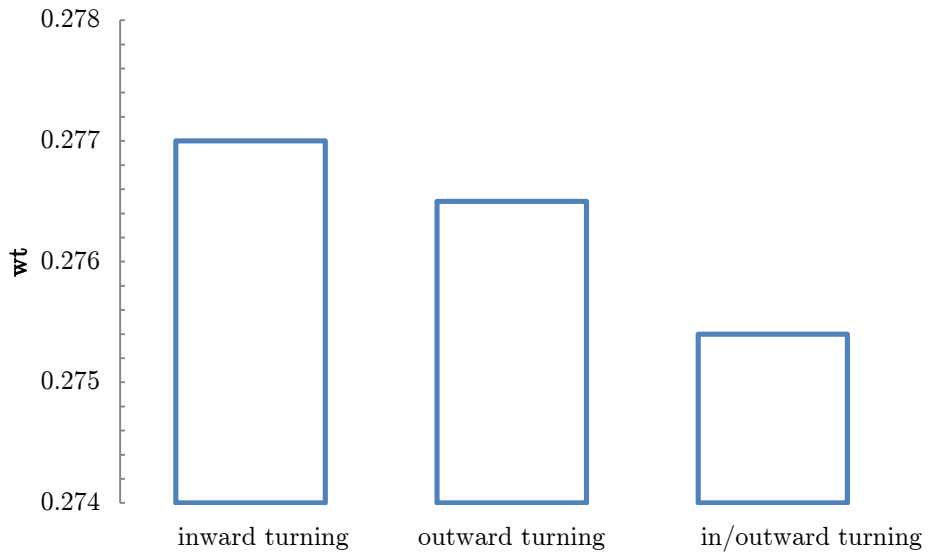

Figure 6.24: Differences between wake fraction for inward, outward and inward-outwards propeller rotation for rudder Y/D=0, zero rudder angle, Fn =0.197 at loaded draught condition.

6.5 Improved stern design

Parametric studies have been conducted to search optimal locations to reduce thrust deduction and increase wake fraction in some cases. The studies conducted were based on pitch diameter variations, propeller diameter variations, propeller direction of rotation and rudder lateral separation. The pitch diameter variations demonstrates that as the pitch distribution is reduced the load distribution from one radius to another also reduces hence the propeller works in a smaller race and the operating point of the propeller shifts to a point of higher efficiency. The behind efficiency increased as the pitch ratio is decreased until P/D = 0.8 after which further decreasing the pitch ratio had no impact on the behind efficiency. Ideally it would have been better to repeat this process for a range of blade area ratios in order to find the optimum blade area ratio but work by Carlton (2007) suggests that P/D is relatively insensitive to blade area ratio. The optimum pitch ratio in general is found to be P/D = 0.8.

In the propeller diameter studies, a range of diameters were considered and the results demonstrated that larger diameters propeller provided the best overall behind efficiency. The optimum diameter selected was 0.2m even though a diameter of 0.22 achieved the best behind efficiency for two reasons:-

1. At a diameter of 0.22m the propeller tip to keel clearance is really small (0.019m) which will result in difficulties when taking out the propeller during dry-docking.
2. Since an optimum quasi propulsive efficiency is required a slight reduction in diameter will results in a gain in hull efficiency which more than offsets a loss in behind efficiency.

Only the lateral separation due to the rudder was carried out on the study to determine the rudder location due to the shorter TSLNG hull stern. The maximum X/D that can be accommodated was 0.26m which is about right for twin screw ships. Note that values from Molland et al. (2007) suggest X/D range between 0.25m to 0.70m. No significant wake gain was achieved with this study with the best option found by placing the rudder directly behind the propeller. The optimum design chosen however is to offset both rudders laterally by 0.2D inwards as such an offset enables the tail shaft to be removed without removing the both rudders.

The direction of rotation of the propeller has important consequences for manoeuvring and efficiency considerations for twin skeg ships. From the propulsive efficiency point of view, Carlton (2007) concluded that the rotation present in the wake field due to the flow around the ship at the propeller plane can lead to gains in propeller efficiency when the

rotation direction is opposite to the direction of rotation in the wake field. However in certain circumstances such as cavitation purposes, the propeller rotation can be considered in relation to the wake rotation. The study of the propeller rotation direction was in general found to be preferably inwards. It should however be stated that it does not necessarily mean that all twin skeg ships with inward rotation have the best propulsive performance since it depends on the detailed design of the twin skeg hull form.

Table 6.6 shows the detailed parameters of the optimum stern design. Here the original design refers to the actual TSLNG parameters before the parametric studies. Improved design 1 is the chosen optimum stern design from the parametric studies. Improved design 2 has been added for comparison purposes. The difference between improved design 2 and improved design 1 is mainly on the position of the rudder. Improved design 2 has the rudders directly behind the propeller at Y/D=0.

Table 6.6: Principal dimensions of TSLNG original and improved designs.

Dimensions	Original Design	Improved Design1	Improved Design2
L_{PP} (m)	9.0767	9.0767	9.0767
B (m)	1.3716	1.3716	1.3716
T (m) loaded/ballast	0.3650/0.2485	0.3650/0.2485	0.3650/0.2485
C_B	0.7360	0.7360	0.7360
Rudder type	balanced rudder	balanced rudder	balanced rudder
Rudder profile	symmetric rudder based on NACA0020 sectional profile		
Lat. area (m^2)	0.0607	0.0607	0.0607
Longitudinal separation (X/D)	0.2600	0.2600	0.2600
Lateral separation (Y/D)	0	0.2D inwards	0
Lateral separation (Z/D)	1	1	1
Rudder aspect ratio (m)	1.8700	1.8700	1.8700
Propeller type	CP	CP	CP
Number of blades, N	5.0000	5.0000	5.0000
Diameter (m)	0.2000	0.2000	0.2000
P/D at 0.7R	1.0000	0.8000	0.8000
Ae/Ao	0.700	0.7000	0.7000
Rotation	inwards	inwards	inwards
Hub ratio	0.227	0.227	0.227

Comparison has been made based on the power requirements for a range of speeds and design draught condition for the original and improved designs. Figures 6.24 and 6.25 present the results of interaction parameters and efficiencies. Detailed breakdown of all components of propulsive coefficients for all the speed ranges and draught can also be found in Tables 6.8-6.20. Improved design 1 tends to provide a greater 1-wt than the original design as seen from Figure 6.24. Improved design 2 showed much closer values of 1-t compared to the original design. The behind efficiency of improved design 1 was superior compared to both the original design and improved design 2 in Figure 6.25. Analysis of the source of behind efficiency gain was attributed to the propeller open water efficiency where the propeller works in a much smaller race at that location and the operating point shifts to a J value which provides higher efficiency. The average η_D was improved by 6% compared to the original design which led to an average power

reduction P_D of 5%. The average power reduction computed for improved design 2 was 7%.

6.6 Conclusions

- Resistance and self-propulsion simulations using the RANS-BEMt method have been performed over a range of operational speeds and draught condition for a future twin skeg LNG carrier ship (TSLNG). The iterative solution procedure provides a straight forward approach to determining the self-propulsion of TSLNG based on the wake field.

- Comparison of the flow pattern with other twin skeg ship model showed the ability of the present simulation to reproduce the bent contour of low velocity region behind the skegs. The axial velocity was found to be approximately three quarters of the ships speed over greater portion of the propeller disc. The velocity plots at various cuts showed the trend in axial flow pattern and the skeg pre swirl. The computed nominal wake fractions for the various speeds may be useful in the design of new skeg geometry since together with a plot of the circumferential mean velocity will give an indication of a measure of the hydrodynamic characteristics for example the capability to earn wake gains both in the circumferential and axial directions behind the skegs.

- Comparison of the resistance simulations showed that the friction resistance agreed well with that of ITTC. The rudder drag was found to be mostly dominated by the pressure component whilst that of the hull drag was dominated by the friction component leading to an overall viscous coefficient which decreases with increasing Froude number whilst the total resistance coefficient increases with increasing Froude number over this Froude number (Fn) range.

- In the self-propulsion studies the BEMt propeller was able to predict the thrust, torque and efficiencies and whilst the propeller influence has been averaged over one blade passage which neglects tip and hub vortices, improvements can be made with the use of a finite-bladed theory which would increase the accuracy in the prediction of the propeller performance and its interaction with the hull.

- The effect of variation of design parameters at the stern on the behavior of the stern flow has been conducted to improve the stern arrangement in view point of self-propulsion performance. StaRting with a base design, an improved design was derived out of four parametric studies. Finally the hydrodynamic performance of the improve stern design was compared with base design. The improve stern

showed a 5% average decrease in delivered power for a range of design speed and draught conditions. It was also shown that a minor change in the geometrical parameter of the propeller such as the pitch ratio or the diameter, although small might result in a significant change in the behind efficiency (η_B).

- It should be emphasized that the simulations were conducted based on constraints put on the hull. Kim et al., (2013) has shown that by releasing the constraints imposed on twin skeg hull during computations further reduction in power could be achieved.

- The ability of the RANS-BEMt to consider non-uniform and tangential inflow conditions makes it suitable for future transient manoeuvring simulations.

- Whilst the RANS-BEMt method has been used to successfully study the LNG carrier stern flow in calm water conditions, improvements can be made to consider the effect of waves, ship motions and oblique flows. For example to represent the variation in the wake on the propeller performance, the local wake fraction must found for every nR and nC subdivision. This can be achieved by probing the inflow at a plane upstream of the propeller or at the propeller disk centre and then updating at each time step. The Goldstein corrections must also be modified to account for the interference between the blades and the unsteady flow. For a propeller operating in oblique flow, the local incidence angle can be very large and may even stall, particularly in model scale. Cavitation can occur which may affect the total load developed by the blade. To account for such behavior the RANS-BEMt may be modified by including the hydrodynamic characteristics of the blade section (if known) for a relatively broad range of angles of incidence in the algorithm. It should be emphasized that although not included in this thesis, the present method has been tested for propeller drift angles of -7.5° with reasonable results. For large propeller drift angles with strong unsteadiness such as trailing and shedding wake structures of variable strength or where strong vortical structures detached from the hull the reliability of the method has not been verified and validated.

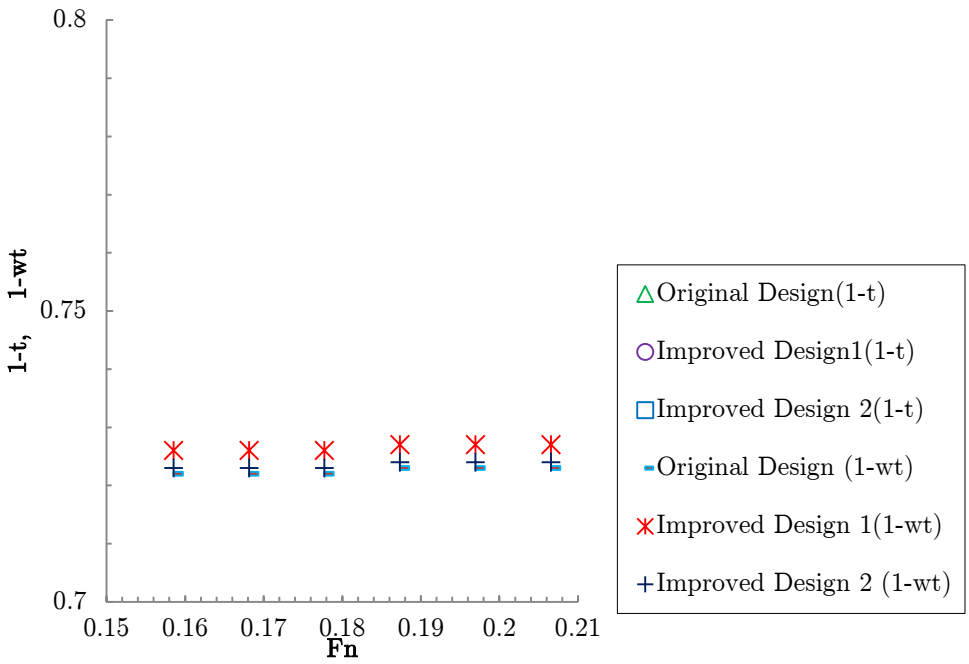

Figure 6.25: Comparison of propulsion parameters for base (original) and improved designs for different design speeds at loaded draught condition.

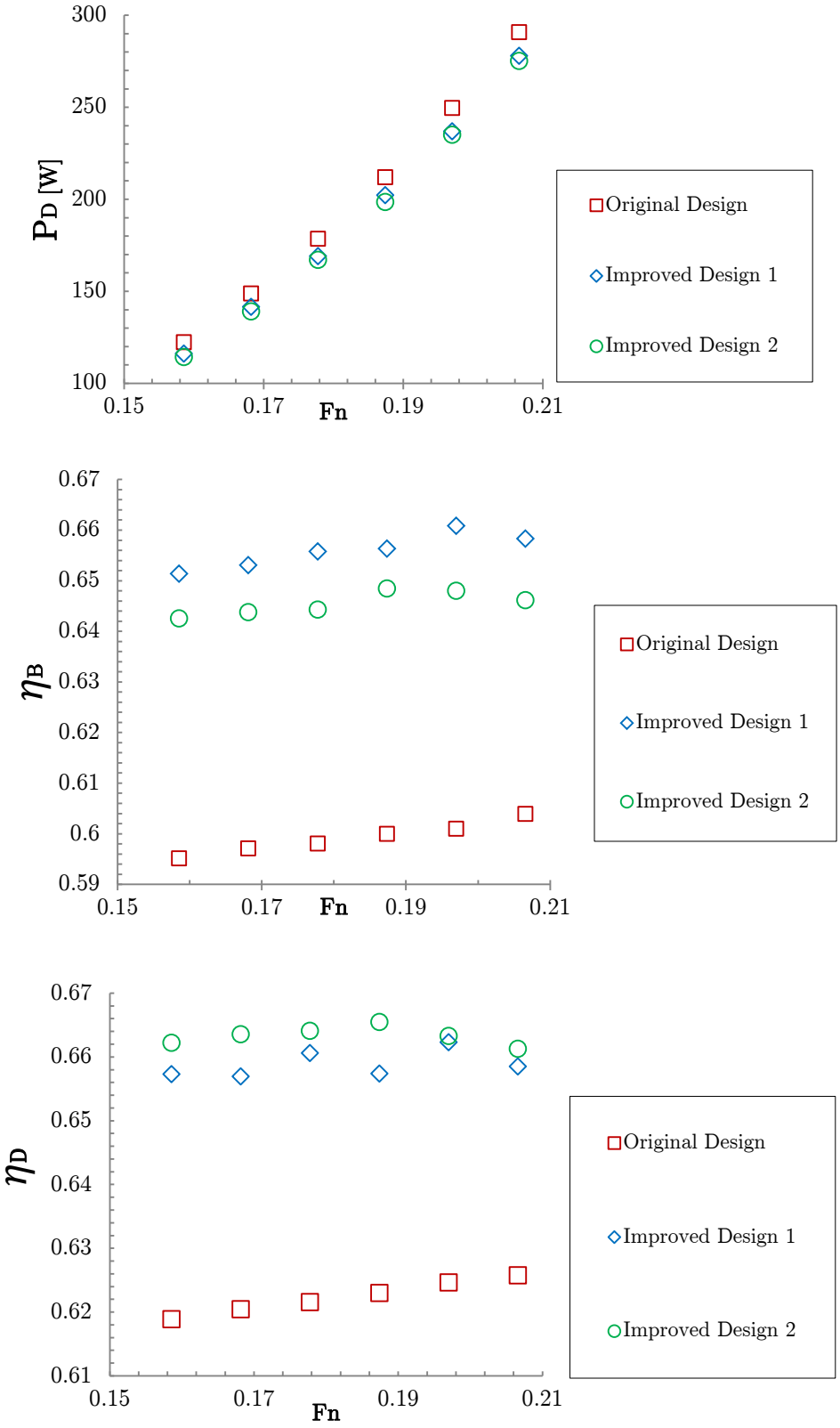

Figure 6.26: Comparison of propulsion parameters for base (original) and improved design for different design speeds at loaded draught condition.

Table 6.7: TSLNG Original Design Resistance Test Prognosis (Loaded Draught).

Model Speed	Froude Number	Reynolds Number	Residuary Resistance Coefficient	Frictional Resistance Coefficient	Total Resistance Coefficient	Total Resistance	Effective Power
Vs[m/s]	Fn[-]	Re$\times 10^6$	$C_R \times 10^{-3}$	$C_F \times 10^{-3}$	$C_T \times 10^{-3}$	R_T [N]	P_E [W]
1.496	0.159	11.429	0.150	2.697	2.842	50.664	75.793
1.587	0.168	12.123	0.220	2.684	2.902	58.207	92.355
1.677	0.178	12.815	0.280	2.670	2.954	66.196	111.033
1.768	0.187	13.508	0.340	2.658	3.000	74.735	132.131
1.859	0.197	14.200	0.400	2.647	3.049	83.911	155.963
1.949	0.206	14.894	0.450	2.634	3.085	93.379	182.026

Water Temperature	15.0°C
Water Density	1025.88kg/m^3
Water Viscosity	1.188×10^{-6}m^2/s
Form Factor (1+k)	1.15
Appendages	twin skeg, twin rudder
Design Condition	Loaded Design Draught

Table 6.8: TSLNG Original Design Propulsion Test Prognosis (Loaded Draught).

Model Speed	Froude Number	Reynolds Number	Wake Fraction	Thrust Deduction	Revolutions	Advance Ratio	Thrust Coefficient	Torque Coefficient
Vs[m/s]	Fn[-]	Re$\times 10^6$	wt	t	rps	J	K_T	$K_Q \times 10$
1.496	0.159	11.429	0.278	0.249	12.355	0.605	0.3091	0.5001
1.587	0.168	12.123	0.278	0.250	13.082	0.607	0.3085	0.4992
1.677	0.178	12.815	0.278	0.250	13.789	0.608	0.3080	0.4984
1.768	0.187	13.508	0.277	0.249	14.500	0.610	0.3074	0.4974
1.859	0.197	14.200	0.277	0.249	15.202	0.611	0.3070	0.4968
1.949	0.206	14.894	0.277	0.251	15.940	0.612	0.3069	0.4966

Water Temperature	15.0°C
Water Density	1025.88kg/m^3
Water Viscosity	1.188×10^{-6}m^2/s
Form Factor (1+k)	1.15
Appendages	twin skeg, twin rudder
Design Condition	Loaded Design Draught

Table 6.9: TSLNG Original Design Table of Efficiencies (Loaded Draught).

Model Speed	Froude Number	Reynolds Number	Hull Efficiency	Behind Efficiency	Quasi Propulsive Efficiency	Delivered Power
Vs[m/s]	Fn[-]	Re$\times 10^6$	η_H	η_B	η_D	P_D[W]
1.496	0.159	11.429	1.0399	0.5952	0.6189	122.464
1.587	0.168	12.123	1.0391	0.5971	0.6204	148.856
1.677	0.178	12.815	1.0393	0.5981	0.6216	178.634
1.768	0.187	13.508	1.0383	0.6000	0.6230	212.092
1.859	0.197	14.200	1.0394	0.6010	0.6246	249.685
1.949	0.206	14.894	1.0362	0.6038	0.6257	290.883

Water Temperature	15.0°C
Water Density	1025.88kg/m^3
Water Viscosity	1.188×10^{-6}m^2/s
Form Factor (1+k)	1.15
Appendages	twin skeg, twin rudder
Design Condition	Loaded Design Draught

Table 6.10: TSLNG Original Design Resistance Test Prognosis (Ballast Draught).

Model Speed	Froude Number	Reynolds Number	Residuary Resistance Coefficient	Frictional Resistance Coefficient	Total Resistance Coefficient	Total Resistance	Effective Power
Vs[m/s]	Fn[-]	Re$\times 10^6$	$C_R \times 10^{-3}$	$C_F \times 10^{-3}$	$C_T \times 10^{-3}$	R_T [N]	P_E [W]
1.529	0.162	11.680	0.190	2.686	2.880	44.775	68.443
1.623	0.172	12.400	0.180	2.672	2.854	50.022	81.187
1.717	0.182	13.121	0.170	2.659	2.826	55.452	95.233
1.802	0.191	13.770	0.130	2.647	2.780	60.065	108.256
1.897	0.201	14.491	0.250	2.635	2.888	69.114	131.087
1.991	0.211	15.212	0.340	2.622	2.964	78.184	155.668

Water Temperature	15.0°C
Water Density	1025.88kg/m^3
Water Viscosity	1.188×10^{-6}m^2/s
Form Factor (1+k)	1.11
Appendages	twin skeg, twin rudder
Design Condition	Ballast Design Draught

Table 6.11: TSLNG Original Design Propulsion Test Prognosis (Ballast Draught).

Model Speed	Froude Number	Reynolds Number	Wake Fraction	Thrust Deduction	Revolutions	Advance Ratio	Thrust Coefficient	Torque Coefficient
Vs[m/s]	Fn[-]	Re× 10^6	wt	t	rps	J	K_T	K_Q×10
1.529	0.162	11.680	0.313	0.199	11.149	0.672	0.2954	0.4767
1.623	0.172	12.400	0.313	0.198	11.949	0.677	0.2878	0.4671
1.717	0.182	13.121	0.313	0.202	12.500	0.685	0.2951	0.4761
1.802	0.191	13.770	0.312	0.204	13.090	0.688	0.2947	0.4756
1.897	0.201	14.491	0.132	0.202	13.500	0.689	0.2941	0.4747
1.991	0.211	15.212	0.312	0.201	14.149	0.692	0.2901	0.4688

Water Temperature	15.0°C
Water Density	1025.88kg/m^3
Water Viscosity	1.188×$10^{-6}$$m^2$/s
Form Factor (1+k)	1.11
Appendages	twin skeg, twin rudder
Design Condition	Ballast Design Draught

Table 6.12: TSLNG Original Design Table of Efficiencies (Ballast Draught).

Model Speed	Froude Number	Reynolds Number	Hull Efficiency	Behind Efficiency	Quasi Propulsive Efficiency	Delivered Power
Vs[m/s]	Fn[-]	Re$\times 10^6$	η_H	η_B	η_D	P_D[W]
1.529	0.162	11.680	1.1671	0.6629	0.7737	88.465
1.623	0.172	12.400	1.1670	0.6639	0.7747	104.794
1.717	0.182	13.121	1.1607	0.6756	0.7842	121.443
1.802	0.191	13.770	1.1577	0.6785	0.7855	137.810
1.897	0.201	14.491	1.1600	0.6794	0.7881	166.332
1.991	0.211	15.212	1.1615	0.6817	0.7918	196.601

Water Temperature	15.0°C
Water Density	1025.88kg/m^3
Water Viscosity	1.188×10^{-6}m^2/s
Form Factor (1+k)	1.11
Appendages	twin skeg, twin rudder
Design Condition	Ballast Design Draught

Table 6.13: TSLNG Improved Design One Resistance Test Prognosis (Loaded Draught).

Model Speed	Froude Number	Reynolds Number	Residuary Resistance Coefficient	Frictional Resistance Coefficient	Total Resistance Coefficient	Total Resistance	Effective Power
Vs[m/s]	Fn[-]	Re$\times 10^6$	$C_R \times 10^{-3}$	$C_F \times 10^{-3}$	$C_T \times 10^{-3}$	R_T [N]	P_E [W]
1.496	0.159	11.429	0.150	2.719	2.864	51.051	76.372
1.587	0.168	12.123	0.220	2.705	2.923	58.628	93.022
1.677	0.178	12.815	0.280	2.690	2.974	66.651	111.796
1.768	0.187	13.508	0.340	2.678	3.021	75.226	132.999
1.859	0.197	14.200	0.400	2.666	3.068	84.441	156.948
1.949	0.206	14.894	0.450	2.653	3.104	93.950	183.139

Water Temperature	15.0°C
Water Density	1025.88kg/m^3
Water Viscosity	1.188×10^{-6}m^2/s
Form Factor (1+k)	1.15
Appendages	twin skeg, twin rudder
Design Condition	Loaded Design Draught

Table 6.14: TSLNG Improved Design One Propulsion Test Prognosis (Loaded Draught).

Model Speed	Froude Number	Reynolds Number	Wake Fraction	Thrust Deduction	Revolutions	Advance Ratio	Thrust Coefficient	Torque Coefficient
Vs[m/s]	Fn[-]	Re× 10^6	wt	t	rps	J	K_T	K_Q×10
1.496	0.159	11.429	0.274	0.267	14.000	0.534	0.2438	0.3180
1.587	0.168	12.123	0.274	0.268	14.820	0.535	0.2433	0.3173
1.677	0.178	12.815	0.274	0.268	15.620	0.537	0.2426	0.3162
1.768	0.187	13.508	0.273	0.270	16.460	0.537	0.2425	0.3157
1.859	0.197	14.200	0.273	0.271	17.150	0.542	0.2416	0.3153
1.949	0.206	14.894	0.273	0.270	18.050	0.540	0.2413	0.3149

Water Temperature	15.0°C
Water Density	1025.88kg/m^3
Water Viscosity	1.188×$10^{-6}$$m^2$/s
Form Factor (1+k)	1.15
Appendages	twin skeg, twin rudder
Design Condition	Loaded Design Draught

Table 6.15: TSLNG Improved Design One Table of Efficiencies (Loaded Draught).

Model Speed	Froude Number	Reynolds Number	Hull Efficiency	Behind Efficiency	Quasi Propulsive Efficiency	Delivered Power
Vs[m/s]	Fn[-]	Re$\times 10^6$	η_H	η_B	η_D	P_D[W]
1.496	0.159	11.429	1.0096	0.6514	0.6577	116.123
1.587	0.168	12.123	1.0083	0.6531	0.6585	141.268
1.677	0.178	12.815	1.0083	0.6558	0.6612	169.084
1.768	0.187	13.508	1.0041	0.6564	0.6591	202.799
1.859	0.197	14.200	1.0028	0.6608	0.6626	236.851
1.949	0.206	14.894	1.0041	0.6690	0.6637	275.946

Water Temperature	15.0°C
Water Density	1025.88kg/m^3
Water Viscosity	1.188×10^{-6}m^2/s
Form Factor (1+k)	1.15
Appendages	twin skeg, twin rudder
Design Condition	Loaded Design Draught

Table 6.16: TSLNG Improved Design Two Propulsion Test Prognosis (Loaded Draught).

Model Speed	Froude Number	Reynolds Number	Wake Fraction	Thrust Deduction	Revolutions	Advance Ratio	Thrust Coefficient	Torque Coefficient
Vs[m/s]	Fn[-]	Re× 10^6	wt	t	rps	J	K_T	K_Q×10
1.496	0.159	11.429	0.278	0.256	13.990	0.535	0.2430	0.3218
1.587	0.168	12.123	0.278	0.256	14.800	0.536	0.2424	0.3213
1.677	0.178	12.815	0.278	0.256	15.600	0.537	0.2420	0.3212
1.768	0.187	13.508	0.277	0.258	16.310	0.542	0.2413	0.3212
1.859	0.197	14.200	0.277	0.259	17.300	0.537	0.2411	0.3210
1.949	0.206	14.894	0.277	0.260	18.085	0.539	0.2410	0.3198

Water Temperature	15.0°C
Water Density	1025.88kg/m^3
Water Viscosity	1.188×$10^{-6}$$m^2$/s
Form Factor (1+k)	1.15
Appendages	twin skeg, twin rudder
Design Condition	Loaded Design Draught

Table 6.17: TSLNG Improved Design Two Table of Efficiencies (Loaded Draught).

Model Speed	Froude Number	Reynolds Number	Hull Efficiency	Behind Efficiency	Quasi Propulsive Efficiency	Delivered Power
Vs[m/s]	Fn[-]	Re$\times 10^6$	η_H	η_B	η_D	P_D[W]
1.496	0.159	11.429	1.0306	0.6426	0.6622	114.454
1.587	0.168	12.123	1.0308	0.6438	0.6636	139.178
1.677	0.178	12.815	1.0307	0.6443	0.6641	167.199
1.768	0.187	13.508	1.0263	0.6484	0.6655	198.544
1.859	0.197	14.200	1.0236	0.6480	0.6633	235.137
1.949	0.206	14.894	1.0242	0.6461	0.6618	275.054

Water Temperature	15.0°C
Water Density	1025.88kg/m^3
Water Viscosity	1.188×10^{-6}m^2/s
Form Factor (1+k)	1.15
Appendages	twin skeg, twin rudder
Design Condition	Loaded Design Draught

Table 6.18: TSLNG Improved Design Two Propulsion Test Prognosis (Ballast Draught).

Model Speed	Froude Number	Reynolds Number	Wake Fraction	Thrust Deduction	Revolutions	Advance Ratio	Thrust Coefficient	Torque Coefficient
Vs[m/s]	Fn[-]	Re× 10^6	wt	t	rps	J	K_T	K_Q×10
1.529	0.162	11.680	0.313	0.234	12.715	0.601	0.2304	0.3083
1.623	0.172	12.400	0.313	0.220	13.695	0.593	0.2230	0.3015
1.717	0.182	13.121	0.313	0.230	14.290	0.600	0.2306	0.3085
1.802	0.191	13.770	0.312	0.235	14.950	0.603	0.2296	0.3075
1.897	0.201	14.491	0.132	0.237	15.660	0.606	0.2285	0.3064
1.991	0.211	15.212	0.312	0.238	16.335	0.601	0.2274	0.3053

Water Temperature	15.0°C
Water Density	1025.88kg/m^3
Water Viscosity	1.188×$10^{-6}$$m^2$/s
Form Factor (1+k)	1.11
Appendages	twin skeg, twin rudder
Design Condition	Ballast Design Draught

Table 6.19: TSLNG Improved Design Two Table of Efficiencies (Ballast Draught).

Model Speed	Froude Number	Reynolds Number	Hull Efficiency	Behind Efficiency	Quasi Propulsive Efficiency	Delivered Power
Vs[m/s]	Fn[-]	Re$\times 10^6$	η_H	η_B	η_D	P_D[W]
1.529	0.162	11.680	1.1155	0.7148	0.7973	85.835
1.623	0.172	12.400	1.1354	0.6980	0.7925	102.445
1.717	0.182	13.121	1.1203	0.7137	0.7996	119.099
1.802	0.191	13.770	1.1126	0.7165	0.7972	135.796
1.897	0.201	14.491	1.1093	0.7193	0.7979	164.283
1.991	0.211	15.212	1.1076	0.7220	0.7997	194.664

Water Temperature	15.0°C
Water Density	1025.88kg/m^3
Water Viscosity	1.188$\times 10^{-6}$m^2/s
Form Factor (1+k)	1.11
Appendages	twin skeg, twin rudder
Design Condition	Ballast Design Draught

Chapter 7

7 Discussions on application of CFD to LNG stern design

The level of detail to which an LNG carrier stern design process is taken, may depend on what is being sought by the designer and the input parameters. Parameters such as sea state, operational range, draught conditions, speed, wake, propeller type and rudder type may be considered as inputs if the requirement is for efficiency purpose. Among these input parameters, the nominal wake field is considered vital as this determines the propeller design and hence rudder geometry to give the required efficiency. The nominal wake field is very much related on the global hull form. Hull forms which employ twin skegs (seen earlier in chapter 6) presents pre swirl to the propeller.

The use of RANS in the analysis of the hull wake and appendages such as twin skegs is a very complex task as the boundary layer of the hull, skegs and the viscous wake needs to be captured with high level of accuracy. This requires good grids and appropriate resolution. The mesh cells in the propeller plane should be able to give circumferential distribution of three components of the velocity, as this information forms an important part of the input conditions to propeller. It is not the size of the grid that determines the accuracy of the nominal wake field, but good experience with its distribution so as to provide very useful information on the underlying physics of the flow. It has been proven from the assessment of the Gothenburg 2010 workshop, (Larsson et al., 2010) that for resistance and nominal wake field computations there is little difference between resistance and the nominal wake field values using low mesh resolution such as three million elements or higher ones such as three hundred million elements. Depending on the Froude number of the twin skeg LNG ship ($\leq$ 0.2 as seen in chapter 5 for double body

computations) the simulation has to take into account the effect of the free surface to get the correct flow into the propeller plane. The VOF method is most widely used due to its low cost in computation compared to other methods and also because it is able to deal with highly non-linear free-surface problems such as wave breaking etc. Attention needs to be given to blending of the free surface to the hull boundary. A method to do this has been outlined in chapter 3 and applied in chapter 5. Good resolution of the free surface and hull boundary layer require strong turbulence modelling and wall treatment so that all aspect of the ship's flow is captured for example the bilge vortices. Although other models were not tested, the SST model coupled with automatic wall treatment has proved to be credible in capturing various aspect of the LNG ship flow.

After the resistance and nominal wake field for the LNG carrier has been achieved the next step in the design phase is to select a suitable propeller and control surface.

Detailed propeller selection and design can be found in Carlton (2007). Here only modification to a few geometrical parameters of the propeller to give a reduced power will be discussed. Initial selection of the twin skeg LNG ship propeller can be made from a data base of existing propellers after which hydrodynamic analysis can then be conducted based on the nominal wake distribution (all three components of velocity in the propeller plane), thrust deduction fraction, effective wake fraction, relative rotative efficiency and delivered power. The analysis to be conducted is mainly discussed in chapter 6 such as selection of the pitch ratio, diameter and blade area ratio to reduce thrust deduction fraction and increase the wake fraction to achieve a reduction in delivered power. The thrust deduction and wake fraction are interaction effect between ship and propeller which is very difficult to capture. The use of RANS to select and analyse propellers have been discussed in section 3.3. A discretized propeller gives the highest fidelity. Since ship-propeller interaction is very difficult to capture, discretizing the ship and propeller will require good resolution around the ship hull, propeller blades, boundary layer and wake with high mesh cells and smaller time steps. This places a high demand on computation (see Table 5.3). It is possible to save cells and central processing unit (CPU) resources and obtain a solution in a shorter time by using a body force model. The BEMt propeller code developed by Molland and Turnock (1996) has proven to be a powerful propeller design tool which can be coupled in a RANS environment. Adopting the sectorial approach proved a novel way to include all the three components of velocity as input to the propeller. The sectorial approach and coupling procedure also allow accurate estimates of the effective wake to be made so as to derive the appropriate momentum source terms.

The RANS-BEMt procedure makes it also easier to conduct analysis on the propeller geometrical parameters discussed above in order to achieve the best overall quasi-propulsive efficiency coefficient to minimize the delivered power requirement for the operational range and draught conditions of the ship.

Although not conducted in this analysis it is possible to search optimal locations to place the propeller for twin skeg ships to earn wake gains (Sakamoto et al., 2013). Once a favourable location has been selected hull modifications can be made for further improvements or the advantages of the rotation in the propeller slipstream can be made use of by subsequently searching various locations in the slipstream to place the rudder.

The final point in the stern design of the LNG carrier ship is the rudder design and its position with respect to the propeller. Usually the rudder can be included with the hull in the RANS computation to determine the nominal wake field to be used as input for the propeller. The determination of the rudder forces is also important for the practical design purpose. For example the longitudinal force influences the propulsive efficiency whilst the transverse force is needed to evaluate the manoeuvrability of the LNG ship. Chapter 4 showed that the RANS computation on the rudder to accurately estimate the forces is very complex. This requires the hull, skeg and propeller flow to be accurately modelled since the inflow to the rudder depends on how accurate they are predicted. The rudder leading edge pressure and suction peaks also need to be adequately resolved to obtain the right forces. Simonsen and Stern (2005) and Phillips et al. (2009) highlight the difficulties in the prediction of rudder forces with large uncertainties and comparison errors between calculated and experimental result unless significantly larger meshes are used. Date and Turnock (2002) indicates values of 5-20M cells to fully resolve the rudder forces.

It can be seen from the discussions that CFD plays a primary role in the detailed stern design process. Information available upon which the stern design is based is also very significant. According to Carlton (2007), there is little value in the use of high level CFD computation requiring detailed input when gross assumption has to be carried out concerning the basis of the design. Figure 7.1 shows a simplified stern design process for an LNG carrier ship. For this process we deliberately limit the OpenFOAM simulations to steady state calculations to minimize computational cost. The design process is based on standard off the shelf propeller and rudder to which modifications can be made to achieve the required power. More complex design procedures can be adopted with extra blocks added when increasing constraints are placed on the design and increasing amounts of basic information are available upon which to base the design. Such increases in complexity may include addition of sea state, mean wake fraction as supposed to circumferential wake distribution to enable the propeller to be wake adapted or addition of rudder inflow velocities to enable twisted rudder designs to be made. An example of a more complex design is shown in Figure 7.2. This embodies most of the current advance numerical design and analysis techniques. It should however be noted that other options such as cavitation on the blades can be included in the design. For such inclusion in the design, then the choice of propeller model is limited to that of an AMI.

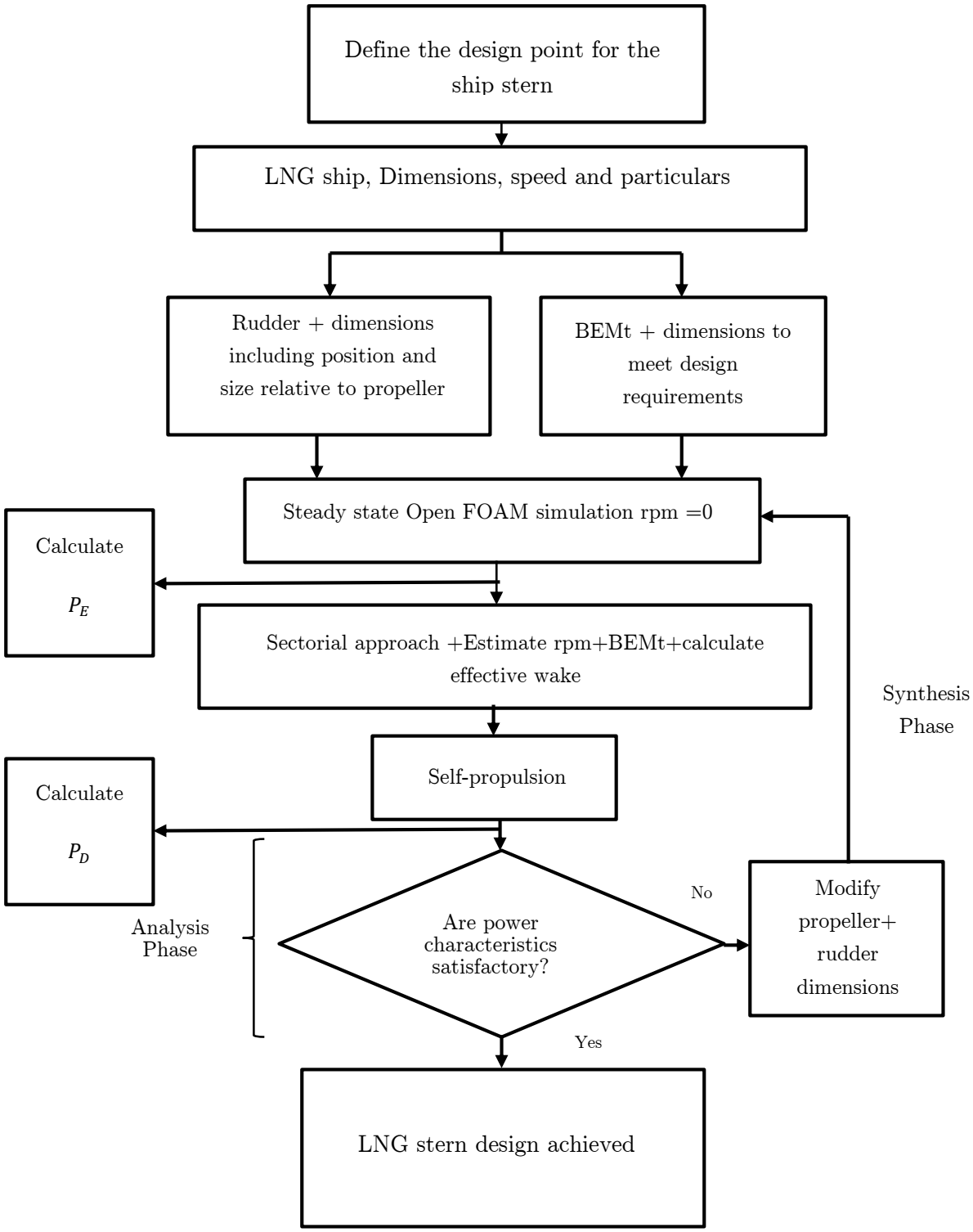

Figure 7.1: Example of a simplified LNG design procedure.

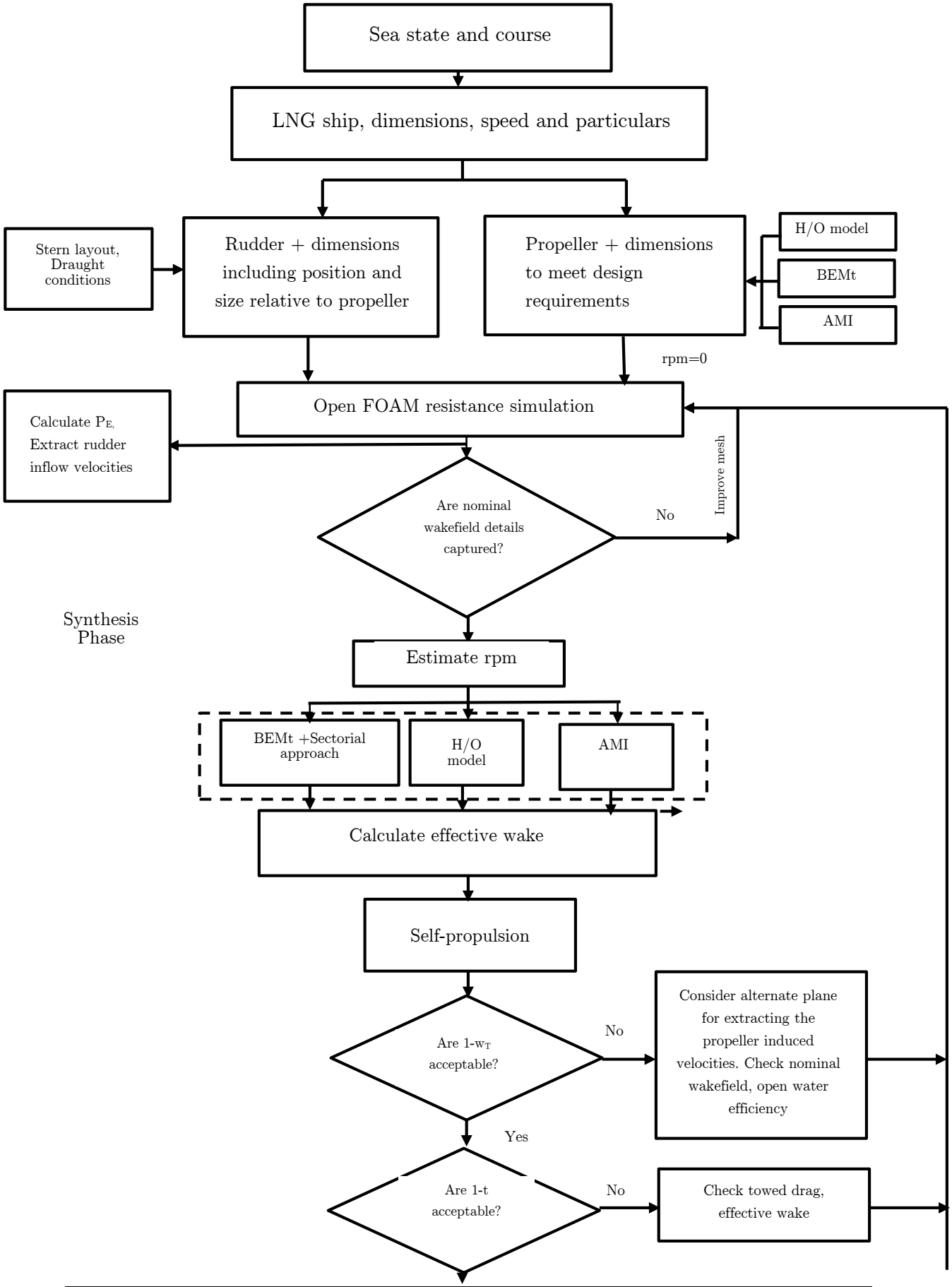
Sea state and course
LNG ship, dimensions, speed and particulars
Stern layout, Draught conditions
Rudder + dimensions including position and size relative to propeller
Propeller + dimensions to meet design requirements
H/O model
BEMt
AMI
rpm=0
Open FOAM resistance simulation
Calculate P_E, Extract rudder inflow velocities
Are nominal wakefield details captured?
No
Improve mesh
Synthesis Phase
Estimate rpm
BEMt +Sectorial approach
H/O model
AMI
Calculate effective wake
Self-propulsion
Are 1-w_T acceptable?
No
Consider alternate plane for extracting the propeller induced velocities. Check nominal wakefield, open water efficiency
Yes
Are 1-t acceptable?
No
Check towed drag, effective wake

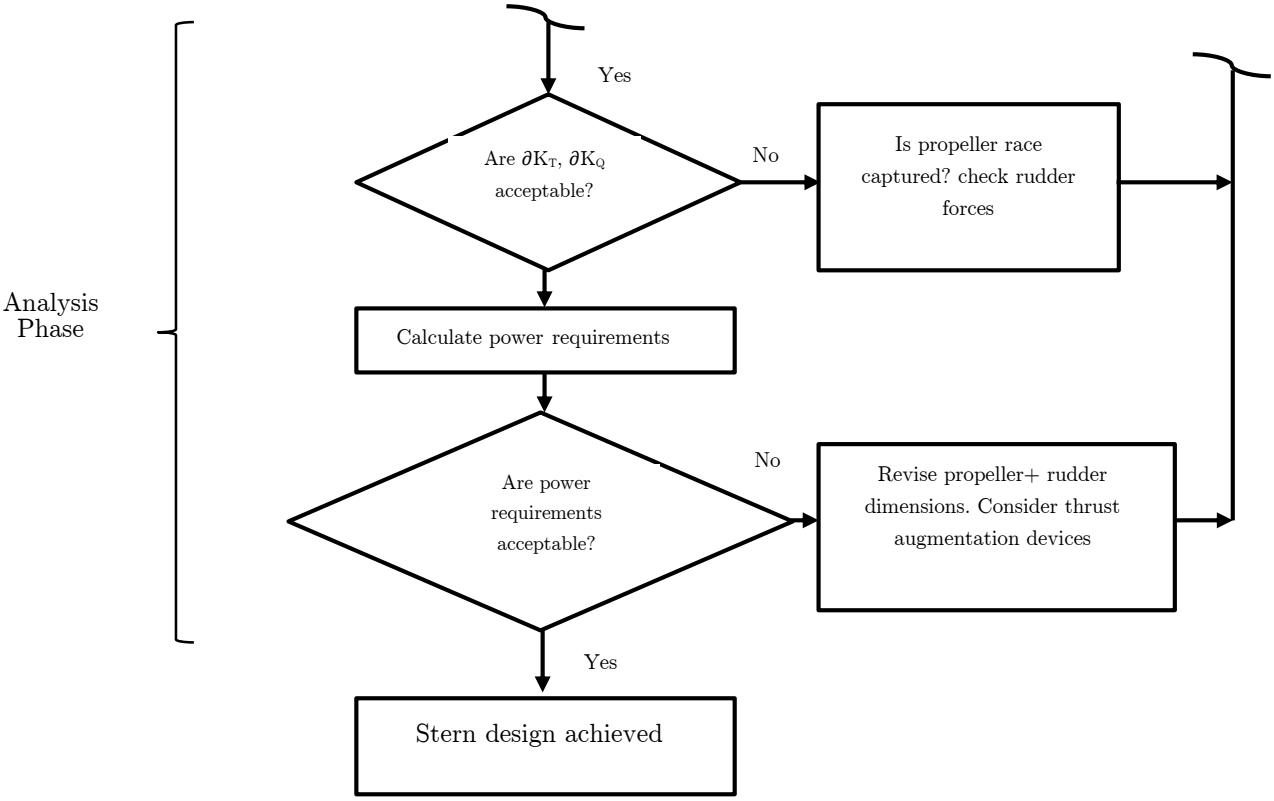

Figure 7.2: Example of a fully integrated synthesis and analysis LNG design procedure

Chapter 8

8 Conclusions and future work recommendations

8.1 Overall

Accurately predicting the stern design for an LNG carrier at the initial stage is very important for its overall propulsive power success, since difficulties there can follow the ship during it entire life span. Usually the time allocation for this process is limited that is why it is paramount that the starting phase should be close to the final at the commencement of the project. Parameters that require careful analysis for an excellent aft body design are:-

1. Nominal wake field of the hull and appendage(s)
2. Choice of appendage (skegs are typical example) aimed at providing good flow towards the propeller(s) control surface (s), without flow separation
3. Choice of propulsor and dimensions to meet design requirements
4. Choice of control surface and dimensions
5. Interaction effect between the hull-propeller and appendage

By considering the above for various speed ranges, it is possible to find optimum solutions for the operating profile of the ship. This thesis has outlined a methodology capable of assessing various aspect of the resistance and powering of a future twin skeg ship using both steady and unsteady CFD analysis methods which balances the trade-off between computational cost and fluid dynamic fidelity and may provide useful knowledge for the initial stern twin skeg LNG ship design stage so that optimum solutions may be found which is economical and suitable to operate.

Chapter 1 of this work presents the need to improve the powering performance of LNG carrier vessels. Areas of the ships hydrodynamics which will require less energy to propel it through the water were identified. This was separated into the total towed resistance, R_T, of the ship and the propulsive efficiency, η_D, determined by the propulsor and its interaction with the hull and appendage. To successfully predict the towed drag then the viscous flow around the ship has to be accurately modelled and the interaction between the hull boundary layer and the viscous wake taken into account. Obtaining the right resistance is also significant in the selection of the correct propulsor and control surface and in the subsequent choice of main engine. Adopting a sectorial approach whereby the wakefield in the propeller plane is discretized into a series of radial nR and circumferential nC subdivisions is potentially a novel way to improve the propulsive performance, since it is possible to consider the local axial and tangential inflow conditions at each sector of the propeller plane thereby giving good estimates of the wake and thrust deduction fraction. Combining this approach with a developed numerical towing tank allows the resistance and powering of twin skeg LNG ships to be assessed.

Chapter 3 details the numerical towing tank techniques which may be used to derive the resistance and powering of the LNG ship. Since the speed and the propeller loading on an LNG carrier is in general, large, it requires a low overall resistance and related good powering performance but also an excellent aft body design, with a good flow towards the propeller(s) and rudder(s), without flow separation. The accuracy of the numerical towing tank should be such that it should be able to model the above requirements. The key focus of the developed towing tank was such that it should be able to look into details the influence of correctly capturing the flow into the propeller plane. A custom mesh technique to blend the near hull refinements with the free surface was discussed.

The sectorial approach was applied to a BEMt propeller code and in conjunction with the custom mesh technique used to predict the resistance and self-propelled parameters of a KCS hull form in calm water conditions in chapter 5. The chapter also discussed the application of numerical approach to LNG stern design. A typical LNG ship design cycle was outlined with key parameters to consider in ensuring a successful stern design. Notable in the stern design cycle is the need to estimate achievable target of speeds and powers. This included the review of propulsor, appendage and the stern hull form. These have to be improved from a resistance and powering point-of-view for the operational profile and loading conditions of the LNG ship.

Chapter 6 then applies the design approach and key parameters together with the numerical towing tank to model the propulsive power of a twin skeg ship.

8.2 Conclusion in relation to objectives

8.2.1 Numerical model - Objective 1

The base set up of a numerical towing tank suitable for modelling the LNG carrier ship is presented in Chapter 3 and is implemented in the open source CFD package OpenFOAM. This is also supported by a mesh algorithm for generating a suitable mesh around the ship. This algorithm enables the boundary layer of the hull and free surface region to be resolved independent of each other. Emphasis is placed on the mesh distribution in the viscous wake to accurately predict the stern flow, in particular the flow into the propeller.

In modelling the LNG propeller in the numerical towing tank, an approach to replicate the propeller flow in a cost effective manner is favoured. A body force propeller was preferred to geometrically modelling the propeller due to its low CPU resources. A method of coupling of a body force propeller based on the blade element momentum theory in a RANS environment was used as part of the numerical towing. Due to the non-uniform nature of the flow to the propeller plane, a sectorial approach was adopted to allow easy extraction of all the three components of the velocity in the propeller plane as input to the BEMt propeller.

The numerical towing tank with the implemented BEMt coupling strategy is used to verify if this methodology can predict the resistance and powering of an LNG carrier ship and other objectives set in this thesis.

8.2.2 RANS-BEMt body force propeller models - Objective 2

Marine propellers can be simulated using body force approach when the requirement to directly mirror the propeller flow is not essential. The body forces approach usually replicate the propeller action by adding the axial and tangential momentum sources around the swept volume of the propeller. By adopting the influence of a ships wake and discretizing the wakefield in the propeller plane into a series of radial nR and circumferential nC subdivisions a novel coupled RANS-BEMt body force propeller model was proposed and compared to other existing propeller models like the Hough and Ordway propeller model and a discretize RANS propeller (AMI). The BEMt propeller proved superior to the other models due to the following reasons:-

- The Hough and Ordway propeller model assumes a constant circumferential distribution of thrust and torque hence does not capture the interaction between the hull on propeller and the rudder on propeller. The coupled RANS-BEMt propeller model and AMI are best suited for capturing the interaction effects hence gives good estimates of the self-propulsion parameters such as the wake fraction, thrust deduction fraction and the quasi propulsive efficiency.

- Unlike the Hough and Ordway model the RANS-BEMt and the AMI calculates the propeller thrust and torque as part of the simulation.

- The RANS-BEMt model captures the changes in propulsive forces as a result of a downstream rudder and increase in side force associated with the acceleration of the propeller race.

- When considering self-propelled simulations as illustrated in Chapter 5, both the Hough and Ordway and the RANS-BEMt are able to give good estimates of global forces seen from the hydrodynamic longitudinal forces values compared with experiment, but the flow field looks different. The RANS-BEMt propeller is able to replicate the swirl effect much better than the Hough and Ordway model thus replicating better the asymmetry in the flow. Both RANS-BEMt and Hough and Ordway model can be used in self-propulsion simulations but the Hough and Ordway can only be used if the flow-field details are not of prime importance as long as the required conditions of the flow head are captured.

- The BEMt compares well with AMI in terms of global forces and flow-field data but the drawback of the AMI is that there is a significant computational expense (typically $\geq$ 30% of the total simulation time for similar setup with RANS-BEMt as seen in chapter 5) hence body force based methods are likely to still be required for self-propelled ship computations.

- Even though the RANS-BEMt has successfully been used for self-propelled simulations and the results looks promising, there is still more scope for improvement in the general stern flow prediction especially the hull and skeg boundary layer and its propagation to the wake at the propeller plane and then to the downstream rudder. Such areas require experience and skill to distribute the high mesh cells around these regions to capture their effects as they have serious consequence on the prediction of the propeller and the downstream rudder loads. Poor prediction of any one of the flow features will have effect on the other. Other areas that needs improvement in the RANS-BEMt approach is the drag coefficient and the lift curve slopes. These can be improved to enable the influence of stall to be included in the algorithm. The influence of blade thickness on the rudder and hull forces and its impact on propulsive efficiency is also very important. The RANS-BEMt approach gives an average representation of the field data over a blade passage thus neglecting tip and hub vortices. When requirement of instantaneous flow variations over a blade passage or detailed blade interaction with waves with requirements for tip and hub vortices prediction and cavitation analysis of the propeller is required the RANS-BEMt

approach will be unsuitable for such analysis. The AMI would be more suited to such problems.

8.2.3 Resistance and Self-Propulsion performance - Objective 3&4

Chapter 4 illustrate the use of the numerical towing tank to assess the interaction between the skeg, rudder and propeller. Computational results for both global and local flow quantities were discussed and compared well with measured values. The method was able to provide useful data and may be used for initial estimates of the propulsive coefficients of skegs and twin screw ships.

The developed methodology was also applied in chapters 5 and 7 to assess the resistance and self-propelled performance of a single screw and twin skeg ship. Resistance simulations were first performed for a KCS ship at a Froude number Fn =0.202 and the influence of the free surface on the global force and moments were assessed. The predicted global forces and moments acting on the towed vessel using a double body approach where a symmetry plane condition is used to account for the undisturbed seabed and taking into account the free surface effect agreed closely with each other. The nominal wake field which is important for the performance of the BEMt propeller showed a smooth boundary layer around the hull, thickening gradually and with smaller distortions in the velocity at the stern when a double body approach is used. Circumferential distribution of nominal wake at various radial locations at the propeller plane showed similar wake peaks in the propeller top position for both conditions. This finding is very important since the computational time for simulating the free surface is significantly much longer compared to a double body approach due to the increased grids and longer run times for the waves to settle.

The self-propelled simulations for the KCS demonstrated the difficulties associated with the prediction of self-propulsion parameters such as the wake fraction and thrust deduction fraction. These are all dependent on the interaction between the hull, propeller and rudder therefore inaccurate prediction in one of the interaction effect will result in an increase or decrease in prediction of the self-propelled parameters. Since the hydrodynamic longitudinal force and the propeller thrust were predicted within 4% of the experiment, it can be concluded that the input to the propeller (nominal wake) was replicated with reasonable accuracy and the resulting propulsive coefficients would have been predicted with much accuracy (even though experimental values of thrust deduction and the quasi propulsive coefficient were not provided).

In the self-propelled simulations for the TSLNG carrier ship the computational results reproduced the bent contour of low velocity region behind the skeg compared to that of Sakamoto et al., (2014). Comparison of the thrust deduction to that of Holtrop (1987) shows that depending on the breadth to draught ratio the use of Holtrop (1987) regression analysis can overestimate the thrust deduction. Most self- propelled simulations using a body force propeller model only consider the effect of axial wake as

that is the predominant component as far as most propeller straight ahead flows are concerned. In most single screw and twin skeg ships an upward flow exists at the aft end which leads to an axial flow component plus a tangential flow component (Molland et al., 2011). The influence of tangential wake investigated showed that by considering the upward flow the true axial component is slightly over-predicted, both the radial and tangential components of wake are modified thus modifying the thrust deduction and hence the propulsive efficiency.

In the parametric study to search optimal locations to maximize 1-t, only the pitch diameter variations, propeller diameter variations, propeller direction of rotation and rudder lateral separation were considered. The pitch diameter variations demonstrates that as the pitch distribution is reduced the load distribution from one radius to another also reduces hence the propeller works in a smaller race and the operating point of the propeller shifts to a point of higher efficiency. Propeller diameter variations were only carried out for four propeller diameters less than 0.22m. This was because due to the design draught conditions of the ship any increment in diameter will result in ventilation issues. Since the wake of the hull was adapted to the propeller as the propeller diameter is reduced the hull efficiency values (average) increases. This is because circumferential average wake values are greater towards the hub. The behind propeller efficiency increased with increasing diameter. The optimum diameter selected was 0.2m even though a diameter of 0.22 achieved the best behind efficiency.

Only the lateral separation due to the rudder was carried out, as there was not much scope for a longitudinal separation analysis due to the shorter hull stern. The maximum X/D that can be accommodated was 0.26m which is about right for twin screw ships. Note that values from Molland et al., (2007) suggest X/D range between 0.25m to 0.70m. No significant gain in thrust deduction (1-t) was achieved with this study with the best option found by placing the rudder directly behind the propeller. The optimum design chosen however was to offset both rudders laterally by 0.2D inwards as such an offset enables the tail shaft to be removed without removing the both rudders.

It is possible for propulsive performance to be different depending on the direction of rotation of the propellers. In this case the propeller rotation direction is in general found to be preferably inwards. It should however be stated that it does not necessarily mean that all twin skeg ships with inward rotation have the best propulsive performance since it depends on the detailed design of the twin skeg hull form.

8.2.4 Future twin skeg ships stern design and powering assessment – Objective 4

In the design of the stern arrangement of a twin skeg ship for propulsive performance improvement, the choice of propulsor, appendage and the three-way interaction between the hull, propulsor and appendage are important. Success with decision making regarding these parameters at the initial design stage will follow the vessel throughout its operational life cycle.

Today CFD tools have shown their usefulness in the detailed design of the stern, where optimal appendages are looked together with wake field and power information. The use of these tools requires understanding the stern flow and its importance which are detailed in Chapter 2 along with a myriad of research into the resistance predictions and characteristics of twin skeg ship. The use of inviscid, potential flow based methods to study the stern flow and hence its resistance capabilities were the backbone of such numerical tools. Unfortunately such methods cannot provide detailed flow field information at the stern especially in the presence of an operating propulsor. For twin skeg ships because viscosity is important only in a thin boundary layer around the ship and the propulsor act in the wake of ships, velocity distribution in the near wake of the boundary layer is important to the performance of the propulsor. Therefore to improve performance in the prediction it is important to establish confidence in the solution of a Reynolds Averaged Navier-Stokes (RANS) equation.

The choice of turbulence model and the schemes will have an impact on replicating the stern flow in detail especially the hull boundary layer, the circulatory flow around the skegs and the shape of the velocity contours at the stern which are important for the choice of the propulsor and appendage.

Several choice of propulsor modelling methods have been discussed but a body force model based on the Molland and Turnock (1996) blade element momentum theory was chosen and then implemented as part of a numerical towing tank in Chapter 3. This was found to be superior to other two existing models as their drawbacks were outlined in studies conducted in Chapters 5. The RANS-BEMt solver is able to replicate the stern flow better and also predicts the interaction effects between the hull, propulsor and rudder as illustrated in Chapter 5. It is also able to capture the changes in propulsive forces associated with a downstream rudder.

The developed methodology was used in the design of the stern arrangements of a twin skeg LNG carrier flow characteristics in Chapter 6, and finally evaluating its power demand. It is envisaged that further reduction in power demands could be achieved if the constraints on the hull form is released.

The developed methodology and the conclusions drawn from this research make it possible to have a potential in future design assessment of future twin skeg ships propulsive power demands. Although sophistication in the methodology, especially in areas of computations cells for self-propulsion simulation and thorough verification and validation would lead much improved design. The results also give indication of how accuracy may be improved in several areas. As computer power increases the level of accuracy may also increase and the demand for experimental methods will be reduced.

Even though the methodology presented in this thesis is mainly used for twin skegs ships, it may also be applicable for other ship types such as single screw, twin screw and other smaller ocean going vessels.

8.3 Recommendations for future work

Based on the work carried out in this study and the experiences acquired from it, the following suggestions for further studies to aid in the understanding and improvements of existing and future twin skeg LNG ship stern design and powering prediction are outlined below:-

- On the background of enhancing the propulsive power of LNG ships, this thesis has mainly focussed on computations based on ideal calm water conditions compared to realistic sea states. Propulsive parameters such as wake fraction, thrust deduction fraction and the propulsive power will vary in sea states compared to calm water conditions. Hence for better estimation of LNG ships resistance and powering, sea state should be incorporated in the computations, and the effect of trim and sinkage should be considered for accurate prediction of these coefficients.

- The impact of course, weather and wave loads on operational reliability of the LNG ship is governed by the hydrodynamic characteristics of the design. Under such conditions, the propeller and rudder working conditions may change. To maintain the LNG design speeds under these conditions then the influence of propeller geometrical parameters such as pitch setting on the power versus speeds have to be considered.
  Question that will need to be addressed are:-
  - what is the impact on delivered power if the propeller is operated at a fixed pitch whilst the speeds are varied?
  - what is the impact on delivered power if the propeller pitch is varied whilst maintaining a constant speed?
  - How do these impact on η_o, η_H and η_R.

- For a propeller operating in oblique flow or encountering wave loads, the local incidence angle can be very large and may even stall, particularly in model scale. Cavitation can occur which may affect the total load developed by the blade. To account for such behaviour the RANS-BEMt may be modified by including the hydrodynamic characteristics of the blade section (if known) for a relatively broad range of angles of incidence in the algorithm. For large trim angles or propeller drift angles with strong unsteadiness such as trailing and shedding wake structures of variable strength or where strong vortical structures detached from

the hull the reliability of the RANS-BEMt method should be verified and validated.

8.4 Concluding remarks

Key strategies for identifying important propeller-rudder and hull interaction effects have been presented along with a propeller performance code based on the blade element momentum theory as part of a developed numerical methodology to enable the powering assessment to be made on twin skeg ships. The results ensure fundamental capability of the developed method in estimating the resistance and self-propulsion characteristics of a twin skeg LNG ship, further improvements outlined in the future work would lead to the method to be more powerful design tool.

List of References

ANSYS., 2010. ANSYS CFX, release 12.1. ANSYS.

Badoe, C., Phillips, A., and Turnock, S.R., 2012. Numerical propeller rudder interaction studies to assist fuel efficient shipping. in Proc. Low Carbon Shipping Conference, Newcastle upon Tyne, 11-12 September 2012.

Badoe, C.E., Winden, B., Hudson, D., Phillips, A.B., and Turnock, S.R., 2013. Self-propulsion in waves using a coupled RANS-BEMt model and active RPM control. in proceedings of the 16th Numerical Towing Tank Symposium, (NuTTS'13), Duisburg, Germany, 2nd - 4th September 2013.

Bakker, A., 2006. Boundary layers and separation, lecture 11. Assessed April 2014, from http:// www.bakker.org/dartmouth06/engs150/11-bl.pdf.

Beck, R.F., Reed, A.M., and Rood, E.P., 1996. Application of modern numerical methods in marine hydrodynamics, SNAME Trans, 104, pp.519–537.

Benini, E., 2004. Significance of blade element theory in performance prediction of marine propellers. Journal of ocean engineering, 31(8-9), pp.957-974.

Bensow, R.E., and Bark, G., 2010. Simulating cavitating flows with LES in OpenFoam. European Conference on Computational Fluid Dynamics (ECCOMAS CFD'10), Lisbon, Portugal, 14-17 June.

Bertram, V., 2000. Practical ship hydrodynamics. Oxford: Butterworth-Heinemann.

Carlton, J., 2007. Marine propellers and propulsion. 2nd edition. Oxford, Butterworth-Heinemann.

Carrica, P.M., Alejandro, M., and Stern, F., 2010. Self-propulsion computations using a speed controller and a discretized propeller with dynamic overset grids. Journal of marine science and technology, 15(4), pp.316-330.

Carrica, P.M., Alejandro, M., and Stern, F., 2011. Full scale self-propulsion computations using a discretized propeller for the KRISO container ship KCS. Journal of computers and fluids marine science and technology, 51, pp.35-47.

Castro, A.M., Stern, F., and Carrica, P.M., 2011. Full scale self-propulsion computations using discretized propeller for the KRISO container ship. Journal of Computers and fluids, 51(1), pp.35-47.

Chao, K., 2005. Numerical Propulsion Simulation for the KCS Container Ship, Proceedings of CFD Workshop Tokyo, Tokyo, Japan, pp.539-545.

Choi, J.E., Kim, J.H., Lee, H.G., Choi, B.J. and Lee, D.H., 2010. Computational prediction of ships speed performance. Journal of marine science and technology, 15, pp.64-77.

Couser, P., Wellicome , J., and Molland, A., 1998. An improved method for the theoretical prediction of the wave resistance of transom-stern hulls using a slender body approach. International Shipbuilding Progress, 45, 331-349.

Date, J.C and Turnock, S.R., 2002. Computational evaluation of the periodic performance of a NACA 0012 fitted with a Gurney flap. Journal of Fluids Engineering 124, 227-234.

Deng, G.B., Queutey, P., and Visonneau, M., 1993. Navier Stokes computation of ship stern flows: a detailed comparative study of turbulence models and discretization schemes. in 6th International Conference on Numerical Ship Hydrodynamics, Iowa City-Iowa.

DNV., 2001. Rules for classification of ships, new buildings, hull and equipment main class, Assessed April 2014,fromhttps://exchange.dnv.com/publishing/rulesship/200107/currentbooklets.pdf.

Eça, L., Hoekstra, M., Windt, J., 2002. Practical Grid Generation Tools with Applications to Ship Hydrodynamics, in 8th International Conference in Grid Generation in Computational Field Simulations, Hawaii, USA.

Epps, B., Ketcham, J., Chryssostomos, C., 2010. Propeller blade stress estimates using lifting line theory. in proceeding of the conference on Grand Challenges in Modelling and Simulations (GCMS'10), pp.442-447.

Flood, K.M., 2002. Propeller performance analysis using lifting line theory, of high lift rudders operating under steady and periodic flow conditions, MSc thesis, Massachusetts Institute of Technology.

Froude, W., 1878. On the elementary relation between pitch slip and propulsive efficiency. Transactions of the Institution of Naval Architects, 19, pp.47–65.

Fujisawa, J., Ukon, Y., Kume, K., and Takeshi, H., 2000. Local velocity measurements around the KCS Model (SRI M.S. No. 631) in the SRI 400m Towing Tank, Ship Perf. Div. Rep. No. 00-003-2, SRI, Tokyo, Japan.

Giles, W., Buckingham, J., Atkins, J., and Jones, A., 2013. An investigation into twin skeg hull forms in auxiliary tanker design. Assessed June 2014, from http://www.bmtdsl.co.uk/media/5045591/BMTDSL-An-Investigation-Into-Twin-Skeg-Hullforms-In-Auxiliary-Tanker-Design-Pacific-October-2013.pdf.

Goldstein, S., 1929. On the Vortex Theory of Screw Propellers. Proc. of the Royal Society, 123, 440, (A).

Gorski, J.J., 2001. Present state of numerical ship hydrodynamics and experiments. in 20th International Conference of Offshore Mechanics and Arctic Engineering, Rio de Janeiro, June3-8.

Hafermann, D., and Marzi, J., 2011. Propulsion enhancements for a greener environment. in Second International Symposium on Marine Propulsors smp'11, Hamburg, Germany.

Han, K., Larsson, L., and Regnström, B.A., 2008. Numerical study of hull- propeller-rudder interaction. In 27th Symposium on Naval Hydrodynamics Konferensbidrag, refereegranskat, 5-10 October.

Hatay, F. F., and Biringen, S., 1995. Direct numerical simulation of low-Reynolds number supersonic turbulent boundary layers.

Henn, D., and Sykes, R., 1999. Large-eddy simulation of flow over wavy surfaces. Journal of Fluid Mech, 383, pp.75–112.

Hino, T., 2005. CFD workshop Tokyo. In Proceedings of the CFD Workshop Tokyo, National Maritime Institute of Japan.

Höerner, S. F., 1965. Fluid dynamic drag. Midland Park, New Jersey.

Hough, G., and Ordway, D., 1965. The Generalized Actuator Disk. Technical Report TARTR 6401, Therm Advanced Research, Inc.

Hydrodynamic characteristics of propellers 2014. Assessed April 2012, from http://traktoria.org/files/personal˙submarine/propulsion/propeller/lecture˙notes hydrodynamic˙characteristics˙of˙propellers.pdf.

IGU, 2013. International Gas Union World LNG Report. Assessed April 2014, from http://www.lngglobal.com/latest/international-gas-union-world-lng-report-2013.html.

Issa, R., 1986. Solution of the implicitly discretised fluid flow equations by operator splitting. Journal of Computational Physics, 62(1), pp.40–65.

ITTC, 1990. Report of the Resistance and Flow Committee. In proceedings of the 19th International Towing Tank Conference, Madrid, Spain, 12–22 September.

ITTC, 1999. The Resistance Committee: Final report and recommendations to the 25th ITTC. In proceedings of the 22nd International Towing Tank Conference.

ITTC, 2008. Recommended procedure and guidelines: Uncertainty analysis in CFD verification and validation methodology and procedures. In proceedings of the 25th International Towing Tank Conference, Fukuoka, Japan.

ITTC, 2011. The propulsion Committee: Final report and recommendations to the 26th ITTC. In proceedings of the 26th International Towing Tank Conference, Rio de Janeiro, Brazil, August28-September.

IWWWFB, 2012. International Workshop on Water Waves and Floating Bodies (IWWWFB27). *in* proceedings of the 27th international workshop on water waves and floating bodies, (IWWWFB27), Copenhagen, Denmark 22-25 April. Assessed September 2014, from http://www.iwwwfb.org/Workshops/27.htm.

Jasak, H., Jemcov, A., and Tukovijc, V., 2007. OpenFOAM: A C++ library for complex physics simulations. In International Workshop on Coupled Methods in Numerical Dynamics. 19th-21st September, Dubrovnik, pp. 47–66.

Kerwin, J.C., 1979. The solution of propeller lifting surface problems by votex lattice method. Report, Department of Ocean Engineering, MIT.

Kim, W.J. and Kim, D.H., 2001. Measurement of flows around modern commercial ship models. Journal Experiments in Fluid, 31, pp.567–578.

Kim, J., Park, I.R., Lee, Y.Y., Yoon, H.S., and Van, S.H., 2006. Flow measurement around a model ship with propeller and rudder. Journal of Experiments in Fluids 20 (4) pp.533-545.

Kim, K., Fabian, T., Nicolas, B., and Hans, L., 2013. Hydrodynamic Optimization of Twin-skeg LNG ships by CFD and Model Testing. in proceedings of the 12th International Symposium on Practical Design of Ships and Other Floating Structures (PRADS), Changwon, Korea, 20-25 October.

Kodama, Y., 1989. Grid generation and flow computations for practical ship hull forms and propellers using the geometrical method and the IAF Scheme. In 5th ICNSH, Hiroshima, Japan.

Kodama, Y., Takeshi, H., Hinatsu, M., Hino, T., Uto, S., Hirata, N., and Murashige, S., 1994. (eds.) Proceedings, CFD Workshop. Ship Research Institute, Tokyo, Japan.

Larsson, L., 1981. SSPA-ITTC Workshop on Ship Boundary Layers. SSPA Publication No. 90, Ship Boundary Layer Workshop Göteburg.

Larsson, L., Patel, V., and Dyne, G., 1991. In Proceedings of the 1990 SSPA-CTH-IIHR Workshop on Ship Viscous Flow. Flowtech International Report No. 2.

Larsson, L., Stern, F., and Bertram, V., 2003. Benchmarking of Computational Fluid Dynamics for Ship Flows: The Gothenburg 2000 Workshop. Journal Ship Research, 47, pp.63–81.

Larsson, L., and Zou, L., 2010. CFD prediction of local flow around the KVLCC2 tanker in fixed condition. A Workshop on Numerical Ship Hydrodynamics: The Gothenburg 2010 Workshop December 8-10, 2010.

Larsson, L., Stern, F., and Visonneau, M., 2013. Numerical Ship Hydrodynamics: An assessment of the Gothenburg 2010 Workshop, Springer.

Lübke, L., and Abdel-Maksoud, 2002. Berechnung des Nachstromfeldes der Groβausführung, STG Sprechtag, Hamburg.

Lübke, L., 2005. Numerical simulation of flow around the propelled KCS, Proceedings of CFD Workshop Tokyo, Tokyo, Japan, pp.587-592.

Maersk, 2011. Annual report, A.P.Moller-Maersk A/S.

Menter, F.R., 1994. Two-equation eddy viscosity turbulence models for engineering applications. AIAA journal, 32(8), pp.1598–605.

Mikkelsen, R., 2003. Actuator Disc Methods Applied to Wind Turbines, Ph.D thesis, University of Denmark.

Molland, A.F and Turnock, S.R., 1990. Wind tunnel test results for a model ship propeller based on a modified wageningen b4.40. Technical report, University of Southampton, Ship Science Report No. 43.

Molland, A.F and Turnock, S.R., 1991. Wind tunnel investigation of propeller loadings on ships rudder performance. Technical report, University of Southampton, Ship Science Report No. 46.

Molland, A.F and Turnock, S.R., 1995. Wind tunnel test on the effect of a ship hull on rudder-propeller performance at different drift angles. Technical report, University of Southampton Ship Science Report No. 76.

Molland, A.F., and Turnock, S.R., 1996. A compact computational method for predicting forces on a rudder in a propeller slipstream. Transactions of the Royal Institution of Naval Architects, 138, pp.227–244.

Molland, A.F., and Turnock, S.R., 2002. Flow straightening effects on a ship rudder due to upstream propeller and hull. In International Shipbuilding Progress. pp. 195–214.

Molland, A.F., and Turnock, S.R., 2007. Marine rudders and control surfaces: principles, data, design and applications, Oxford: Butterworth-Heinemann.

Molland, A.F, Turnock, S.R., Hudson, D.A., 2011. Ship resistance and propulsion: practical estimation of ship propulsive power, Cambridge: University Press.

Muntean, T., 2008. Ship propulsion train efficiency sensing, Wartsila Technical Journal.

Muscari, R., Felli M., and Di Mascio, A., 2010. Numerical and experimental analysis of the flow around a propeller behind a fully appended hull. in 28th Symposium on Naval Hydrodynamics, Pasadena, CA USA.

Notteboom, T.E. and Vernimmen, B., 2008. The effect of high fuel costs on liner service configuration in container shipping. Journal of Transport Geography, 17(5), pp.325–337.

OpenCFD, 2011. OpenFOAM: The Open Source CFD Toolbox. User Guide Version 2.1.0

Patankar, S.V., and Spalding, D.B., 1972. A calculation procedure for heat, mass and momentum transfer in three-dimensional parabolic flows. International Journal of Heat and Mass Transfer, 15, pp.1787–1806.

Patel, V.C., 1988. Ship stern and wake flows: Status of experiment and theory. in 17th Symposium on Numerical Hydrodynamics, The Hague, Netherlands.

Phillips, A.B., Turnock, S.R., and Furlong, M.E., 2009. Evaluation of manoeuvring coefficients of a self-propelled ship using a blade element momentum propeller model coupled to a Reynolds averaged Navier Stokes flow solver. Ocean Engineering, 36(15-16), pp.1217–1225.

Phillips, A.B., Turnock, S R and Furlong, M.E., 2010. Accurate capture of rudder-propeller interaction using a coupled blade element momentum-RANS approach. Ship Technology Research (Schiffstechnik), 57(2), 128-139.

Pien, P.C., 1961. The calculations of marine propellers based on lifting surface theory. Journal of Ship Research, 5(2), pp.1-14.

Quadvlieg, F., Valkhof, H., and Dallinga, R., (2003). MARIN plays key role in design of booming LNG fleet, MARIN Report No 81. Assessed April 2014, from http://www.marin.nl/web/Publications/Publication-items/MARIN-plays-key-role-in-design-of-booming-LNG-fleet.htm.

Rankine, W.J.M., 1865. On the mechanical principles of the action of the propeller. Transactions of the Institution of Naval Architects, 6, pp.13–39.

Sakamoto, N., Kawanami, Y., Uto, S., and Sasaki, N., 2013. Estimation of Resistance and Self-propulsion characteristics for a Low L/B Twin-Skeg Container Ship by High- Fidelity RANS Solver. Journal of Ship Research, 57(1), pp.24-41.

Seol, H., Jung, B., Suh, J.C., and Lee, S., 2002. Prediction of non-cavitating underwater propeller noise. Journal of sound and vibration, 257(1), pp.131-156.

SIMMAN, (2008). Workshop on verification and validation of ship manoeuvring simulation methods, Copenhagen, April 14 -16.

SIMMAN, (2014). Workshop on verification and validation of ship manoeuvring simulation methods. Assessed April 2014, from www.simman2014.dk/cms/site.aspx?p=13307.

Simonsen, C., 2000. Propeller–Rudder Interaction by RANS, Ph.D thesis, University of Denmark.

Simonsen, C., and Stern, F., 2003. Verification and Validation of RANS manoeuvring simulation of Esso Osaka: effects of drift and rudder angle on forces and moments. Journal of Computers and Fluids, 32, pp.1325-1356.

Simonsen, C and Stern, F., 2005. RANS manoeuvring simulation of Esso Osaka with rudder and body-force propeller. Journal of Ship Research, 49(2), pp.98-120.

SSPA, 2009. SSPA Newsletter 46/2009: "Green Hydrodynamic Design".

Stainer, M.J., 1998. Investigations into propeller skew using a RANS code. Part2: Scale effect. International Shipbuilding Progress, 45, (443), pp.253-265.

Starke, A.R., Windt, J., and Raven, H.C., 2006. Validation of viscous flow and wake field predictions for ships at full scale. 26th ONR Symposium on Naval Hydrodynamics, Rome, Italy.

Stern, F., Wilson, R.V., Coleman, H.W., and Paterson, E.G., 2001. Comprehensive approach to Verification and Validation of CFD simulations. Part 1: Methodology and procedures, Journal of Fluids Engineering, 123, (4), pp.793-802.

Stern, F., Castro, A.M., and Carrica, P.M., 2010. Self-propulsion computations using a speed controller and a discretize propeller with dynamic overset grids, Journal of Marine Science Technology, 15, pp.316-330.

Tahara, Y., and Stern, F., 1996. A large-domain approach for calculating ship boundary layers and wave fields for non-zero Froude number. Journal of Computational Physics, 127, pp.398-411.

Tachmindji, A.I., and Milam, A.B., 1957. The calculation of the circulation for propellers with finite hub having 3, 4, 5, 6 blades. DTMB Report No. 1141.

Ubbink O. and Issa R.I., (1999), Method for capturing sharp fluid interfaces on arbitrary meshes, J. Comput. Phys., 153, 26-50Journal of marine science and technology, 11, pp.209-228.

Van Beek, T., 2004. Technology Guidelines for Efficient Design and Operation of Ship Propulsors, Marine News, Wärtsilä Propulsion, Netherlands BV.

Versteeg, H.K., and Malalasekere, W., 2007. An Introduction to Computational Fluid Dynamics: The Finite Volume Method, 2nd edition, Pearson Prentice Hall.

Visonneau, M., Queutey, P., and Deng, G.B., 2006. Model and full-scale free-surface viscous flows around fully-appended ships. ECCOMAS CFD, Egmond aan Zee.

Wang, X., and Walters, K., 2012. Computational analysis of marine propeller performance using transition-sensitive turbulence modeling. Journal of Fluids Engineering, 134(7), pp.071107.

Weller, H.G., Tabor, G.R., Jasak, H. and Fureby, C., 1998. A tensorial approach to computational continuum mechanics using object-oriented techniques. Computers in Physics, 12(6), pp.620–631.

Wieghardt, K., 1982. Kinematics of ships wake flow: The Seventh David Taylor (Memorial) Lecture, DTNSRDC Report 81/093.

Wieghardt, K., and Kux, J., 1980. Nomineller nachstrom auf grund von windkanalversuchen, jahrbuch der schiffbautechnischen gesellschaft, 74, pp.303–318.

Wiesmann, A., 2010. Slow steaming-a viable long term option. WARTSILÄ Technical Journal 02.2010, 49-55.

Yunming, Q.Y.Q., Zuyuan, L., Xide, C. and Chengsheng, Z., 2010. Numerical calculation of manoeuvring hydrodynamic forces of drift ship based on SST k-w turbulence model. *in* 2nd International Conference on Computer Engineering and Technology (ICCET), 16-18 April.

Zhang, Z., Wu, C., Huang, S., Zhao, F., and Weng, Z., 2010. Numerical simulation of free surface flow of KCS and the interaction between propeller and hull. *in* Proceedings of the Gothenburg 2010 Workshop, December 8-10, 2010.

Appendix 1

Example of code

```
//////////////////////////RANS-BEMt////////////////////////////////////////////////////////////////////////

#define N  2000     // Maximum number of iterations

//////////////////Define the (cylindrical) region for the body force ////////////////

 const scalar yo (readScalar(bodyForceDict.lookup("yo")));const scalar yo2
(readScalar(bodyForceDict.lookup("yo2")));const scalar zo
(readScalar(bodyForceDict.lookup("zo")));const scalar xmin
(readScalar(bodyForceDict.lookup("xmin")));const scalar xmax
(readScalar(bodyForceDict.lookup("xmax")));const scalar PropRadius
(readScalar(bodyForceDict.lookup("PropRadius")));const scalar HubRadius =
0.2*PropRadius;

const scalar rps (readScalar(bodyForceDict.lookup("rps")));
const scalar Dia = 2*PropRadius;
vector unitVector(bodyForceDict.lookup("directionVector"));
unitVector /= mag(unitVector);

////////////////////Read in properties of segment subdomains//////////////////////
const int No˙R =10;  //Number of  radial slices nR
const int No˙Theta =3; //Number of circumferential slices nC
///////////////BLADE ELEMENT BEGINS HERE//////////////////////////

//////////////////////////////BLADE ELEMENT CONSTANTS ////////////////

scalar VV=0.0;
const scalar LA=0.97;
const scalar RT=0.045;
const scalar LM=0.8*11.3;
```

```
const scalar LI=0.8*12.67;
const scalar deltaX =0.05;

//////////////////////////////Propeller
Parameters//////////////////////////////

// Define propeller parameters from open-water data this is used for BEMT
const scalar J(readScalar(bodyForceDict.lookup("J")));
const scalar P˙D(readScalar(bodyForceDict.lookup("P˙D")));
const scalar BARatio(readScalar(bodyForceDict.lookup("BARatio")));
const scalar NosBlades(readScalar(bodyForceDict.lookup("NosBlades")));   //number of
blades
const scalar rho(readScalar(bodyForceDict.lookup("rho")));   //density
//Calculate parameters of segment subdomains:
const scalar dTheta = (360/No˙Theta)*constant::mathematical::pi/180; // theta is in
radians
const scalar dR  = (HubRadius+(PropRadius-HubRadius))/(No˙R);

//////////////////////////Nominal wake details for propeller//////////////////////

//wake fraction matrix[RADIUS][SECTORS]//Portpropeller
scalar W˙T[No˙Theta][No˙R]=
{
        {0.0, 0.0, 0.0, 0.0, 0.0, 0.0, 0.0, 0.0, 0.0, 0.0},
        {0.0, 0.0, 0.0, 0.0, 0.0, 0.0, 0.0, 0.0, 0.0, 0.0},
        {0.0, 0.0, 0.0, 0.0, 0.0, 0.0, 0.0, 0.0, 0.0, 0.0},
};

//wake fraction matrix[RADIUS][SECTORS]//Stbd propeller
scalar W˙T2[No˙Theta][No˙R]=
{
        {0.0, 0.0, 0.0, 0.0, 0.0, 0.0, 0.0, 0.0, 0.0, 0.0},
        {0.0, 0.0, 0.0, 0.0, 0.0, 0.0, 0.0, 0.0, 0.0, 0.0},
        {0.0, 0.0, 0.0, 0.0, 0.0, 0.0, 0.0, 0.0, 0.0, 0.0},
};

//////////////////////Tangential wake details for port
propeller//////////////////////

////////////VTT is taken to be wake fraction in the plane of the propeller and
tangential to the radial direction (see Molland &Turnock
2011)/////////////////////////
```

```
//Tangential wake fraction matrix[RADIUS][SECTORS]//port propeller
scalar STT[No˙Theta][No˙R]=
{
        {0.0, 0.0, 0.0, 0.0, 0.0, 0.0, 0.0, 0.0, 0.0, 0.0},
        {0.0, 0.0, 0.0, 0.0, 0.0, 0.0, 0.0, 0.0, 0.0, 0.0},
        {0.0, 0.0, 0.0, 0.0, 0.0, 0.0, 0.0, 0.0, 0.0, 0.0},
};
//Tangential wake fraction matrix[RADIUS][SECTORS]//stbd propeller
scalar STT2[No˙Theta][No˙R]=
{
        {0.0, 0.0, 0.0, 0.0, 0.0, 0.0, 0.0, 0.0, 0.0, 0.0},
        {0.0, 0.0, 0.0, 0.0, 0.0, 0.0, 0.0, 0.0, 0.0, 0.0},
        {0.0, 0.0, 0.0, 0.0, 0.0, 0.0, 0.0, 0.0, 0.0, 0.0},
};
////////////////////////////////////////////////////////////////////////////
////
//main Iteration Loop (for each blade element!)
float PA[10] =
{
        {0.0, 0.0, 0.0, 0.0, 0.0, 0.0, 0.0, 0.0, 0.0, 0.0}; //Pitch Distribution along blade
length relative to pitch distribution at R=0.7

float C2[10] =
{
        {0.0, 0.0, 0.0, 0.0, 0.0, 0.0, 0.0, 0.0, 0.0, 0.0}; //Chord Distribution along blade
length r

////////////////////////////////////////////////////////////////////////////
////
for (int n = 0; n < No˙Theta; n++)  //loop over sectors
_
scalar VV=0.0;
for (int i = 1; i < No˙R-1; i++)  //assuming hub radius of 0.2R iterate through blade
elements to 0.9R assume zero thrust and torque at tip
{
        J˙local =J*(1-W˙T[n][i]);
        VTT=STT[n][i]/(1-W˙T[n][i]);
        PR[i] = P˙D * PA[i]; // Pitch diameter ratio at blade element
        C1 [i] = C2[i]*BARatio*4.0/(NosBlades*0.5);
```

```
        scalar CP = NosBlades*C1[i]; //Nc/D
         X[i] = (i+1)/20.0; //x/R
        AI[i] = 0; // Assume initial Angle of Attack=0
        scalar TD = RT-(RT*0.935)*X[i];
        TC[i] = TD/C1[i];

//////////////////////////////////////////////////////////////////////////////
//////////////////////////////////////////////////////////

          // Sub loop iterates on angle of attack
          for(int j = 0; j< N; j = j + 1)
         {
                scalar HA =
          Foam::atan(PR[i]/(constant::mathematical::pi*X[i]))/constant::mathematical::pi*1
80-AI[i];// Calculate local hydrodynamic pitch angle - phi (deg)
     scalar H1 = Foam::tan(HA/180*constant::mathematical::pi); // tan phi
     scalar AA = J˙local/(constant::mathematical::pi*X[i]); // tan psi (undisturbed flow
angle?)
     scalar EI = AA/H1;  // Ideal Efficiency
     EA[i] = 0.9*EI;  // Local Efficiency Estimate
     AE = 0.0; // tan(gamma) =atan(Cd(i)/Cl(i)) assume =0.0
     scalar KF = X[i]*H1; // Lambda parameter for Goldstein correction
     FTT = VTT*AA; //wake rotation factor a"
////////////////////////////// Calculate Goldtein Correction, K
///////////////////////////////////
    //Tachmindij correction
scalar phii= HA*constant::mathematical::pi/180;
scalar corr= (-0.000000000004*pow(phii,6))+(0.0000000005*pow(phii,5))-
(0.000000009*pow(phii,4))+(0.0000009*pow(phii,3))-
(0.00008*pow(phii,2))+(0.0006*phii)-(0.0004);

     scalar SF = NosBlades/(2.0*KF)-0.5;
     scalar F1 = Foam::cosh(SF);
     scalar F2 = Foam::cosh(SF*X[i]);
     scalar F3 = F2/F1;
     scalar F4 = Foam::acos(F3);
     scalar K=2.0*F4/constant::mathematical::pi+corr;
//////////////////////////////////////////////////////////////////////////////
      GK[i] = K; //Store local Goldstien Correction to an array
//////////////////////////////////////////////////////////////////////////////
////
```

```
            // subsubloop - iterates local efficency
            for (int counter2 =0; counter2< N; counter2++)
                {
                // Remember that FTT is set to +ve for downgoing blade( with
                    upwards flow) do change the sign to -ve  if the case is upgoing
                    blade( with downwards flow)

             FA[i] = (1-EI+FTT)/(EI+AA*AA/EA[i]); // axial flow factor
            KT[n][i] =
constant::mathematical::pi*pow(J˙local,2)*X[i]*K*FA[i]*(1+FA[i]);
                // local dKT/dx
             AE = Foam::tan(AE/180*constant::mathematical::pi); // tan(gamma)
             FT[i] = 1-EI*(1+FA[i]+FTT);   // a' tangential flow factor
////////////////////Calculate required lift coefficient - CL
/////////////////////////
            CL[i] = KT[n][i]*Foam::cos(HA/180*constant::mathematical::pi);
            CL[i] = CL[i]*4/pow(constant::mathematical::pi,2)/(pow(X[i],2));
            CL[i] = CL[i]/(pow((1-FT[i]+FTT),2)*(1-H1*AE)*CP);
////////////////////%Calculate Drag Coefficient CD
/////////////////////////////
      scalar F6 =  0.0107+(AI[i]+1.0)*(-0.0015+AI[i]*(0.0015+0.000965*(AI[i]-1.0)));
      scalar F7 = -0.03833+(AI[i]+1.0)*(0.0133+AI[i]*(-0.015-0.01166*(AI[i]-1.0)));
      scalar F8 =  0.8193+(AI[i]+1.0)*(-0.0138+AI[i]*(0.0903+0.079*(AI[i]-1.0)));
      scalar F9 = -3.076+(AI[i]+1.0)*(-0.0728+AI[i]*(-0.3162-0.2437*(AI[i]-1.0)));
      CD[i] = F6+TC[i]*(F7+(TC[i]-0.06)*(F8+F9*(TC[i]-0.12)));
/////////////////////////////
            scalar AG = CD[i]/CL[i];
            AE = Foam::atan(AG)/constant::mathematical::pi*180; //  gamma
            scalar EZ = AA/Foam::tan((HA+AE)/180*constant::mathematical::pi);

          if (abs(EZ-EA[i]) ¡ 0.001)   // Initial estimate of local efficiency EA(I) is
sufficiently
          close to calculated value

           {

      //////camber corrections for various BARs switch on according to the desired
BAR //


        //float K2[10] {0.0, 0.0, 0.0, 0.0, 0.0, 0.0, 0.0, 0.0, 0.0, 0.0};//BAR



                scalar U1 = -0.65*KF*KF+1.1*KF+0.664;
```

```
                scalar U2 = (0.85+(KF-0.3)*(-4.0+(KF-0.4)*(15.42-47.95*(KF-0.5))));
                U2 = -0.09+(KF-0.2)*U2;
                scalar U3 = (1.375+(KF-0.3)*(-3.75+(KF-0.4)*(20.85-75.7875*(KF-
0.5))));
          U3 = -0.2+(KF-0.2)*U3;
                scalar K1 = U1+(BARatio-0.4)*(U2+U3*(BARatio-0.8));
                CC[i] = K1*K2[i];
        ////////////////////////////////////////////////////////////////////
          if (VV==1) {
                        MC[i] = MT[i]*TC[i];
                        AC =(CC[i]*CL[i]/LI-MC[i])*LM/0.1097+(MC[i]*LI/LA);
                    }
          else if (VV==5) {

                    MC[i]=0.5*TC[i];
                         AC = (CC[i]*CL[i]/LI-MC[i])*LM/0.1097+(CL[i]/LA);
                        MT[i] = MC[i]/TC[i];
                        }

          else {
                    AC = CL[i]/LA;
                    MC[i]= CL[i]/LI;
                    MC[i]= MC[i]*CC[i];
                        }
        ////////////////////////////////////////////////////////////////////
         if (MC[i] <0.5*TC[i]) {
                       MT[i]=MC[i]/TC[i];
                        }
            else {
                    VV=5;
                    MC[i] = 0.5*TC[i];
                    AC = (CC[i]*CL[i]/LI-MC[i])*LM/0.1097+(CL[i]/LA);
                    MT[i]= MC[i]/TC[i];
                    EA[i] = EZ;
                    }

////////////////////////////////////////////////////////////////////

      };  //end subsubloop
```

```
////////////////////////////////////////////////////////////////////////////////
/
    if (abs((AC-AI[i])/(AC))¡0.1) {  // subloop converged difference between angle of
attack  assumed AI and calculated angle of attack AC <0.1*AC
                    KQ[n][i]=4.935*J˙local*X[i]*X[i]*X[i]*K*FT[i]*(1+FA[i]); // calculate
dkq/dx
                                    ″

      else {
           AI[i]=(AC+AI[i])/2;     // New Guess of Angle of Attack AI(i)
          ″


////////////////////////////////////////////////////////////////////////////////
///
  }; // end sub loop
};// end main loop
////////////////////////////////////////////////////////////////////////////////

//////////////////////SECTORIAL APPROACH//////////////////////////////
//Reset segment Volumes to zero at the beginning of each time step.
for (int n=0;n<No˙Theta; n++) //loops over sector
{
       for (int i=3;i <No˙R-1; i++) //loops over radius
       {
        segmentVolume [n][i] = 0;
       }
  }
//Reset segment Volumes to zero at the begining of each timestep.
for (int n=0;n<No˙Theta; n++) //loops over sector
{
       for (int i=3;i<No˙R-1; i++) //loops over radius
       {
        segmentVolume2 [n][i] = 0;
       }
}
////////////// Start loop through all cells in mesh to define segment volumes
//////////////
//const vector& cellCenter = vector::zero;
```

```
forAll(mesh.cells(),cellI)
{
// Loop over all the cells in the mesh
 ++numCells;
// Check containment of each cell centre
        const vector& cellCenter = mesh.C()[cellI];
          const scalar dy = cellCenter[1] - yo;
        const scalar dz = cellCenter[2] - zo;
        const vector r(0,dy,dz);
          const scalar radius = mag(r);
          scalar Theta =
(Foam::atan2((float)dz,(float)dy)/constant::mathematical::pi*180)*constant::mathematica
l::pi/180;// calculates the angle in radians

           if(Theta<0) {

                Theta=(2*constant::mathematical::pi)+Theta;
                      }
//////////////////////Define segment
volumes////////////////////////////////
for (int n=0; n<No˙Theta; n++)
{
        scalar ThetaSeg = ((n* dTheta)+(dTheta/2)); //This is calculating the angle in
        radians

       for (int i=3; i<No˙R-1; i++)
            {
            Outer˙R = (HubRadius+(PropRadius-HubRadius))*((i+1)/((float)No˙R));
            Rseg = Outer˙R+(dR/2);
            if ((cellCenter[0] < xmax) &&
            (cellCenter[0] >  xmin) &&
            (Theta < ThetaSeg +(dTheta/2)) &&
            (Theta >  ThetaSeg -(dTheta/2)) &&
            (radius > Rseg) &&
            (radius < Rseg+dR)) {
                  ++numInside;
                  totalVolume += mesh.V()[cellI];
                  segmentVolume[n][i] += mesh.V()[cellI];
        }
                }
```

```
                    }
                        }


//////////////////////////////////////////////////////////////////////////////
////

// Set the body force magnitude
if (totalVolume <  0){
//const vector& cellCenter = vector::zero;
forAll(mesh.cells(),cellI)
{
// Loop over all the cells in the mesh
++numCells;

//convert to cylindrical coordinate system
        const vector& cellCenter = mesh.C()[cellI];  //
        const scalar dy = cellCenter[1] - yo;
      const scalar dz = cellCenter[2] - zo;
      const vector r(0,dy,dz);
        const scalar radius = mag(r);
       scalar Theta =
(Foam::atan2((float)dz,(float)dy)/constant::mathematical::pi*180)*constant::mathematica
l::pi/180;// calculates the angle in radians

         if(Theta¡0)–
             Theta=(2*constant::mathematical::pi)+Theta;
         ”
//////////////////////////////////////////////////////////////////////////////
/////////////////
//Define momentum source terms:
//scalar axialForce;
for (int n=0; n<No˙Theta; n++)
        {
      scalar ThetaSeg = ((n* dTheta)+(dTheta/2));
       for (int i=3; i¡No˙R-1; i++)
            {
             Outer˙R = (HubRadius+(PropRadius-HubRadius))*((i+1)/((float)No˙R));
             Rseg = Outer˙R+(dR/2);

         if ((cellCenter[0] < xmax) &&
```

```
            (cellCenter[0] >  xmin) &&
            (Theta < ThetaSeg +(dTheta/2)) &&
            (Theta >  ThetaSeg -(dTheta/2)) &&
            (radius > Rseg) &&
            (radius < Rseg+dR)) {

        // calculate forces(Thrust &Torque)
        axialForce =
((KT[n][i]*deltaX)*rho*pow(rps,2)*pow(Dia,4))/(segmentVolume[n][i])/rho/No˙Theta;
        tangentialForce =
((KQ[n][i]*deltaX)*rho*pow(rps,2)*pow(Dia,5))/mag(r)/(segmentVolume[n][i])/rho/No˙T
heta;
        vector tempForce(axialForce, -dz/mag(r)*tangentialForce,
dy/mag(r)*tangentialForce);
        bodyForce[cellI] = tempForce;

            // as a diagnostic, compute total integrated thrust & torque added
              totalThrust1 += axialForce * mesh.V()[cellI]*rho;
              totalTorque1 += tangentialForce * mag(r) * mesh.V()[cellI]*rho;
              totalVolume1 += mesh.V()[cellI];
            }

                }

                        }

                                }

                                        };

////////////////////////////////////////////////////////////////////////////
//////////////////////
```

```
////////////////////////////////RANS-HO////////////////////////////////////////////////////////////////////////////

///////////////PROPELLER DATA/////////////////////////////////
// Read J at peak efficiency from open-water curve
// Use as initial guess
scalar J(readScalar(bodyForceDict.lookup("J")));

//const scalar Uship (readScalar(bodyForceDict.lookup("Uship")));
const scalar Uship
(readScalar(runTime.controlDict().subDict("shipForces").lookup("magUInf")));
const scalar rhoInf
(readScalar(runTime.controlDict().subDict("shipForces").lookup("rhoInf")));
scalar n(Uship/(J*Dp));

// Hook to libforces and calculate drag
    //const forcesMoments fm =
    forcesMoments fm =
        forces
        (
            "topLevelForce",
            mesh,
            runTime.controlDict().subDict("shipForces")
        ).calcForcesMoment();

    vector totForce = fm.first().first() + fm.first().second();
    scalar drag = totForce.x()/diskFraction;

// Integrate volume of cells in propeller disk
scalar analyticalTotalVolume(3.1415*(tipRadius*tipRadius-
hubRadius*hubRadius)*(xmax-xmin));

forAll(mesh.cells(),cellI)
{
// Loop over all the cells in the mesh
    ++numCells;
    // Check containment of each cell center
    const vector& cellCenter = mesh.C()[cellI];
    const scalar dy = cellCenter[1] - yo;
    const scalar dz = cellCenter[2] - zo;
    const vector r(0,dy,dz);

    if ((pos(xmax-cellCenter[0])) &&
```

```
      (pos(cellCenter[0]-xmin)) &&
      (pos(tipRadius-mag(r))) &&
      (pos(mag(r)-hubRadius))) {
    ++numInside;
    integratedVolume += mesh.V()[cellI];
      }

//////////////////////////////////////////////////////////////////////////////
//////////////////////////////////////////////////////

 #define N 100    // Maximum number of iterations
  scalar J0(J);
  scalar f;
  scalar dfdx;
  scalar tol(1e-6);

  // set thrust equal to drag
  scalar thrust = drag;
  scalar torque (0.0);
  scalar Kt (0.0);
  scalar Kq (0.0);

  // set initial guess for rps (n) and Kt
  n = Uship/(J0*Dp);
  Kt = thrust/(rhoInf*pow(n,2)*pow(Dp,4));

///////////////CURVE  FIT FROM OPEN-WATER////////////////////////
  const scalar a0(readScalar(bodyForceDict.lookup("a0")));
  const scalar a1(readScalar(bodyForceDict.lookup("a1")));
  const scalar a2(readScalar(bodyForceDict.lookup("a2")));
  const scalar a3(readScalar(bodyForceDict.lookup("a3")));
  const scalar a4(readScalar(bodyForceDict.lookup("a4")));
  const scalar a5(readScalar(bodyForceDict.lookup("a5")));

  const scalar b0(readScalar(bodyForceDict.lookup("b0")));
  const scalar b1(readScalar(bodyForceDict.lookup("b1")));
  const scalar b2(readScalar(bodyForceDict.lookup("b2")));
  const scalar b3(readScalar(bodyForceDict.lookup("b3")));
  const scalar b4(readScalar(bodyForceDict.lookup("b4")));
  const scalar b5(readScalar(bodyForceDict.lookup("b5")));

  // Iteration loop
```

```
  for(int i = 0; i < N; i = i + 1) {
    J0 = J;
    // Evaluate the function and its derivative
    // f is a 5th-order polynomial curve-fit for KT(J)
    f = a5*pow(J0,5) + a4*pow(J0,4) + a3*pow(J0,3) + a2*pow(J0,2) + a1*J0
          + a0 - pow(J0,2)*thrust/(rhoInf*pow(Uship,2)*pow(Dp,2));
    dfdx = 5.*a5*pow(J0,4) + 4.*a4*pow(J0,3) + 3.*a3*pow(J0,2) + 2.*a2*pow(J0,1)
          + a1 - 2.*J0*thrust/(rhoInf*pow(Uship,2)*pow(Dp,2));

    // Newton-Raphson step
    J = J0 - f/dfdx;
    n = Uship/(J*Dp);
    Kt = thrust/(rhoInf*pow(n,2)*pow(Dp,4));
////////////////////////////////////////////////////////////////////////////

    // Check for convergence and quit if done
    if(mag(J0-J) <tol) {

      Kq = 0.1*(b5*pow(J0,5) + b4*pow(J0,4) + b3*pow(J0,3) + b2*pow(J0,2) + b1*J0
+ b0);
      torque = pos(Kq)*Kq*rhoInf*pow(n,2)*pow(Dp,5);
        }
                        }

////////////////////////////////////////////////////////////////////////////
////////////////////////////////////////////////////////////

#  include "ktkq.H"

// Set the body force magnitude

if (integratedVolume < 0) {
      forAll(mesh.cells(),cellI)
      {
          // Check containment of each cell center
          const vector& cellCenter = mesh.C()[cellI];
          const scalar dy = cellCenter[1] - yo;
          const scalar dz = cellCenter[2] - zo;
          const vector r(0,dy,dz);

          if   ((pos(xmax-cellCenter[0])) &&
```

```
            (pos(cellCenter[0]-xmin)) &&
                    (pos(tipRadius-mag(r))) &&
                (pos(mag(r)-hubRadius))) –
            rstar=(mag(r)-hubRadius)/(tipRadius-hubRadius);

            tdist = 1.0;
            qdist = 1.0;
        tdist = 3.5183*rstar*::sqrt(1.0-rstar);
            qdist = 2.3757*rstar*::sqrt(1.0-rstar) /((1.0-
hubRadius/tipRadius)*rstar+hubRadius/tipRadius);
            dt = thrust/(integratedVolume/diskFraction)*tdist/rhoInf; // normalize
by rhoInf for simpleFoam
            dq = torque/mag(r)/(integratedVolume/diskFraction)*qdist/rhoInf; //
normalize by rhoInf for simpleFoam

            vector tempForce(dt, -dz/mag(r)*dq, dy/mag(r)*dq);
            bodyForce[cellI] = tempForce;
            // as a diagnostic, compute total integrated thrust & torque added
            integratedThrust += dt * mesh.V()[cellI] * rhoInf; // add rho back in for
integration check
            integratedTorque += dq * mag(r) * mesh.V()[cellI] *rhoInf; // add rho
back in for integration check
        }
    }
}

// Hook to libforces and calculate drag

    forcesMoments fmNew =
        forces
        (
            "topLevelForce",
            mesh,
            runTime.controlDict().subDict("shipForces")
        ).calcForcesMoment();

        totForce = fmNew.first().first() + fmNew.first().second();
        drag = (totForce.x())/diskFraction;
////////////////////////////////////
```

Appendix 2

Rudder and propeller interaction

A2.1 Introduction

Ships rudders are mostly placed in the slipstream of the propeller. Those placed outside of the propeller slipstream are ineffective at zero ship speed. By placing the rudder in the slipstream of the propeller, it utilizes some of the rotational energy in the propeller slipstream, contributing to an increase in propulsive efficiency. The main problem associated with investigating a rudder downstream of a propeller is the induction of swirl velocity and axial acceleration by the propeller. Accurate prediction of the magnitude of the swirl and local velocity is key to successful analysis.

This paper investigates the interaction between a rudder placed downstream of a body force propeller model based on the Hough and Ordway (1965) prescribed thrust and torque distribution to examine the influence of swirl velocity on the forces developed on the rudder. Results are compared with experiments by Molland and Turnock (1991, 1995, 2007), using a modified Wageningen B4.40 propeller and Rudder No.2.

A2.2 Rudder and propeller interaction Case study

A2.2.1 Details of experiment

The experimental data for this study was based on wind tunnel test performed by Molland and Turnock (1995) at the University of Southampton *3.5* x *2.5m* RJ Mitchell wind tunnel. It comprises of a wall mounted all movable rudder model of 0.667m chord length, 1m span and 1.5m aspect ratio based on a NACA0020 section shape and a modified four bladed Wageningen B4.40 propeller. Turbulence strips were attached to the

rudder at a distance of 5.7% from the leading edge of the chord on both sides of the rudder. The experiments were carried out at a propeller advance coefficient J = 0.35. The influence of longitudinal separation was not investigated hence the propeller was constantly fixed at X/D = 0.39. Numerical simulations were performed at rudder angles of -10°, 0° and 10°. Figures A2.1 and A2.2 shows the experimental setup. The propeller and rudder parameters are also shown in Table A2.1.

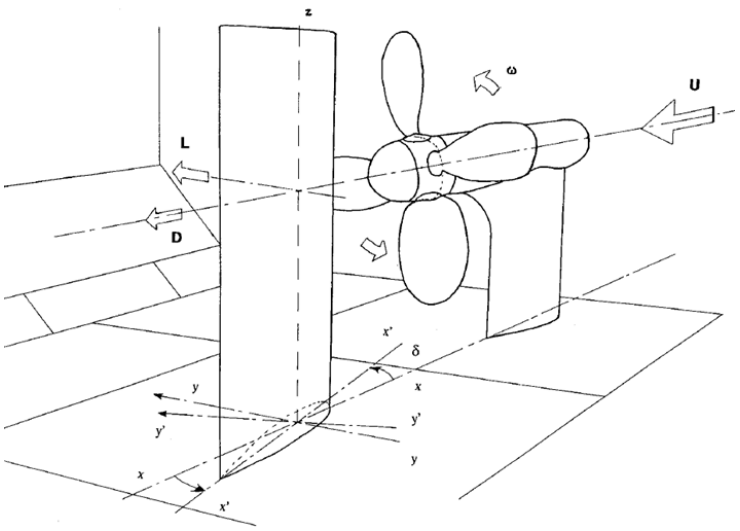

Figure A2.1: Rudder propeller configuration, Molland and Turnock (1991).

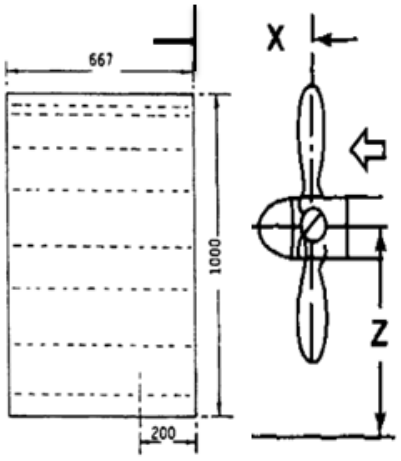

Figure A2.2: Rudder dimensions (mm) and propeller location, Molland and Turnock (1991).

Table A2.1: Propeller data.

Propeller parameter	Dimensions/Type
Number of blades	4
Diameter (mm)	800
Blade area ratio	0.40
Boss diameter [max] (mm)	200
Mean pitch ratio P/D	200
Rake (deg)	0.0
Blade root thickness ratio	0.050
Sections shape	Based on Wageningen B series
Blade outline shape	Based on Wageningen but with reduced skew

A2.2.2 Model domain and boundary conditions

The lateral dimensions of the fluid domain exactly matched that of the wind tunnel, with the domain extending 8 rudder chord lengths upstream and 12 rudder chord lengths downstream. The rudder is turned within the solution domain around the pivot at 0.3c from the leading edge. Free slip wall boundary conditions were used for the wind tunnel walls and roof whilst a no slip wall condition was ensured on the tunnel floor. The air inlet velocity (V) is set at 10 m/s with corresponding pressure set to zero gradient for consistency. At the outlet, fixed value condition (zero relative pressure) was used for the pressure whilst zero gradient condition was used for the velocity. The rudder geometry was modeled by using a no slip wall boundary condition. Since rotating propeller geometry (Figure A2.1) was not used, and only its effect on the flow was included, additional differences between physical and numerical model was introduced. To obtain a smooth distribution of body forces, it was important to identify cells belonging to the actuator disc region and the correct momentum source applied to only those cells. For all calculations, the magnitude of the propeller forces was taken from open water data, Molland and Turnock (1990). The sources imposed on the RANS grid (actuator disc domain) were then derived from equations given in (2.20) and (2.21). By using such approach the action of the rudder on propeller was not incorporated in the simulations.

A2.2.3 Grid generation

The calculations were performed using a single block topology generated in OpenFOAM. An initial background mesh was generated using blockMesh utility, defining the size of the computational domain, with grid node distribution of around $n_\xi = 80$, $n_\eta = 16$, and in the wake $n_\zeta = 12$ of the rudder section. Specific areas of interest within the domain were then specified for refinement in progressive layers. An unstructured non-uniform

hexahedral mesh was then created using the SnappyHexMesh utility within OpenFOAM. The mesh structure was designed to be denser in the vicinity of the rudder geometry and gradually lesser elements near boundaries by using refinement boxes (Figure A3.3a). Such approach enables the simulation run economical. Ten elements were used to capture the boundary layer of the rudder (Figure A2.3c&d) with the first grid node located at 0.0006c away from the rudder (y^+ of 30). The typical size of the final computational mesh was of the order of 4.5 million cells with about 500K elements in the propeller domain. A separate mesh was built for each rudder angle. In addition to this, the grid was clustered around the tip and wake region to resolve the tip vortex and the wake. A three dimensional view of the rudder is illustrated in Figure A2.3a-d details of the mesh.

A2.2.4 Grid sensitivity studies

Sensitivity studies could not be carried out due to the unstructured, non-uniform meshing approached used. Mesh distribution in the propeller domain differs for each rudder incidence considered. This approach made it difficult to use the validation procedure outlined in section 2.3.4. However, Table A2.2 shows the lift and drag obtained using the coarse, medium and fine mesh.

Table A2.2: Mesh sensitivity J =0.35, $\delta = 10^{o}$

Parameter	Coarse 40*x*8*x*6	Medium 57*x*11*x*8	Fine 80*x*16*x*12	Data
Number of Elements	1.5M	3.5M	4.5M	
Lift coefficient, C_L	1.30	1.27	1.22	1.2505
Drag coefficient, C_D	0.20	0.186	0.1477	0.109

.

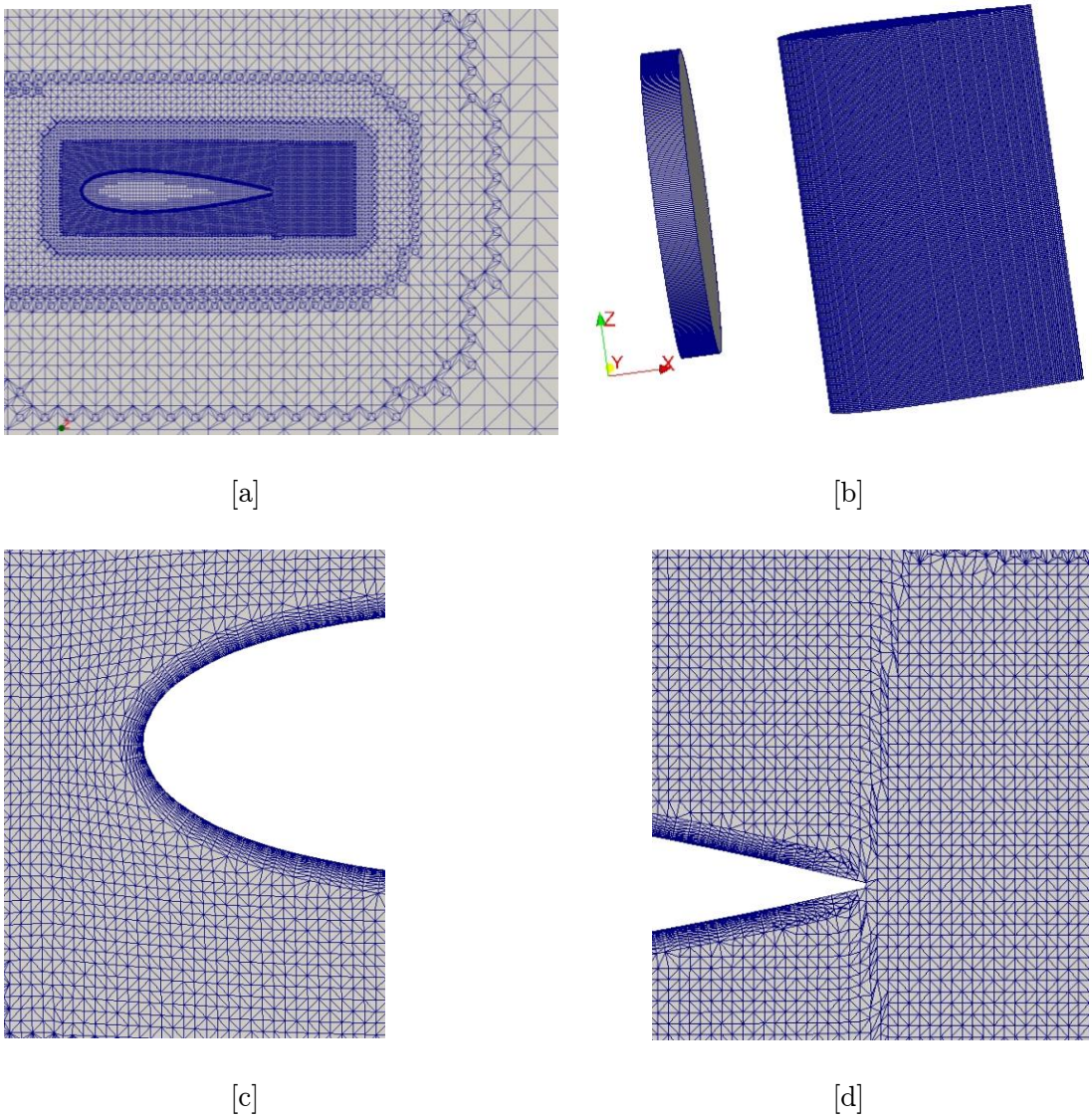

[a] [b]

[c] [d]

Figure A2.3: Details of mesh; [a] horizontal cross-section through the computational mesh, [b] three dimensional view of rudder and propeller region and mesh structure applied to the rudder surface, [c]rudder leading edge [d] rudder trailing edge.

A2.3 Results

A2.3.1 Lift and Drag characteristics

Figures A2.4 and A2.5 compares the experimental and numerical lift and drag results respectively for [a] the rudder freestream characteristics and [b]including the propeller. Results are also compared with Simonsen (2000) and Phillips (2009) who both performed similar investigations using the CFDSHIP-IOWA and ANSYS CFX code respectively and using a Hough and Ordway thrust and torque distribution. Lift slope $\partial C_L/\partial\delta$, values are also compared, Table A2.3. Propeller effects can be seen clearly from the lift and drag plots. In contrast to the free stream rudder, there is an increase in both lift and drag characteristics, this is due to the propeller race significantly increasing the inflow velocity to the rudder. The rudder behind a propeller also has a lift coefficient different from zero for zero rudder incidence. The reason is that due to the rotation in the slipstream, combined with the axial velocity, a local incidence is introduced over the part of the rudder in the slipstream. This local incidence results in a net lift force which is different from zero. The drag coefficient is similar between -10^O and $+10^o$. As rudder incidence is increased, a slight under or over prediction in propeller force will result in a higher or lower local incidence over the part of the rudder in the slipstream. This in turn affects the net drag experienced by the rudder. This can be seen in the results of the drag coefficient plots with an over prediction in rudder drag at -10^O and $+10^o$. At high propeller loadings (lower advance coefficient, J) lift curve slope, $\partial C_L/\partial\delta$ increases, propeller induced velocities predicted using momentum theory under predicts the lift curve slope, (Molland and Turnock, 2007). This can be seen in Table 4.3.

Table A2.3: Mesh sensitivity J =0.35, $\delta = 10^O$

Data	$\partial C_L/\partial\delta$
Molland &Turnock (2007)	0.132
Molland &Turnock (SSR90)	0.136
Simonsen (2000)	0.147
Phillips (2009)	0.136
Numerical-HO	0.129

.

A2.3.2 Rudder Pressure Distribution

Accurate determination of the pressure distribution on the rudder surface is important in the performance of the rudder since it can determine the forces on the rudder. The forces on the rudder however are also controlled by the speed and incidence of the flow downstream of the propeller. To accurately determine the rudder pressure distribution, hence lift characteristics, the magnitude of the swirl and acceleration induced in the flow

by the propeller model has to be accurate, in order to deliver the correct inflow to the rudder. Rudder inflow velocities were extracted and compared with experimental results (Figure A2.6). The propeller code could not recreate the inflow around the rudder root and part of the rudder in hub regions. All other areas including the tip, the inflow velocities were created much better. Figure A2.7 compares the plot of pressure distribution at eight spanwise locations of the rudder from the root to the tip. The computed pressure distribution represented by the local pressure coefficient Cp is given by:

$$Cp = \frac{P - P_\infty}{0.5\rho U^2} \tag{A2.1}$$

where $P - P_\infty$ is the local pressure; ρ is the density and U is the free stream velocity.
Pressure distribution for the rudder freestream characteristics are also plotted in Figure A2.8. Results of the plot in Figure A3.7 are outlined below.

- Span 700mm: - Close to the wall and outside the propeller slipstream, pressure distribution could not be recreated. This is because the floor boundary layer was neglected; hence interaction between the floor and the root could not be modelled.
- Span 230mm: - Just in the slipstream of the propeller, agreement was good for both sides of the rudder at both leading and trailing edge.
- Span 390mm: - Close to centre of slipstream. Local incidence was accurately predicted, resulting in both pressure peaks at suction and pressure side of the rudder and at the leading edge showing good agreement with experiment. The same can be said around the trailing edge.
- Span 530mm: - Centre of slipstream in areas close to the propeller hub. Pressure plots showed poor agreement with experiment. This was expected since the propeller model used does not take into account the effect of the hub. Therefore the interaction between the hub and the part of the rudder close to it could not be modelled.
- Span 700mm: - Same effect as Span 530mm observed. Local inflow angle resulting from the hub was not accurately predicted, resulting in pressure peaks at both sides of the rudder close to leading edge not accurately predicted.

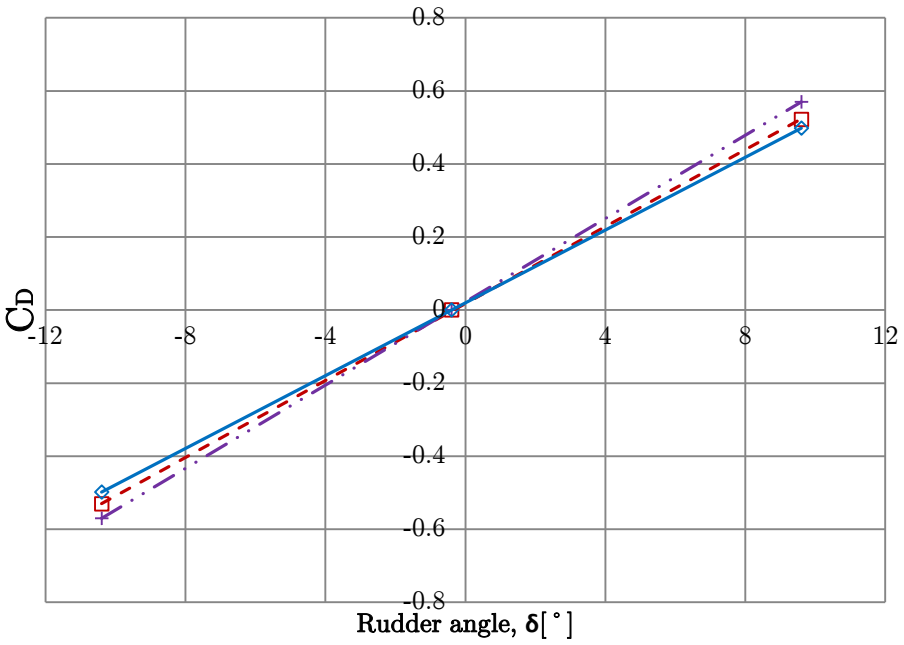

[a]

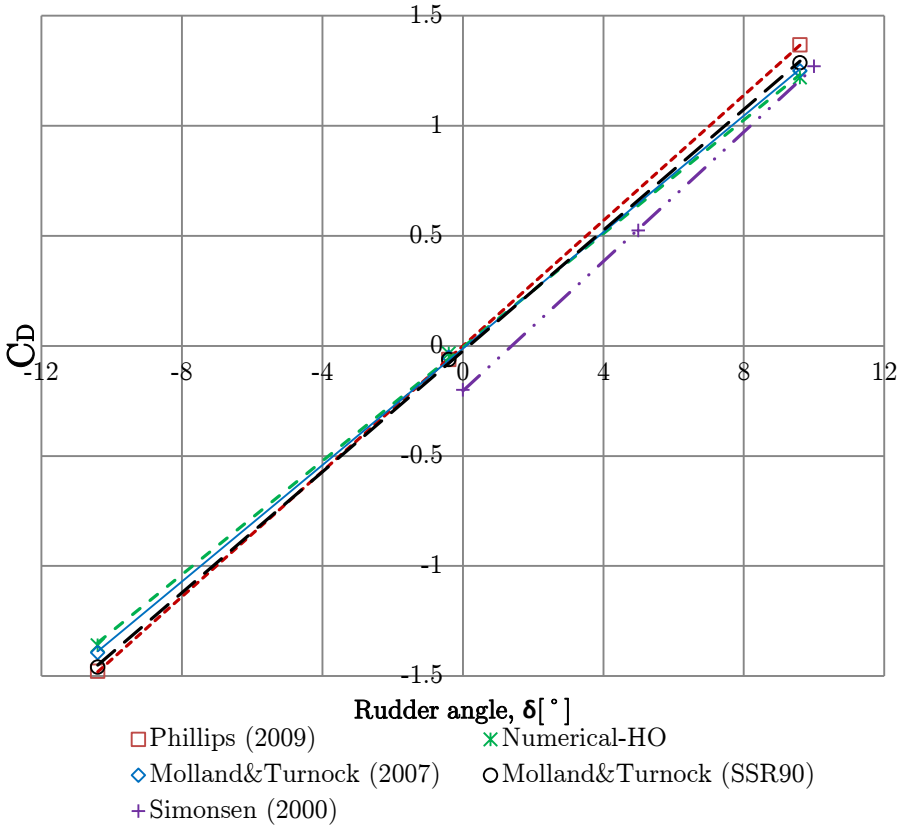

[b]

Figure A2.4: Rudder lift performance[a] freestream [b] J = 0.35

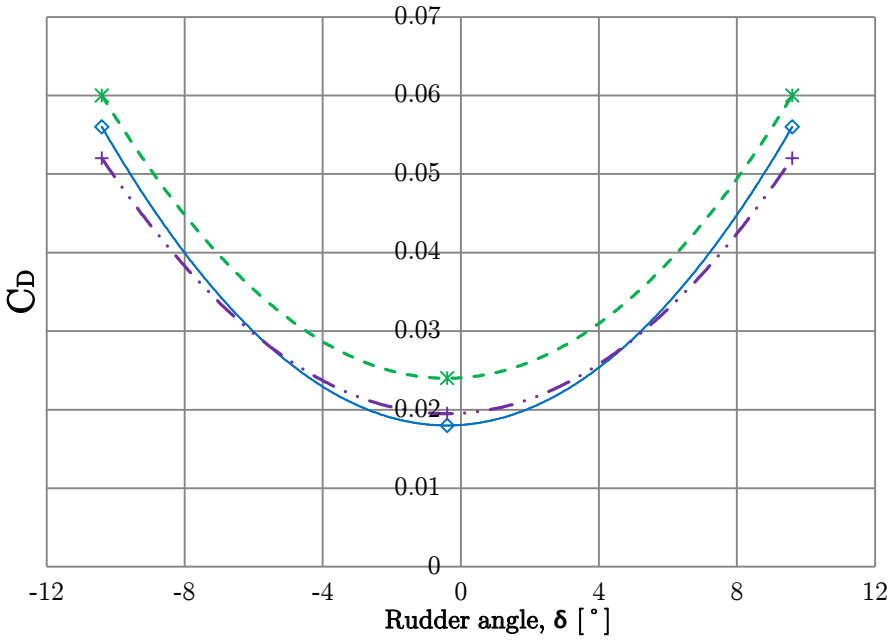

[a]

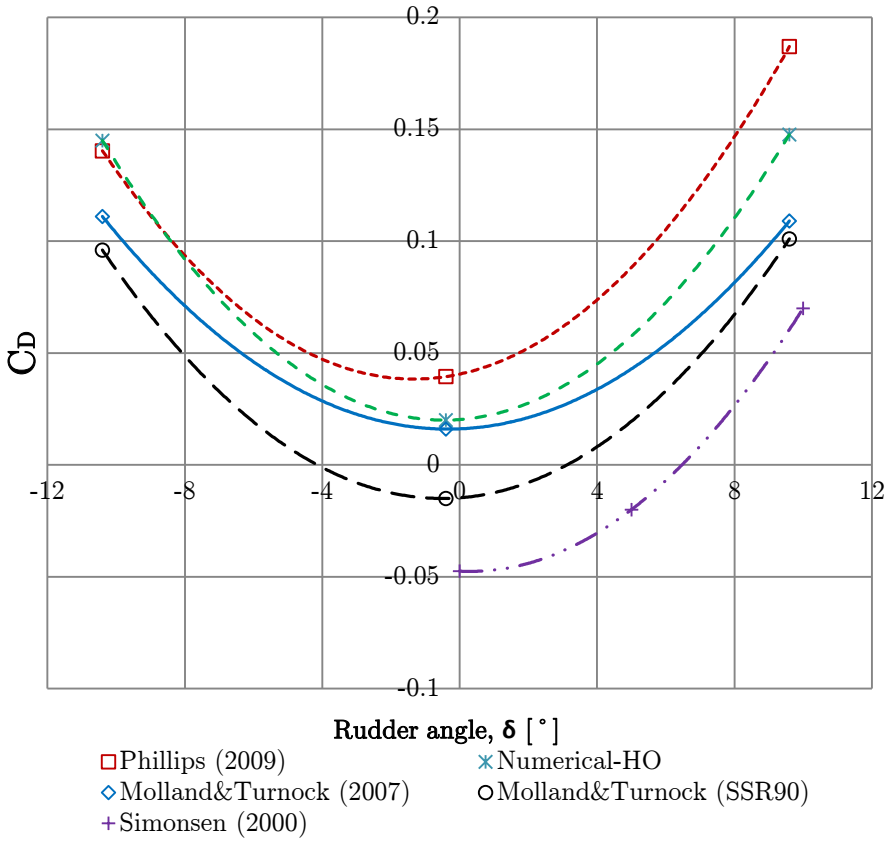

[b]

Figure A2.5: Rudder drag performance[a] freestream [b] J = 0.35

- Span 830mm, 940mm, 970mm: - Areas around the rudder tip. Good agreement was observed for the plots of pressure distribution. The resulting tip vortex introduces unsteadiness in the flow. This unsteadiness could not be fully captured

due to by the level of mesh density used. Works by Date, (2004) highlight the difficulties in resolving the rudder tip vortex unless significantly larger meshes (approx. 20M) are used. This accounted for the minor differences observed in the plots.

Similar tendency were observed for the freestream rudder pressure plots. All location considered showed good agreement with the experiments, with all lower surfaces having favourable pressure gradient with decreasing pressures from the leading edge to mid chords. The formation of suction peak at the upper surface can also be observed. The bulge in the Span 970mm is due to the tip vortex. This was not captured due to similar reasons outlined above.

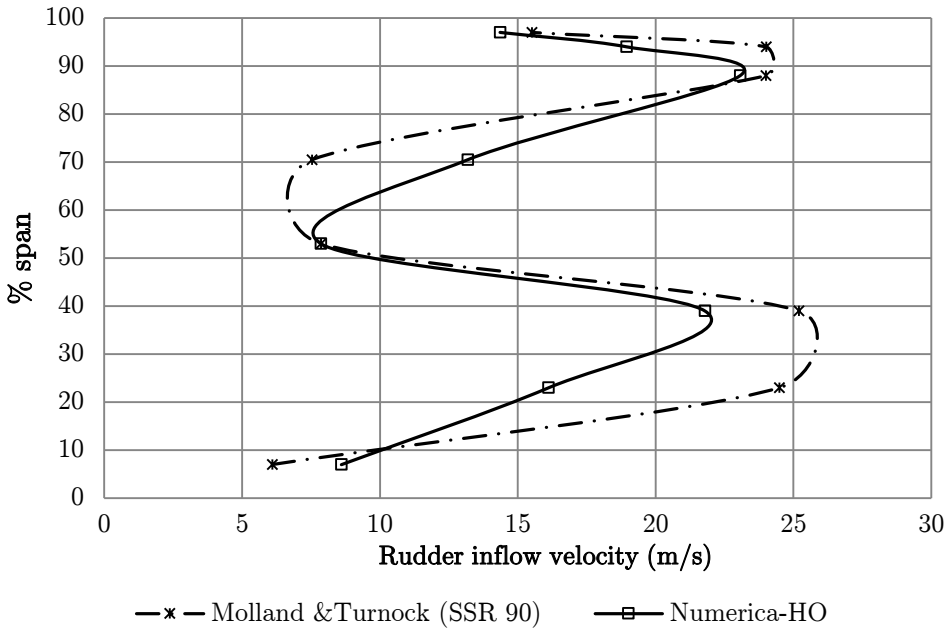

Figure A2.6: Rudder inflow velocity, J = 0.35, δ = 9.6.

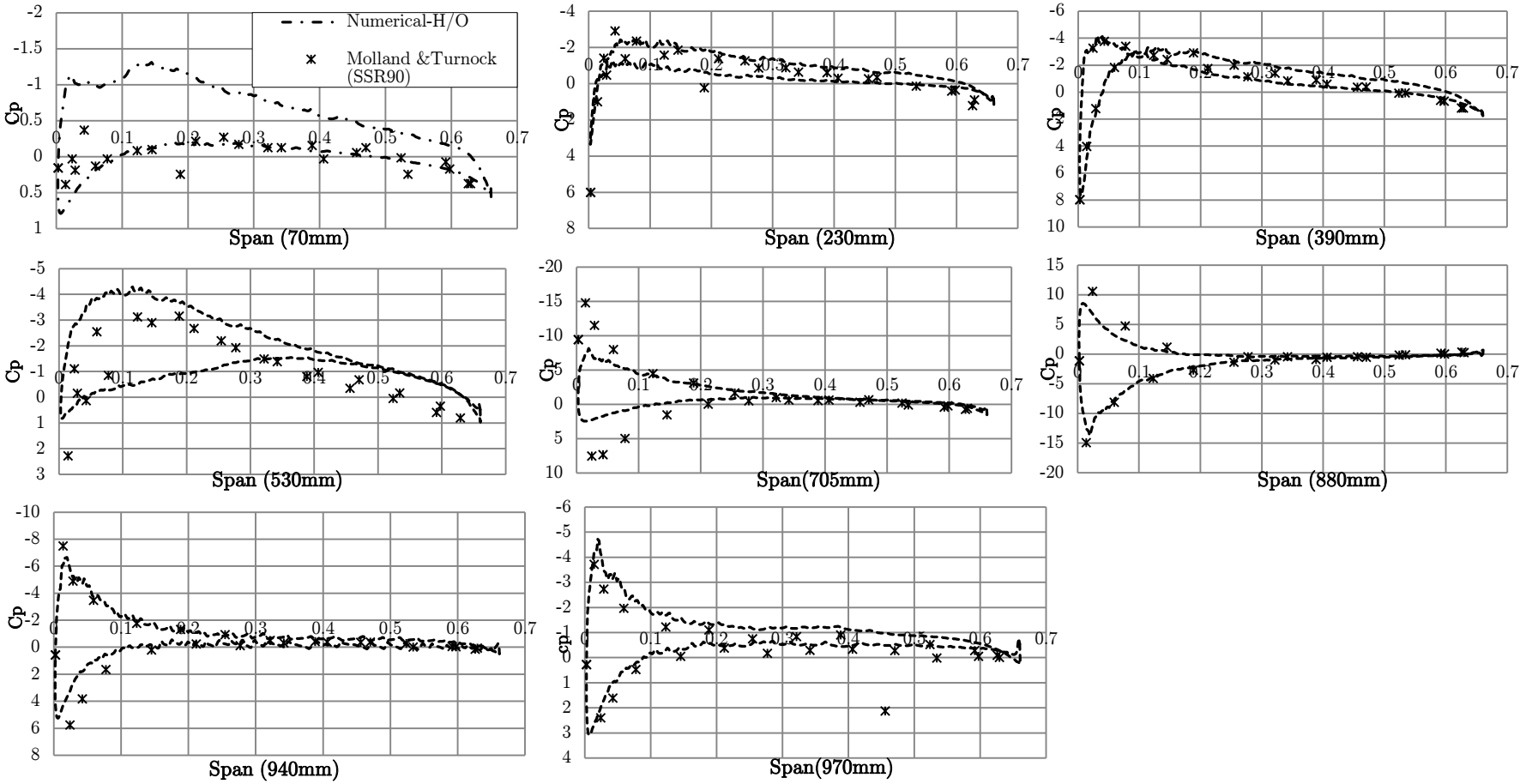

Figure A2.7: Rudder pressure distribution, J = 0.35, δ = 9.6

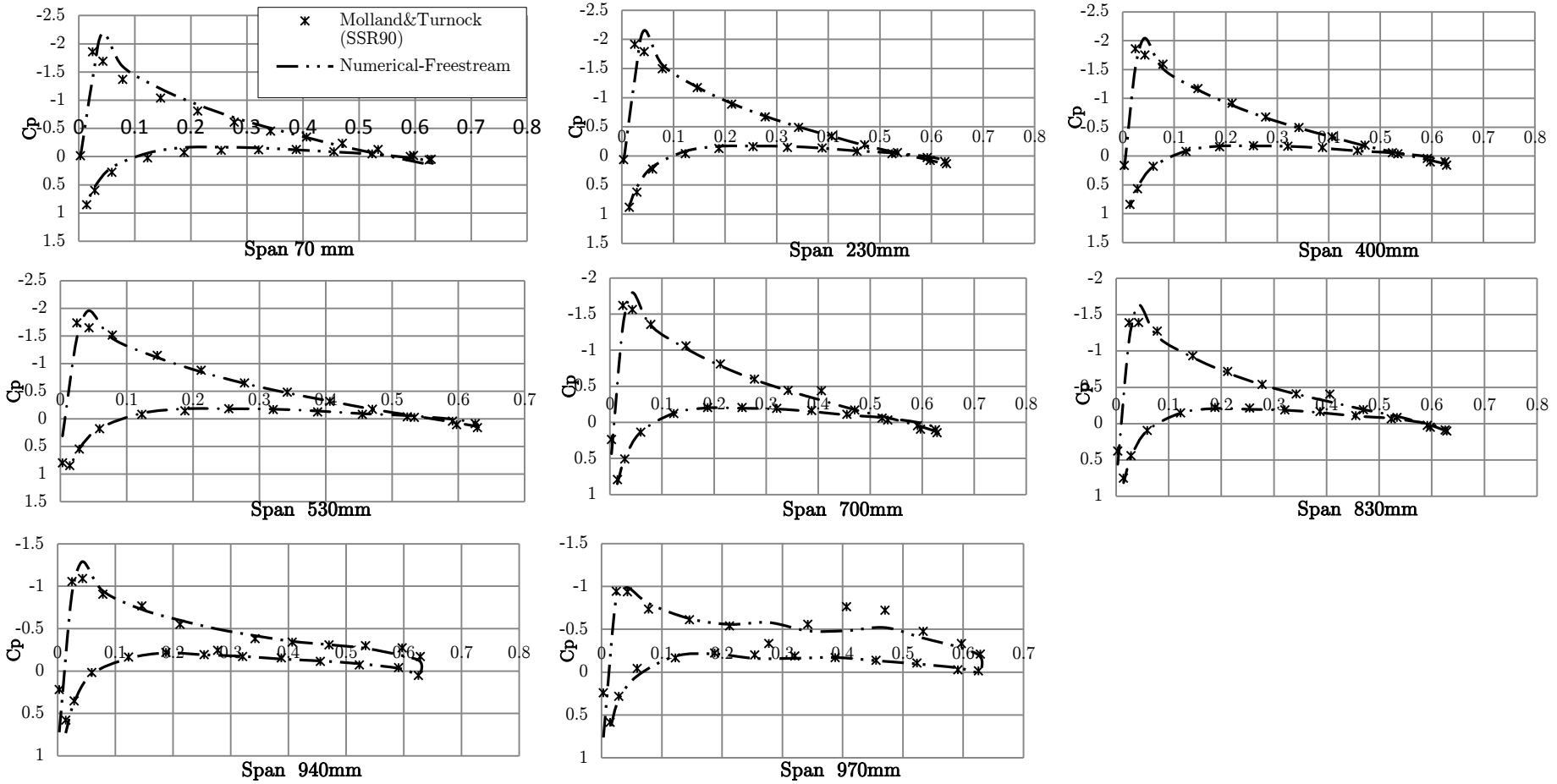

Figure A2.8: Chordwise pressure distribution at selected positions of span; Freestream rudder No.2, $\delta = 9.6^{o}$

A2.3.3 Velocity distribution at the rudder

Figure A2.9 shows the axial velocity contours and cross flow vectors at different x positions along the rudder and in the wake. This was calculated in order to provide information on the influence of the propeller on the flow around the rudder and its wake. Six locations were considered and the results are outlined below:

- X = 0.07chords:- Around the leading edge of the rudder. Propeller effect is seen over part of the rudder in the slipstream, with high axial velocity at both sides of the rudder. Early development of the tip vortex can also be observed.
- X = 0.22chords:- The developing tip vortex and swirl in the flow forces high velocity regions on the pressure side (right side) to the root. Alternatively, the high velocity region at the suction side also moves upwards. Tip vortex rotates in the same direction as the propeller.
- X = 0.38chords:- The same effect as 0.22chords is observed. Fully developed tip vortex which is caused by the pressure difference between suction and pressure sides is observed. Shift in propeller race is more toward the pressure side as compared to 0.22chords.
- X = 0.75chords:- Rudder trailing edge. Tip vortex is seen to dominate the flow, and draws more fluid from the suction side to the pressure side.
- X = 1.12chords:- The rudder wake mixes with the surrounding fluid. Fully developed tip vortex breaks up and forms secondary vortices.
- X = 1.50chords:- Highly distorted propeller race. Rudder wake is almost completely mixed with the surrounding fluid. Secondary vortices can still be observed.

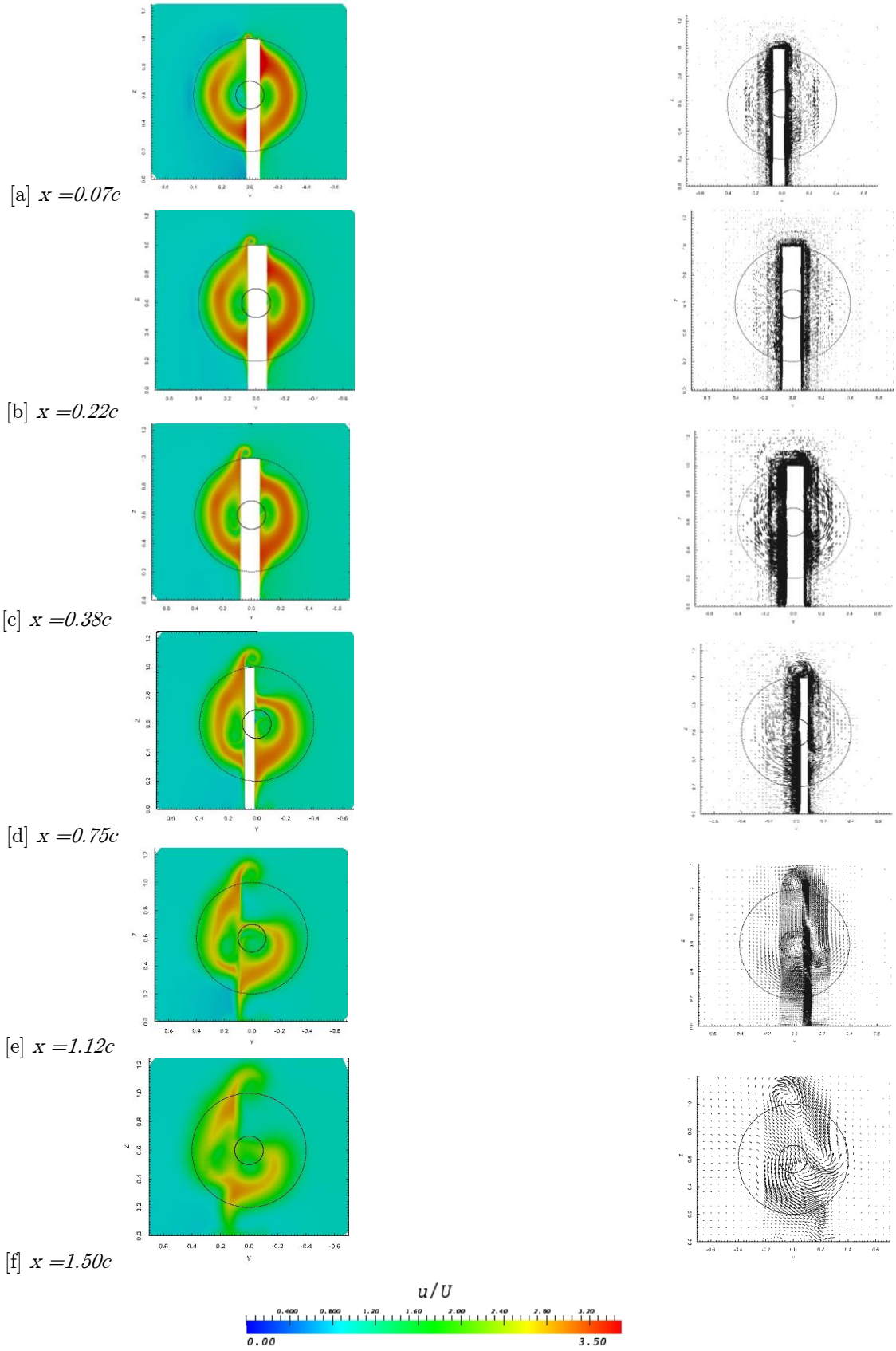

Figure A2.9: Axial velocity contours and cross flow vectors at various x positions, $\delta = 10^{o}$

A2.4 Conclusions

- In the current chapter, a numerical study on the interaction between the propeller, rudder and hull has been presented. The flow around the rudder has been calculated using RANS method and an actuator disc propeller model with load distribution based on the Hough and Ordway (1965).The study was aimed at investigating the interaction between the propeller and the rudder in a uniform inflow conditions and also to provide some knowledge and experience necessary for the generating a full numerical propeller, rudder and hull model. The results highlight that simple body force propeller approaches can be quickly and reliably used to predict rudder forces within 10% of experimentally calculated values.
- When a rudder is place in the race of the propeller, lift increases, when compared to a rudder in freestream. This lift increases with increased propeller loading.
- The velocity plots showed the ability of the propeller model in accelerating the flow axially over part of the rudder in the slipstream. The rotation in the slipstream changes the local incidence along the rudder.
- The propeller model was able to recreate the rudder pressure distributions and the resulting lift coefficient compared well with experiment. Because the propeller rig was neglected, there could have been some flow straightening which was not captured and might have contributed to the discrepancies in the rudder drag.
- The key limitation of the methodology presented above is the impact of the rudder on the performance of the propeller. Because the propeller forces were prescribed the influence of rudder flow on the propeller flow was not captured.
- The numerical simulation allows easy extraction of the local inflow angles to the rudder. This is important for the purpose of cavitation since twisted rudder configurations can be rapidly developed based on bespoke inflow.

To conclude this chapter and to relate this investigation to a full scale twin skeg ship's rudder and propeller geometries, since the lift curve slope was within 5% of the experimental value, the Hough and Ordway propeller model can be considered acceptable for initial investigation on the influence of standard ship propellers on downstream rudders. The most conspicuous failing of the Hough and Ordway propeller model is that the resulting flow will look very different to that induced by a rotating propeller. This is because the blockage effect of the rudder on the propeller and the radial and circumferential variations along the blades cannot be captured with this approach. However for the initial estimation of power losses, exact "mirroring" of the flow is not essential as long as the required conditions of the flow (head) are adequately captured.